



MDOT State Study 316 – Development of Advanced Landslide Investigation Protocol Using Geophysical Methods for Mississippi

FINAL REPORT



Sadik Khan, Ph.D., P.E.

Farshad Amini, Ph.D., P.E.

Rakesh Salunke, E.I.

Masoud Nobahar Ph.D., E.I.

Department of Civil and Environmental Engineering,

Jackson State University,

1400 J.R. Lynch Street, JSU Box 17068

Jackson, MS 39217-0168, USA

June 30, 2023

FHWA Technical Report Documentation Page

1. Report No. FHWA/MDOT-RD-23-316	2. Government Accession No.	3. Recipient's Catalog No.	
4. Title and Subtitle Development of Advanced Landslide Investigation Protocol Using Geophysical Methods for Mississippi		5. Report Date: June 30, 2023	
		6. Performing Organization Code	
7. Author(s) Sadik Khan, Ph.D., P.E. https://orcid.org/0000-0002-0150-6105 Farshad Amini, Ph.D., P.E., F.ASCE https://orcid.org/0000-0003-2899-0045 Rakesh Salunke, E.I. https://orcid.org/0000-0003-2466-1121 Masoud Nobahar, Ph.D., E.I. https://orcid.org/0000-0001-8457-7234		8. Performing Organization Report No. State Study 316	
		9. Performing Organization Name and Address Mississippi Department of Transportation PO Box 1850 Jackson, MS 39215-1850	
		10. Work Unit No. (TRAIS)	
		11. Contract or Grant No. SPR-2020-00(001)/108365-1011000	
12. Sponsoring Agency Name and Address		13. Type Report and Period Covered July 01, 2020 to June 30, 2023	
		14. Sponsoring Agency Code	
15. Supplementary Notes			
<p>16. Abstract</p> <p>Slope failures frequently occur in highway embankments in Mississippi due to the existence of highly expansive Yazoo Clay. In addition, the Mississippi climate, especially the high volume of precipitation, plays a major role in the development of landslides. State Study 316 was undertaken to evaluate the landslides throughout the states employing Advanced Geophysical and Near Surface Remote Sensing tools such as electrical resistivity imaging (ERI), LiDAR technology, and drone imaging. These tools were utilized to identify failed areas, determine their depth, and evaluate crucial soil parameters such as moisture content. Six repaired highway slopes were monitored to collect data on in-situ moisture content, matric suction, temperature variations, and deformation to evaluate their long-term performance. Additionally, ERI, LiDAR, drone imaging, and other advanced investigations were conducted on 20 failed slope sites to evaluate the causes and mechanism failure.</p> <p>The results of the ERI testing showed that shallower depths had higher resistivity values due to unsaturated soil, cracks, displaced disturbed soils, and air pockets that increased the air void ratio. The DEMs generated from drone imagery helped estimate the amount of displaced soil, identify the depth of the slip surface, and recreate failure conditions using numerical modeling tools. The stacked surface profiles developed from the LiDAR point cloud showed details of extreme surficial movement and helped accurately quantify the settlement. The DEMs and the surface profiles can be used as baseline data for future comparisons. Adopting these advanced tools for future research will significantly advance the quality of site investigations and increase the reliability of the design of transportation GEO infrastructures in Mississippi.</p>			
17. Key Words Expansive Soil, Landslide, Geophysical Method, Performance		18. Distribution Statement Unclassified	
19. Security Classified Unclassified	20. Security Classified Unclassified	21. No. of Pages: 213	22. Price

DISCLAIMER

Neither Jackson State University nor the Mississippi Department of Transportation endorse service providers, products, or manufacturers. Trade names or manufacturers' names appear herein solely because they are considered essential to the purpose of this report. The contents of this report do not necessarily reflect the views and policies of the sponsoring agency.

MDOT STATEMENT OF NONDISCRIMINATION

The Mississippi Department of Transportation (MDOT) operates its programs and services without regard to race, color, national origin, sex, age or disability in accordance with Title VI of the Civil Rights Act of 1964, as amended, and related statutes and implementing authorities.

MISSION STATEMENTS

Mississippi Department of Transportation (MDOT)

MDOT is responsible for providing a safe intermodal transportation network that is planned, designed, constructed and maintained in an effective, cost efficient and environmentally sensitive manner.

Research Division

MDOT Research Division supports MDOT's mission by administering Mississippi's State Planning and Research (SP&R) Part II funds in an innovative, ethical, accountable, and efficient manner, including selecting and monitoring research projects that solve agency problems, move MDOT forward, and improve the network for the traveling public.

ACKNOWLEDGMENTS

The authors sincerely appreciate the contributions made to the study by Cindy Smith, P.E. and Alex Middleton, P.E. of the Research Division; and Griffin Sullivan, P.E. and Ian La Cour, P.E. of the MDOT Material Division. The authors also sincerely acknowledge the contributions of Mike Stroud, P.E.

TABLE OF CONTENTS

DISCLAIMER	ii
MDOT STATEMENT OF NONDISCRIMINATION	iii
MISSION STATEMENTS	iii
ACKNOWLEDGMENTS	iv
Executive Summary	1
Chapter 1 Introduction	2
1.1 Background.....	2
1.2 Objectives	3
1.3 Methodology.....	3
Chapter 2 Landslide Investigation Methods	5
2.1 Landslides.....	5
2.2 Expansive Soil	5
2.2.1 Clay Soil Mineralogy	7
2.3 Climate Factors That Impact Expansive Clay Soil.....	9
2.4 Advanced Landslide Investigation Methods	9
2.4.1 Geophysical Field Investigations, Using Electrical Resistivity Imaging (ERI)	9
2.4.2 Remote Sensing in Field Investigations, Using Unmanned/Uncrewed Aerial Vehicles (UAVs).....	11
2.4.3 Remote Sensing in Field Investigations, Using Light Detection and Ranging (LiDAR)	13
Chapter 3 Investigations of Instrumented Slopes	15
3.1 Site Selection	15
3.2 Field Instrumentation.....	16
3.3 Instrumented Slope 1 (I-Slope 1): I220N Ramp Toward I55N Highway Slope	18
3.3.1 Field Monitoring Results	19
3.4 Instrumented Slope 2 (I-Slope 2): Metrocenter Highway Slope	25
3.4.1 Field Monitoring Results	26
3.5 Instrumented Slope 3 (I-Slope 3): Terry Road Highway Slope	31
3.5.1 Field Monitoring Results	33
3.6 Instrumented Slope 4 (I-Slope 4): Highland Drive Highway Slope.....	38

3.6.1	Field Monitoring Results	40
3.7	Instrumented Slope 5 (I-Slope 5): Sowell Road Highway Slope	44
3.7.1	Field Monitoring Result.....	46
3.8	Instrumented Slope 6 (I-Slope 6): McRaven Road Highway Slope.....	51
3.8.1	Field Monitoring Results	53
3.9	I220S Ramp Toward I20E Highway Slope	59
Chapter 4	Investigation of Highway Slopes Using Remote Sensing and Geophysical	
Testing Tools	61
4.1	Advanced Evaluation of Instrumented Slope Sites	61
4.1.1	Instrumented Slope 1: I220N Ramp toward I55N	62
4.1.2	Instrumented Slope 2: MetroCenter Highway Slope	72
4.1.3	Instrumented Slope 3: Terry Road Highway Slope	79
4.1.4	Instrumented Slope 4: Highland Drive Highway Slope	89
4.1.5	Instrumented Slope 5: Sowell Road Highway Slope	97
4.1.6	Instrumented Slope 6: McRaven Road Highway Slope	105
4.2	Advanced Evaluation of the Failed Slope Sites.....	113
4.2.1	Failed Slopes Site Selection.....	113
4.2.2	Failed Slope 2: I-20 Slide Repair Near Exit 100	115
4.2.3	Failed Slope 3: SR 25 Southbound 1.0-mile North of the Rankin/Scott Co Line	118
4.2.4	Failed Slope 4: SR 25/43 Interchange.	119
4.2.5	Failed Slope 5: Big Black River	128
4.2.6	Failed Slope 6: Metrocenter ERI Test Site	133
4.2.7	Failed Slope 7: US 49 South Slope.....	139
4.2.8	Failed Slope 8: 178 Union Slide	142
4.2.9	Failed Slope 9: Dogwood.....	144
4.2.10	Failed Slope 10: US 49 North Slope Profile Summer 2021	146
4.2.11	Failed Slope 12: Big Black River I20 Eastbound Slope	149
4.2.12	Failed Slope 13: US 51 South near Gallatin St.....	151
4.2.13	Failed Slope 14: US 49 Slope in Simpson County (Vetiver Site).	153
4.2.14	Failed Slope 15: Slope Along US 27	160
4.2.15	Failed Slope 17: I-20 EB Approx 1 Mile E of SR 481 at Forrest Near MP 89 Along Mainline Inside Slope	163

4.2.16	Failed Slope 18: I-55 NB Exit Ramp at Wynndale Rd Interchange Along Outside Backslope	169
4.2.17	Failed Slope 19: Mannsdale Rd HW 463 NB (Madison Site).....	174
4.2.18	Failed Slope 20: Mannsdale Rd HW 463 SB (Madison Site).....	177
Chapter 5	Application of Advanced Landslide Monitoring Methods	179
5.1	Introduction	179
5.1.1	Instrumentation	179
5.1.2	Electrical Resistivity Imaging (ERI).....	179
5.1.3	LiDAR.....	179
5.1.4	UAV	180
5.2	ERI, LiDAR and UAV for Site Characterization	180
5.2.1	Site Description & Methodology	180
5.2.2	Data Collection	180
5.2.3	Data Analysis & Results	182
5.3	Predicting Soil Moisture from UAV Images and Machine Learning Methods.....	193
5.4	Comparison of ERI and Instrumentation for Quantifying Soil Moisture Content and Soil Matric Suction.....	196
5.4.1	Field Instrumentation	197
5.4.2	ERI Testing Results	200
5.4.3	Soil Resistivity vs. Soil Matric Suction	201
5.5	Integrating ERI and UAV Results with Numerical Modeling for Back-Calculations of Soil Strength Properties	201
Chapter 6	Conclusion.....	204
References	207

LIST OF FIGURES

Figure 1.1 Moisture and Suction Variation Profiles from FEM Flow Analysis: (a) Initial Condition, (b) 7 Days after 2 in. Rainfall in One Day (<i>from Khan et al. 2020</i>).....	3
Figure 2.1 Seasonal Fluctuations in Water Content and Suction (Blight, 1997).....	7
Figure 2.2 Layout of Clay Mineral Classification (TO: One tetrahedral sheet to one octahedral and TOT: an octahedral sheet in the middle of two tetrahedral sheets) (Tournassat et al., 2015)	8
Figure 2.3 Photogrammetry Tools: (a) Drone with sensor payloads, (b) Lidar and Thermal Camera Sensors, (c) Lidar Terrestrial Scanner	12
Figure 2.4 Drone LiDAR and Photogrammetry Outcomes	13
Figure 3.1 HWS Locations in Jackson (Reference Sites)	15
Figure 3.2 Instrumentation Layout at Each I-Slope and Images of the Individual Sensors	17
Figure 3.3 Location of I-Slope 1	18
Figure 3.4 Instrumentation Layout at I-Slope 1	19
Figure 3.5 Displacements at Inclinator 1 at I-Slope 1.....	20
Figure 3.6 Deformations in the As-Built Section from surficial levels of Inclinator 1 at I-Slope 1.....	20
Figure 3.7 Horizontal Displacements of the Inclinator 2 at I-Slope 1	21
Figure 3.8 Variations of Lateral deformation at I-Slope 1’s Repaired Section	21
Figure 3.9 Variation of parameters at I-Slope 1 (a) Matric Suction, (b) Moisture Content and Rainfall data from Instrumentation 1	22
Figure 3.10 Variation of parameters at I-Slope 1 (a) Matric Suction, (b) Moisture Content and Rainfall data from Instrumentation 2.....	23
Figure 3.11 Variation of parameters at I-Slope 1 (a) Matric Suction, (b) Moisture Content and Rainfall data from Instrumentation 3.....	23
Figure 3.12 Variations of Air and Soil Temperature at I-Slope 1 (a) Instrumentation 1, (b) Instrumentation 2, and (c) Instrumentation 3.....	24
Figure 3.13 Location of I-Slope 2.....	25
Figure 3.14 Instrumentation layout at I-Slope 2	26
Figure 3.15 Displacements at Inclinator 1 at I-Slope 2.....	27
Figure 3.16 Overtime Lateral Deformation at the Top of Inclinator 1 at I-Slope 2.....	27
Figure 3.17 Displacements at Inclinator 2 at I-Slope 2.....	28
Figure 3.18 Overtime Lateral Deformation at the Top of Inclinator 2 at I-Slope 2.....	28
Figure 3.19 Variation of parameters at I-Slope 2 (a) Matric Suction, (b) Moisture Content and Rainfall data from Instrumentation 1	29
Figure 3.20 Variation of parameters at I-Slope 1 (a) Matric Suction, (b) Moisture Content and Rainfall data from Instrumentation 2.....	30

Figure 3.21 Variation of parameters at I-Slope 1 (a) Matric Suction, (b) Moisture Content and Rainfall data from Instrumentation 3	30
Figure 3.22 Variations of Air and Soil Temperature at I-Slope 1 (a) Instrumentation 1, (b) Instrumentation 2, and (c) Instrumentation 3.....	31
Figure 3.23 Location of I-Slope 3.....	32
Figure 3.24 Instrumentation Layout at I-Slope 3.....	33
Figure 3.25 Displacements at Inclinator 1 (as built section) of I-Slope 3.....	34
Figure 3.26 Overtime Lateral Deformation near the Top of Inclinator 1 (as built section) at I-Slope 3	34
Figure 3.27 Displacements at Inclinator 2 (repaired section) of I-Slope 3	35
Figure 3.28 Overtime Lateral Movement at the Top of Inclinator 2 (repaired section) at I-Slope 3.....	35
Figure 3.29 Variation of parameters at I-Slope 3 (a) Matric Suction, (b) Moisture Content and Rainfall data from Instrumentation 1	36
Figure 3.30 Variation of parameters at I-Slope 3 (a) Matric Suction, (b) Moisture Content and Rainfall data from Instrumentation 2.....	37
Figure 3.31 Variation of parameters at I-Slope 3 (a) Matric Suction, (b) Moisture Content and Rainfall data from Instrumentation 3.....	37
Figure 3.32 Variations of Air and Soil Temperature at I-Slope 1 (a) Instrumentation 1, (b) Instrumentation 2, and (c) Instrumentation 3.....	38
Figure 3.33 Location of I-Slope 4.....	39
Figure 3.34 Instrumentation and Inclinator at I-Slope 4	40
Figure 3.35 Displacements at Inclinator 1 at I-Slope 4.....	41
Figure 3.36 Overtime Lateral Deformation at the Top of Inclinator 1 at I-Slope 4.....	41
Figure 3.37 Variation of parameters at I-Slope 4 (a) Matric Suction, (b) Moisture Content and Rainfall data from Instrumentation 1.....	42
Figure 3.38 Variation of parameters at I-Slope 4 (a) Matric Suction, (b) Moisture Content and Rainfall data from Instrumentation 2.....	43
Figure 3.39 Variation of parameters at I-Slope 4 (a) Matric Suction, (b) Moisture Content and Rainfall data from Instrumentation 3.....	43
Figure 3.40 Variations of Air and Soil Temperature at I-Slope 4 (a) Instrumentation 1, (b) Instrumentation 2, and (c) Instrumentation 3.....	44
Figure 3.41 Location of I-Slope 5.....	45
Figure 3.42 I-Slope 5 Instrumentation Layout.....	46
Figure 3.43 Displacements at Inclinator 1 at I-Slope 5.....	47
Figure 3.44 Overtime Lateral Deformation at the Top of Inclinator 1 at I-Slope 5.....	47

Figure 3.45 Displacements at Inclinator 2 at I-Slope 5.....	48
Figure 3.46 Variation of parameters at I-Slope 5 (a) Matric Suction, (b) Moisture Content and Rainfall data from Instrumentation 1	49
Figure 3.47 Variation of parameters at I-Slope 5 (a) Matric Suction, (b) Moisture Content and Rainfall data from Instrumentation 2.....	49
Figure 3.48 Variation of parameters at I-Slope 5 (a) Matric Suction, (b) Moisture Content and Rainfall data from Instrumentation 3.....	50
Figure 3.49 Variations of Air and Soil Temperature at I-Slope 5 (a) Instrumentation 1, (b) Instrumentation 2, and (c) Instrumentation 3.....	51
Figure 3.50 Location of I-Slope 6.....	52
Figure 3.51 Instrumentation Layout at I-Slope 6.....	52
Figure 3.52 Displacements at Inclinator 1 at I-Slope 6.....	53
Figure 3.53 Overtime Lateral Deformation at the Top of Inclinator 1 at I-Slope 6.....	54
Figure 3.54 Displacements at Inclinator 2 at I-Slope 6.....	54
Figure 3.55 Overtime Lateral Deformation at the Top of Inclinator 2 at I-Slope 6.....	55
Figure 3.56 Variation of parameters at I-Slope 6 (a) Matric Suction, (b) Moisture Content and Rainfall data from Instrumentation 1	56
Figure 3.57 Variation of parameters at I-Slope 6 (a) Matric Suction, (b) Moisture Content and Rainfall data from Instrumentation 2.....	56
Figure 3.58 Variation of parameters at I-Slope 6 (a) Matric Suction, (b) Moisture Content and Rainfall data from Instrumentation 3.....	57
Figure 3.59 Variations of Air and Soil Temperature at I-Slope 6 (a) Instrumentation 1, (b) Instrumentation 2, and (c) Instrumentation 3.....	58
Figure 3.60 Location of I-Slope 7	59
Figure 3.61 Displacement at I-Slope 7.....	60
Figure 3.62 Overtime lateral deformation in I-Slope 7.....	60
Figure 4.1 Slope 1 Location.....	63
Figure 4.2 Slope 1 ERI Line A: (a) Spring 2021, (b) Summer 2021, (c) Fall 2021, (d) Winter 2021/Spring 2022, (e) Fall/Winter 2022.....	64
Figure 4.3 Slope 1 ERI Line B: (a) Spring 2021, (b) Summer 2021, (c) Fall 2021, (d) Winter 2021/Spring 2022, (e) Fall/Winter 2022.....	65
Figure 4.4 Site 1 Drone Image (Summer 2021).....	67
Figure 4.5 Site 1 Drone Image (Fall 2021)	67
Figure 4.6 Slope 1 Drone Images: (a) DEM, (b)Topography (Spring 2022).....	68
Figure 4.7 Slope 1 Drone Images: (a) DEM, (b)Topography (Fall 2022).....	69

Figure 4.8 LiDAR Point Cloud Surface Topography Instrumented Slope 1: I220 - I55N (a) Summer 2021 (b) Fall 2021 (c) Spring 2022 (d) Fall/Winter 2022 Section (e) Overlaid Surface Profile A-A' (f) Overlaid Surface Profile B-B'	72
Figure 4.9 Location of Slope 2.....	73
Figure 4.10 Slope 2 ERI Line A: (a) Spring 2021, (b) Summer 2021, (c) Fall 2021, (d) Winter 2021/Spring 2022, (e) Fall/Winter 2022.....	73
Figure 4.11 Slope 2 ERI Line B: (a) Spring 2021, (b) Summer 2021, (c) Fall 2021, (d) Winter 2021/Spring 2022, (e) Fall/Winter 2022.....	74
Figure 4.12 Image Taken by Drone of Slope 2 (Summer 2021).....	75
Figure 4.13 Drone Image of Slope 2 in Fall 2021: (a) DEM, (b) 3D Model and Surface Profile 76	
Figure 4.14 Drone Image DEM of Slope 2 (Fall 2022).....	77
Figure 4.15 Season Variations in Slope 2's LiDAR Point Cloud Surface Topography: (a) Summer 2021, (b) Fall 2021, (c) Spring 2022, and (d) Fall 2022.....	79
Figure 4.16 Seasonal Variations in Slope 2's LiDAR Point Cloud Surface Profiles: (a) Section A-A', (b) Section B-B', (c) Section C-C'	79
Figure 4.17 Location of Slope 3 and ERI Test Lines.....	80
Figure 4.18 ERI Line A of I-Slope 3: (a) Spring 2021, (b) Summer 2021, (c) Fall 2021, (d) Winter 2021/Spring 2022, (e) Fall/Winter 2022.....	81
Figure 4.19 ERI Line B of I-Slope 3: (a) Spring 2021, (b) Summer 2021, (c) Fall 2021, (d) Winter 2021/Spring 2022, (e) Fall/Winter 2022.....	82
Figure 4.20 Digital Elevation Model based on Drone Imagery of Instrumented Slope 3 (Summer 2021)	83
Figure 4.21 Drone Imagery of Slope 3: (a) Digital Elevation Model, (b) 3D Model, and Surface Profile (Fall 2021).....	84
Figure 4.22 Drone Imagery of Slope 3: (a) Digital Elevation Model, (b) 3D Model, and Surface Profile (Fall 2021).....	85
Figure 4.23 LiDAR Point Cloud Surface Topography of Slope 3 Depicting Seasonal Variations: (a) Summer 2021, (b) Fall 2021 (c) Spring 2022 (d) Fall 2022.....	88
Figure 4.24 LiDAR Point Cloud Surface Profiles of Slope 3 with Seasonal Variations: (a) Section A-A', (b) Section B-B'	88
Figure 4.25 Location of Slope 4, with ERI Test Lines	89
Figure 4.26 Line A of Slope 4: (a) Spring 2021, (b) Summer 2021. (c) Fall 2021, (d) Winter 2021/Spring 2022, (e) Fall/Winter 2022.....	90
Figure 4.27 Line B of Slope 4: (a) Spring 2021, (b) Summer 2021, (c) Fall 2021, (d) Winter 2021/Spring 2022, (e) Fall/Winter 2022.....	91
Figure 4.28 Digital Representation Derived from Drone Imagery of Slope 4 (Summer 202) ...	92
Figure 4.29 Digital Representation of Slope 4 Derived from Drone Imagery (Fall 2021).....	92

Figure 4.30 Digital Representation of Slope 4 Derived from Drone Imagery (Spring 2022)	93
Figure 4.31 Drone Imagery of Slope 4 in Fall/Winter 2022: (a) Digital Elevation Model, (b) 3D Model and Surface Profile, (c) Surface Topography	94
Figure 4.32 LiDAR Point Cloud Surface Topography Seasonal Variations in Slope 4: (a) Summer 2021, (b) Fall 2021, (c) Spring 2022, (d) Fall 2022.....	96
Figure 4.33 LiDAR Point Cloud Surface Profiles of Seasonal Variations for Slope 4: (a) Section A-A', (b) Section B-B'	97
Figure 4.34 Slope 5 ERI Test Lines Location.....	97
Figure 4.35 Results from ERI testing of Line A of Slope 5: (a) Spring 2021, (b) Summer 2021, (c) Fall 2021, (d) Winter 2021/Spring 2022, (e) Fall/Winter 2022	98
Figure 4.36 Line B of Slope 5: (a) Spring 2021, (b) Summer 2021, (c) Fall 2021, (d) Winter 2021/Spring 2022, (e) Fall/Winter 2022.....	99
Figure 4.37 Slope 5 Drone Image (Summer 2021).....	100
Figure 4.38 Drone Image of Slope 5 (Fall 2021).....	101
Figure 4.39 Slope 5 Drone Image Fall/Winter 2022: (a) Digital Elevation Model, (b) 3D Model & Surface Profile, and (c) Surface Topography	102
Figure 4.40 LiDAR Point Cloud Surface Topography Seasonal Variations in Slope 5: (a) Summer 2021, (b) Fall 2021, (c) Spring 2022, (d) Fall 2022.....	104
Figure 4.41 LiDAR Point Cloud Surface Profiles Seasonal Variations for Slope 5: (a) Section A-A' and (b) Section B-B'	105
Figure 4.42 Location of ERI Test Lines in Slope 6	106
Figure 4.43 Slope 6 ERI Line A: (a) Spring 2021, (b) Summer 2021, (c) Fall 2021, (d) Winter 2021/Spring 2022, and (e) Fall/Winter 2022	106
Figure 4.44 Slope 6 ERI Line B: (a) Spring 2021, (b) Summer 2021, (c) Fall 2021, (d) Winter 2021/Spring 2022, and (e) Fall/Winter 2022	107
Figure 4.45 Drone Image of Slope 6 (Summer 2021).....	108
Figure 4.46 Drone Image of Slope 6 (Fall 2021).....	108
Figure 4.47 Drone Images of Slope 6 (Fall/Winter 2022): (a) Digital Elevation Model, (b) 3D Model & Surface Profile, (c) Surface Topography & Profile.....	110
Figure 4.48 LiDAR Point Cloud Surface Topography Seasonal Variations of Slope 6: (a) Summer 2021, (b) Fall 2021, (c) Spring 2022, and (d) Fall/Winter 2022.....	112
Figure 4.49 LiDAR Point Cloud Surface Profiles of Seasonal Variations in Slope 6: (a) Section A-A', (b) Section B-B'	113
Figure 4.50 Drone 3D Model and LiDAR 3D Model of Slope 6	113
Figure 4.51 Geo-location of Failed Slopes	115
Figure 4.52 Location of Failed Slope 2.....	116

Figure 4.53 ERI Test Results of Failed Slope 2: (a) Line A and (b) Line B	116
Figure 4.54 Drone Images of Failed Slope 2	117
Figure 4.55 Failed Slope 2: (a) Surface Topography and (b) Surface Profile	118
Figure 4.56 ERI Location in Failed Slope 3.....	119
Figure 4.57 ERI Test Results of Failed Slope 3.....	119
Figure 4.58 Failed Slope 4: Slope along SR25 SB SR 25/43 Interchange	120
Figure 4.59 ERI Test Results of Failed Slope 4 -Slope along SR25 SB: (a) Line A, (b) Line B, (c) Line C.....	120
Figure 4.60 Location of ERI Lines at Failed Slope 4 - SR25/43 Interchange Left Abutment ..	121
Figure 4.61 ERI Test Results of Failed Slope 4 at Left Abutment: (a) Line D and (b) Line E	121
Figure 4.62 ERI Test Location of Failed Slope 4- SR25/43 Interchange Right Abutment	122
Figure 4.63 Failed Slope 4 ERI Test Results - SR25/43 Interchange Right Abutment (a) Line F and (b) Line G.....	122
Figure 4.64 Slope 4 Failures: (a) Failure along SR25, (b) Failure of Left Abutment, (c)Failure of Right Abutment.....	124
Figure 4.65 Slope 4 Slide Failure: (a) LiDAR Point Cloud Surface Topography, (b) Surface Profile	125
Figure 4.66 Failed Left Abutment of Slope 4: (a) LiDAR Point Cloud Surface Topography, (b) Surface Profile Section A-A', (c) Surface Profile Section B-B'	126
Figure 4.67 Failed Right Abutment in Slope 4: (a) LiDAR Point Cloud Surface Topography, (b) Surface Profile Section A-A', (c) Surface Profile Section B-B'	127
Figure 4.68 Location of ERI Test Lines in Failed Slope 5 (Big Black River).....	128
Figure 4.69 ERI Test Results of Section 1 of Failed Slope 5: (a) Line A, (b) Line B.....	128
Figure 4.70 ERI Test Results of Section 2 of Failed Slope 5: (a) Line C, (b) Line D.....	129
Figure 4.71 ERI Test Results of Failed Slope 5, Section 3: (a) Line E (b) Line F	129
Figure 4.72 Drone Images of Failed Slope 5: (a) Digital Elevation Model, (b) Surface Topography and Profile (Summer 2021).....	130
Figure 4.73 LiDAR Point Cloud Surface Topography and Profile of Section 1 of Big Black River	131
Figure 4.74 LiDAR Point Cloud Surface Topography and Profile of Section 2 of Big Black River	132
Figure 4.75 LiDAR Point Cloud Surface Topography and Profile of Section 3 of Big Black River Site	132
Figure 4.76 Location of Test Lines for Failed Slope 6	133
Figure 4.77 ERI Test Results for Failed Slope 6: (a) Line A, (b) Line B, (c) Line C, (d) Line D	134

Figure 4.78 Drone Images for Failed Slope 6: (a) Digital Elevation Model, (b) Surface Topography and Profile (Summer 2021)	135
Figure 4.79 Drone Images for Failed Slope 6: (a) DEM, (b) 3D Model View, (c) Surface Topography and Profile (Fall/Winter 2022)	137
Figure 4.80 LiDAR Point Cloud Surface Topography of Failed Slope 6: (a) Summer 2021, (b) Fall 2021, (c) Overlaid Surface Profile	139
Figure 4.81 Location of ERT Test Lines for Failed Slope 7.....	140
Figure 4.82 ERI Test Results of Failed Slope 7: (a) Line A, (b) Line B, (c) Line C.....	141
Figure 4.83 Drone images of Failed Slope 7 (Summer 2021)	142
Figure 4.84 Location of ERI Test Lines in Failed Slope 8	143
Figure 4.85 Results of ERI Test Results for Failed Slope 8: (a) Line A, (b) Line B, (c) Line C	143
Figure 4.86 Location of ERI Test Lines in Failed Slope 9	144
Figure 4.87 ERI Test Results for Failed Slope 9 -Dogwood Slope: (a) Line A, (b) Line B, (c) Line C.....	144
Figure 4.88 Drone Images of Failed Slope 9 (Summer 2021).....	145
Figure 4.89 LiDAR Point Cloud Surface of Failed Slope 9: (a)Topography and (b) Profile View	146
Figure 4.90 Location of ERI Test Lines in Failed Slope 10	147
Figure 4.91 ERI Test Results for Failed Slope 10: (a) Line A, (b) Line B, (c) Line C	147
Figure 4.92 Drone Images of Failed Slope 10 (Summer 2021).....	148
Figure 4.93 LiDAR Point Cloud Surface Topography and Profile View of Failed Slope 10 ...	149
Figure 4.94 ERI Test Lines in Failed Slope 12.....	150
Figure 4.95 ERI Results of Failed Slope 12: (a) Line A (b) Line B	150
Figure 4.96 Drone Images of Failed Slope 12 Captured in Summer 2021: (a) Digital Elevation Model, (b) Surface Topography and Profile	151
Figure 4.97 Drone Images of Failed Slope 13: (a) Digital Elevation Model, (b) Surface Topography (Summer 2021).....	153
Figure 4.98 Location of ERI Test Lines in Failed Slope 14	154
Figure 4.99 ERI Test Results of Failed Slope 14: (a) Line A (b) Line B	154
Figure 4.100 Drone Images of Failed Slope 14: (a) Digital Elevation Model, (b) Surface Topography & Profiles, (c) 3D Model & Surface Profile (Spring 2022)	156
Figure 4.101 Drone Images of Failed Slope 14: (a) Digital Elevation Model, (b) Surface Topography & Profiles, (c) 3D Model & Surface Profile (Fall 2022).....	158
Figure 4.102 LiDAR Point Cloud Surface Topography for Failed Slope 14: (a) Fall 2021, (b) Fall 2022.....	159

Figure 4.103 LiDAR Point Cloud Overlayed Surface Profiles for Failed Slope 14: (a) Profile Section A-A', (b) Profile Section B-B'	160
Figure 4.104 Drone Images of Failed Slope 15: (a) Digital Elevation Model (b) Surface Topography and Profile (Fall 2021)	161
Figure 4.105 LiDAR Point Cloud Surface Topography and Profile View for Failed Slope 15 (Fall 2021)	162
Figure 4.106 ERI Test Lines at Failed Slope 17	163
Figure 4.107 ERI Test Results of Failed Slope 17: (a) Line A (b) Line B	163
Figure 4.108 Drone Images of Failed Slope 17 from Fall 2021: (a) Digital Elevation Model and (b) Surface Topography and Profile	165
Figure 4.109 Drone Images of Failed Slope 17: (a) Digital Elevation Model, (b) Surface Topography, (c) 3D Model & Surface Profile (Fall 2022)	167
Figure 4.110 LiDAR Point Cloud Surface for Failed Slope 17: (a)Topography, (b) Surface Profile (Fall 2021).....	168
Figure 4.111 LiDAR Point Cloud Surface of Failed Slope 17: (a) Topography, (b) Surface Profile View (Fall 2022).....	169
Figure 4.112 Location of ERI Test Lines in Failed Slope 18	170
Figure 4.113 ERI Test Results of Failed Slope 18: (a) Line A and (b) Line B	170
Figure 4.114 Drone Images of Failed Slope 18: (a) Digital Elevation Model, (b) Surface Topography, and (c) 3D Model and Surface Profile (Fall 2022).....	172
Figure 4.115 LiDAR Point Cloud Surface Topography of Failed Slope 18: (a) Surface Topography, (b) Surface Profile Section A-A', (b) Surface Profile Section B-B' (Fall 2022).	173
Figure 4.116 Location of ERI Test Lines in Failed Slope 19	174
Figure 4.117 ERI Test Results of Failed Slope 19: (a) Line A and (b) Line B	174
Figure 4.118 Drone Images of the DEM and Surface Profile of Failed Slope 19 (Spring 2022)	175
Figure 4.119 LiDAR Point Cloud Surface Topography for Failed Slope 19: (a) Fall 2021 and (b) Spring 2022.....	176
Figure 4.120 LiDAR Point Cloud Overlayed Surface Profiles for Failed Slope 19.....	177
Figure 4.121: ERI Test Lines at Failed Slope 20.....	177
Figure 4.122 ERI Test Results of Failed Slope 20: (a) Line A and (b) Line B	178
Figure 4.123 Drone Images of DEM for Failed Slope 20 (Spring 2022)	178
Figure 5.1 Sites Selected for Comparing Results of Geophysical and Remote Sensing Investigations	181
Figure 5.2 Schematic of Methodology (Nobahar et al., 2023)	182

Figure 5.3 ERI Test Results of Line A, B, C & D for Slope along I220N and I55 N Interchange	183
Figure 5.4 ERI Test Site for Slope at Metrocenter (I220S Exit 1B Ramp Toward US80): (a) UAV Orthomosaic Image, (b) UAV DSM, (c) UAV 3D DSM, (d) UAV DTM, (e) UAV Surface Profile	184
Figure 5.5 ERI Test Site for Slope at Metrocenter (I220S Exit 1B Ramp Toward US80): (a) LiDAR Surface Topography Summer 2021, (b) LiDAR Surface Topography Fall/Winter 2022, (c) LiDAR Stacked Surface Profiles	185
Figure 5.6 ERI Test Results for Lines A & B for Slope along I20E Before Exit 100.....	186
Figure 5.7 Slope at I20 EB Exit 100: (a) UAV Orthomosaic Image, (b) UAV DSM, (c) UAV 3D Model, (d) UAV DEM, (e) UAV Surface Profile.....	187
Figure 5.8 LiDAR Results: Surface Topography and Profile View	188
Figure 5.9 ERI Test results for Lines A, B & C for Failed Slope along US49S toward Jackson	189
Figure 5.10 Slope at US49S 20 EB Exit 100: (a) UAV Orthomosaic Image, (b) UAV DSM, (c) UAV Surface Profile.....	190
Figure 5.11 ERI Test Results of Line A, B, and C for Failed Slope along Hwy 25 at MS25/43 Interchange.....	191
Figure 5.12 Slope along SR 25: (a) UAV Orthomosaic Image, (b) UAV DSM, (c) UAV Surface Profile.....	192
Figure 5.13 Slope along SR 25 LiDAR Results: Surface Topography and Profile.....	193
Figure 5.14 Methodology of Predicting Soil Moisture from UAV Images(Salunke et al., 2023)	194
Figure 5.15 Regions of Interest in Optical Images for Pixel Value Extraction	195
Figure 5.16 XGB Model’s Prediction of Soil Moisture Content	195
Figure 5.17 TIR Image of Sowell Road: (a) Dawn and (b) Mid-day.....	196
Figure 5.18 Soil Moisture Prediction Model based on Land Surface Temperature	196
Figure 5.19 Methodology for Developing Resistivity vs Soil Moisture and Soil Suction Models (<i>Nobahar et al. 2022 Geotechnics</i>).....	198
Figure 5.20 (a) Instrumentation in I-Slopes, (b) In-situ Sensor vs Lab Measurement of θ	199
Figure 5.21 Results from Instrumentation for Suction vs. Rainfall at I-Slope 3: (a) Crest, (b) Middle.....	199
Figure 5.22 Instrumentation Results of θ vs Rainfall at I-Slope 3: (a) Crest, (b) Middle.....	200
Figure 5.23 ERI Results of I-Slope 3: (a) Crest, (b) Middle.....	200
Figure 5.24 (a) Resistivity vs Soil Moisture Content, (b) Resistivity vs Matric Suction	201
Figure 5.25 Metrocenter ERI Test Results (I220 S Exit 1B).....	202

Figure 5.26 Metrocenter Drone DEM Deformation (I220S Exit 1B).....	202
Figure 5.27 2D Finite Element Mesh of Slope 1	203
Figure 5.28 Deformation at Failure (when $FS < 1$) with Slip Surface Field Observations	203

LIST OF TABLES

Table 3.1 Locations of Selected Highway Slopes (from Khan et al., 2020).....	16
Table 3.2 Field Instrumentation for Data Collection	17
Table 4.1 Locations of Selected Highway Slope's (<i>from</i> Khan et al., 2020).....	62
Table 4.2 Location of Failed Highway Slopes.....	114
Table 5.1 Soil Parameters of Slope Back-calculated with Numerical Modeling.....	203

EXECUTIVE SUMMARY

The geotechnical infrastructure (geo-infra) assets such as highway earth slopes, embankments, and road and railway subgrades integral to transportation infrastructure are becoming increasingly vulnerable due to extreme precipitation caused by hurricanes and slow-moving storm systems. For instance, a slow-moving storm system in August 2022 resulted in record-breaking torrential downpours in the capital city of Jackson, Mississippi (MS) in the United States of America and severely impacted transportation geo-infrastructure. The extreme precipitation triggered cascading hazards such as flash flooding, soil erosion, buckled and completely washed-out roadway and railway subgrades, scouring, and landslides. Problems originating from such extreme rain events are compounded in Mississippi by the expansive Yazoo clay pervasive in the region and the scorching summers and extreme rainfalls that weaken its shear strength properties and cause shallow and deep-seated landslides and failures. Warning systems and timely evaluations are imperative for taking preventative measures and lessening the impact on geo-infrastructure assets. The traditional in-situ geo-infra evaluation methods are outdated, expensive, and produce spatially restricted information. Many assets go unmonitored and fail without notice due to the absence of monitoring devices. This study investigated the performance of failed and repaired highway embankment side slopes impacted by extreme weather events using advanced non-destructive testing (NDT) methods.

Advanced, multi-faceted, rapid evaluation techniques, including geophysical and remote sensing approaches with high spatial and temporal resolutions, were implemented in this study to evaluate highway embankment slides. Electrical resistivity imaging (ERI), uncrewed aerial vehicles (UAVs) mounted with optical and thermal sensors, and light detection and ranging (LiDAR) technology were used to collect georeferenced subsurface and above-surface data. The data were post-processed and analyzed using resistivity inversion, numerical modeling, statistical analysis, and machine learning methods to extract vital information before performing a comparative analysis. The LiDAR and drone DEM were used to analyze the variations of the surface and settlement profiles. The researchers identified the slope failure characteristics by analyzing the UAV photogrammetry data. ERI analysis of embankment lines revealed multiple low resistivity areas that indicated the presence of zones of highly saturated soil that can reduce suction and lead to slide failures. ERI image profiles also confirmed the depths of slip surfaces marked by areas of high resistivity due to the presence of loose soil with air voids.

Results from processing the cross-platform data were compared and analyzed for insights into the deep and shallow depths of the failed geo-infrastructure assets. The results provided valuable insights into surficial soil movement with varying weather patterns and subsurface moisture. For instance, wet zones in the subsurface, indicated by low electrical resistivities for an extended period, indicated an imminent problem. The first signs of significant surficial movement detected through periodical LiDAR scanning should trigger immediate action. Combining remote sensing and geophysical investigations will help develop a faster, cost-effective, and more reliable methodology for evaluating geo-infra-assets. Advanced evaluation techniques described in this study will significantly advance the quality of site investigations, reduce risk and increase the reliability of the design of transportation geo-infrastructure in Mississippi.

CHAPTER 1 INTRODUCTION

1.1 Background

Landslides could be defined as the movement of rocks, debris, or soil down a slope (Cruden and Varnes, 1996). Landslides are a highly destructive natural disaster causing loss of life, property (Juang et al., 2019) and extensive damage to infrastructure worldwide. The occurrence of landslides is influenced by various factors such as rainfall, local terrain, geology, geomorphology, soil composition, tectonic activity, land use, and land cover (Meena et al., 2021). Landslides from shallow slope failures refer to surface instabilities along cuts, fill slopes, embankments, earth dams, and levees. Such shallow landslides around transportation infrastructure are increasingly becoming common in the United States.

Transportation geo-infrastructure assets such as highway earth slopes and embankments are integral to transportation infrastructure, but in Mississippi, they are becoming increasingly vulnerable due to extreme rainfall events. The highway slopes are impacted by bursts of high-intensity downpours and slow-moving weather systems that dump a tremendous amount of water, and the problem is compounded because most of the highway slopes are built on the expansive-Yazoo clay that is pervasive in the region. Due to the inherent nature of high-plastic clay, the cyclic pattern of hot summers and extreme rainfall weakens the Yazoo clay's shear strength properties and causes shallow and deep-seated landslides and failures. The clay undergoes significant swelling and shrinkage, leading to the formation of desiccation cracks in the surface layers that allow moisture to permeate and collect at deeper levels of the soil in perched states and make the slope highly vulnerable to failure. It is essential to monitor soil moisture, groundwater levels, and soil movement to prevent such failures.

State Study 286 (Khan et al., 2020), supported by the Mississippi Department of Transportation (MDOT), found that slopes stabilized with H-piles are stable initially but experience movement over time. The study also found that the intensity and duration of rainfall, the soil's permeability, and surface runoff result in perched water zones in slopes built on Yazoo clay. The flow analysis performed in the study revealed that the suction in the unsaturated zone of the slope drops continuously after rainfall, reducing the integrity of the shallow layers. Figure 1.1 shows variations of surficial moisture at the initial condition and 7 days after 2 in. of rain fell in one day. Another finding of the study was that an active zone of 12 ft. existed within the slopes, which was confirmed by the sliding depths previously observed. The perched water under the active zones exacerbated the slope movement and eventually caused sliding failures. The wet and dry cycles of seasonal variations also have an adverse effect on Yazoo clay, as they first reduce the shear strength to residual, then to a fully softened state. Therefore, to prevent expensive repairs, it is important to prevent the accumulation of perched water zones in Yazoo clay slopes and closely monitor the surficial movement.

The traditional in-situ evaluation methods are outdated, expensive, and produce spatially restricted information. Many assets fail without notice because they have not been monitored due to the absence of in-situ monitoring devices. Warning systems and timely evaluations are imperative preventative measures and can mitigate the impact of failure on highway slopes and embankments. Frequent geo-structure health monitoring is essential for averting risks and ensuring asset longevity.

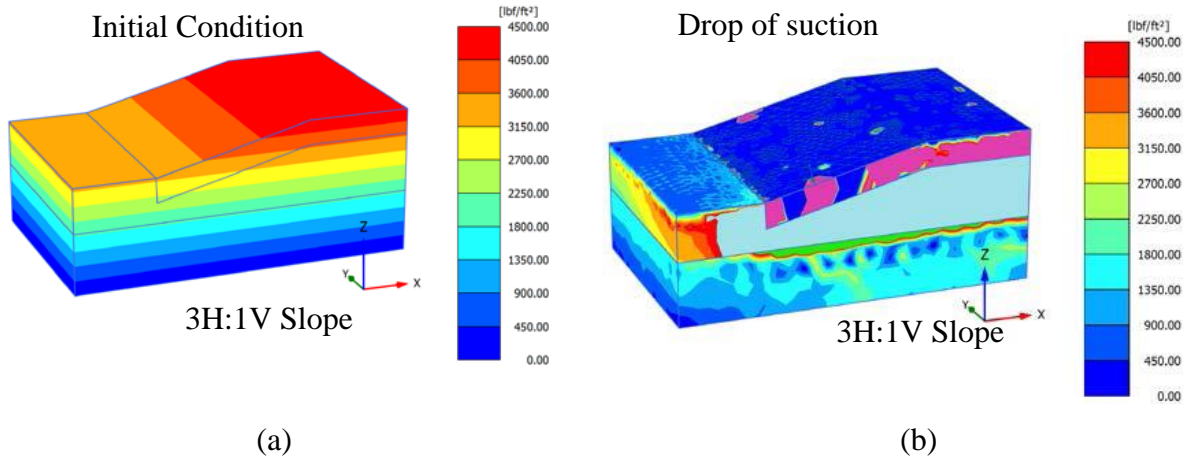


Figure 1.1 Moisture and Suction Variation Profiles from FEM Flow Analysis: (a) Initial Condition, (b) 7 Days after 2 in. Rainfall in One Day (*from Khan et al. 2020*)

Infrastructure monitoring techniques based on remote sensing have grown in popularity in recent years; however, identifying vulnerable geo-structures still requires boots-on-the-ground inspections. Such manual inspections are geared towards assessing the risk and performance of the infrastructure after extreme events. However, they are expensive and time-consuming at a time when quick action is needed.

1.2 Objectives

State Study 316 was conducted to understand the performance of highway slopes containing Yazoo clay and other Mississippi Soil, using Advanced Geophysical method and near-earth Remote Sensing Technique to investigate 6 repaired and instrumented slopes during varying seasons and to evaluate the condition of 20 other failed slopes. The extended scope of the study included collecting data from drone imaging, LiDAR surveys, and instrumentation data over a period of time.

Advanced investigation techniques adopted in this project will improve transportation infrastructure system operations, and identifying and performing required maintenance will eventually lead to a safer and more resilient intermodal transportation infrastructure network in Mississippi. Early identification of vulnerable or failing assets is crucial for strategizing repairs and maintenance activities, and combining remote sensing methods with geophysical investigations facilitates advanced performance monitoring methodology for integrating the Geotechnical Asset Management (GAM) framework. Furthermore, the georeferenced digital elevation models can be incorporated into workflows that will employ deep learning models integrated with geospatial analysis to aid in geotechnical and infrastructure asset management. High-quality DEM data, in tandem with deep learning models, can be used to quickly detect and classify transportation infrastructure assets and remotely identify vulnerabilities and defects.

1.3 Methodology

Advanced, multi-faceted, rapid evaluation techniques, including geophysical and remote sensing approaches with a high spatial and temporal resolution, were implemented to evaluate highway embankment side slopes. Electrical resistivity imaging (ERI), Uncrewed Aerial Vehicles (UAVs) mounted with optical and thermal sensors, and Light Detection and Ranging (LiDAR)

technology were some of the methods used to collect georeferenced subsurface and above-surface data. In addition, moisture content, matric suction, and rainfall intensity data were collected over a period of several years from the in-situ instrumentation installed in boreholes. The data were post-processed and analyzed using resistivity inversion, numerical modeling, statistical analysis, and machine learning methods to extract vital information. A comparative analysis of the multifaceted data was then performed to develop insights into the status of the slope's surface and subsurface.

CHAPTER 2 LANDSLIDE INVESTIGATION METHODS

2.1 Landslides

Landslides have the potential of significantly harming transportation infrastructure risking life and property (Bordoni et al., 2018.; Nappo et al., 2021; Postance et al., 2018). Naturally, transportation infrastructure are at risk of failure from cascading effects of landslides. (Nordiana et al., 2018) (Meena et al., 202). This cause and effect can be clearly seen in the case of highway pavements that fail from settlements and cracking due to the embankment side slope landslides.

Several studies (Kim et al., 2004; Sajinkumar et al., 2020; Khan et al., 2019; Nobahar et al., 2022, 2023; Salunke et al., 2023; Marino et al., 2020) have attributed landslides to rainfall induced increase in soil moisture level, resulting in a decrease in suction and an increase in pore water pressure. These changes have a detrimental effect on the soil's shear strength and friction angle, rendering it more vulnerable to failure. Further the geo-infrastructure asset's soil type plays a significant role in the initiation and propagation of landslides (Luino et al., 2022). For instance, expansive clays when used to build geotechnical assets such as highway slopes cause severe problems to the supported transportation infrastructure.

Mississippi's transportation infrastructure supported by expansive clay fill slopes are prone to slide failures, influenced by rainfall (Khan et al., 2020; Kim et al., 2004; Suk et al., 2022). Due to the cyclic shrink-swell behavior caused by seasonal moisture changes, the initially high shear strength of the soil strength gradually decreases to its fully softened shear strength (Wright, 2007; Khan et al., 2016; Hossain et al., 2016). Additionally, during high intensity rainfall events, water infiltrates the slope through desiccation cracks and gets trapped creating perched water condition. This condition increases excess pore water pressure. The combination of fully softened shear strength and the presence of a perched water zone is the primary cause of shallow slope failure (Khan et al., 2015). A detailed account of the expansive soil in Mississippi and its mineralogy is provided in the following sections.

2.2 Expansive Soil

Surface soils are comprised of swelling clays in several parts of the United States (Olive et al., 1989). A significant number of embankments, levees, and earth dams located in regions dominated by expansive clay, particularly in southern states such as Texas, Louisiana, Mississippi, Alabama, and Colorado, are constructed using expansive soils. Unfortunately, these soils are prone to experiencing shallow slope failure within a few years after construction. When exposed to an increase in moisture content, expansive soils progress from a partially saturated state to a saturated state, which often results in heaving. For instance, the expansive Yazoo formation clay typically found in Jackson Mississippi area when mixed with water changes in volume by 100% to 235% between oven dry and liquid limit states (Lee 2012). They also exhibit another characteristic known as shrink behavior, which is the inverse of swelling. Shrinkage is evidenced by the appearance of cracks on the soil surface that occur when the soil loses moisture due to natural or human-made causes. In general, depending on the moisture content, expansive soils have a moderate-to-high plastic index, significant bearing capacity, and varying strength (Kalantari 2012). Expansive soils have been observed in a variety of locations throughout the

world, but they are most prevalent in areas with arid-to-semiarid climates. Clayey minerals dominate the architecture of swelling soils, allowing them to absorb water between their layers and then undergo volume changes (Bowels 1988, Murphy, 2010).

Natural hazards in the United States could be grouped into six categories, based on their ability to damage, or destroy built infrastructure: earthquakes, landslides/slope failures, expansive soils, hurricanes, tornadoes, and floods -not in that particular order. Expansive soil and storms may be the second most catastrophic natural hazards in terms of economic damages (Chen 1988, Murphy 2010). When working with expansive soils, an increased awareness of issues that are frequently encountered may facilitate constructing roadway pavements that have a good potential for long-term serviceability that may have a positive economic impact by reducing losses.

Due to their vast geographic distribution and the poor performance of currently available design approaches, volume changes in expansive soils have been designated as one of the most financially harmful geologic hazards (Jones and Holtz 1973). Wray and Meyer (2004) estimated that expansive soils directly result in annual losses of more than 15 billion USD in the United States. Numerous researchers (e.g., Mitchell 1980 and Lytton et al., 2005) developed models to simulate the deformations of partially saturated soils, but few of them are capable of characterizing the behavior of expansive clays, and none are predictive. This confusing soil behavior would be easier to understand if more comprehensive field studies were accessible. Long-term monitoring is unavoidably necessary to ascertain the link between long-term deformations and changes in moisture content and suction in the soil (Khan et al., 2020).

Recent research indicates that the expansive behavior of soils can be better understood when the matric suction is considered (Alonso et al., 1990) and indicates that suction is not based on the mineralogy of the soil but rather on the chemistry of the pore water that saturates it (Pulat et al., 2014). Suction has been demonstrated to be a critical component in determining how clays behave in terms of volume change. In general, natural soils in dry and semiarid regions remain somewhat saturated for most of the year, with only seasonal variations in moisture content. The soil-water characteristic curve (SWCC) illustrates a link between these two variables.

The schematic profile of the subsurface in Figure 2.1 shows that the range of water content and suction fluctuation diminish with depth. Characterization of the active depth to which substantial fluctuations are seen is critical for understanding seasonal influences on ground motions.

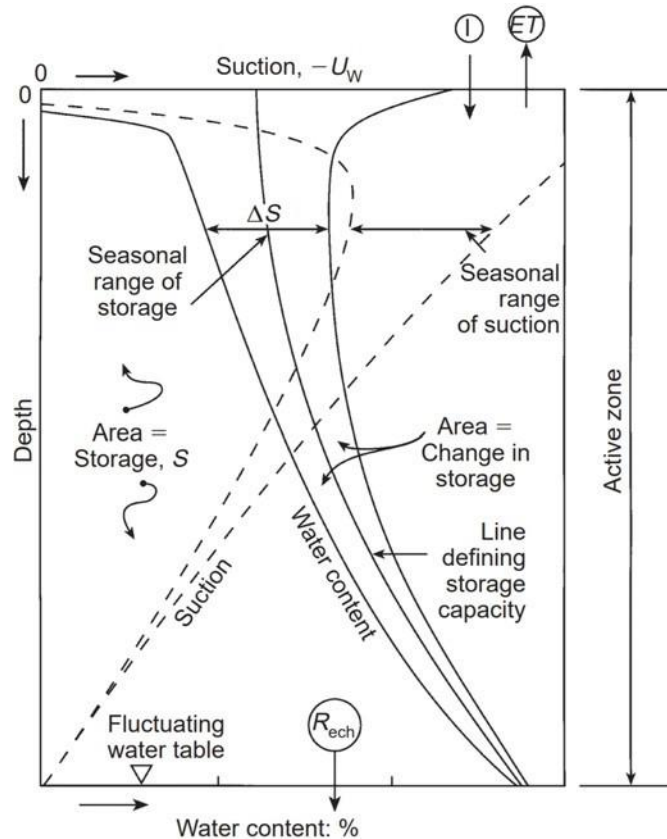


Figure 2.1 Seasonal Fluctuations in Water Content and Suction (Blight, 1997)

The behavior of expansive soil is highly dependent on changes in its moisture content, which cause volumetric deformation that gradually damages essential infrastructures such as foundation slabs, bridges, roadways, and residential homes. Expansive soil is present in both humid and arid/semi-arid environments and covers nearly a quarter of the United States (Nelson and Miller 1992). Annually, it alone results in more financial losses (approximately 15 billion dollars) to US property owners than earthquakes, floods, hurricanes, and tornadoes combined (Jones and Jefferson 2012). The current chapter summarizes the physical and mechanical properties of expansive soil that are cited in the literature.

To understand the behavior of expansive soil, it is vital to study changes in temperature, soil moisture balance, evapotranspiration, and the frequency of dry and wet periods. However, the shrink-swell characteristics of expansive soil are not solely determined by monthly moisture levels or climatic variations at a particular location. The soil's index properties, mineralogy, and the percentage of clay content, also play a significant role in soil behavior.

2.2.1 Clay Soil Mineralogy

The geologic past, sedimentation, and local climate significantly affect the genesis and dispersion of expanding materials worldwide and contribute, either alone or in combination, to the creation of expansive soils. The phrase “expansive material” refers to any earth substance that changes significantly in volume when exposed to water (Snethen et al., 1975). Variation in expansion size is dependent on the presence of active clay minerals, such as montmorillonite and its combinations. Under certain conditions, other clay minerals, such as chlorites and

vermiculites, are also active. Kaolinites and illites are not considered active minerals, but if sufficient amounts are present, they may contribute to expansive qualities (Snethen et al., 1975). Figure 2.2 depicts three distinct forms of clay minerals. Additionally, one may see how the presence of cations affects the clay mineral classification arrangements.

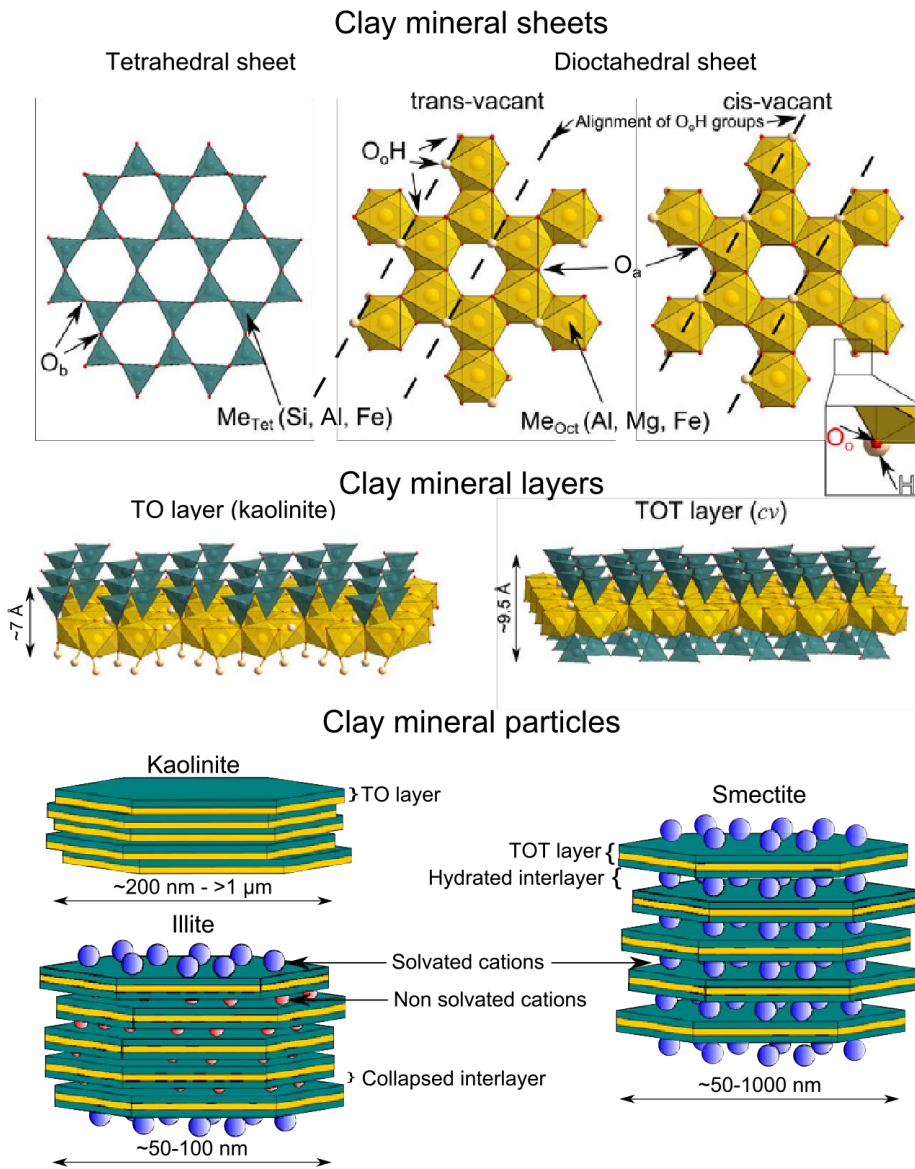


Figure 2.2 Layout of Clay Mineral Classification (TO: One tetrahedral sheet to one octahedral and TOT: an octahedral sheet in the middle of two tetrahedral sheets) (Tournassat et al., 2015)

The presence and storage of Montmorillonite largely influences the distribution of expansive materials. The creation or origin of montmorillonite is aided by the action of the following conditions, either individually or in combination: weathering, diagenetic modification of preexisting minerals, and hydrothermal alteration, with the most significant being weathering and diagenesis (Tardy et al. 1970).

2.3 Climate Factors That Impact Expansive Clay Soil

A greater understanding of the climatic characteristics that alter the structural features of infrastructure/structural systems (earth dams and pavements) would considerably improve the design and longevity of highways, as well as the construction of infrastructures. Fluctuations in moisture, suction, and temperature impact the quality of both natural and artificial highway slopes and weathered and unweathered layers and affect their long-term performance.

Over the past five decades, the southeastern United States regions have seen a 20% increase in the occurrence of extremely heavy precipitation. This trend of significant increase in extreme rain events is expected to continue in the coming years, with even more substantial increases projected for the remainder of the century (Karl, 2009).

Changes in moisture are primarily caused by rainfall, intrusion through fractures, wet-dry cycles, leakages, and evapotranspiration (Hedayati 2014). Increased moisture content weakens shallow soil layers, compromising their stability for strong bonding. Variations in moisture content can cause swelling and shrinking that result in surficial cracks in shallow weathered soil layers in highway slopes with a high plastic concentration, resulting in increased maintenance costs for transportation authorities (Zapata and Houston 2008). Temperature fluctuations cause variations in the permeability and suction in soil layers at shallower depths and can cause severe deformation. (Minor changes in the soil's temperature have also been observed at deeper depths.) Wet-dry cycles result in expansion and contraction cracks that can extend deep into the soil deeper layers. This issue is particularly acute in Texas, where summer air temperatures can reach as high as 95 °F (Khan et al., 2020). A few scholars have tried to correlate the characteristics of expansive soil with environmental elements to account for the effects of moisture and temperature. Shirazi (2014) investigated the effects of temperature on the hydro-mechanical behavior of expansive clay's physical and engineering properties. To conduct an accurate analysis, however, the profiles should be estimated across the depth contributing to the overall performance of the slope layers. Khan et al. (2020) identified this depth as the active zone, which may extend to 12 ft.

2.4 Advanced Landslide Investigation Methods

Warning systems and timely assessments are preventative measures that lessen the impact of landslides on assets such as highway slopes and embankments. However, traditional evaluation methods are expensive and produce spatially restricted information. For instance, borehole instrumentation is limited to providing localized information of a failed slope; it cannot provide information on a wider area. Unfortunately, many assets fail without notice because they were not monitored due to the absence of in-situ monitoring devices. The development of a robust methodology for landslide investigation and preventative measures is greatly needed. Advanced non-destructive testing (NDT) methods, including geophysical and remote sensing techniques, are increasingly being used for asset evaluation and performance monitoring. Electrical resistivity imaging (ERI), LiDAR, and Uncrewed Aerial Vehicles (UAVs) are best suited for evaluating the subsurface and surficial variations of the highway slopes.

2.4.1 Geophysical Field Investigations, Using Electrical Resistivity Imaging (ERI)

Electrical resistivity imaging (ERI) is a non-destructive technology utilized for investigating and characterizing soils. This technique allows for the efficient and rapid assessment of larger subsurface areas compared to traditional destructive methods. By measuring the

electrical resistivity of the soil, ERI provides valuable information about the subsurface composition and properties. This enables researchers and engineers to gain insights into the geological structures, moisture distribution, and other relevant parameters without causing any damage to the soil or surrounding environment.

In a field study, Mertzanides et al. (2020) applied electrical resistivity imaging to prove that annual crop yields are highly dependent on hydrological processes in unsaturated zones. They found that the gravimetric soil moisture point measurements and electromagnetic sensor profiles correlated well with the soil resistivity data, exhibiting a power model relationship. They deemed ERI a trustworthy soil moisture-monitoring tool for precise irrigation in highly heterogeneous, clay-rich soils. It is evident that ERI enables hydraulic conductivity estimation of both near-surface and deep subsurface layers and unique soil strata information (Muñoz-Castelblanco et al., 2012)].

Siddiqui. & Osman(2012) and Mulyono et al. (2019) found that ERI method to be a less expensive and time-efficient way of studying soil hydrological characteristics compared with the traditional expensive and time-consuming method requiring drilling, test pits, and trenching. Siddiqui. & Osman(2012) stated ERI can be beneficial in accurately assessing engineering properties, defining subsurface properties of soil, and establishing reliable correlations between electrical resistivity and other soil properties before beginning the design process for any structure. Furthermore, the ERI method is far less invasive and does not disturb the soil's strata as opposed to the traditional invasive investigation methods.

Samouëlian et al. (2005) advocated that its non-destructive and highly sensitive nature makes ERI a very attractive tool for determining the subsurface properties. ERI helps with subsurface soil moisture mapping and informs about the soil's horizontal thickness and bedrock depth without digging. Other advantages they mentioned are that it can be used as a proxy for the spatial and temporal variability of a large number of physical soil properties and is applicable to a variety of contexts, including groundwater exploration, landfills and solute transfer delineation, and agronomic management by identifying areas of excessive compaction or soil horizon thickness and bedrock depth and assessing the soil's hydrological properties.

ERI surveys have been successfully carried out at slope failure sites to understand the underground soil composition and moisture accumulation (Nordiana et al., 2018) , and gain a better understanding of the factors contributing to slope failure (Koehn et al., 2019; Muñoz-Castelblanco et al., 2012; Nobahar et al., 2023; Samouëlian et al., 2005a). ERI results guide practitioners in developing appropriate mitigation strategies based on the obtained information. Many past studies have implemented ERI in the investigation of landslides and for other geotechnical applications.

Hen-Jones et al. (2017) showed that electrical resistivity imaging technology could identify changes in internal ground conditions that precede failure, making ERI a suitable tool for risk assessment. Their study successfully resolved the preliminary geophysical–geotechnical relationships necessary for developing an ERI-based slope stability assessment system.

Jongmans & Garambois (2007) demonstrated that electrical resistance imaging could produce two- and three-dimensional images that depict the distribution of electrical resistivity in the subsoil and make it possible to identify resistivity contrasts that are primarily attributable to the lithological nature of the terrain and the variation in water content. Perrone et al. (2014)

determined that the ERI method can effectively analyze the resistivity distribution in areas that have experienced landslides. Their study asserted ERI's capability in identifying the areas with a high-water content and assessing the need for slope stabilization.

Using the ERI method, Gallipoli et al. (2000) implemented a plan to detect landslide-impacted areas in the Apennines of Southern Italy. Investigations into landslides could benefit from the utility of this tool, which is both valuable and cost-effective. Koehn et al. (2019) used ERI as a cost-effective method for developing detailed subsurface images of landslides.

Remote Sensing methods fall within the umbrella of geophysical investigation methods because they gather geotechnical and geological data using the electromagnetic spectrum (Ranjbar, 2011). Satellites, UAVs, and LiDAR have been successfully implemented in remote sensing studies focusing on the earth's surface, soils, vegetation, and natural disasters such as landslides.

(Burns & Madin, 2009; Ciampalini et al., 2016) (Ahmad et al., 2022; Hussain et al., 2023; Samsonov & Blais-Stevens, 2023) Landslide susceptibility mapping, detection & inventory building have been performed using Satellite imagery & GIS tools (Ahmad et al., 2022; Hussain et al., 2023; Samsonov & Blais-Stevens, 2023), LiDAR (Burns & Madin, 2009; Ciampalini et al., 2016) and drone imagery (Nappo et al., 2021; Tilon et al., 2022; Whitehurst et al., 2022). Furthermore, several studies have incorporated advanced technologies, such as deep learning techniques, to classify and detect landslides (Hussain et al., 2023; Mondini et al., 2023; Nappo et al., 2021).

Although satellite data has proved helpful in landslide susceptibility mapping and detecting landslides, there are several disadvantages. Satellite images are coarse, such as those from Landsat 8 that provide 30m (~98 ft.) resolution, and they often struggle with poor quality due to cloud cover. Furthermore, temporal spacing is also a significant problem with satellite imagery due to no control over the time the satellite will pass over the area of interest. Therefore, satellite imagery is inconvenient for a timely, detailed site-level investigation of landslides impacting transportation geo-infrastructure such as highway slopes. In contrast, UAV and LiDAR offer higher-resolution imagery and point cloud information. These technologies also offer complete control over the data collection timeline with as many repetitions as needed, which is crucial for the timely performance monitoring of transportation infrastructure assets.

2.4.2 Remote Sensing in Field Investigations, Using Unmanned/Uncrewed Aerial Vehicles (UAVs)

Remote sensing is the science and technology of capturing, processing, and analyzing physical data from sensors in space, air, and ground (Chen et al., 2016). Its ability to collect data can be used in many different applications, including mapping natural activities, assessing the potential for hazards, and mitigating their impact when they occur. Advances in technologies in the last decade, such as the increase in wireless internet accessibility, advances in UAV as a flexible platform, enhancements in digital cameras, developments in digital images analysis, and progress in small satellites (Chen et al., 2016); have led to an increased demand for remote sensing in a wide variety of fields. Remote sensing techniques are helpful in monitoring and assessing natural hazards by creating early warning systems that give authorities time to evacuate people when necessary and obtain data from sites that are hard to reach due to difficult terrain or may impose danger to workers' lives.

Studies have used UAV-based remote sensing methodology for a variety of applications within transportation asset management, including estimating soil moisture content (Salunke et al., 2023), mapping slope failures (Nobahar et al., 2023), assessing pavement defects (Nappo et al., 2021) and assessing landslide susceptibility. Nappo et al. used photogrammetry methods and 3D representations to study pavements affected by a slowly moving landslide.

Kader & Altunel (2021) supported using drones for monitoring slopes, declaring that drone is superior to all other methods of investigation for periodic status monitoring or monitoring slope failures. Drones' functionalities have expanded alongside the increasing demand for UAV technologies, leading to their widespread adoption in civilian contexts, according to Shahmoradi et al. (2020). Due to UAV's ability to quickly inspect an area for potential hazards or emergencies, they are increasingly commonplace in many fields, such as mining, agriculture, construction, geotechnical, and transportation infrastructure monitoring.

Tan et al. (2022) used UAVs to conduct inspections of road slopes because of their ability to render high-definition images of the slope's environment, safety level, and geological conditions. They plan to use the technology for various inspections in future projects.

Rashid et al. (2022) investigated the stability of rock slopes in both wet and dry seasons by utilizing a thermal sensor mounted on a drone. Their study illustrated how drone-based remote sensing can be applied to examine rock slopes and determine whether they are stable by analyzing thermal images of the surface temperature.

Sluijs et al. (2018) showed that UAVs offer several advantages in determining the impacts of permafrost terrain and northern infrastructure dynamics on infrastructure. They also considered the gap between field scale studies and remote sensing observations.

Embankment slopes support a substantial majority of Mississippi's roads and are susceptible to failure due to rainfall, temperature, and expansive clay. The time-efficient UAV investigation technique increases the number of assets that can be monitored and screened for deeper investigations. UAVs offer efficient assets performance monitoring and maintenance, saving time, cost, workforce, technology, outcomes, performance, and reliability. UAVs can be equipped with LiDAR-based infrared sensors with various features that can be used to monitor the slope's performance with various applications (Figure 2.3).

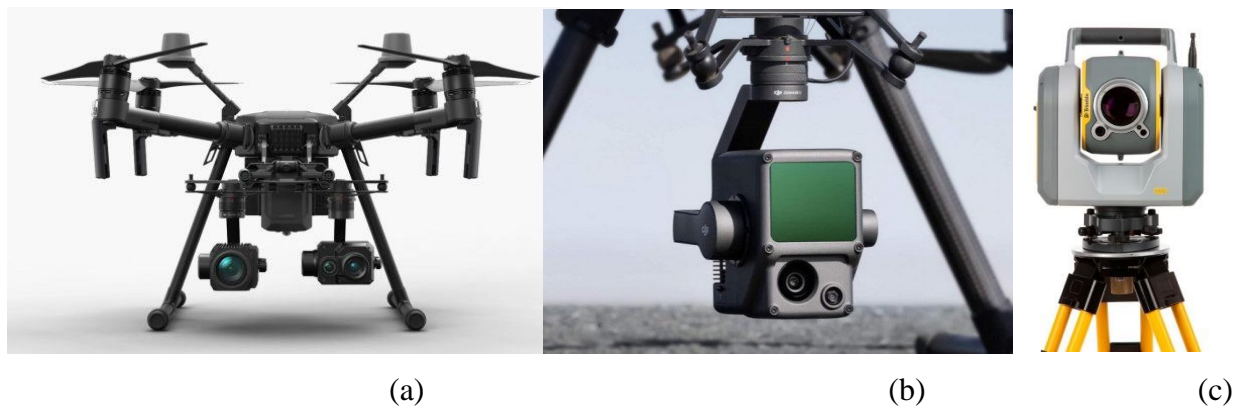


Figure 2.3 Photogrammetry Tools: (a) Drone with sensor payloads, (b) Lidar and Thermal Camera Sensors, (c) Lidar Terrestrial Scanner

2.4.3 Remote Sensing in Field Investigations, Using Light Detection and Ranging (LiDAR)

Like high-quality UAV imagery, Terrestrial LiDAR Scanning produces dense point cloud data to investigate high-interest areas (Luo et al., 2018; Marx et al., 2019), such as landslides and transportation infrastructure assets. Conducting multiple periodic LiDAR surveys of the areas of interest enables monitoring subtle deformations in the soil mass and identifying potential risks (Wolf et al., 2014). Several studies have tested the application of LiDAR in landslide investigations, transportation infrastructure asset monitoring in general.

Hatta Antah et al. (2021) claim that LiDAR is useful in designing roads, as it not only simplifies the design process, but the precise topographical data information that it provides lowers the risks associated with building roads in places that are prone to rockfalls or landslides (Figure 2.4).

Lynch et al. (2013) examined the various advanced methods of slope stability investigations and used LiDAR to monitor the slope's movement, erosion, and deposition. Susaki 2012, proposed a filtering algorithm that precisely separates ground data from LiDAR measurements and produces an estimated digital terrain model (DTM). It makes use of planar surface characteristics and connectivity with locally lowest points to enhance the removal of ground points. Utilization of reference data showed that their algorithm gives more precise ground points than commercial filtering software.

In a study conducted by Conte and Coffman (2012), a comparison was made between the results obtained from slope stability back-analysis and the measurements obtained using both a total station and LiDAR. The researchers found that while total station provided valuable information, the surfaces generated by LiDAR were more precise, allowing for a more accurate monitoring of head scarps and vertical deformation of slopes.

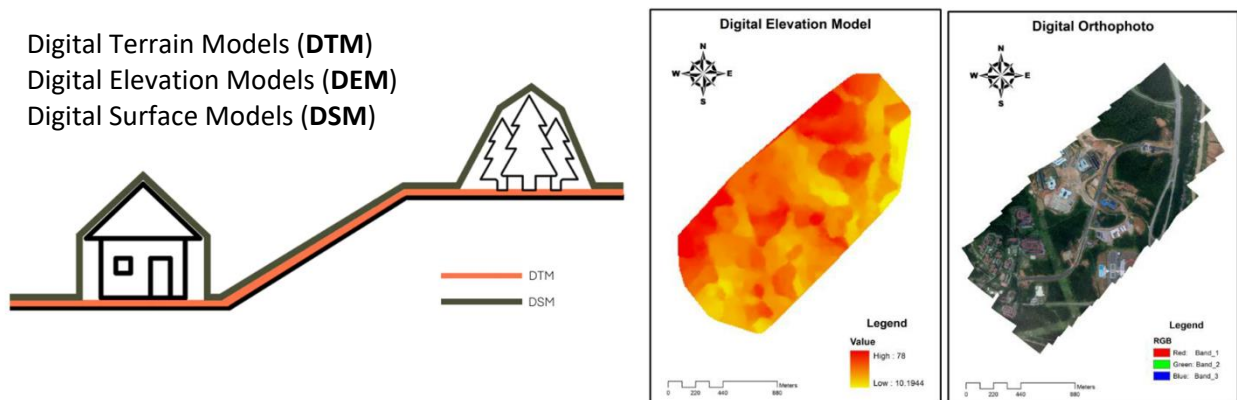


Figure 2.4 Drone LiDAR and Photogrammetry Outcomes

Gargoum & El-Basyouny (2017) highlighted the potential of LiDAR's high point density dataset to automate the extraction of highway features and geometrically assess attributes like stopping sight distance. They believed that LiDAR datasets could revolutionize highway safety audits.

Liu et al. (2012) implemented LiDAR scanning to provide precise clearance data for bridge surfaces. They determined the vertical clearance by utilizing static terrestrial LiDAR scans of a bridge deck and the ground points beneath the deck.

Jaboyedoff et al. (2012) stated that LiDAR is primarily used to create high-resolution digital elevation models for landslide investigation. The method utilizes a laser to generate precise electromagnetic radiation and capture displacement data for landslide analysis, aiding in understanding kinematics and failure mechanisms.

CHAPTER 3 INVESTIGATIONS OF INSTRUMENTED SLOPES

3.1 Site Selection

The six highway slopes in the Jackson, Mississippi metroplex that are presented in Figure 3.1 and Table 3.1 were selected for continued monitoring by the extension of State Study 286 because they had exhibited early signs of movement or had a record of failure and repair. MDOT hired Thompson Engineering to perform a cone penetration test (CPT) prior to field instrumentation, and Jackson State University's (JSU) Geo-Development research team observed the operation. The data from the CPT and site instrumentation were used by the JSU team to perform an engineering analysis.

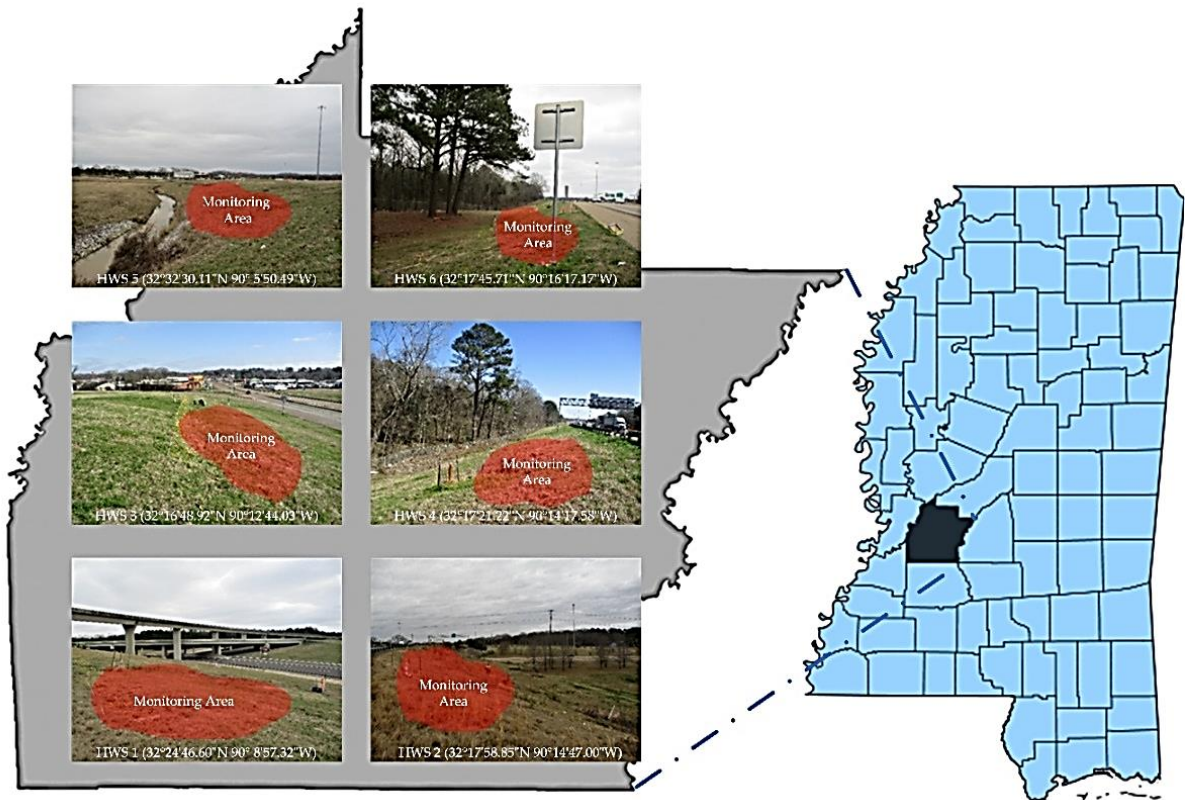


Figure 3.1 HWS Locations in Jackson (Reference Sites)

Table 3.1 Locations of Selected Highway Slopes (from Khan et al., 2020)

Site No	Site Location	Site Coordinate
I-Slope 1	I220N Ramp Toward I55N	32°24'46.60"N, 90° 8'57.32"W
I-Slope 2	enter	32°17'58.85"N, 90°14'47.00"W
I-Slope 3	Terry Road	32°16'48.92"N, 90°12'44.03"W
I-Slope 4	Highland Drive	32°17'21.22"N, 90°14'17.58"W
I-Slope 5	Sowell Road	32°32'30.11"N, 90° 5'50.49"W
I-Slope 6	McRaven Road	32°17'45.71"N, 90°16'17.17"W

3.2 Field Instrumentation

Field instrumentation was implemented at the six slopes to monitor several variables, including moisture content, matric suction, soil temperature, air temperature, and rainfall intensity. Each slope was equipped with industrial-grade sensors such as GS-1 moisture sensors, Meter Teros 21 soil water potential sensors, an ECRN-50 tipping-bucket rain gauge, EM50 data logger, and RT-1 air temperature sensor. In addition, two 30 ft. long inclinometer casing pipes were installed to track slope movement. The sensors were strategically placed at the crest, middle, and toe of the slopes, with moisture and water potential sensors positioned at various depths within 15 ft.-deep boreholes. The arrangement of the field instrumentation can be seen in Figure 3.2, and the specific sensor locations and quantities are detailed in Table 3.2.

Cables approximately 150 ft. long were used to install 20 sensors and 2 inclinometer castings in each of the slopes investigated. Each sensor was connected to data loggers using a 3.5 mm stereo audio extension cable to ensure continuous recording of in situ measurements. The field instrumentation installation process took approximately one month. Following installation, the data loggers were programmed to collect data on an hourly basis from the moisture sensors, water potential probes, soil temperature sensors, rain gauges, and air temperature sensors. Table 3.2 provides the monitoring schedule for all six slopes. The JSU GeoDevelopment research team visited each site bi-weekly to obtain inclinometer readings.

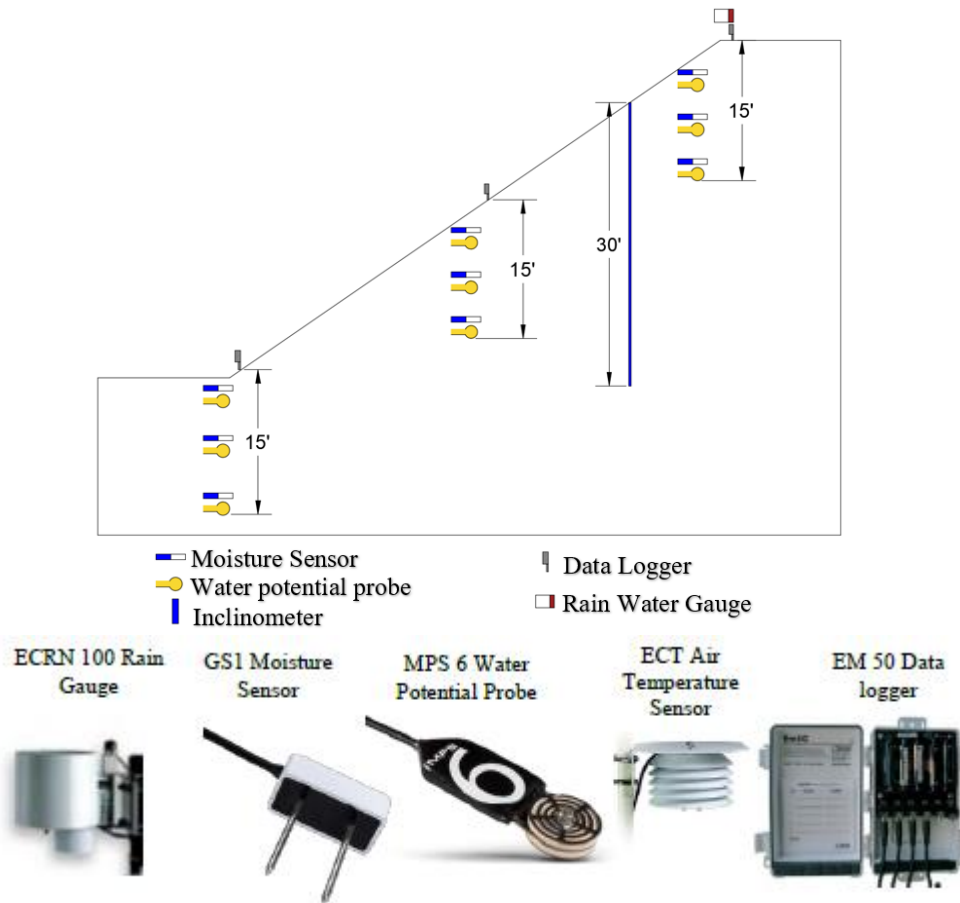


Figure 3.2 Instrumentation Layout at Each I-Slope and Images of the Individual Sensors

Table 3.2 Field Instrumentation for Data Collection

Sensor Name	Purpose	Location	Depth (ft.)	Number of Sensors
ECRN 100 Rain Gauge	Collect Precipitation Data	Slope middle	Above slope surface	1
GS1 Moisture Sensor	Collect Volumetric Moisture Content	Crest, middle, toe	5, 10, 15	9
MPS 6 Water Potential Probe	Collect Matric Suction and Soil Temperature Data	Crest, middle, toe	5, 10, 15	9
ECT Air Temperature	Collect Precipitation Data	Slope middle	Above slope surface	1
EM 50 Data Logger	Data Collection and Storage	Slope middle	Above slope surface	4

3.3 Instrumented Slope 1 (I-Slope 1): I220N Ramp Toward I55N Highway Slope

I-Slope 1 experienced movement in the past and was repaired using H-piles by MDOT. The repaired section was compared to the as-built section to assess its performance. Figure 3.3 provides the location and a photograph of I-Slope 1 for reference.

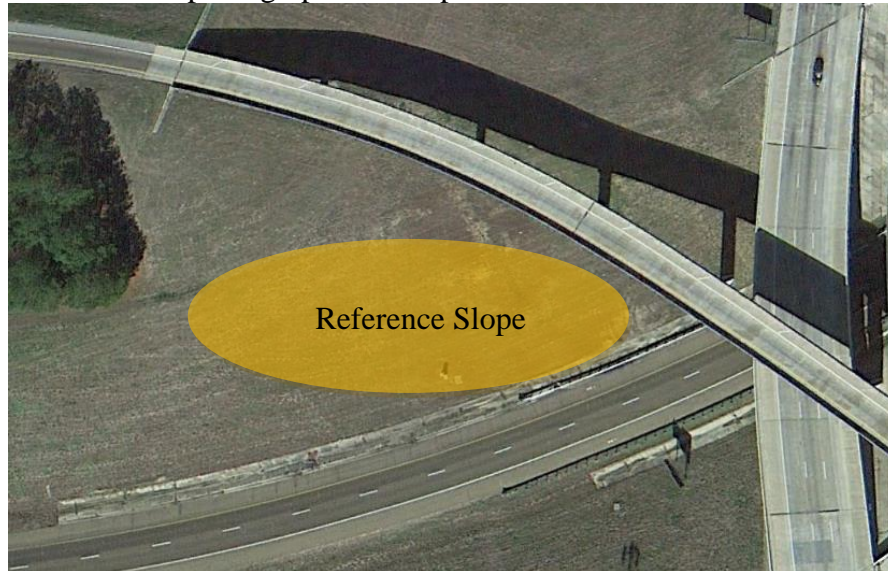


Figure 3.3 Location of I-Slope 1

Two 15 ft. boreholes, labeled as Instrumentations 1 and 2 in Figure 3.4, were drilled and instrumented in the as-built section of I-Slope 1. Another 15 ft. deep borehole, known as Instrumentation 3 in Figure 3.4, was drilled and instrumented in the repaired area. Instrumentation 1 was positioned at the crest of the slope, while Instrumentations 2 and 3 were placed in the middle. At each instrumentation location, moisture sensors and water potential sensors were installed at depths of 5 ft (1.5 m), 10 ft (3 m), and 15 ft (5 m). Furthermore, at Instrumentation 1, a rain gauge and air temperature sensor were installed. In the as-built section, Inclinator 1 was positioned, and in the repair section, Inclinator 2 was installed. Both inclinometers were placed in the middle of the slopes.

can be seen in Figure 3.4.



Figure 3.4 Instrumentation Layout at I-Slope 1

3.3.1 *Field Monitoring Results*

Data was collected from the data loggers and frequent intervals and analyzed by the JSU GeoDevelopment research team. Data collected from the inclinometer was analyzed to map movement along the grade of the slope. Results were compiled and are presented in this section.

3.3.1.1 *Slope Movement Data*

The slope inclinometer measurements were collected at 2 ft. intervals along the inclinometer pipe to observe the horizontal movement of the slope. The inclinometer data was then analyzed to determine the slope's movement. Figure 3.5 and Figure 3.6 display the horizontal movement data from Inclinometer 1 at the as-built section and the time-dependent movement along the crest of the slope, respectively. Similarly, Figure 3.7 and Figure 3.8 show the horizontal movement data from Inclinometer 2 at the repaired section and the time-dependent movement along the crest of the slope. The figures indicate that no significant movement was observed in either section, or the performance of both slope sections was satisfactory.

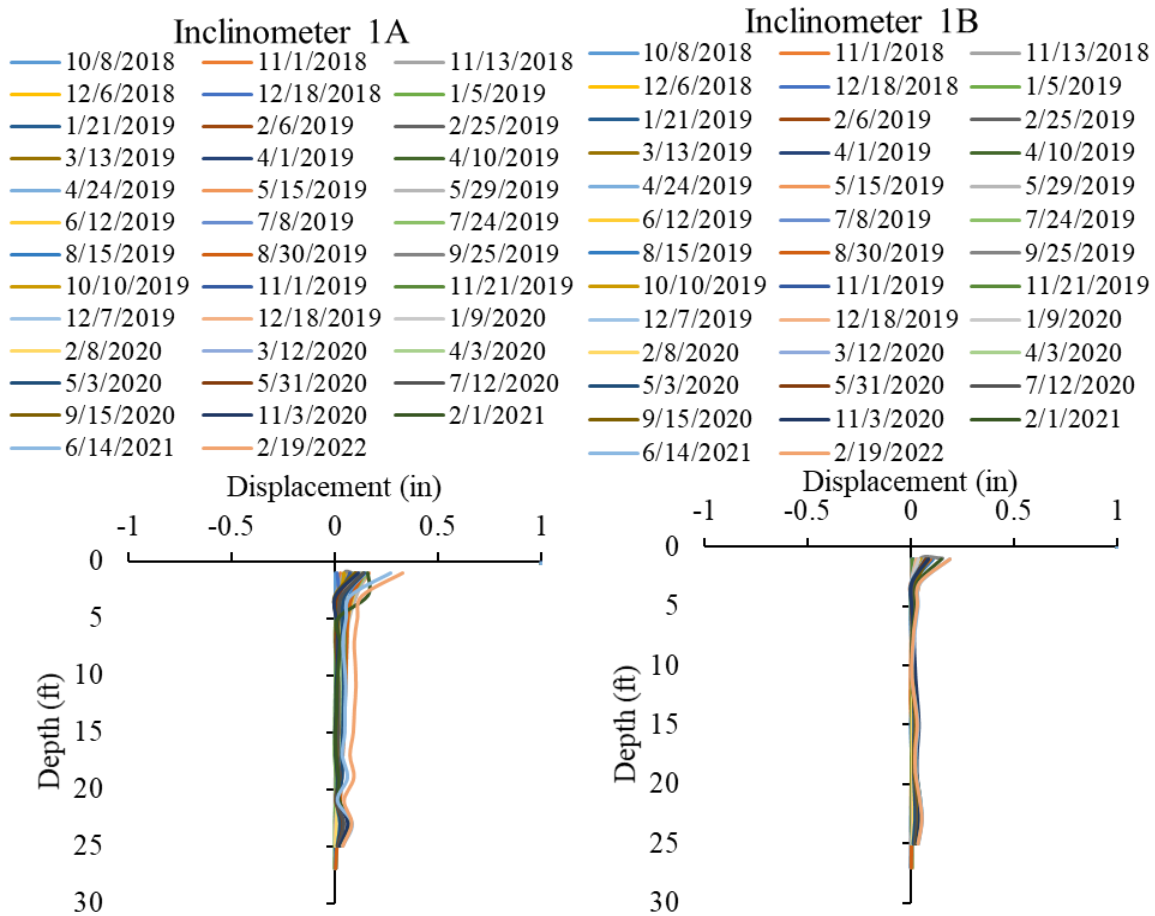


Figure 3.5 Displacements at Inclinator 1 at I-Slope 1

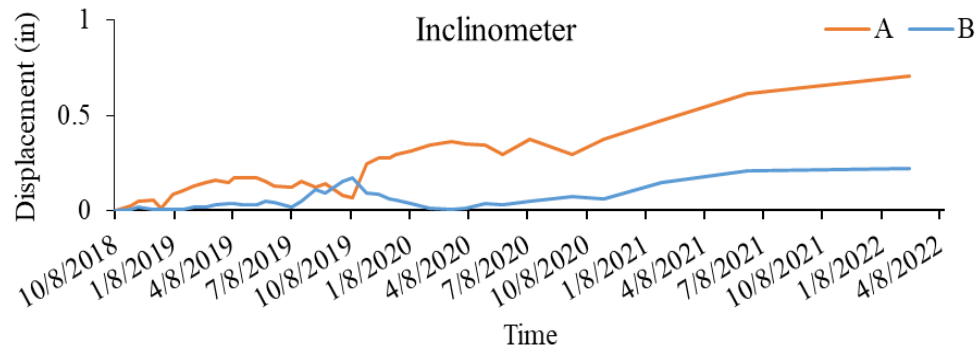


Figure 3.6 Deformations in the As-Built Section from surficial levels of Inclinator 1 at I-Slope 1

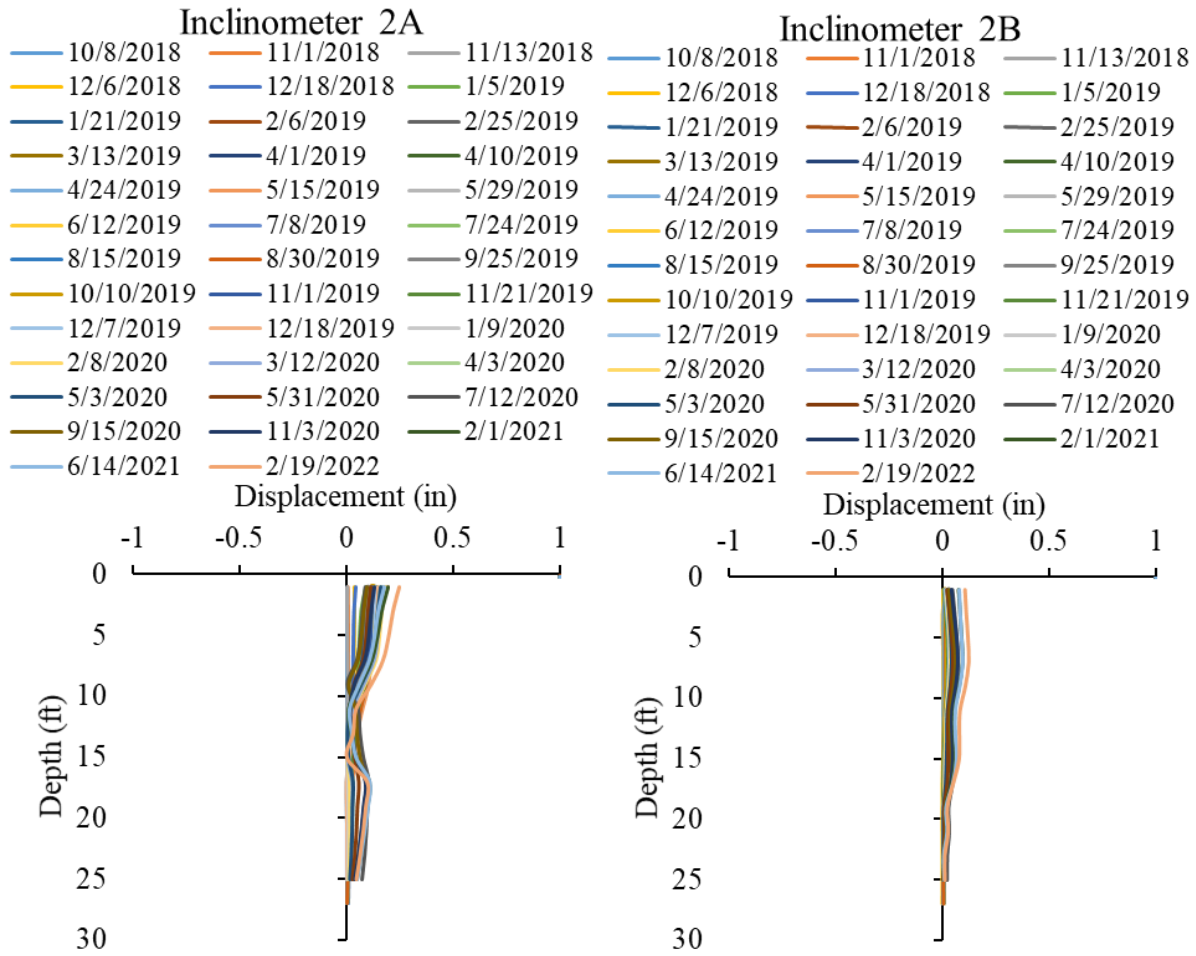


Figure 3.7 Horizontal Displacements of the Inclinator 2 at I-Slope 1

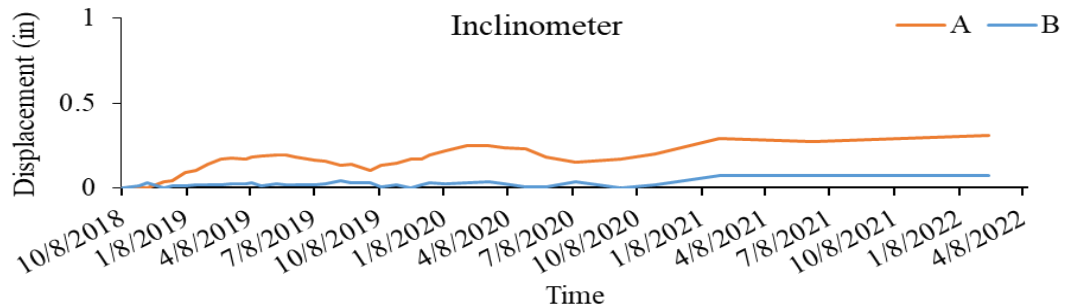


Figure 3.8 Variations of Lateral deformation at I-Slope 1's Repaired Section

3.3.1.2 Field Instrumentation Data

The sensors collected data at the crest, middle, and toe of the slope, and variations in the in situ matric suction profile and moisture content at 5 ft. (1.5 m), 10 ft. (3 m), and 15 ft. (5 m) depths with rainfall are presented in Figures 3.9 to Figure 3.11. The moisture content and matric suction variations at Instrumentation 1, Instrumentation 2, and Instrumentation 3 are presented in Figure 3.9, Figure 3.10 and Figure 3.11, respectively. The highest rainfall occurred in late December 2018, but few variations in moisture content were observed at any of the three depths within the 2-year monitoring period; the matric suction showed no variations.

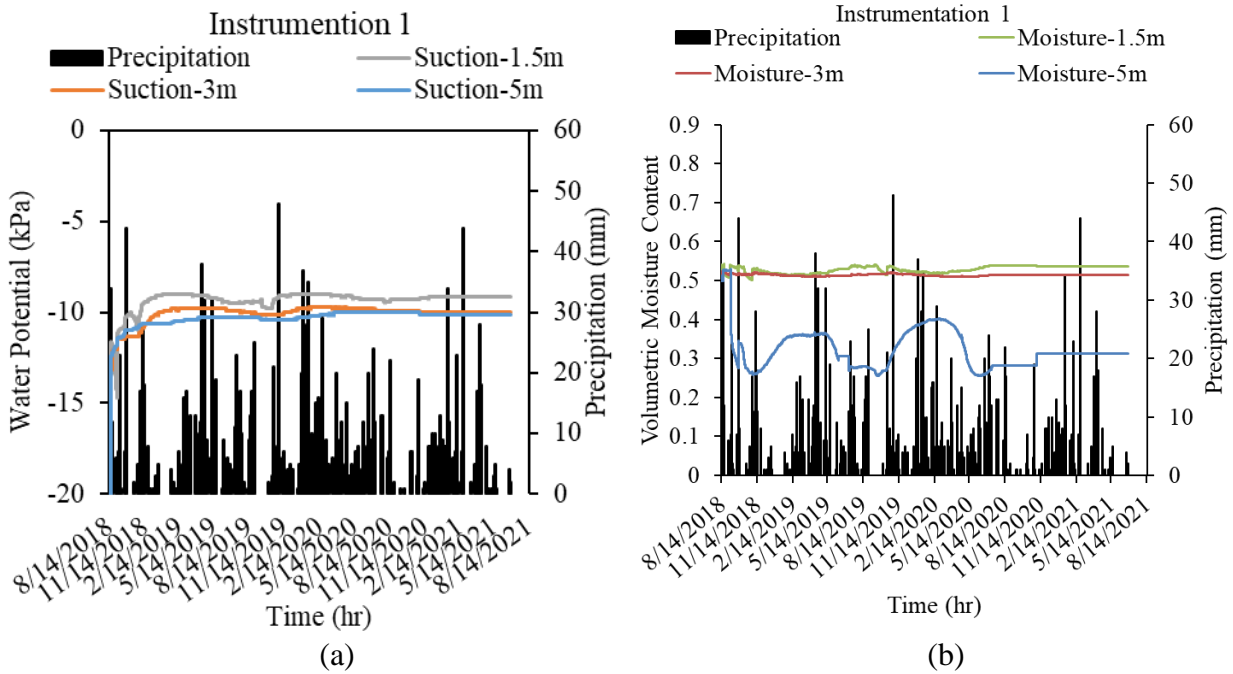


Figure 3.9 Variation of parameters at I-Slope 1 (a) Matric Suction, (b) Moisture Content and Rainfall data from Instrumentation 1

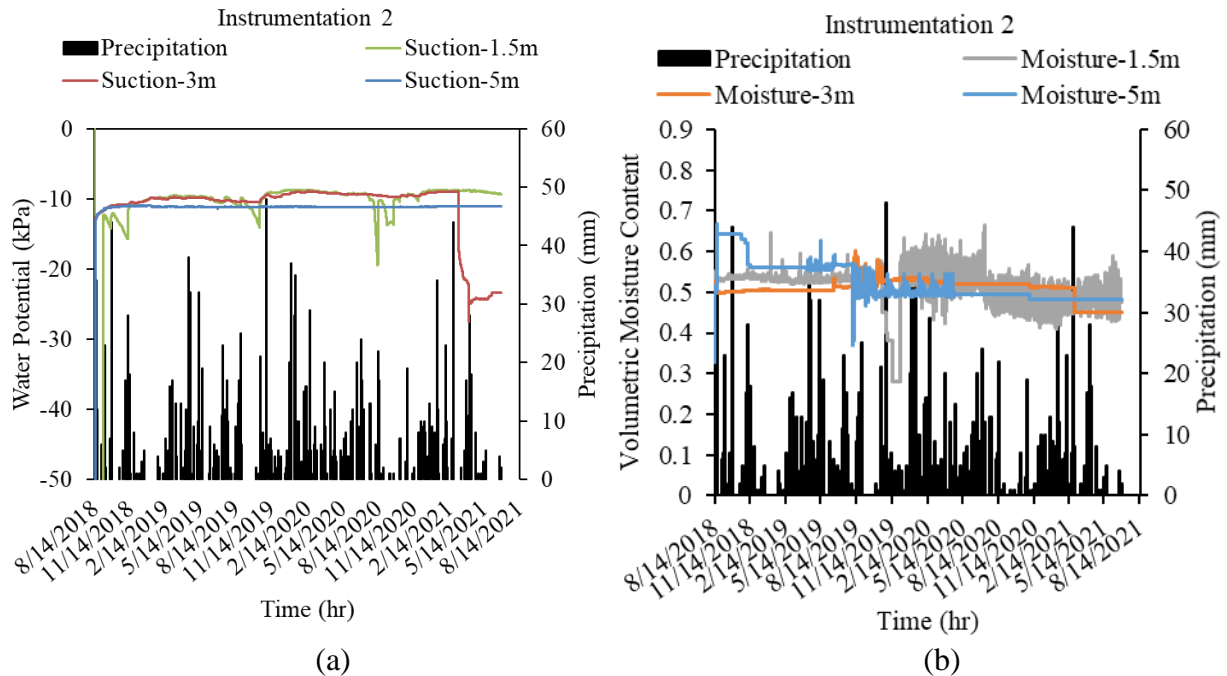


Figure 3.10 Variation of parameters at I-Slope 1 (a) Matric Suction, (b) Moisture Content and Rainfall data from Instrumentation 2

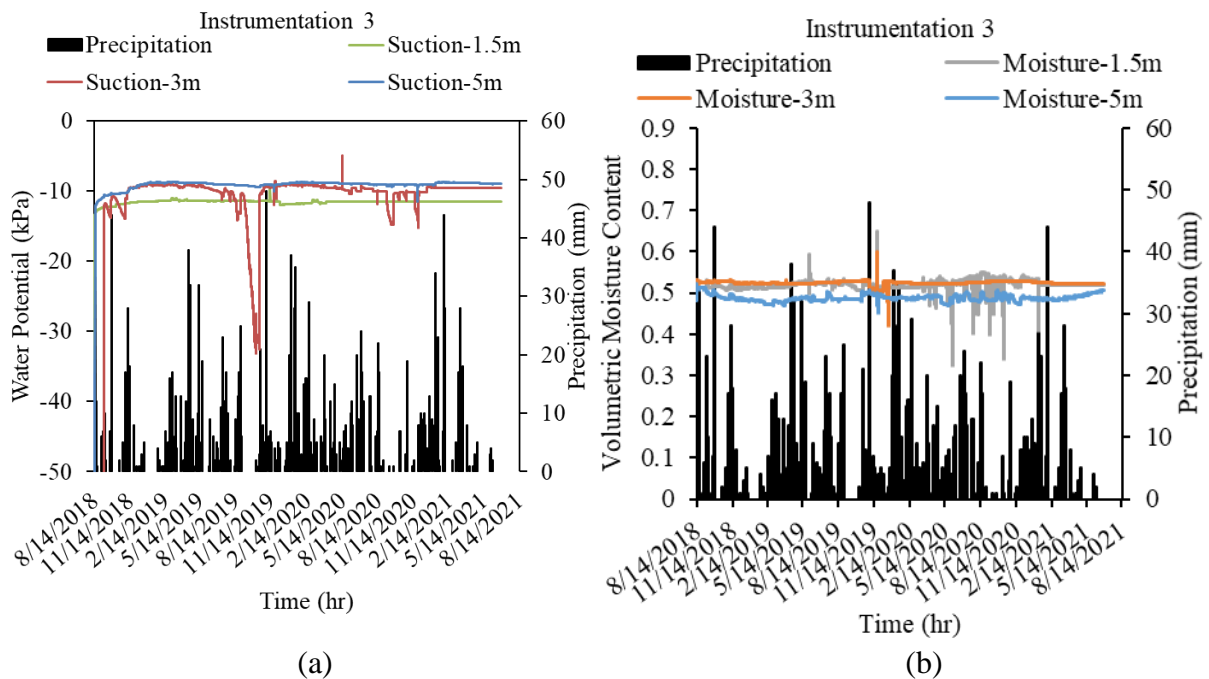


Figure 3.11 Variation of parameters at I-Slope 1 (a) Matric Suction, (b) Moisture Content and Rainfall data from Instrumentation 3

Figures 3.9 to 3.11 present variations in the moisture content(volumetric) with time. The moisture content changes at the site slopes' soil layers are influenced by the water infiltration after rainfall events. Typically, variations in moisture content are inversely related to variations in the

matric suction profile. This means that the soil moisture content increases during and immediately after rainfall while the matric suction decreases (Hossain et al., 2013). Yazoo Clay exhibits minimal changes in soil water content at deeper depths and a steady matric suction profile. The soil was saturated at all depths during rainfall, and the volumetric moisture content was between 0.5 to 0.7. Figures 3.9 to 3.11 illustrate the consistent and minimal variations in matric suction with rainfall at different depths in both the crest and middle of the slope. The soil below approximately 5 ft. (1.5 m) depth was fully saturated, despite the low permeability of Yazoo Clay hindering the downward movement of rainwater. The suction values increased with depth at the slope crest, but this trend differed at Instrumentation 2 and Instrumentation 3 in the middle of the slope.

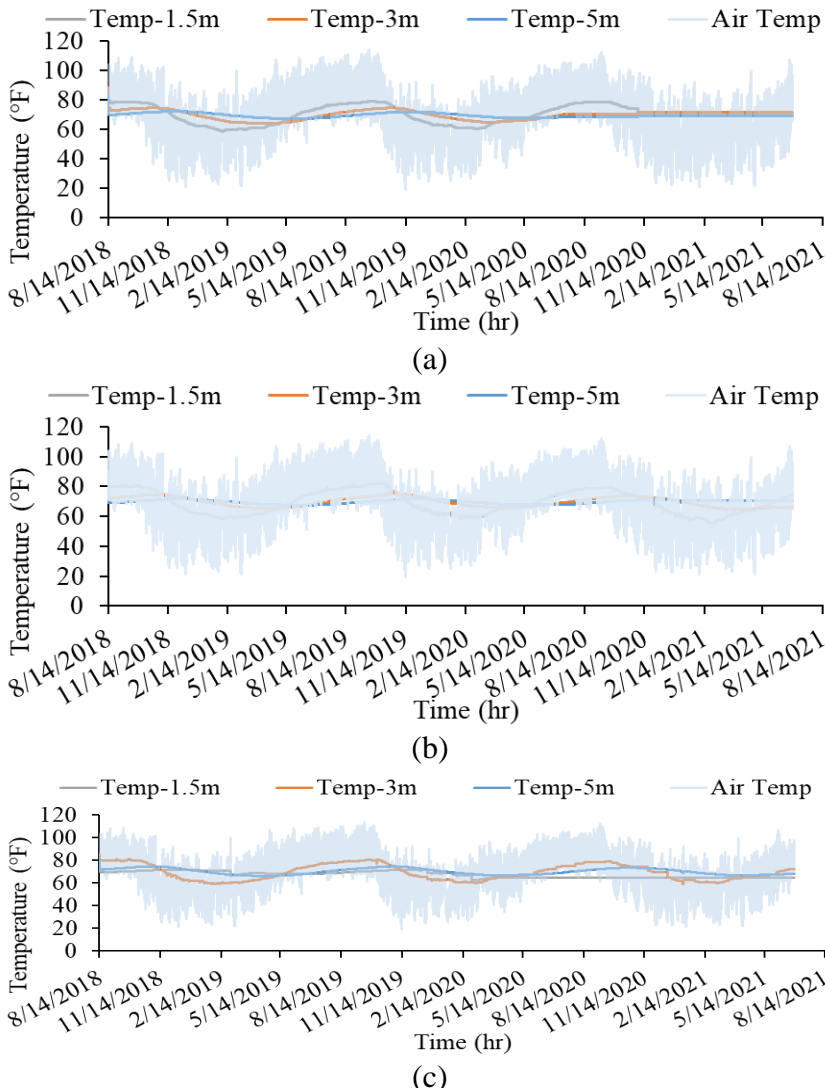


Figure 3.12 Variations of Air and Soil Temperature at I-Slope 1 (a) Instrumentation 1, (b) Instrumentation 2, and (c) Instrumentation 3

3.4 Instrumented Slope 2 (I-Slope 2): Metrocenter Highway Slope

I-Slope 2, situated near Metrocenter, is a 3H:1V slope with a height of 23 ft. The slope experienced a failure near the I-220N bridge and was subsequently repaired by installing H-piles at the crest. Both the repaired section and the original as-built slope were chosen for monitoring. Figure 3.13 provides a visual depiction of the slope's location.



Figure 3.13 Location of I-Slope 2

Instrumentation was carried out in the reinforced section of I-Slope 2 at the crest, middle, and toe. Three 15 ft. boreholes (Instrumentation 1, Instrumentation 2, and Instrumentation 3) were drilled and instrumented accordingly. Figure 3.14 illustrates the locations of these boreholes. Each instrumentation location was equipped with a moisture sensor and a water potential sensor at depths of 5 ft, 10 ft, and 15 ft. Additionally, Instrumentation 1 had a rain gauge and an air temperature sensor installed. Furthermore, Inclinator 1 was installed at the reinforced section; inclinometer 2 was installed at the as-built section. Both were installed in the middle of the slope.

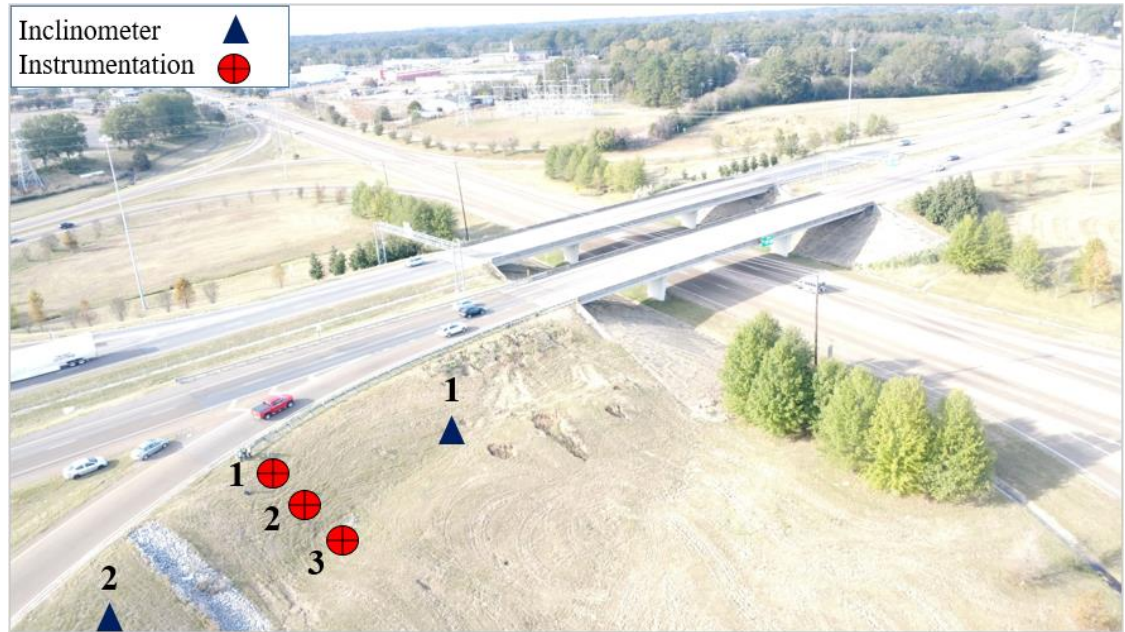


Figure 3.14 Instrumentation layout at I-Slope 2

3.4.1 *Field Monitoring Results*

3.4.1.1 *Slope Movement Data*

The slope's horizontal movement data was obtained by collecting measurements at 2 ft. intervals along the slope inclinometer pipe. These measurements were then analyzed to determine the movement of the slope. Figure 3.15 presents the data from Inclinometer 1 at the reinforced section, while Figure 3.18 shows the time-dependent movement at the slope's surface. Similarly, Figure 3.15 displays the horizontal movement data from Inclinometer 2 at the as-built section, and Figure 3.18 represents the time-dependent movement at the slope's surface. The figures indicate no significant movement in either section, demonstrating satisfactory slope performance. It should be noted that the inclinometer was struck by an external object at the surface in late 2021, rendering the results from late 2021 inconsistent with the previously observed trend shown in Figure 3.17.

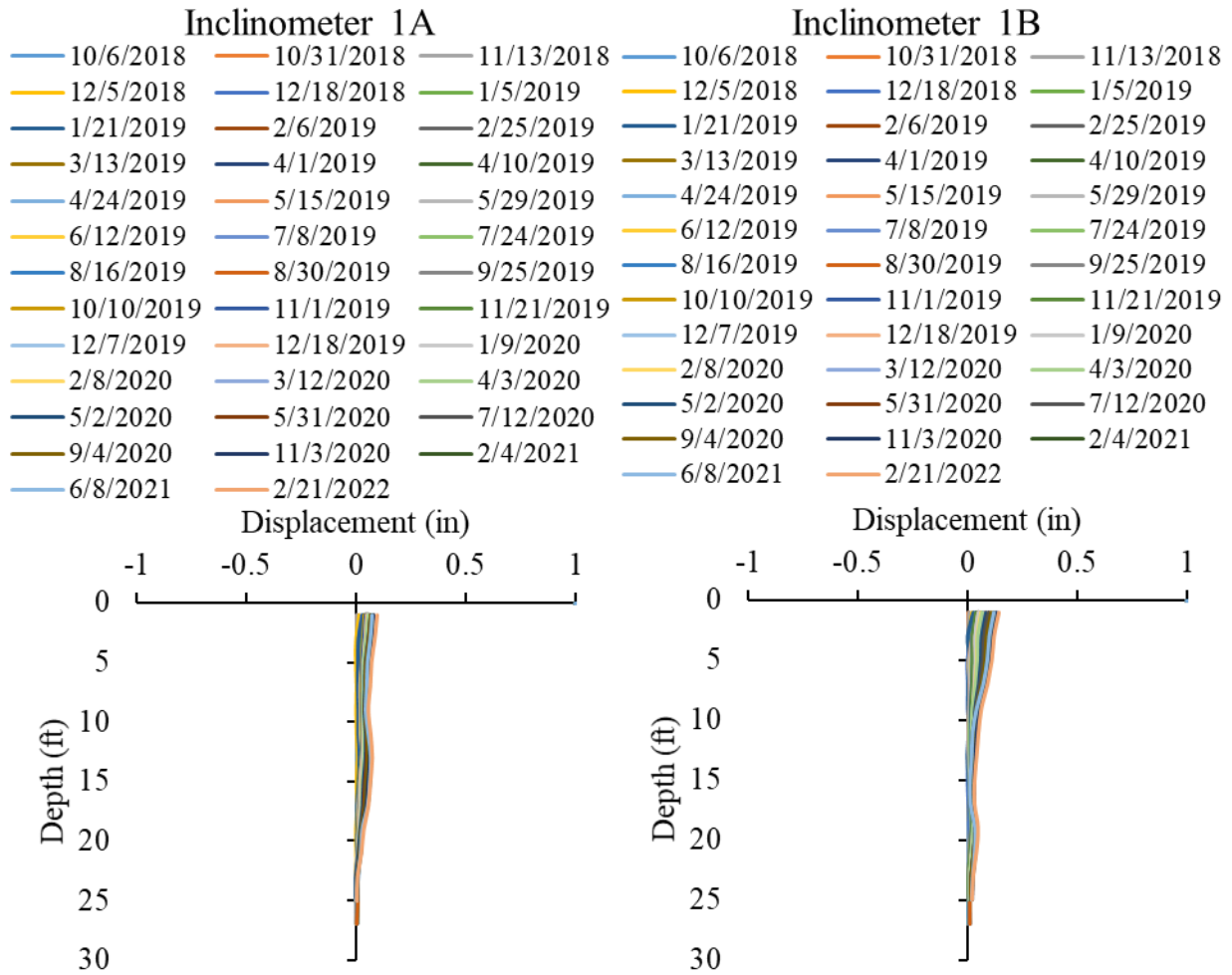


Figure 3.15 Displacements at Inclinator 1 at I-Slope 2

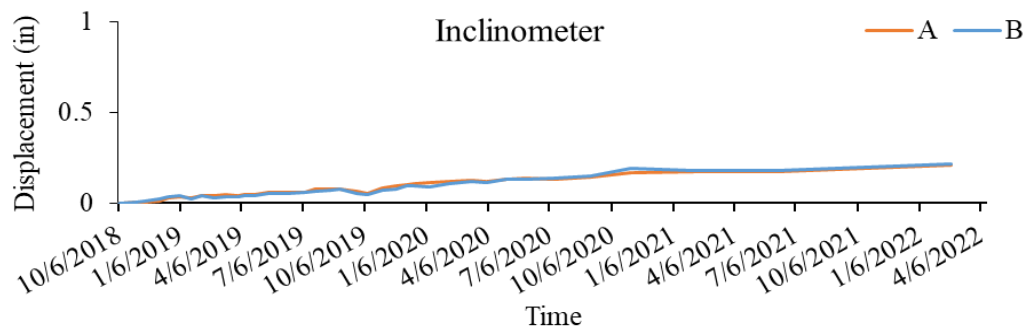


Figure 3.16 Overtime Lateral Deformation at the Top of Inclinator 1 at I-Slope 2.

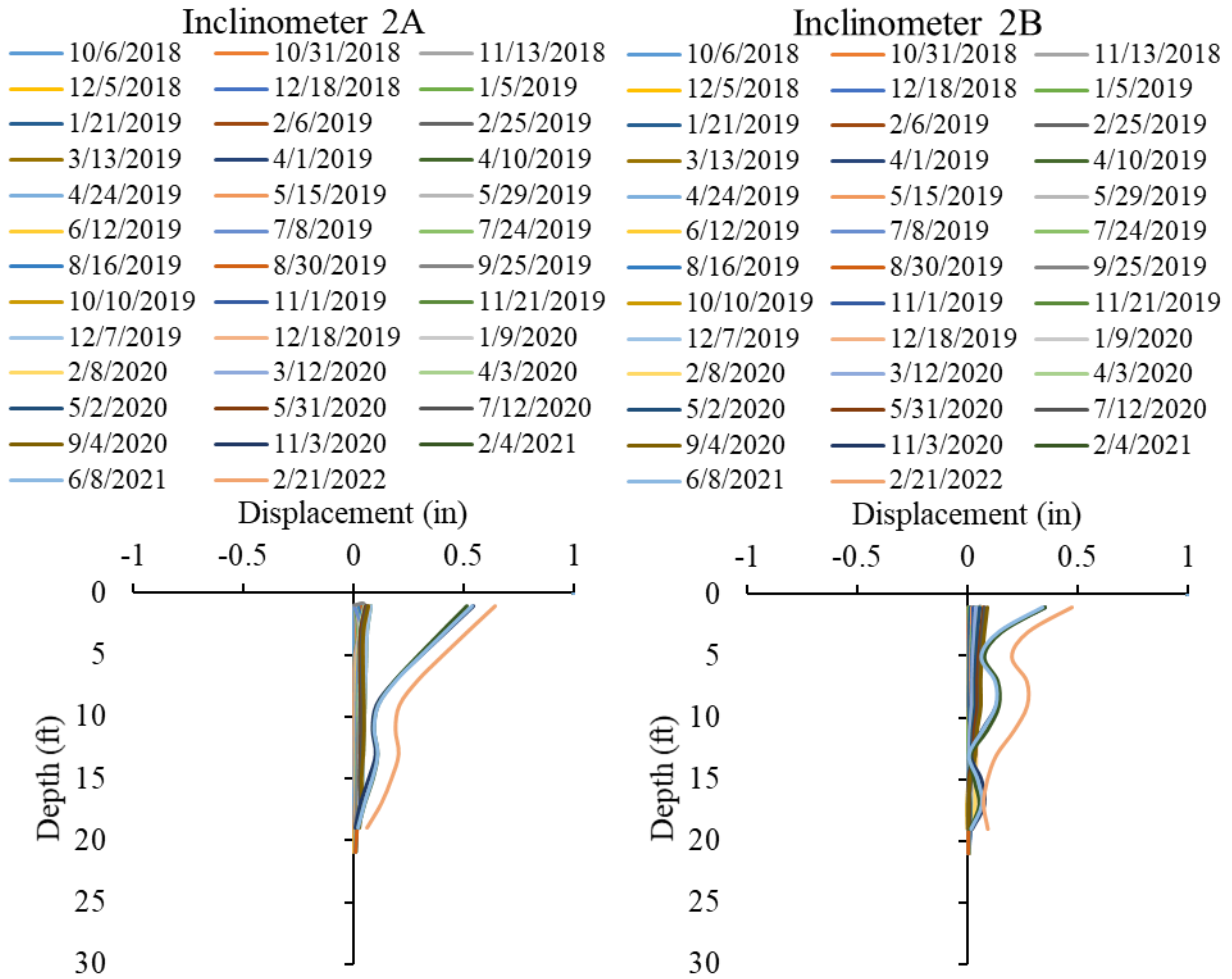


Figure 3.17 Displacements at Inclinerometer 2 at I-Slope 2

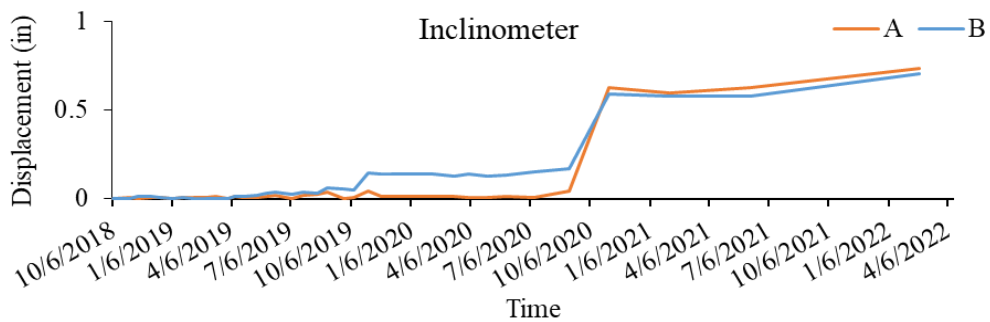


Figure 3.18 Overtime Lateral Deformation at the Top of Inclinerometer 2 at I-Slope 2.

3.4.1.2 Instrumentation Data

Figures 3.19, 3.20, and 3.21 display the variations in the in situ matric suction profile and moisture content at depths of 5 ft. (1.5 m), 10 ft. (3 m), and 15 ft. (5 m) with rainfall. During the initial three months after Instrumentation 1 and Instrumentation 2 installation, an initial variation in moisture was observed, indicating an adjustment period for moisture distribution. However, no

changes were observed in the matric suction at these locations. Minimal moisture variations were observed at the crest of the slope (Instrumentation 1) over the two-year monitoring period. In contrast, variations were observed at the middle of the slope (Instrumentation 2) during the summer and late December of 2019, indicating rainwater infiltration. Surface cracks near the slope's toe were observed, and a significant moisture variation was detected, suggesting rainwater infiltration through the cracks.

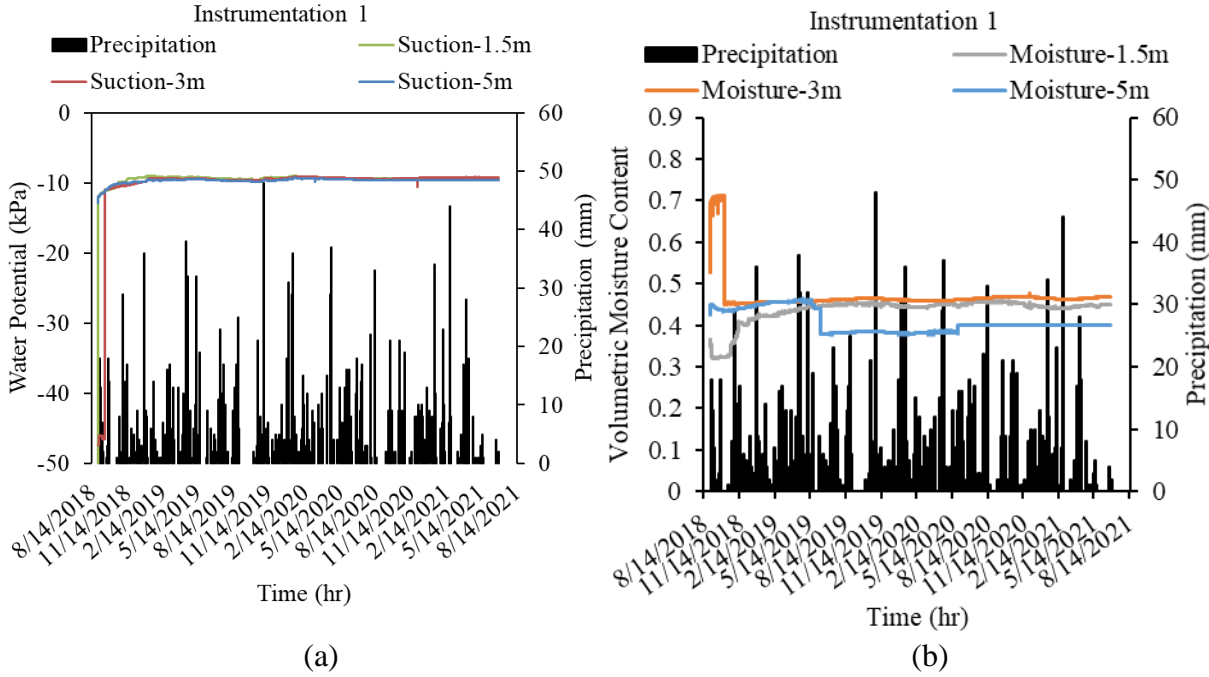


Figure 3.19 Variation of parameters at I-Slope 2 (a) Matric Suction, (b) Moisture Content and Rainfall data from Instrumentation 1

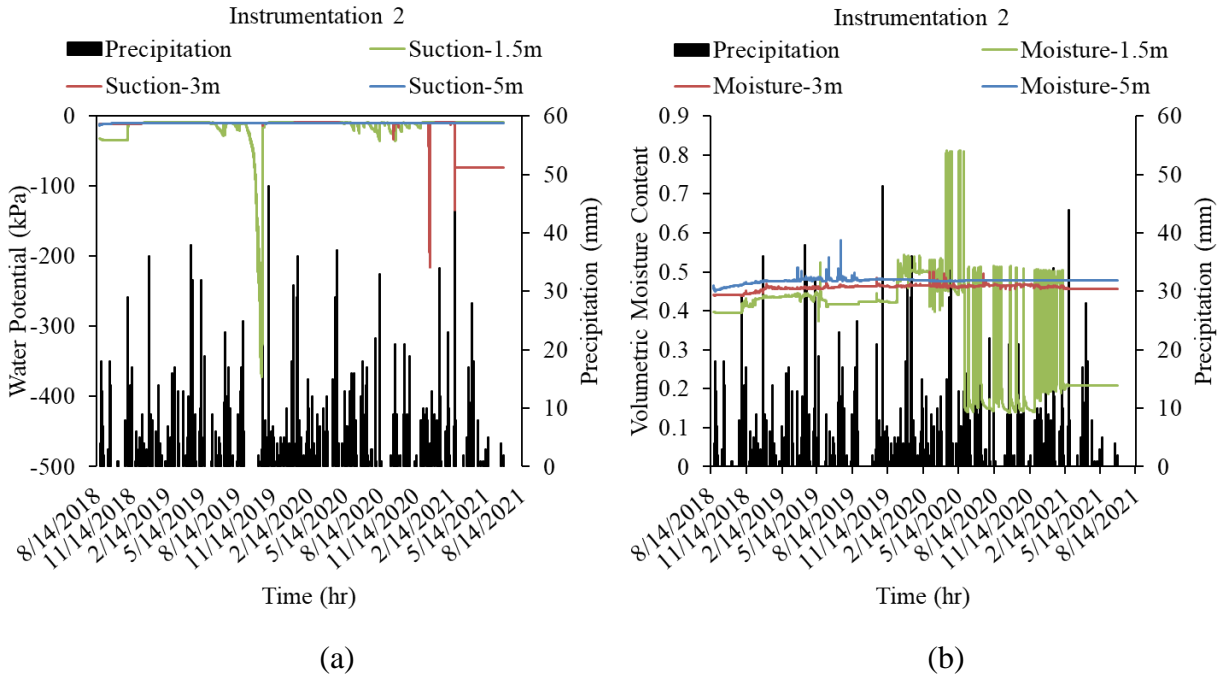


Figure 3.20 Variation of parameters at I-Slope 1 (a) Matric Suction, (b) Moisture Content and Rainfall data from Instrumentation 2

Figure 3.19 to Figure 3.21 display the variations of in situ matric suction with daily rainfall data at different depths (5 ft., 10 ft., and 15 ft.) in the slope's crest, middle, and toe. The matric suction exhibited a low and steady change at the middle and toe of the slope.

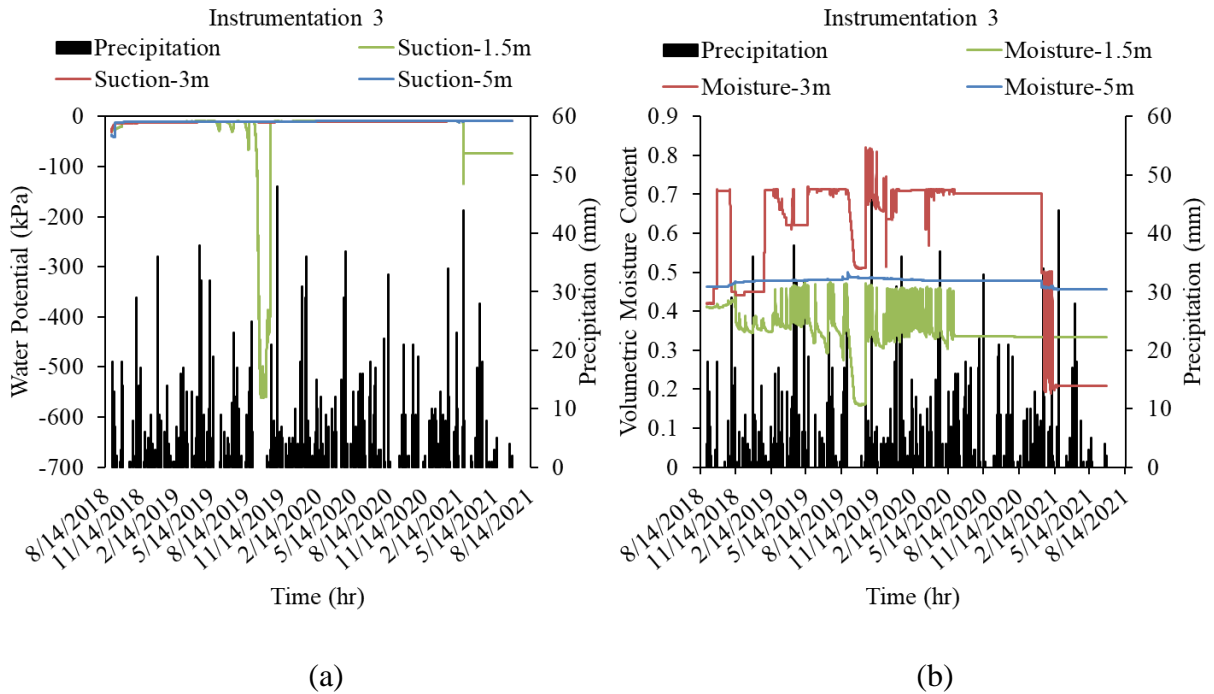


Figure 3.21 Variation of parameters at I-Slope 1 (a) Matric Suction, (b) Moisture Content and Rainfall data from Instrumentation 3

Figure 3.22 illustrates the variations in in-situ soil and air temperatures at Instrumentation 1, 2, and 3. The soil temperature at shallow depths (5 ft. and 10 ft.) showed fluctuations corresponding to the changes in air temperature, while the temperature at the deeper depth (15 ft.) remained constant.

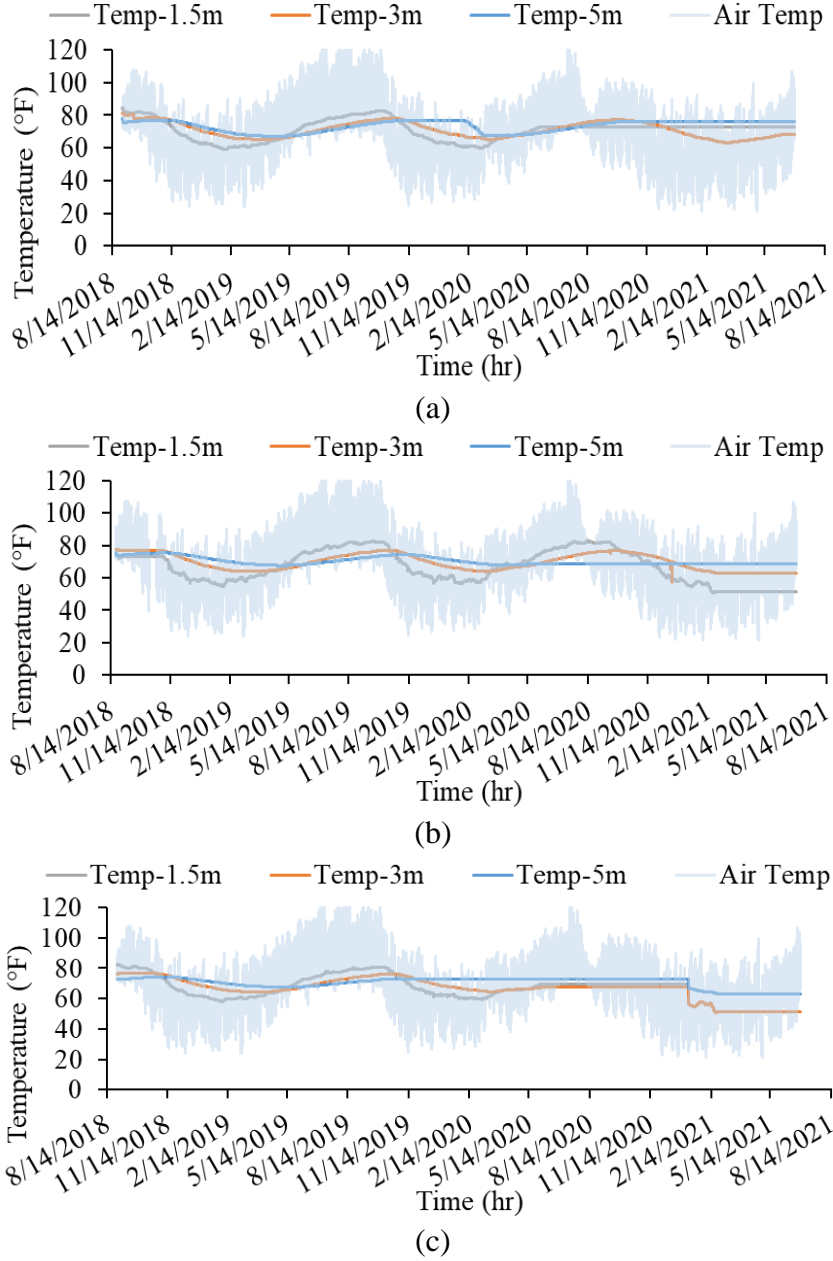


Figure 3.22 Variations of Air and Soil Temperature at I-Slope 1 (a) Instrumentation 1, (b) Instrumentation 2, and (c) Instrumentation 3

3.5 Instrumented Slope 3 (I-Slope 3): Terry Road Highway Slope

I-Slope 3, depicted in Figure 3.23, is a 15 ft. high slope with a grade range of 3.5 H: 1V to 4H: 1V. It is situated along the I20E exit toward Terry Road. This slope encountered shallow landslides near the bridge, which were subsequently remediated using H-piles.

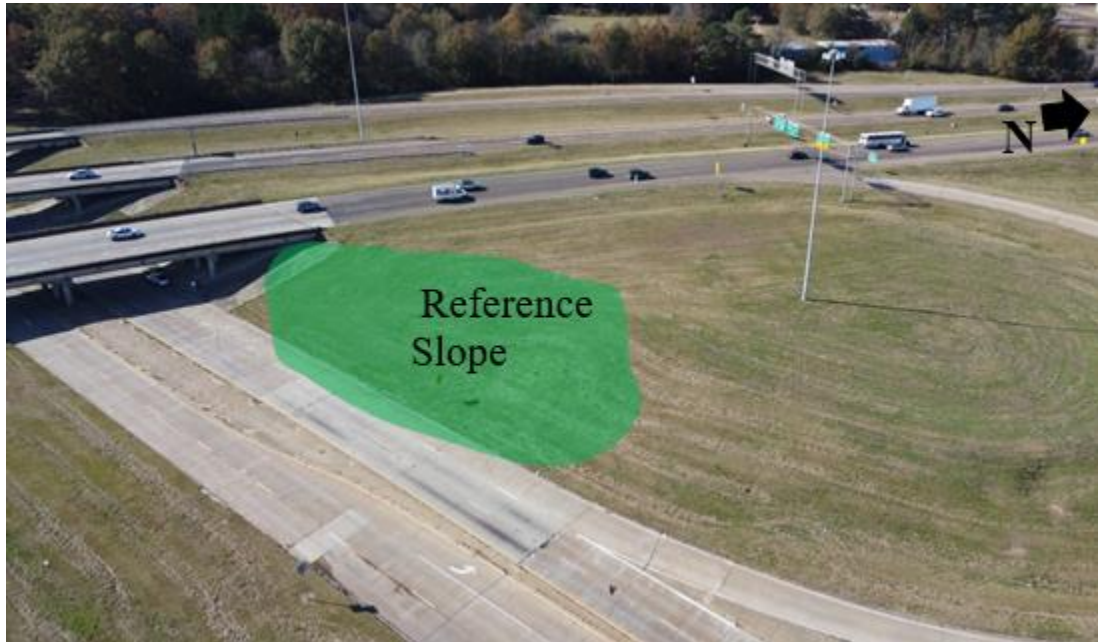


Figure 3.23 Location of I-Slope 3

I-Slope 3 consists of reinforced and as-built sections. The reinforced section includes Instrumentation 1 and 2, while the as-built section includes Instrumentation 3. Figure 3.24 illustrates the locations of these instrumentation points. Instrumentation 1 borehole is positioned at the crest of the slope, while Instrumentation 2 and Instrumentation 3 are located in the middle of the slope. Each instrumentation location is equipped with moisture and water potential sensors at depths of 5 ft (1.5 m), 10 ft (3 m), and 15 ft (5 m). Instrumentation 1 also features a rain gauge and air temperature sensor. Additionally, two inclinometers were installed in the middle of both sections, whose locations are presented in Figure 3.24. Inclinometer 1 was installed at the as-built section, and Inclinometer 2 was installed at the repaired section.



Figure 3.24 Instrumentation Layout at I-Slope 3

3.5.1 *Field Monitoring Results*

3.5.1.1 *Slope Movement Data*

Inclinometer data collected at 2 ft. intervals down the pipe were collected and analyzed to assess the slope's movement. Figure 3.25 shows the horizontal movement data from Inclinometer 1 in the reinforced section, while Figure 3.28 illustrates the time-dependent movement at the slope's surface. The analysis revealed that the as-built section of I-Slope 3 experienced movement starting in January 2019, with a maximum displacement of 1.6 inches at the slope surface within a year. The movement occurred at a shallow depth of approximately 6 ft. and requires maintenance. On the other hand, Inclinometer 2 in the reinforced section exhibited no movement, indicating satisfactory performance at the repaired section of the slope.

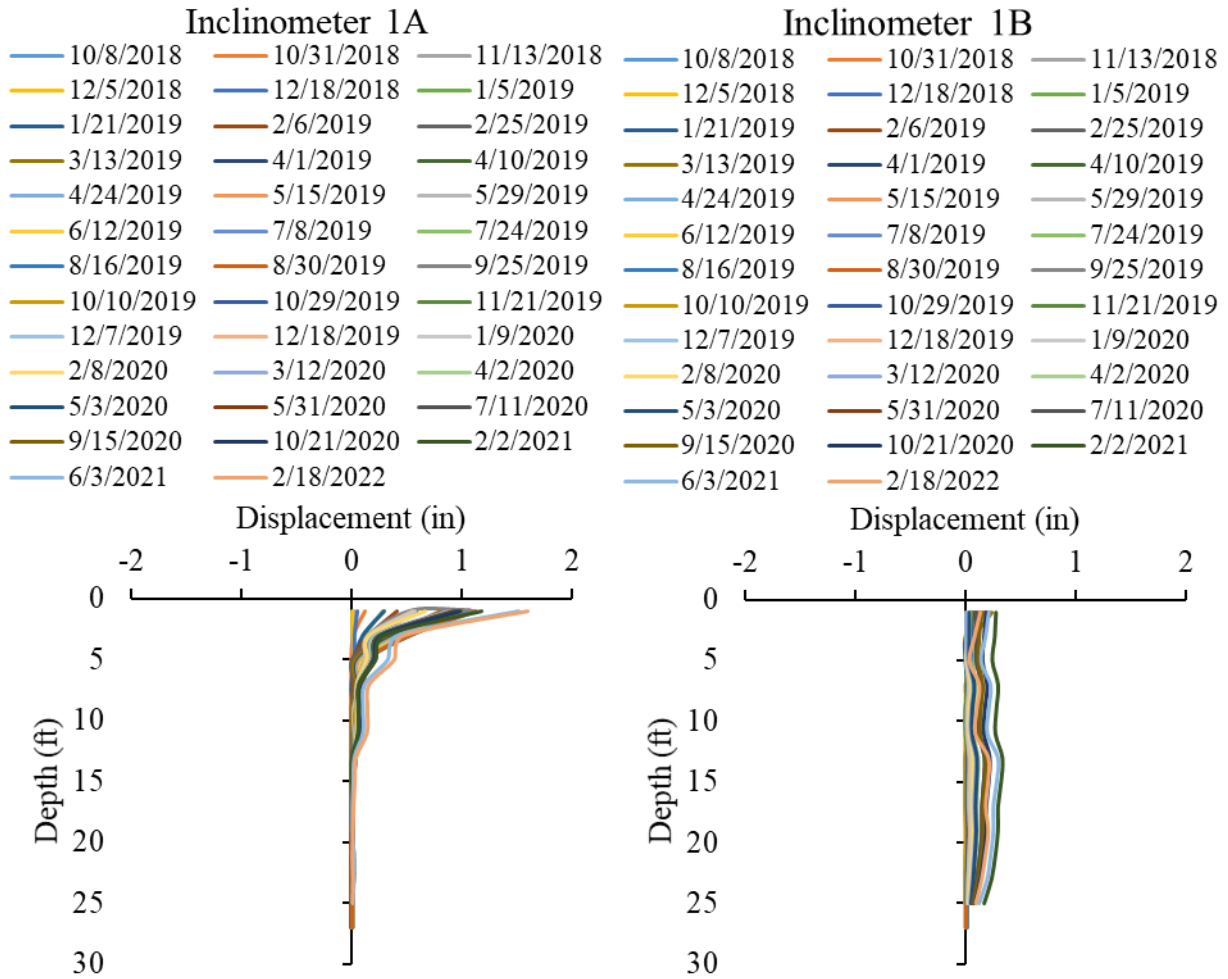


Figure 3.25 Displacements at Inclinator 1 (as built section) of I-Slope 3

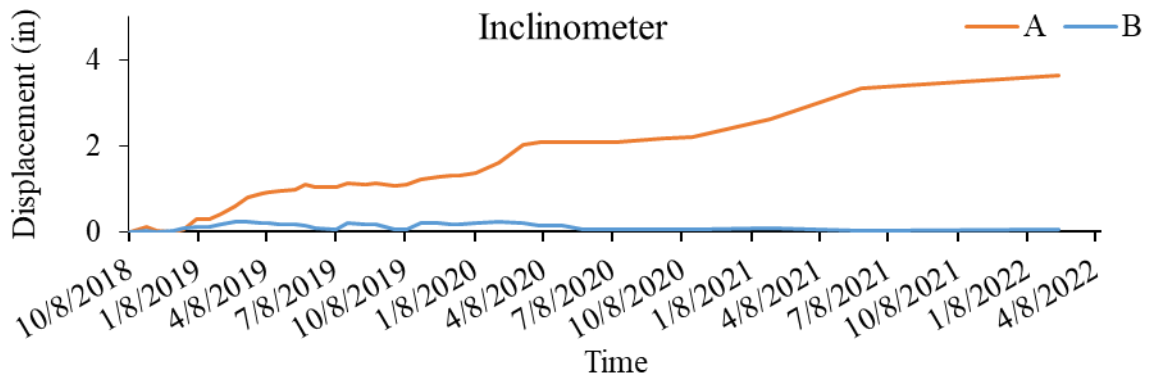


Figure 3.26 Overtime Lateral Deformation near the Top of Inclinator 1 (as built section) at I-Slope 3

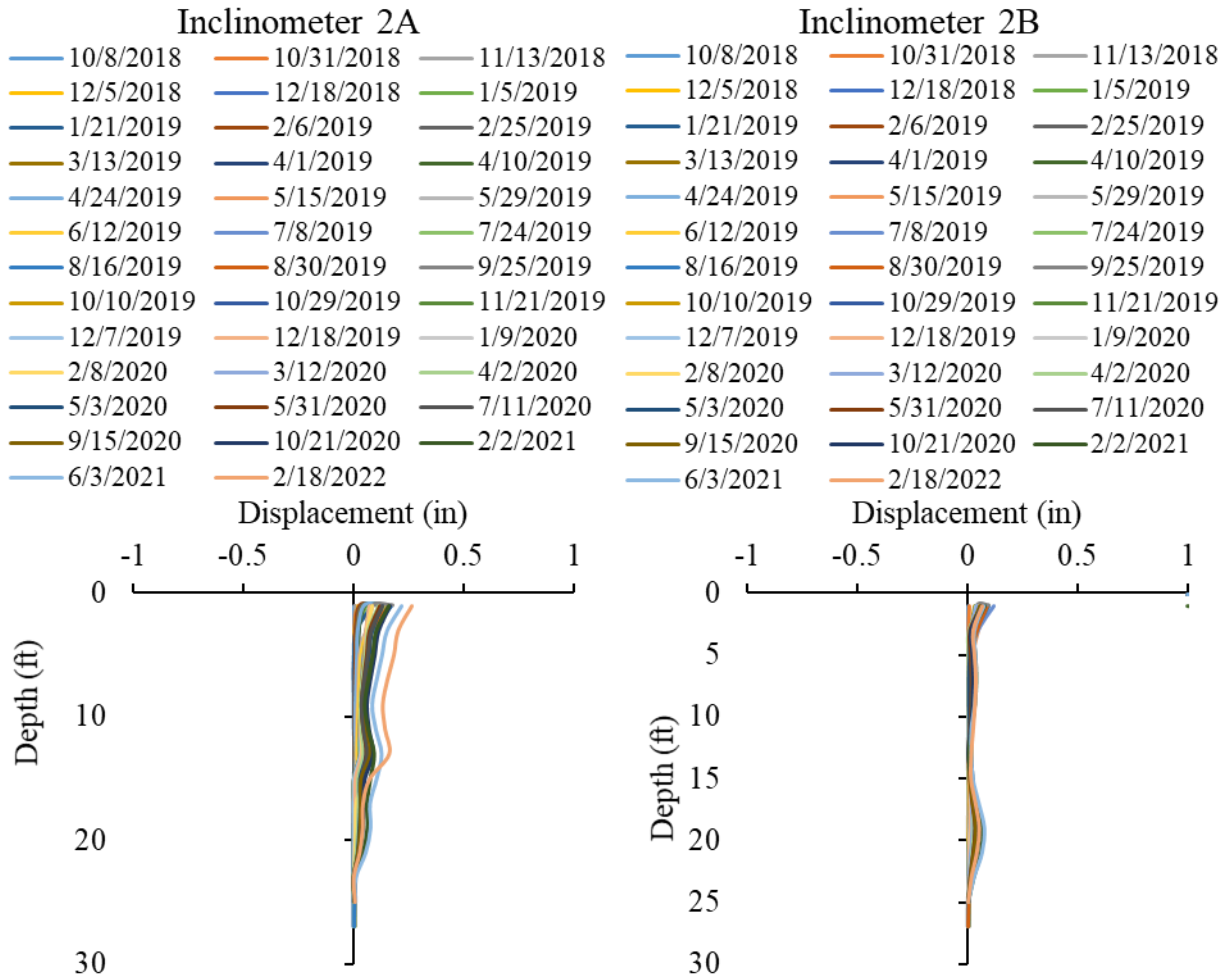


Figure 3.27 Displacements at Inclinator 2 (repaired section) of I-Slope 3

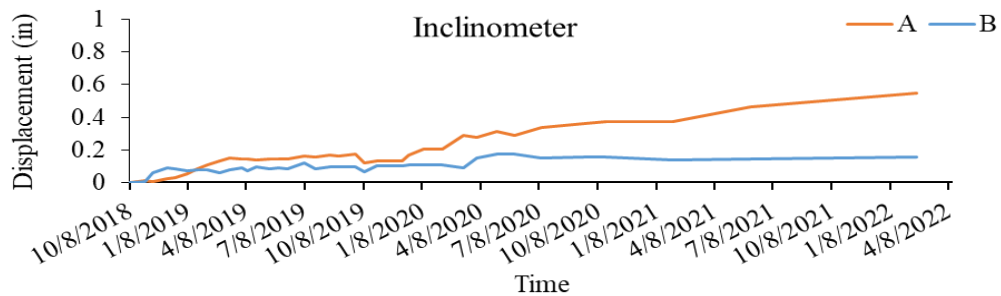


Figure 3.28 Overtime Lateral Movement at the Top of Inclinator 2 (repaired section) at I-Slope 3.

3.5.1.2 Field Instrumentation Data

Figure 3.29, Figure 3.30, and Figure 3.31 illustrate the variations in the in situ matric suction profile and moisture content at different depths with rainfall. The monitoring results from Instrumentation 1 indicate that the matric suction initially reached a high value and then stabilized at a low value for the rest of the monitoring period, indicating a fully saturated condition. The volumetric moisture content remained constant during the two-year monitoring period, indicating

a consistently saturated state. The middle sections of the reinforced and as-built areas showed similar suction variations, with indications of rainwater intrusion in the volumetric moisture content. However, the overall moisture content remained constant over time. The constant moisture content and matric suction at Instrumentation 2 and Instrumentation 3 are attributed to the presence of a perched water condition in the slope.

In January 2019, the as-built section began to experience shallow movements, as shown in Figures 3.29 and 3.31. It is important to highlight that no movement was detected in the reinforced section which was stabilized using H-piles. The H-piles' stabilization has effectively prevented further slope movement in that section.

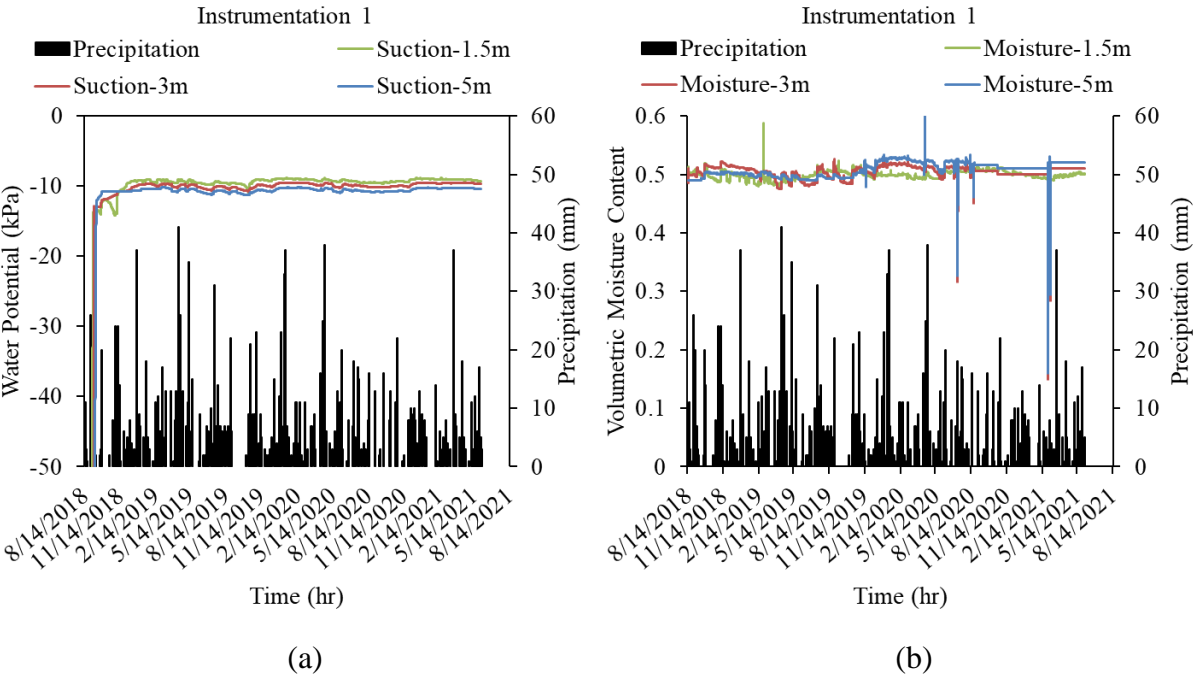


Figure 3.29 Variation of parameters at I-Slope 3 (a) Matric Suction, (b) Moisture Content and Rainfall data from Instrumentation 1

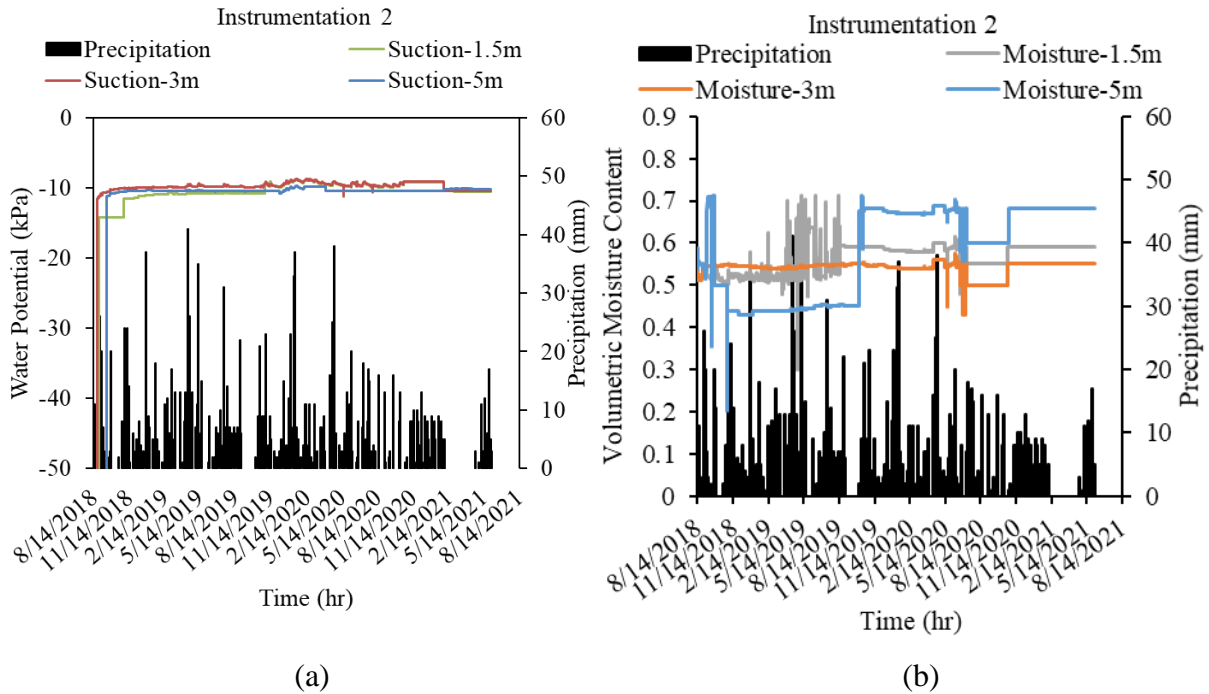


Figure 3.30 Variation of parameters at I-Slope 3 (a) Matric Suction, (b) Moisture Content and Rainfall data from Instrumentation 2

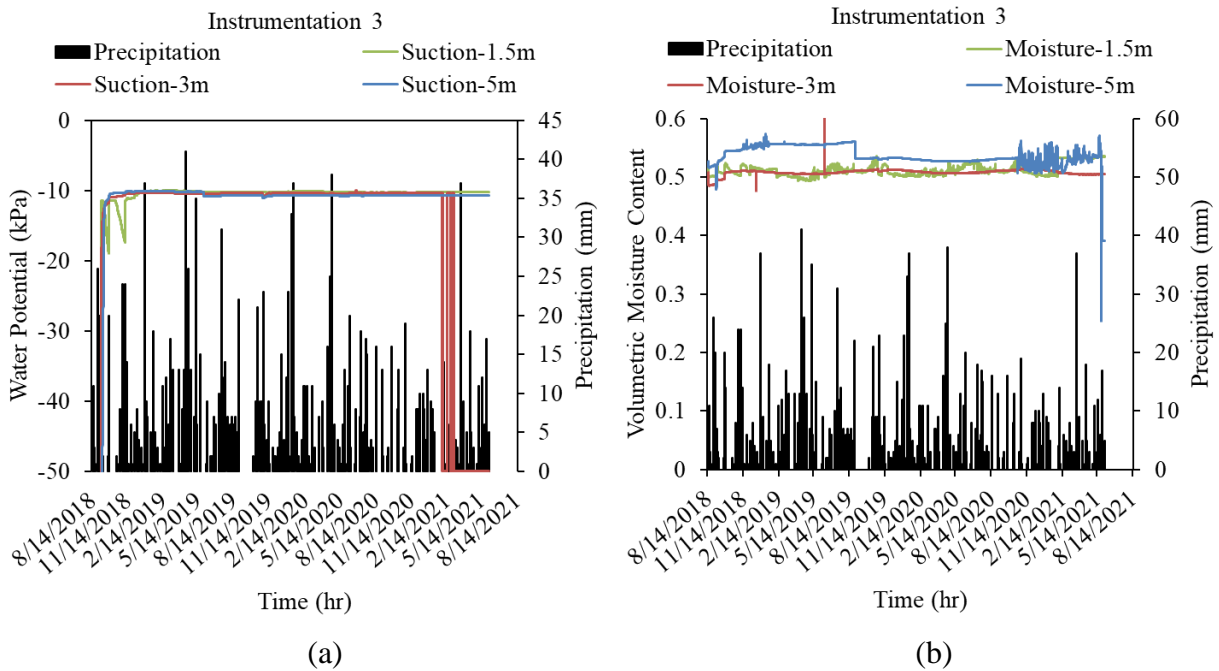


Figure 3.31 Variation of parameters at I-Slope 3 (a) Matric Suction, (b) Moisture Content and Rainfall data from Instrumentation 3

Figure 3.32 presents the in-situ soil and air temperature variations collected from Instrumentation 1 to Instrumentation 3. The temperature of the soil at shallow depths varied

somewhat with changes in the air temperature. At deeper depths, however, the soil temperature remained constant.

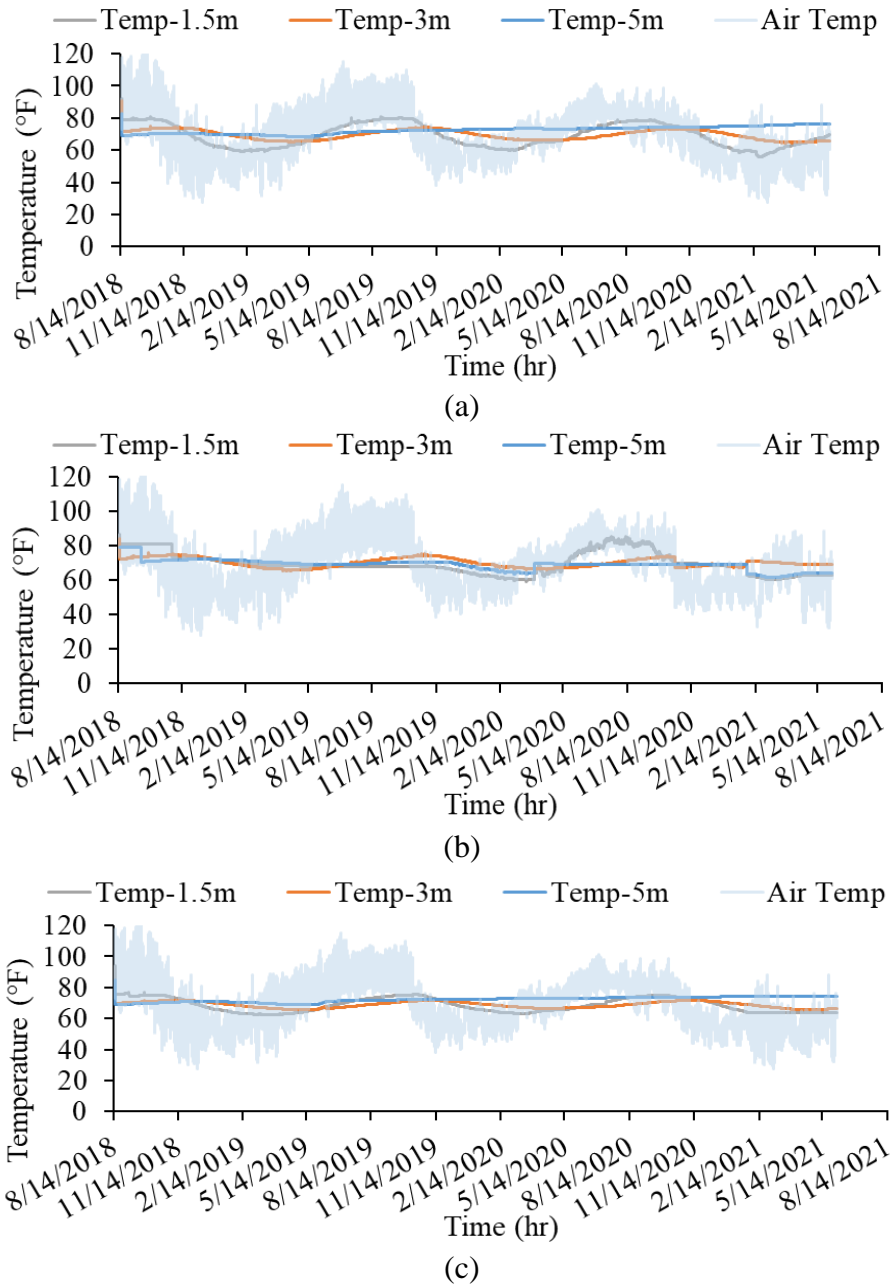


Figure 3.32 Variations of Air and Soil Temperature at I-Slope 1 (a) Instrumentation 1, (b) Instrumentation 2, and (c) Instrumentation 3

3.6 Instrumented Slope 4 (I-Slope 4): Highland Drive Highway Slope

Slope 4, located along I20 E near Highland Drive, is a 3.5H:1V slope with a height of 20 ft. Notably, no pre-existing failure areas were reported for this slope, so the investigation focused solely on the as-built section. Figure 3.33 provides a visual representation of the slope's location.



Figure 3.33 Location of I-Slope 4

In the reinforced section of I-Slope 4, three 15 ft. boreholes (Instrumentation 1, Instrumentation 2, and Instrumentation 3) were drilled and equipped with instrumentation at the crest, middle, and toe of the slope, as depicted in Figure 3.34. The instrumentation included moisture and water potential sensors installed at depths of 5 ft (1.5 m), 10 ft (3 m), and 15 ft (5 m) at each location. Additionally, a vertical inclinometer was installed in the middle of the slope near Instrumentation 2 to measure slope displacement. Near Instrumentation 1, a rain gauge and air temperature sensor were installed to monitor precipitation and atmospheric conditions. Detailed photographs of the sensor installations can be seen in Figure 4.38. Furthermore, an inclinometer was installed at a depth of 30 ft. in the middle of the slope to assess deeper slope movements.



Figure 3.34 Instrumentation and Inclinometer at I-Slope 4

3.6.1 *Field Monitoring Results*

3.6.1.1 *Slope Movement Data*

Inclinometer measurements were conducted along the slope inclinometer pipe at 2 ft. intervals to gather data on the horizontal movement of the slope. The collected data were then analyzed to assess the slope's movement. Figure 3.35 displays the horizontal movement data from Inclinometer 1, while Figure 3.36 illustrates the time-dependent movement at the surface of the slope. The data reveals that no significant movement was observed; however, some movement was detected at depths ranging from 5 ft. to 10 ft. During the field inspection, it was noted that a void had formed near Inclinometer 1, as depicted in Figure 3.36, due to erosion of the slope surface. To address this issue, it is recommended to backfill the void with lean clay fill materials.

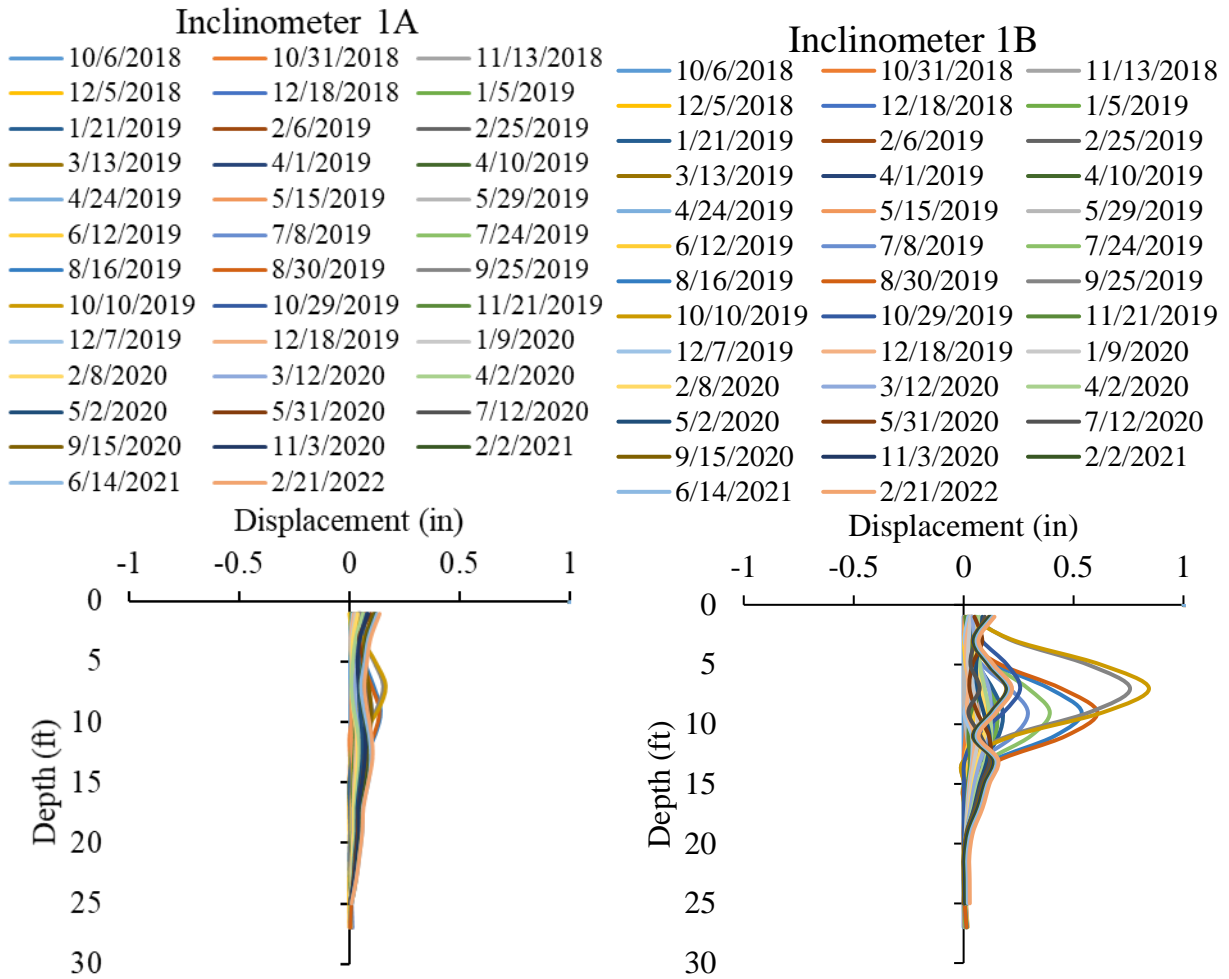


Figure 3.35 Displacements at Inclinator 1 at I-Slope 4

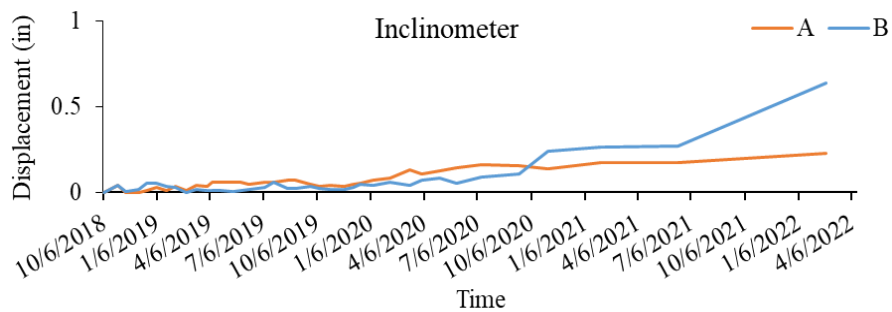


Figure 3.36 Overtime Lateral Deformation at the Top of Inclinator 1 at I-Slope 4

3.6.1.2 Field Instrumentation Data

Figures 3.37, 3.38, and 3.39 provide insight into the variations of the in situ matric suction profile and moisture content at different depths (5 ft., 10 ft., and 15 ft.) with rainfall. Specifically, Figure 3.39 showcases the monitoring results from Instrumentation 1, indicating that the volumetric moisture content remained constant over the two-year monitoring period. Similarly,

the matric suction exhibited a consistently low value of 10 kPa (209 psf). As previously discussed in the context of Slope 3, this consistent low value of matric suction and constant moisture content suggest that the soil is nearing a fully saturated condition. Therefore, it is highly likely that a perched water formation exists within the slope.

Figure 3.39 reveals significant fluctuations in moisture content at all depths in the middle of the slope, accompanied by lower matric suction values at 5 ft. (1.5 m) and 10 ft. (3 m) depths compared to the value at 15 ft. (5 m) depth. This indicates the infiltration of rainwater into the slope. Similar moisture and matric suction variations were observed at the toe of the slope. Notably, the fill material used in the slope reconstruction has high permeability, allowing consistent rainwater infiltration. However, this fill material is underlain by Yazoo Clay, which has very low permeability. As a result, rainwater infiltrates the fill material and creates a perched water condition, leading to a ponding effect within the fill soil's pore space. The movement observed in Inclinomometer 1 at depths of 5 ft. (1.5 m) to 10 ft. (3 m) is attributed to this perched water condition and the void formation resulting from soil erosion at the slope's surface.

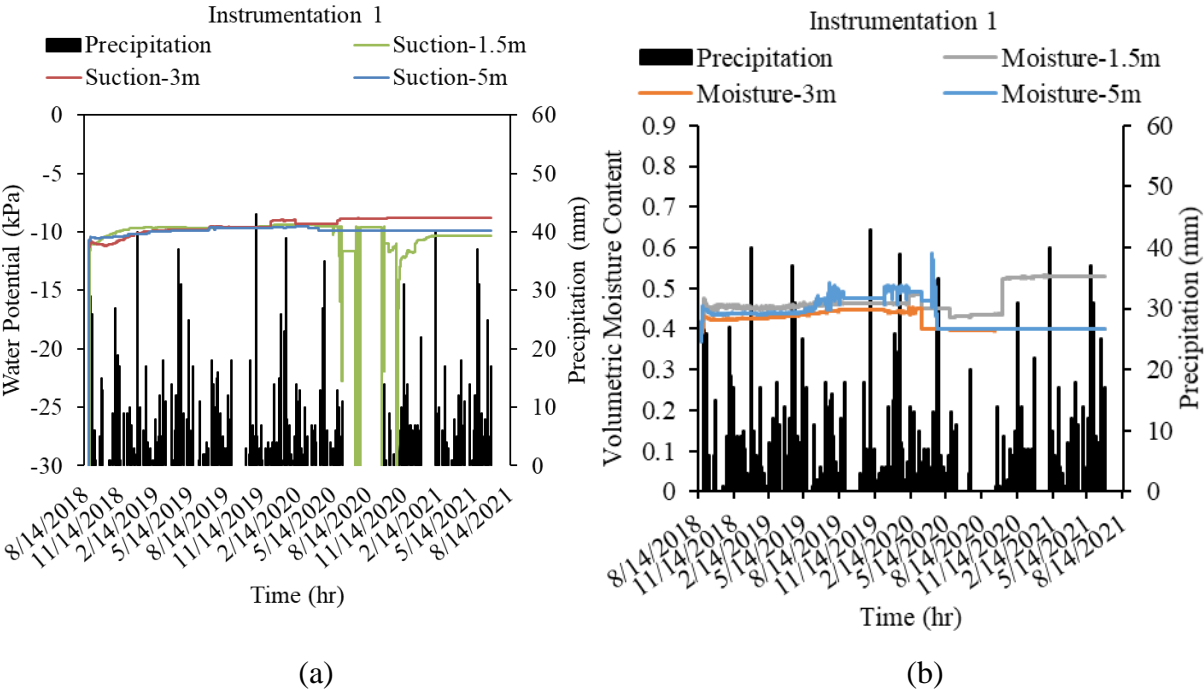


Figure 3.37 Variation of parameters at I-Slope 4 (a) Matric Suction, (b) Moisture Content and Rainfall data from Instrumentation 1.

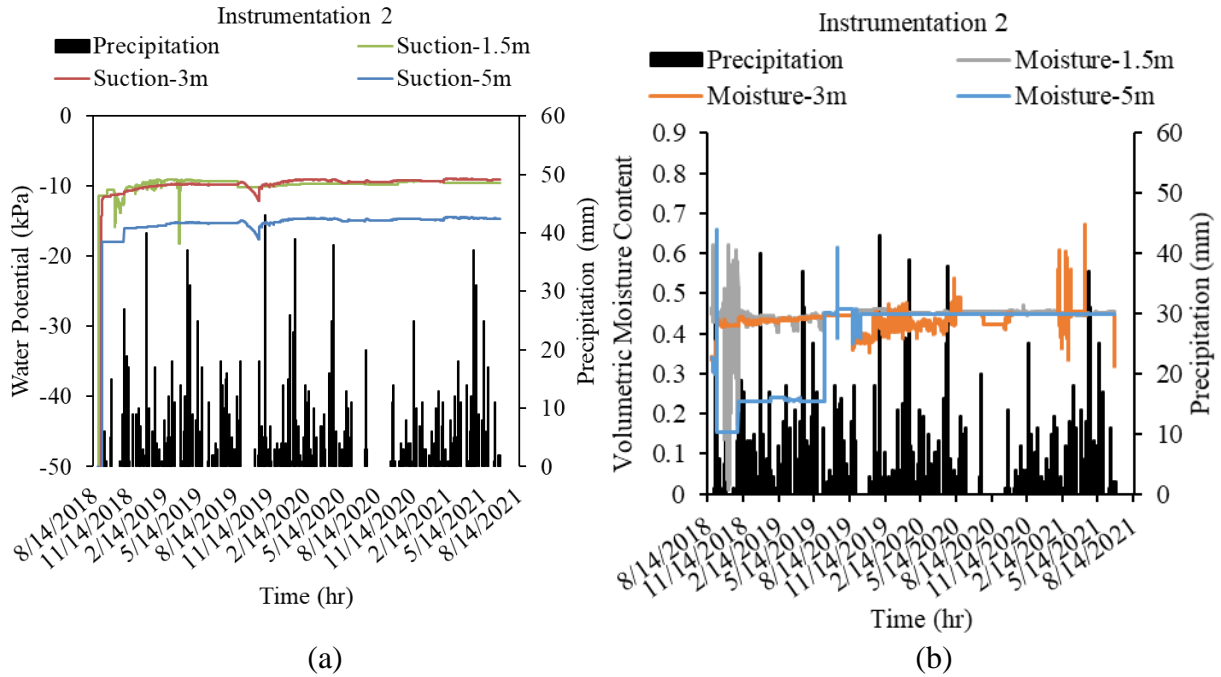


Figure 3.38 Variation of parameters at I-Slope 4 (a) Matric Suction, (b) Moisture Content and Rainfall data from Instrumentation 2

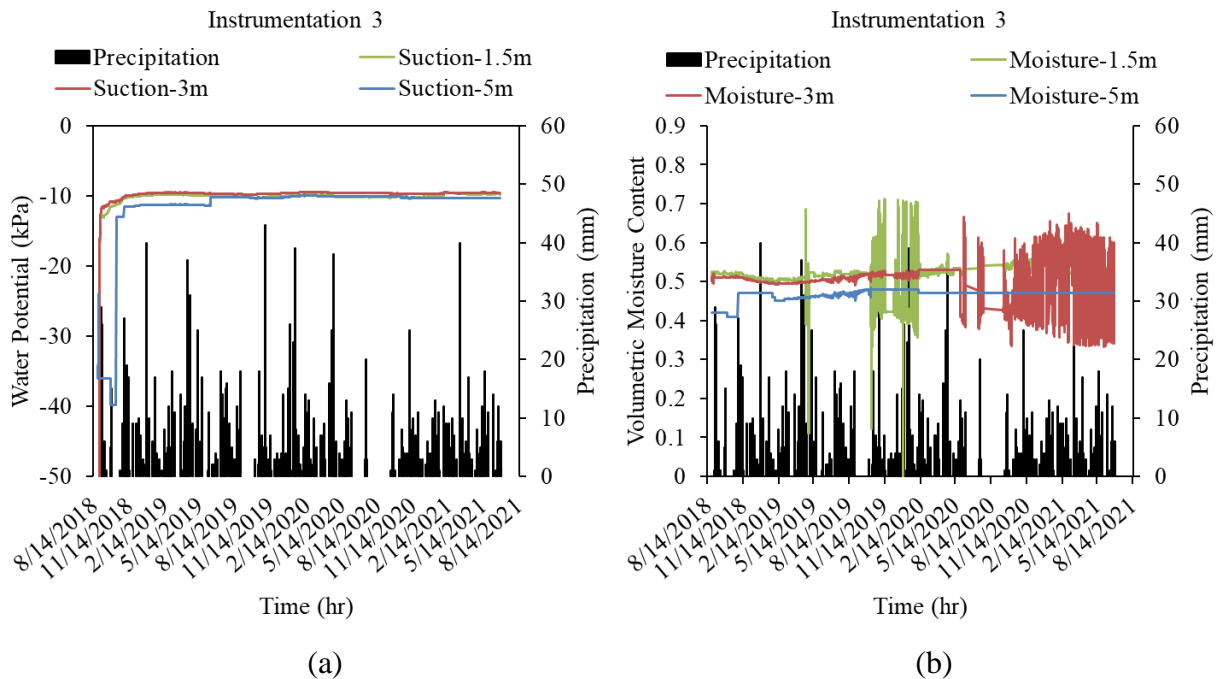


Figure 3.39 Variation of parameters at I-Slope 4 (a) Matric Suction, (b) Moisture Content and Rainfall data from Instrumentation 3

Figure 3.40 displays the soil and air temperature variations at Instrumentation 1 to Instrumentation 3. The soil's temperature at shallow depths showed some fluctuations, while the temperature at 15 ft. (5 m) depth remained relatively stable with minimal changes.

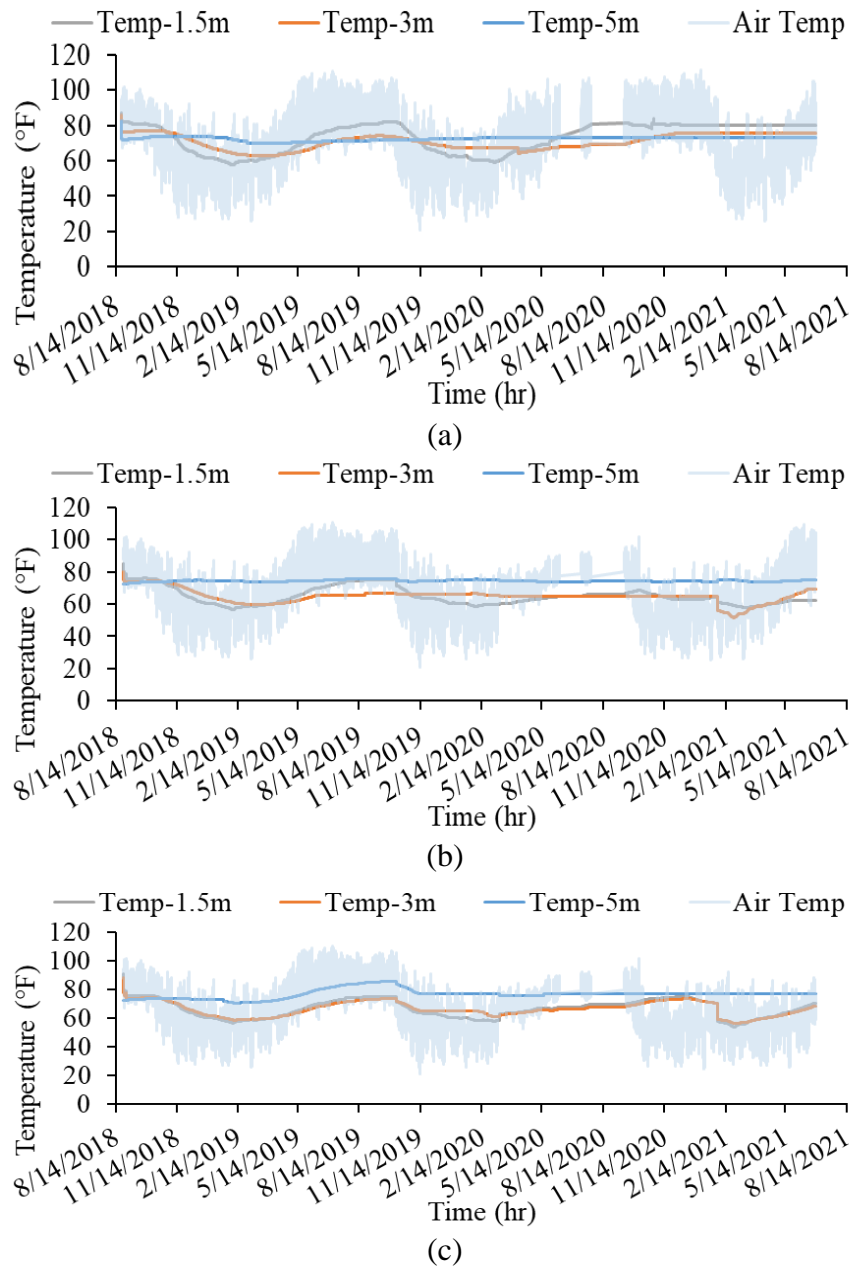


Figure 3.40 Variations of Air and Soil Temperature at I-Slope 4 (a) Instrumentation 1, (b) Instrumentation 2, and (c) Instrumentation 3

3.7 Instrumented Slope 5 (I-Slope 5): Sowell Road Highway Slope

I-Slope 5, located along the exit of I55 South toward Sowell Road, experienced a slide with a failure depth of 15 ft. The slope was rebuilt and repaired using 40 ft. long H-piles of HP 14 x 74 at the middle of the slope. Additionally, two layers of uniaxial geogrid were installed from the middle to the toe of the slope. The repaired and as-built sections were selected as study

areas for further investigation and monitoring. The details of the slope and repair methods are depicted in Figure 3.41.

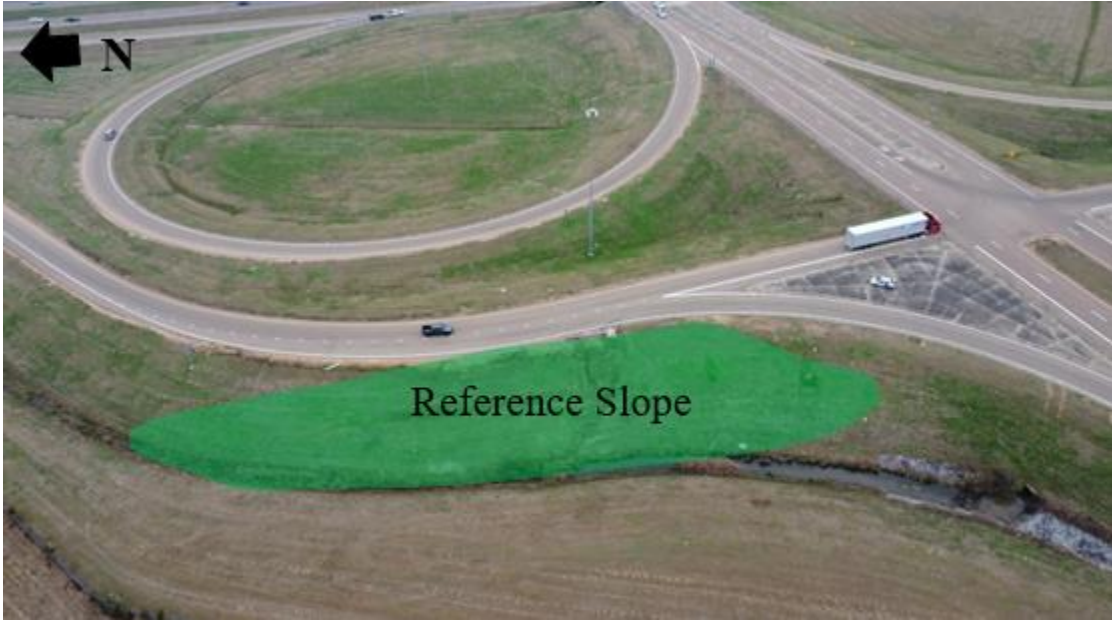


Figure 3.41 Location of I-Slope 5

Two 15 ft. boreholes, Instrumentation 1 and Instrumentation 2, were drilled and instrumented in the as-built section of I-Slope 5. A 15 ft. borehole, Instrumentation 3, was also drilled and instrumented in the reinforced section. Instrumentation 1 is located at the crest of the slope, while Instrumentations 2 and 3 are situated in the middle. At each instrumentation location, moisture and water potential sensors were installed at depths of 5 ft (1.5 m), 10 ft (4 m), and 15 ft (5 m). Furthermore, a rain gauge and air temperature sensor were installed at Instrumentation 1. Photos of the sensor installations can be seen in Figure 3.42. The Inclinator 1 and 2 installations were carried out in the middle of the slope. Both inclinometers have a depth of 40 ft., and Inclinator 1 is installed in the as-built section, while Inclinator 2 is installed in the repair section.

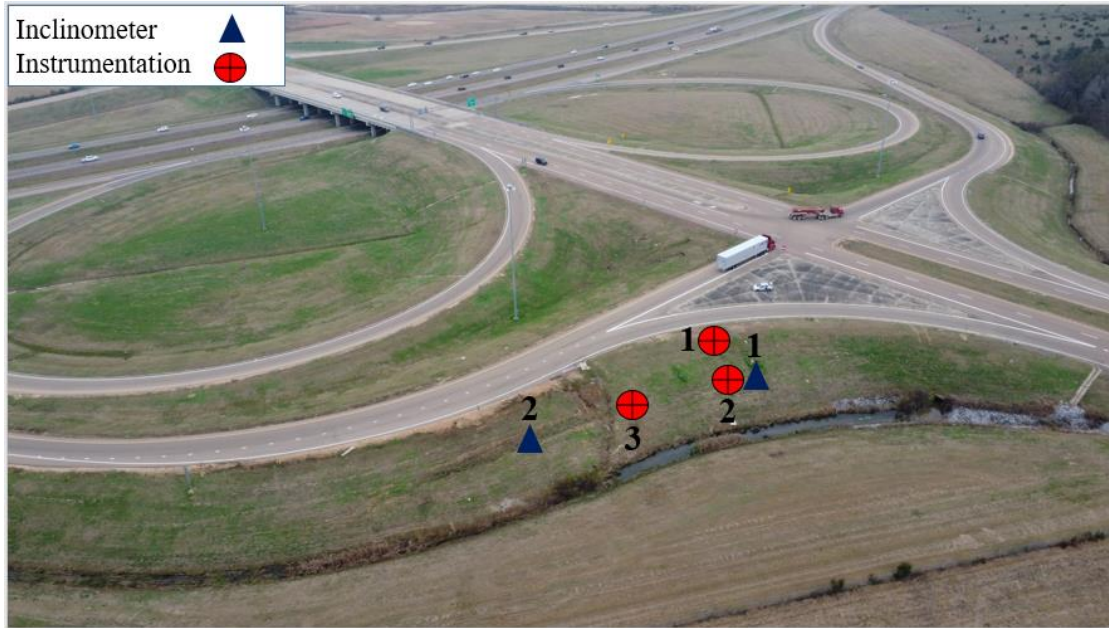


Figure 3.42 I-Slope 5 Instrumentation Layout

3.7.1 Field Monitoring Result

3.7.1.1 Movement Data

Data on the horizontal movement of the slope was obtained through inclinometer measurements taken at 2 ft. intervals along the slope. The collected data was then analyzed to determine the slope's movement. Figure 3.43 presents the horizontal movement data from Inclinometer 1 at the reinforced section, while Figure 3.44 displays the time-dependent movement at the slope's surface. Notably, no significant movement was observed in the as-built section of the slope, indicating a stable and satisfactory performance.

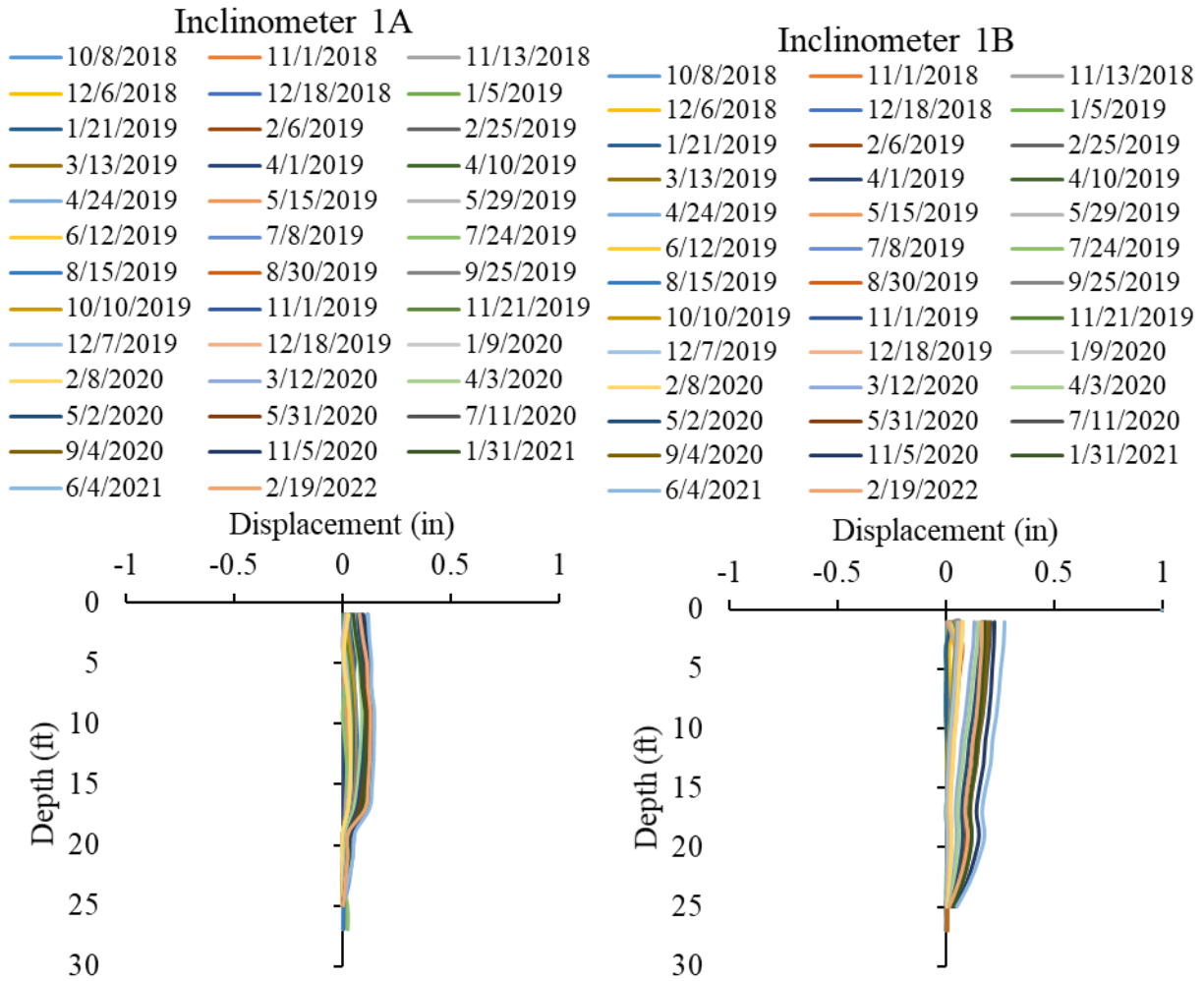


Figure 3.43 Displacements at Inclinator 1 at I-Slope 5

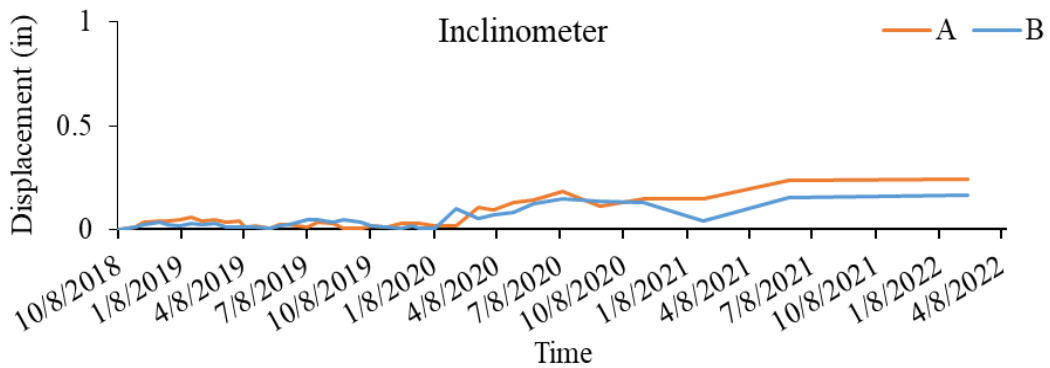


Figure 3.44 Overtime Lateral Deformation at the Top of Inclinator 1 at I-Slope 5.

Figure 3.45 displays the horizontal displacement data obtained from Inclinator 2 in the repaired section. The data shows a sliding movement of 14 ft. (4.4 m) depth that occurred in November 2018. An aerial image of the failed slope can be seen in Figure 3.42. The slope was repaired using 40 ft. long H-piles of size HP 14x74 to address the issue. These piles were spaced

at 4 ft. center-to-center in the middle of the slope. The H-piles provided sufficient resistance in the active part of the slope and effectively prevented movement in the upper pavement ramp. However, it is important to note that the bottom part of the slope that experienced landslides was not reinforced. A detailed finite element analysis of the failure was conducted, and the results can be found in Chapter 5 of the study.

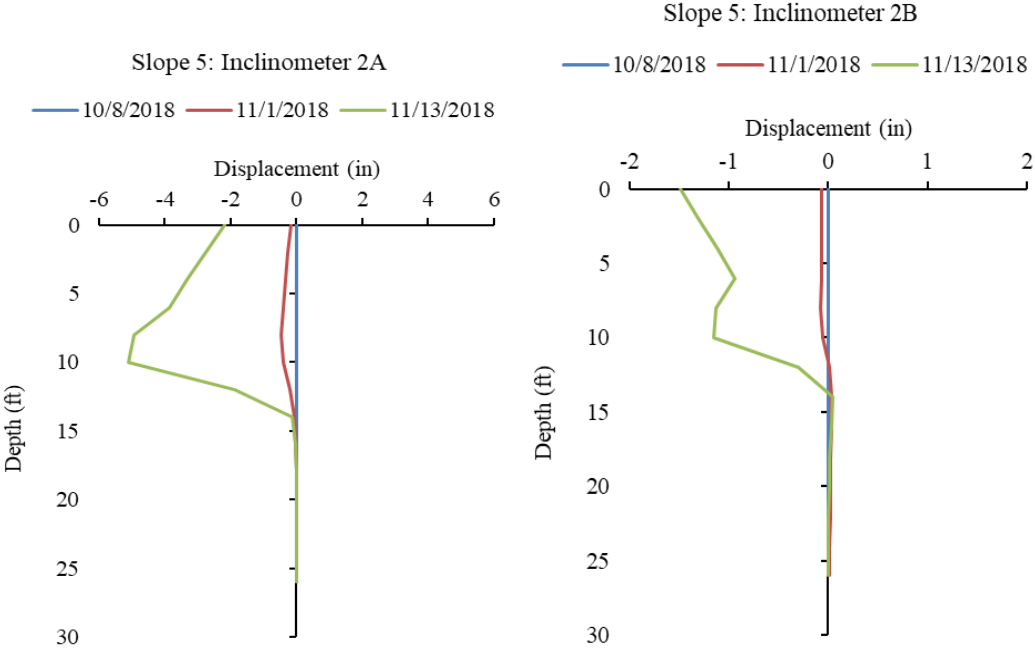


Figure 3.45 Displacements at Inclinator 2 at I-Slope 5

3.7.1.2 Field Instrumentation Data

Figures 3.46, 3.47, and 3.48 provide valuable insights into the moisture content changes and daily rainfall distribution at different locations on Slope 5. The data captured the period from September 2018 to April 2019, focusing on the rainfall events before the slope failure. The instrumentation data revealed that the matric suction, a measure of soil moisture tension, remained constant after two to four months of the observation period. The lowest suction value was observed at the top part of the slope, indicating a combination of low shear strength and high moisture content. Significant moisture variations were observed during the dry period, particularly at depths of 5 ft. (1.5 m) and 10 ft. (4 m). These variations suggest that the slope experienced desiccation/shrinkage cracks during the summer of 2019. These cracks acted as preferential paths for rainwater infiltration, increasing the slope's moisture content. Overall, the data highlights the complex interplay between rainfall, moisture content, and slope behavior, providing important insights for understanding the factors contributing to slope failure.

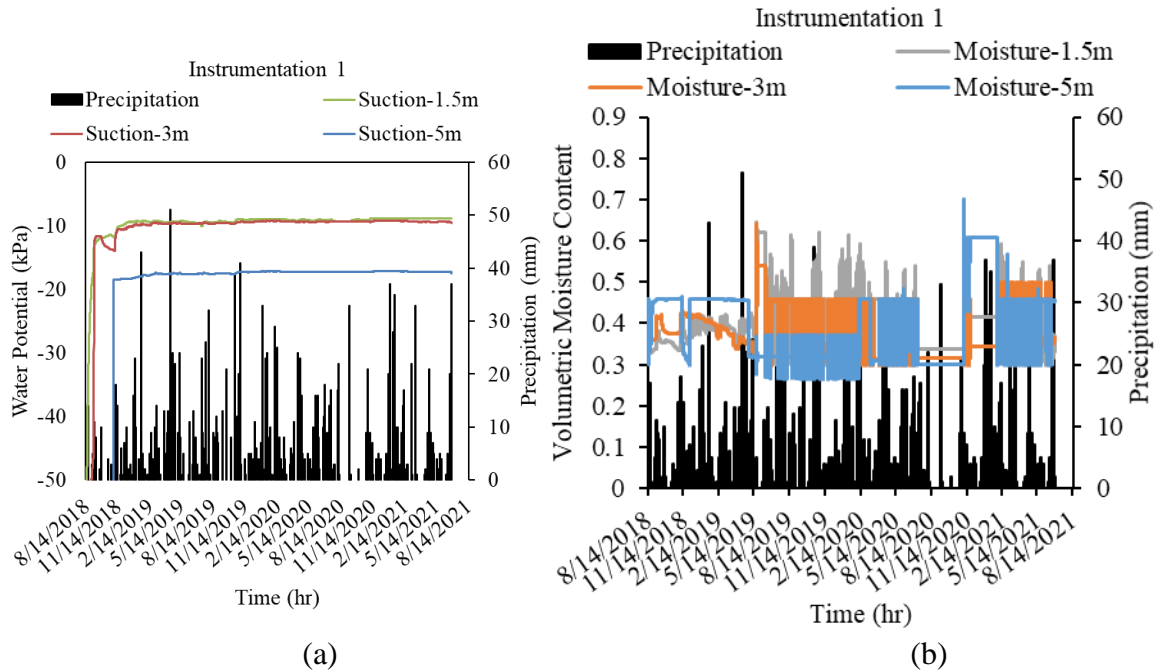


Figure 3.46 Variation of parameters at I-Slope 5 (a) Matric Suction, (b) Moisture Content and Rainfall data from Instrumentation 1

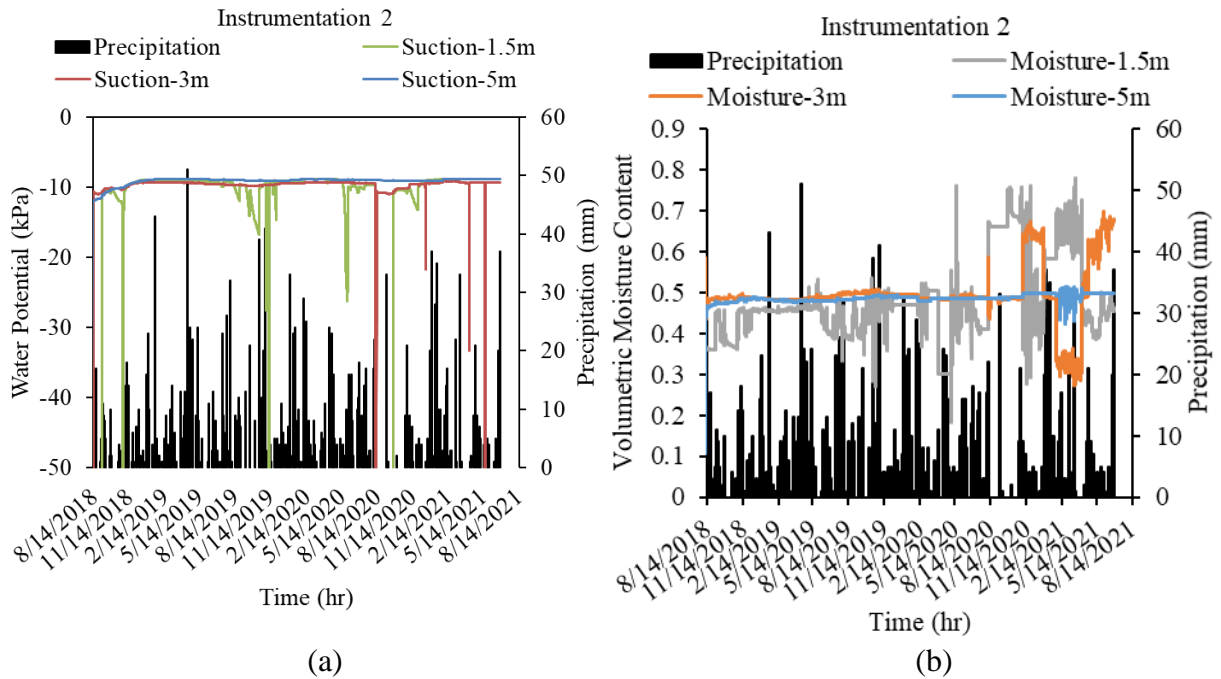


Figure 3.47 Variation of parameters at I-Slope 5 (a) Matric Suction, (b) Moisture Content and Rainfall data from Instrumentation 2

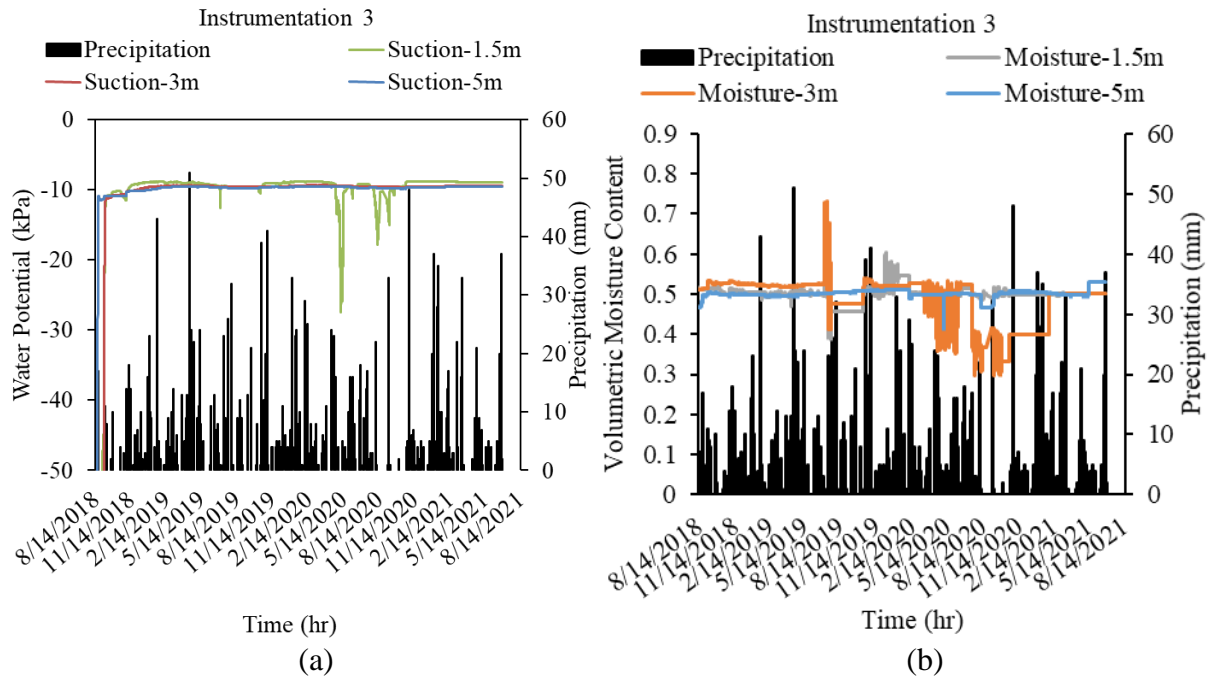


Figure 3.48 Variation of parameters at I-Slope 5 (a) Matric Suction, (b) Moisture Content and Rainfall data from Instrumentation 3

Figure 3.49 depicts the in-situ variations of soil and air temperature at Instrumentation 1 to Instrumentation 4 in I-Slope 5. The data shows minimal changes in soil temperature at deeper depths, while at shallower depths, the temperature fluctuates in accordance with the variations in air temperature. This observation highlights the impact of atmospheric conditions on the shallow layers of the slope and its relevance in assessing slope stability and performance.

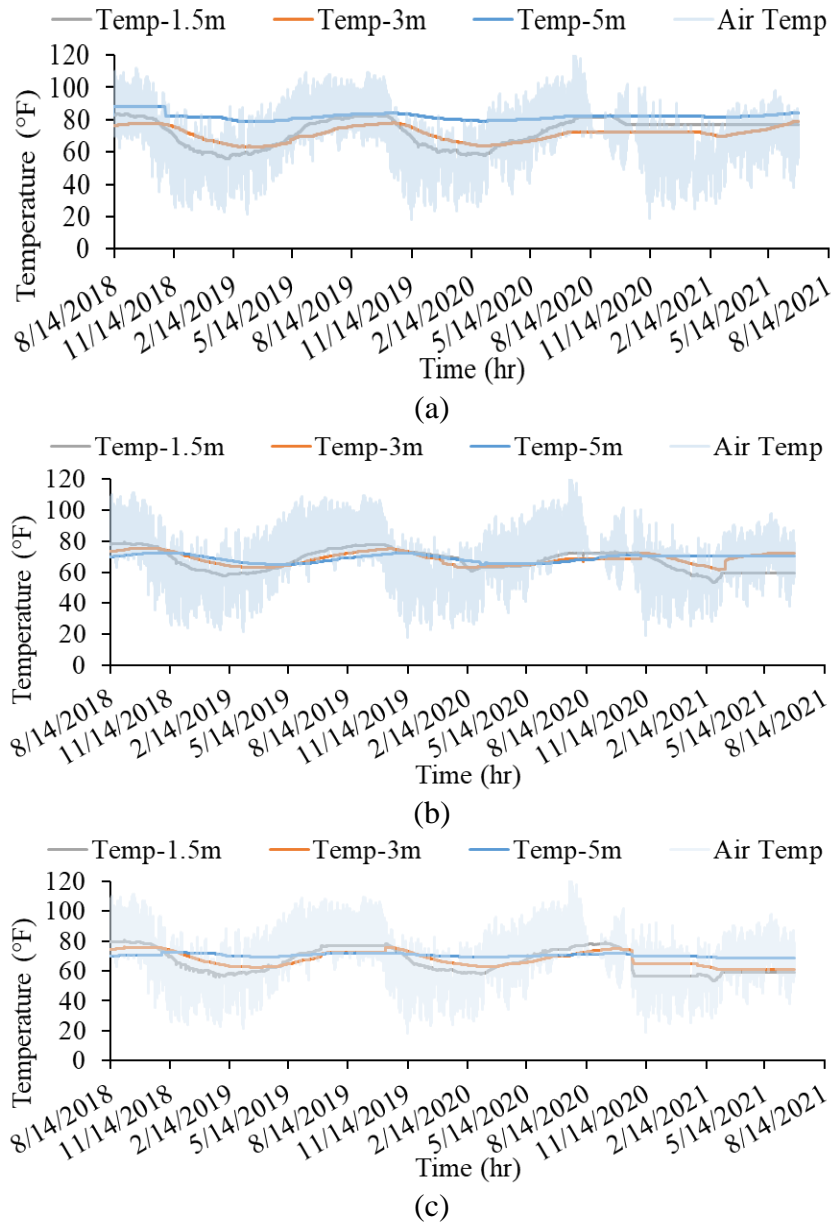


Figure 3.49 Variations of Air and Soil Temperature at I-Slope 5 (a) Instrumentation 1, (b) Instrumentation 2, and (c) Instrumentation 3

3.8 Instrumented Slope 6 (I-Slope 6): McRaven Road Highway Slope

I-Slope 6, a 5H: 1V slope with a height of 15 ft., is located along I20E near McRaven Road, as shown in Figure 3.50. Part of the slope that had shown prior movement had been rebuilt and re-graded to reinstate the drainage structure. The repaired section and the as-built section were included in this study for analysis and evaluation.



Figure 3.50 Location of I-Slope 6

In the repaired section of the slopes two 15 ft. boreholes, designated as Instrumentation 1 and Instrumentation 2, were dug and sensors were placed. The locations of the instrumentation boreholes are presented in Figure 3.51. Another 15 ft. deep borehole was installed in the as-built section at location instrumentation 3 in Figure 3.51. Instrumentation 1 was installed at the crest, while Instrumentation 2 and Instrumentation 3 were placed in the middle of the slope. At each instrumentation location, moisture and water potential sensors were installed at depths of 5 ft (1.5 m), 10 ft (5 m), and 15 ft (5 m). Instrumentation 1 at I-Slope 6 also included a rain gauge and air temperature sensor. Inclinator 1, a 50-ft slope inclinometer, was installed in the repaired section, while Inclinator 2 was installed in the as-built section.

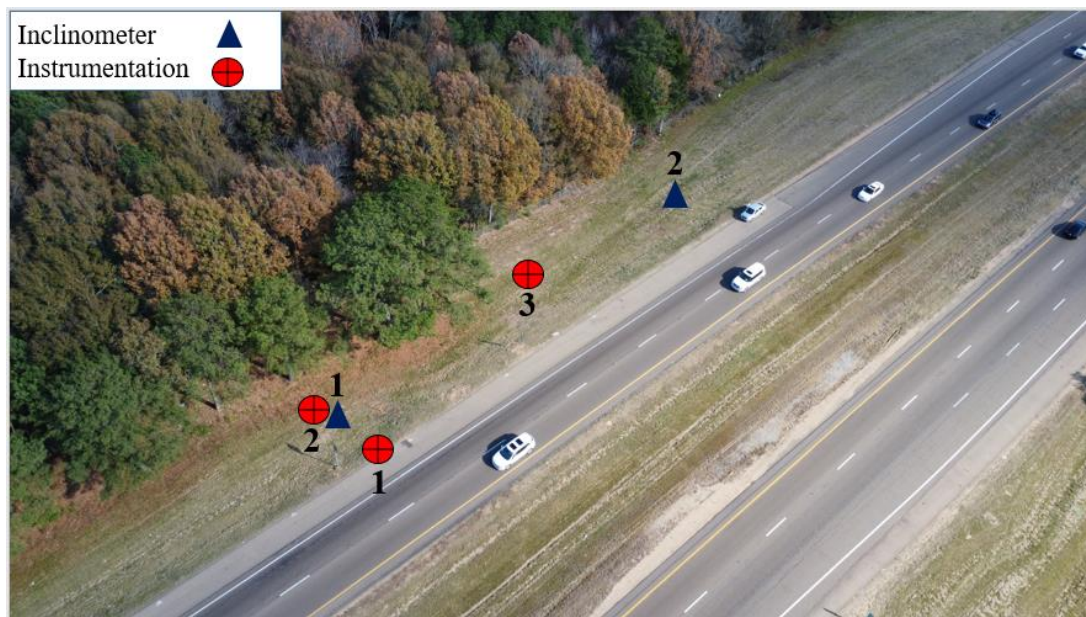


Figure 3.51 Instrumentation Layout at I-Slope 6

3.8.1 Field Monitoring Results

3.8.1.1 Slope Movement Data

The slope's horizontal movement was assessed using slope inclinometer measurements taken every 2 ft. along the inclinometer pipe. The analysis of the data revealed the following:

- In the repaired section, depicted in Figures 3.52 and 3.53, no significant movement was observed, indicating satisfactory performance.
- In the as-built section, shown in Figures 3.52 and 3.53, movement of up to 5 inches was observed at the surface during the monitoring period. The depth of the slope movement was approximately 5 ft., indicating a shallow slope failure. Maintenance and repair are required to address this issue.

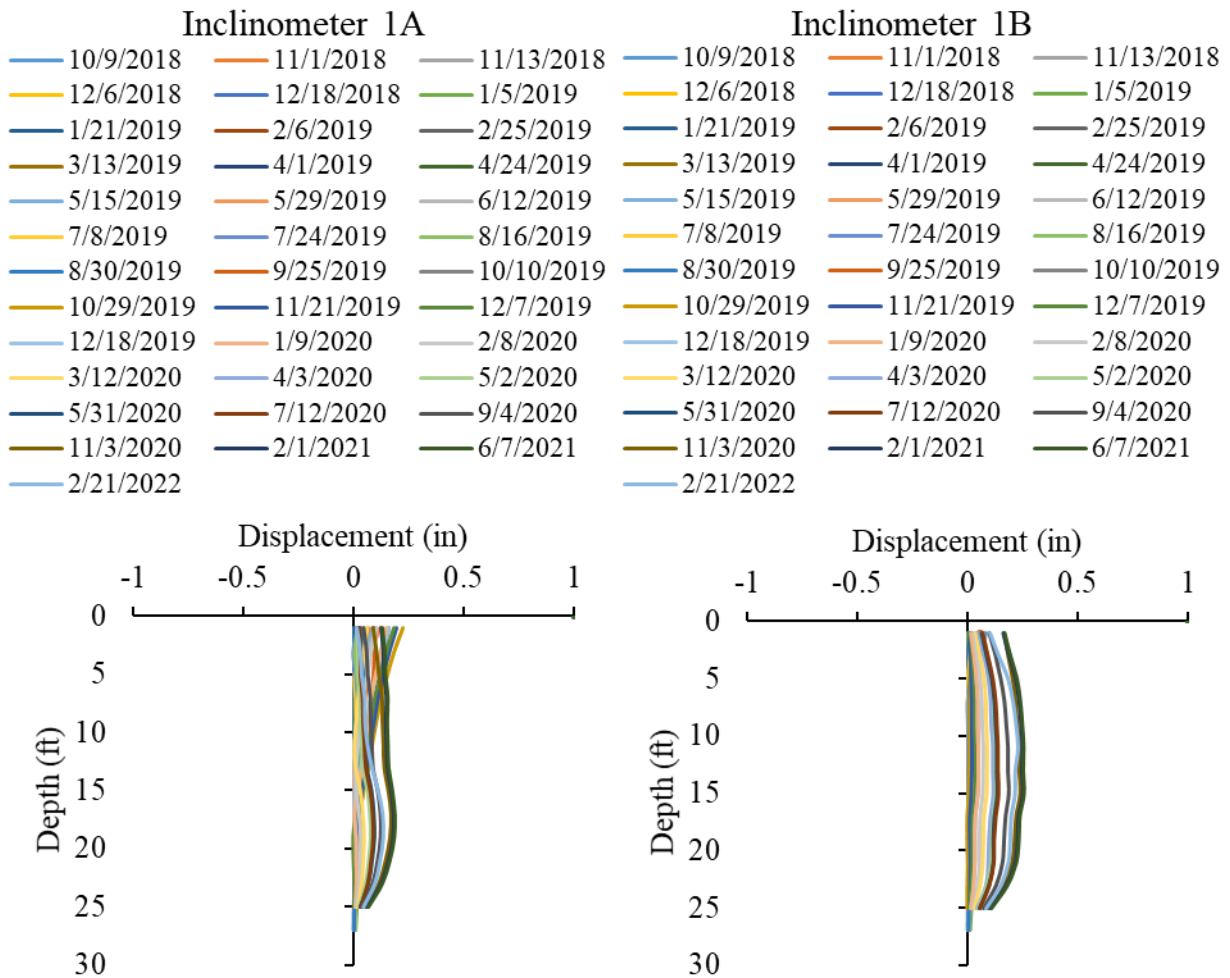


Figure 3.52 Displacements at Inclinometer 1 at I-Slope 6

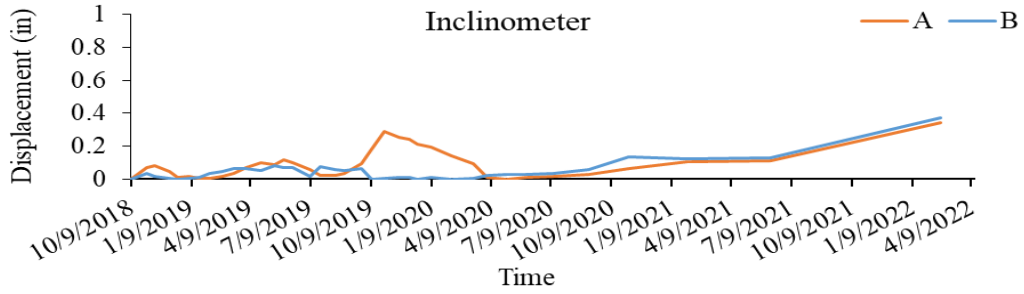


Figure 3.53 Overtime Lateral Deformation at the Top of Inclinometer 1 at I-Slope 6

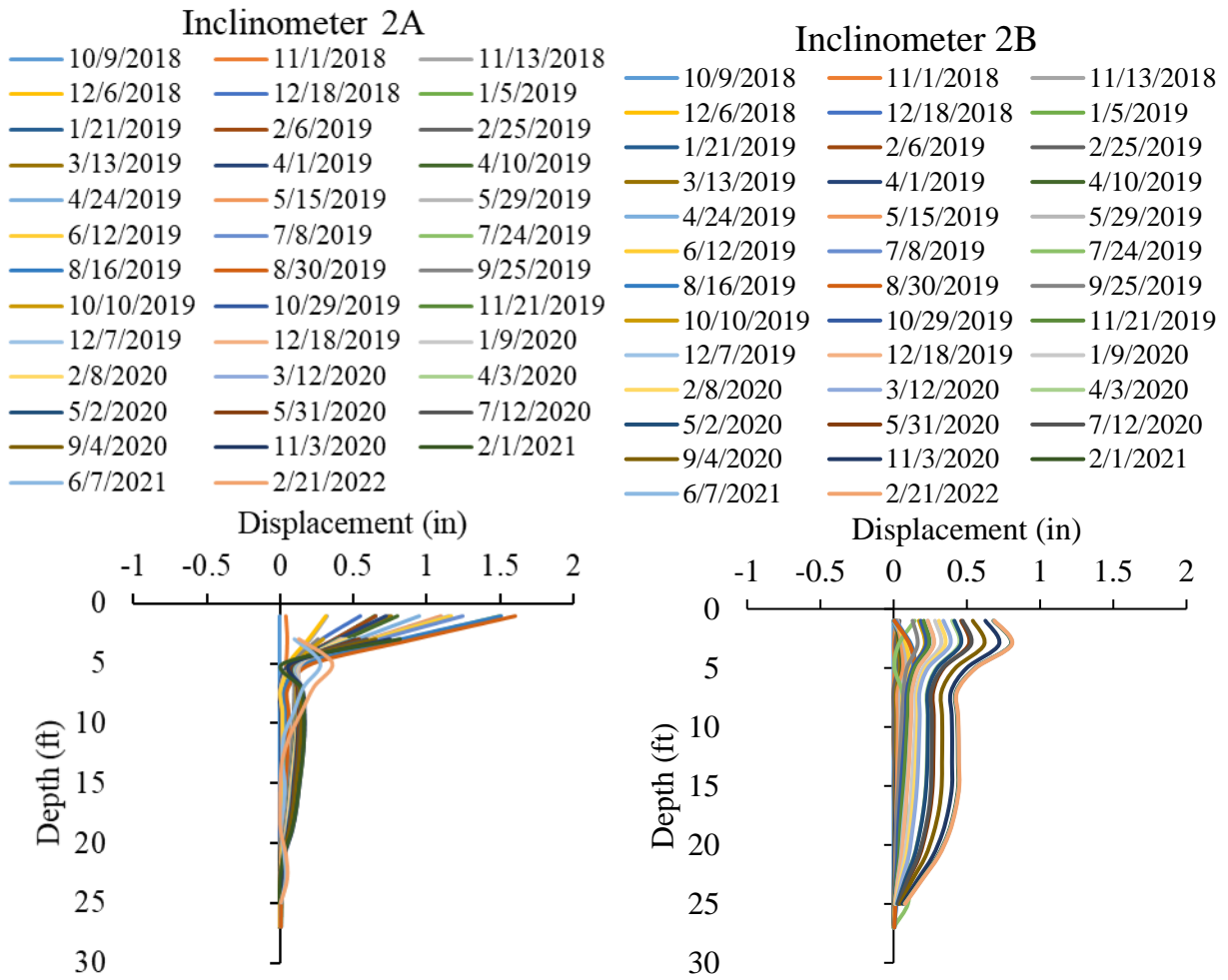


Figure 3.54 Displacements at Inclinometer 2 at I-Slope 6

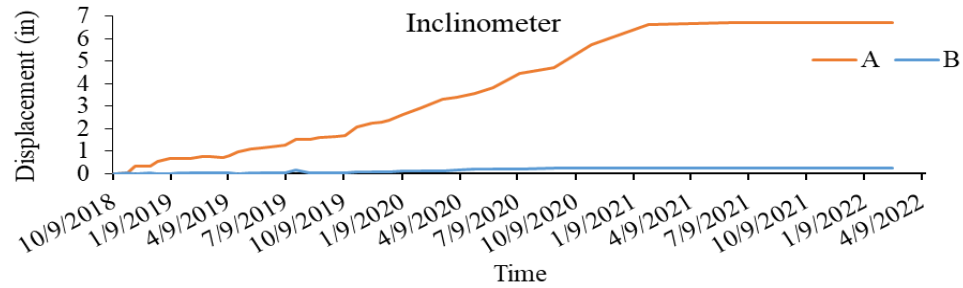


Figure 3.55 Overtime Lateral Deformation at the Top of Inclinometer 2 at I-Slope 6

3.8.1.2 Field Instrumentation Data

The variations in the in situ matric suction profile and moisture content with rainfall at different depths (5 ft., 10 ft., and 15 ft.) were analyzed at Instrumentation 1, Instrumentation 2, and Instrumentation 3. The findings are as follows:

- Figures 3.56, 3.57, and 3.58 present the variations in matric suction and moisture content at the respective instrumentation locations.
- At Instrumentation 1, the matric suction initially remained high for approximately three months and then stabilized at a low value of 10 kPa for the rest of the monitoring period. The volumetric moisture content also remained constant throughout the two-year monitoring period.
- The constant low matric suction and consistently high moisture content indicate that the soil is nearly fully saturated, suggesting the presence of perched water conditions.
- Similar matric suction variations were observed in the middle of the slopes for both the repaired and as-built sections, as depicted in Figure 3.56 and Figure 3.57.
- The overall moisture content remained constant during the monitoring period, with some peaks and drops observed during summer 2019, indicating rainwater infiltration.
- The constant moisture content and matric suction at Instrumentation 2 and Instrumentation 3 are attributed to perched water conditions, similar to what was observed in I-Slope 5, which experienced a shallow slide in the as-built section.
- The movement in the as-built section of the slope is attributed to the formation of perched water at the top of the slope. However, it is important to note that the repaired section also experiences a similar perched water zone but does not exhibit movement due to the repairs implemented.

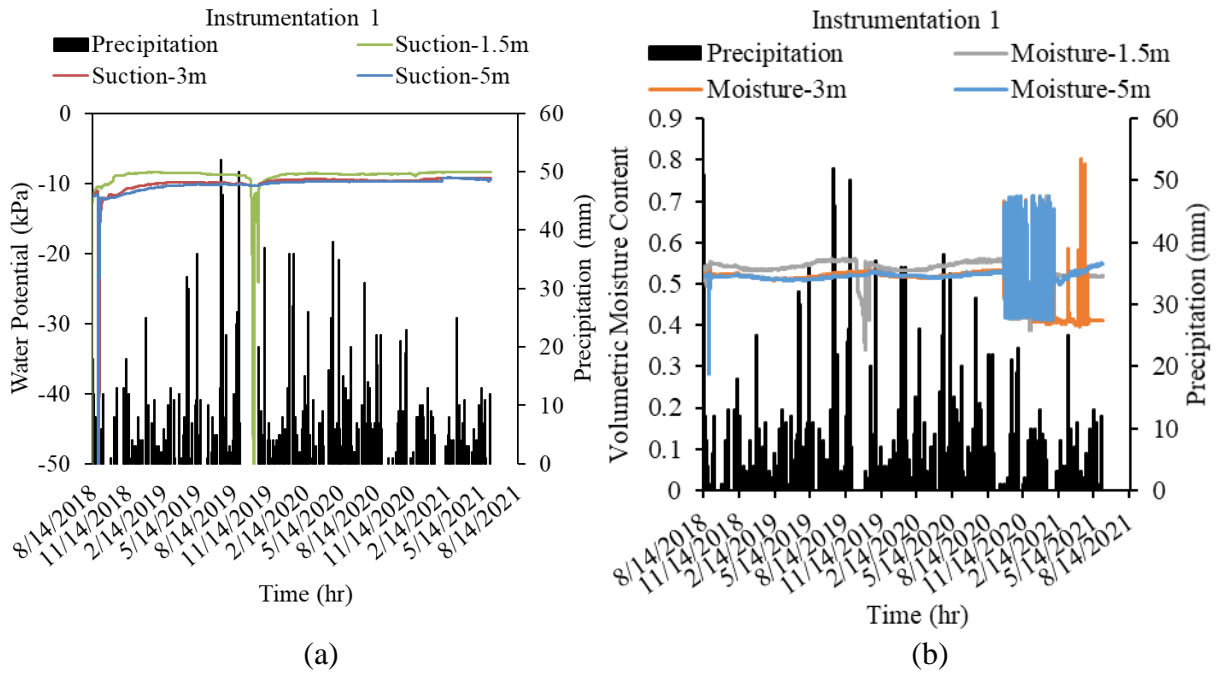


Figure 3.56 Variation of parameters at I-Slope 6 (a) Matric Suction, (b) Moisture Content and Rainfall data from Instrumentation 1

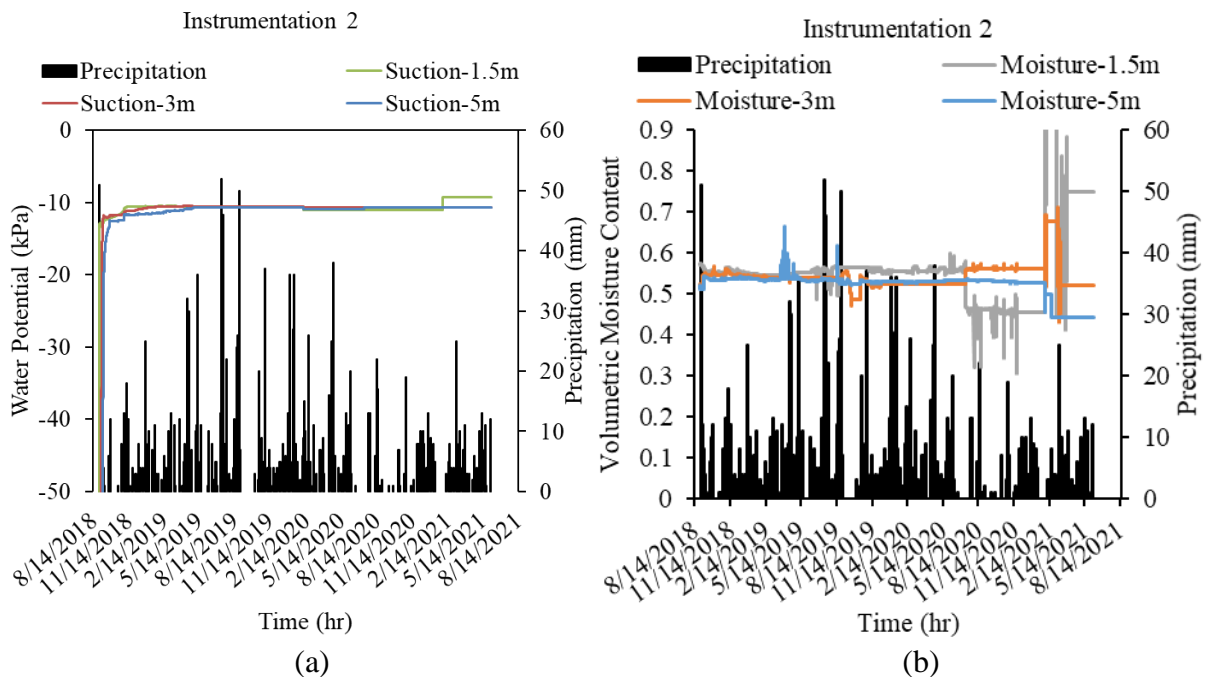


Figure 3.57 Variation of parameters at I-Slope 6 (a) Matric Suction, (b) Moisture Content and Rainfall data from Instrumentation 2

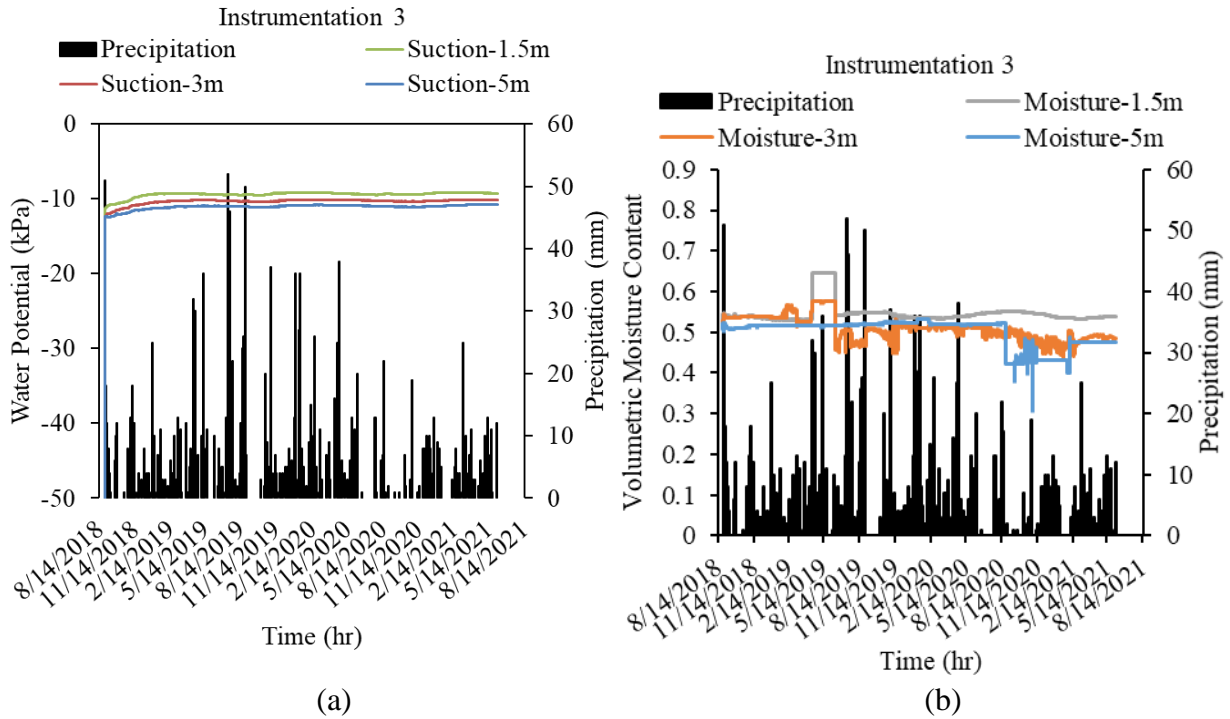
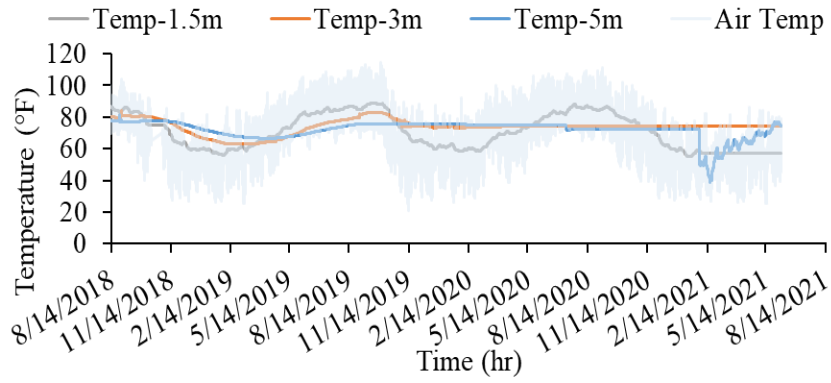


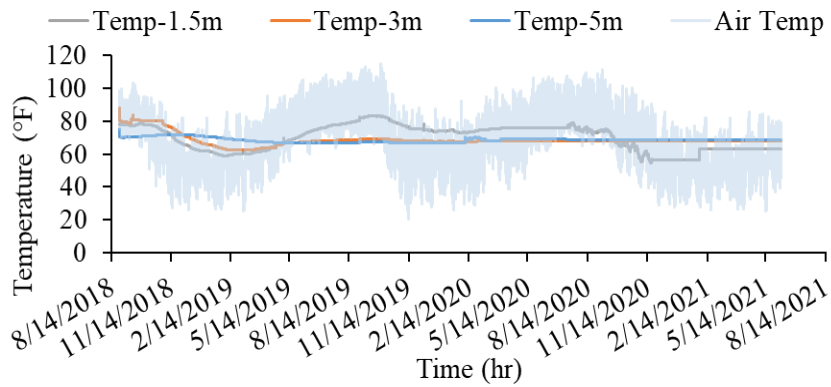
Figure 3.58 Variation of parameters at I-Slope 6 (a) Matric Suction, (b) Moisture Content and Rainfall data from Instrumentation 3

Figure 3.59 illustrates the soil and air temperature variations from Instrumentation 1 to Instrumentation 3 in I-Slope 6. The findings are as follows:

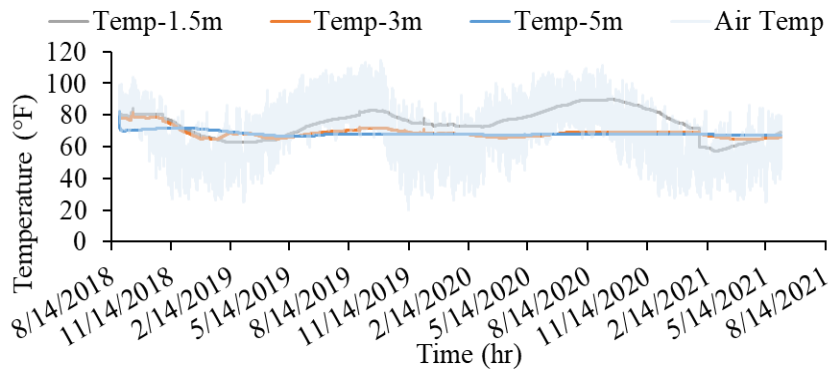
- Minor changes in soil temperature were observed at deeper depths, similar to the behavior observed in other slopes.
- At shallower depths, the soil temperature varied in response to changes in the air temperature.



(a)



(b)



(c)

Figure 3.59 Variations of Air and Soil Temperature at I-Slope 6 (a) Instrumentation 1, (b) Instrumentation 2, and (c) Instrumentation 3

3.9 I220S Ramp Toward I20E Highway Slope

I-Slope7 is located along the exit from I220 South toward I20 East; the location is shown in Figure 3.60. The slope was repaired using H-piles, and a slope inclinometer was installed to monitor movement in the repaired area. JSU's GeoDevelopment research team monitored the slope movement every two weeks, and the lateral overtime deformation variations are presented in Figures 3.61 and 3.62. The figures show no significant deformation or movement in the slope.



Figure 3.60 Location of I-Slope 7

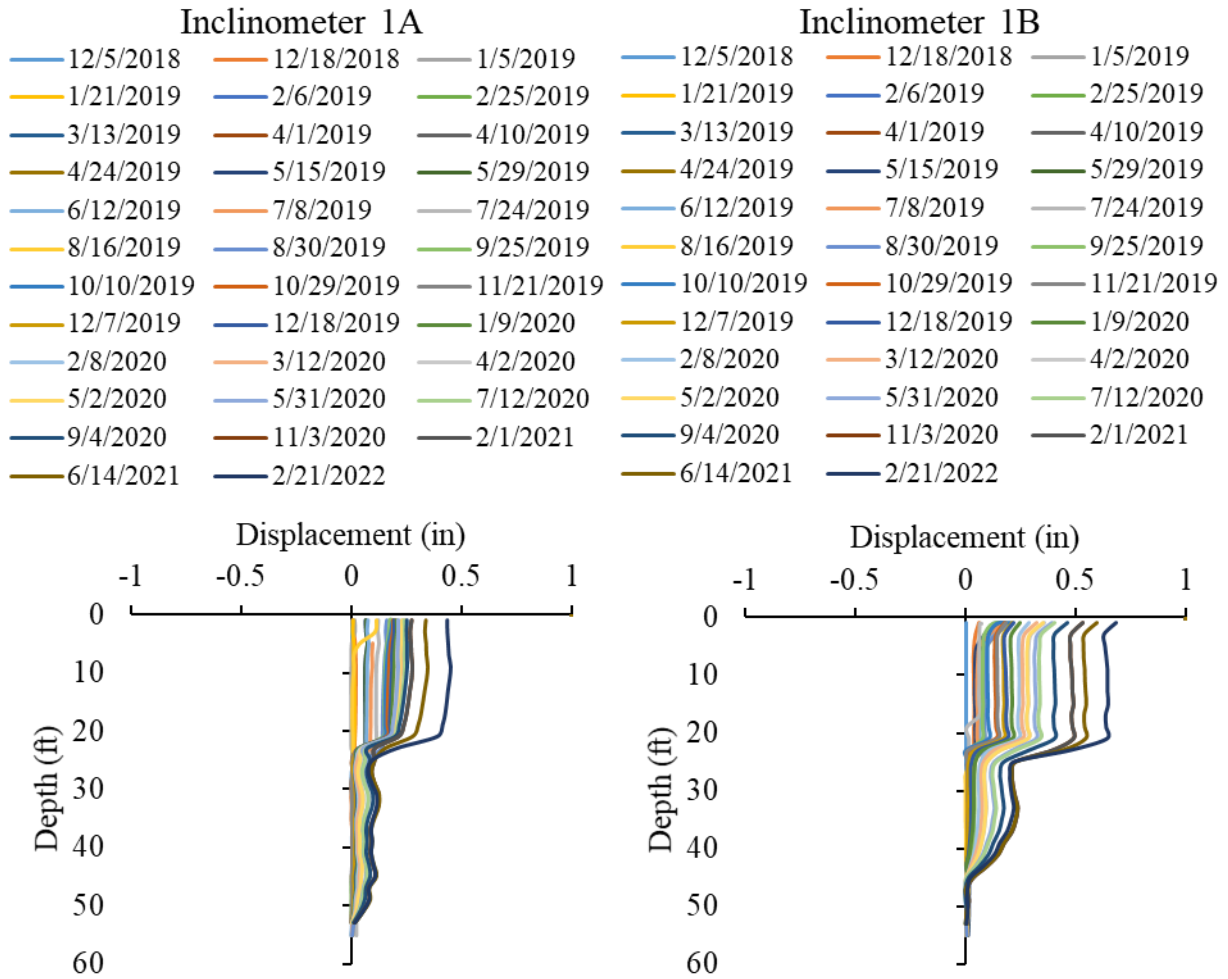


Figure 3.61 Displacement at I-Slope 7

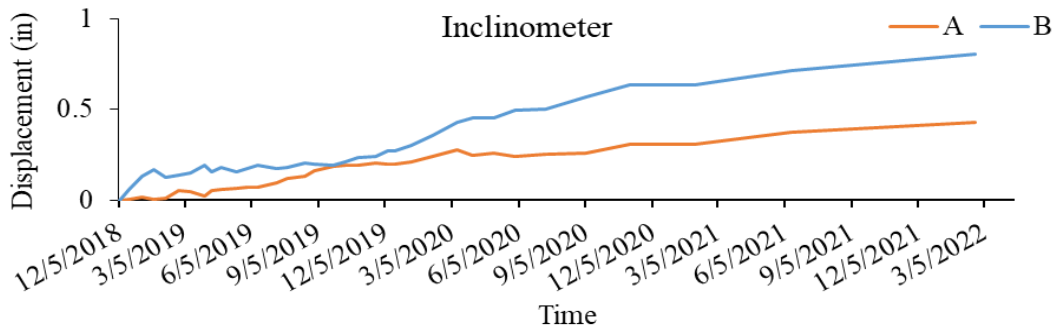


Figure 3.62 Overtime lateral deformation in I-Slope 7

CHAPTER 4 INVESTIGATION OF HIGHWAY SLOPES USING REMOTE SENSING AND GEOPHYSICAL TESTING TOOLS

Geotechnical assets, including slopes, embankments, and retaining walls, don't directly carry traffic loads but are essential to the strong performance of transportation assets. The degradation of transportation infrastructure is directly linked to underlying issues with geotechnical assets, gradual deterioration over time, and exposure to environmental factors. Geological conditions, such as the pervasive expansive clay in Mississippi, further compound the problems by increasing the risk of extreme soil deformation in highway embankment slopes, earthen structures, retaining walls, bridge and railway abutments and foundations. The life of these geotechnical assets can be increased by performing a periodic assessment of their condition and carrying out the required maintenance; inaction escalates maintenance costs and leads to catastrophic failures without warning. As demonstrated by Anderson et al. (2016) and other cases, allowing geotechnical assets to fail before repairing them often proves more costly than implementing regular maintenance. Annual repairs of failed slopes consume a considerable portion of the maintenance budget for various transportation departments in several southern states of this country.

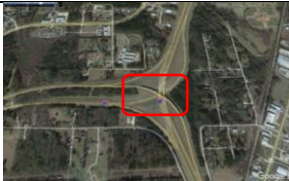
Traditional asset management practices typically involve creating inventories or databases by collecting information through boots-on-ground surveys of one asset at a time (Kimmerling & Thompson, 2015). In this study, LiDAR imaging was employed to examine the surface movement of the chosen slope sites. LiDAR is a technology that uses laser light to measure the distance to a target and captures the reflected light with a sensor. Apart from its primary application in distance measurement, LiDAR has various other uses. These include measuring structural static deflection, determining bridge clearance, detecting structural issues, construction site overseeing, and it is widely regarded as the next generation of surveying technology (Pieraccini et al., 2007; Liu et al., 2010a, 2010b; Lefevre, 2000; Kayen et al., 2006; Bian et al., 2011; Chen, 2010). Unmanned Aerial Vehicle (UAV) or drone-based photogrammetry is being increasingly being used to monitor infrastructures.

Multichannel electrical resistivity imaging (ERI) is a non-destructive method of site investigation and soil characterization that provides continuous information horizontally and vertically of the subsurface soil and is used for investigating multiple geotechnical and geological issues. ERI offers several advantages over traditional subsurface site investigation methods, as highlighted by multiple studies (Samouëlian et al., 2004; Hossain et al., 2018; Khan et al., 2012; Kibria and Hossain, 2012; Manzur et al., 2016; Khan et al., 2016). These advantages include the ability to provide a continuous image of subsurface conditions, coverage of large areas in a short time, cost-effectiveness, information about site heterogeneity and areas with high moisture content, and fast data processing.

4.1 Advanced Evaluation of Instrumented Slope Sites

This section presents the results of field testing that was conducted on the six repaired and instrumented slopes, using drones, LiDAR, and ERI.

Table 4.1 Locations of Selected Highway Slope's (*from Khan et al., 2020*)

Slope No.	Site Location	Site Coordinate	Aerial view
I-Slope 1	I220N Ramp Toward I55N	32°24'46.60"N, 90° 8'57.32"W	
I-Slope 2	Metro Center	32°17'58.85"N, 90°14'47.00"W	
I-Slope 3	Terry Road	32°16'48.92"N, 90°12'44.03"W	
I-Slope 4	Highland Drive	32°17'21.22"N, 90°14'17.58"W	
I-Slope 5	Sowell Road	32°32'30.11"N, 90° 5'50.49"W	
I-Slope 6	McRaven Road	32°17'45.71"N, 90°16'17.17"W	

4.1.1 Instrumented Slope 1: I220N Ramp toward I55N

Data collected for Instrumented Slope 1 between summer 2021 and fall/winter 2022 were derived from ERI, LiDAR, and drones, and the data analysis results are presented in the following section.

4.1.1.1 ERI

ERI surveys using SuperSting R8/IP equipment captured resistivity distribution images of the subsurface. The data was analyzed with EarthImager 2D software using ERI inversion, which maps resistivities through an iterative process based on least-squares inversion. The software compares field-measured apparent resistivities to calculated resistivities, adjusting them until the root mean squared (RMS) error falls below 5%.

ERI was performed on Instrumented Slope 1, covering 270 ft. (82.3 m) along the width of the slope. Resistivity image profiles at the crest (Line A) and midway (Line B) of the slope were plotted. The location of the slope and the ERI test line are presented in Figure 4.1. Results for Line A, which was tested from spring 2021 through fall/winter 2022, are presented in Figure 4.2 (a – e). Resistivity was high (30-50 ohm-m) in the unsaturated zone (above 8 ft. or 2.5 m) but decreased to less than 5 Ohm-m near the saturated zone. At depths greater than 15 ft., wetter zones were present. (Wet zones move around and vary as seasons change.) The ERI results for Line B are presented in Figure 4.3 (a-e). Areas with higher resistivity along the shallower depths of the slope were characterized by loose soil occurring from slope movement. Deeper soils with lower resistivities were characterized by wetter zones due to perched water conditions.



Figure 4.1 Slope 1 Location

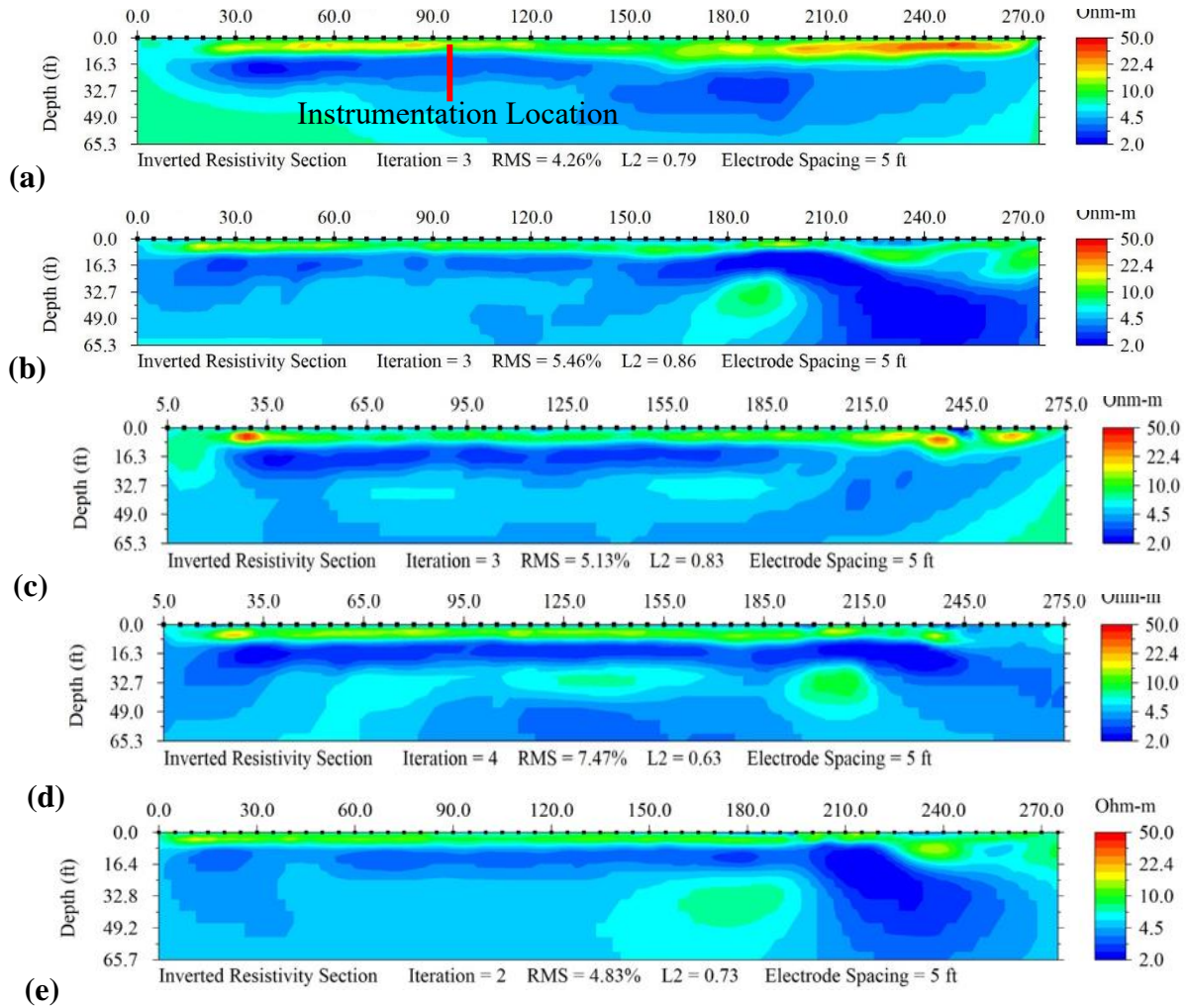


Figure 4.2 Slope 1 ERI Line A: (a) Spring 2021, (b) Summer 2021, (c) Fall 2021, (d) Winter 2021/Spring 2022, (e) Fall/Winter 2022

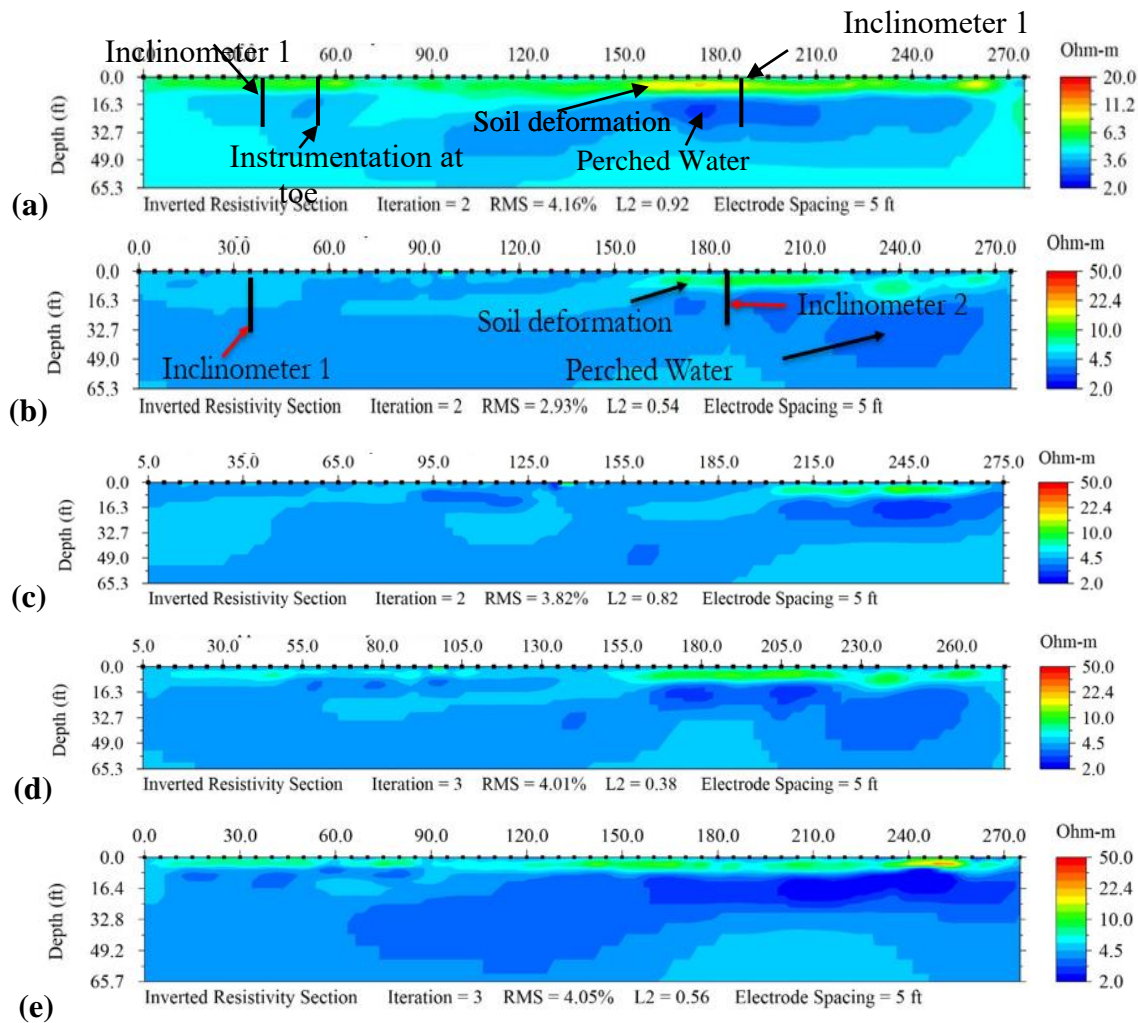


Figure 4.3 Slope 1 ERI Line B: (a) Spring 2021, (b) Summer 2021, (c) Fall 2021, (d) Winter 2021/Spring 2022, (e) Fall/Winter 2022

4.1.1.2 Unmanned Aerial Vehicles

Unmanned aerial vehicles (UAVs), commonly known as drones, are an accurate and automated method of collecting high-resolution image data. They provide an excellent alternative to the more time-consuming and laborious conventional methods of inspecting and assessing geotechnical assets because they can quickly capture high-resolution photogrammetric survey data, flying across large sites and producing images in a fraction of the time required by conventional methods.

- A DJI drone was equipped with a high-resolution RGB camera and a thermal camera that were used to capture high-resolution images.
- Images taken by the drone were georeferenced by the GPS on board.
- Thermal imagery helped determine the surface temperature to help identify anomalies.

Processing the images captured by a drone is a crucial step in obtaining useful information from aerial imagery. The following steps were taken to take and process the images for this study.

1. Image Acquisition: The desired flight path was set up using the DJI GO application for smartphones, and the controls for the drone were set to capture overlapped images at an altitude of resolution. A DJI drone equipped with a high-resolution RGB camera was flown at an altitude of 100 – 200 feet.
2. Image Transfer: Captured images were transferred to a computer for processing.
3. Image Stitching: The next step was to stitch the individual images together to create a single large image, also known as a mosaic. Image stitching was done using specialized software that analyzed the images and automatically identified common features or tie points, such as road intersections, medians, and other points of interest that were used to align and stitch the images together.
4. Georeferencing: Georeferencing is the process of assigning real-world coordinates to the image, allowing it to be accurately placed on a map. This was done by using ground control points (GCPs) that were identifiable in both the image and on the ground. GCPs can be placed manually or by using GPS and surveying equipment.
5. Image Analysis: Once the images were stitched and georeferenced, they were analyzed, using specialized software. The analysis can include creating 3D models, generating elevation maps, calculating volumes, and/or identifying features such as buildings or trees.

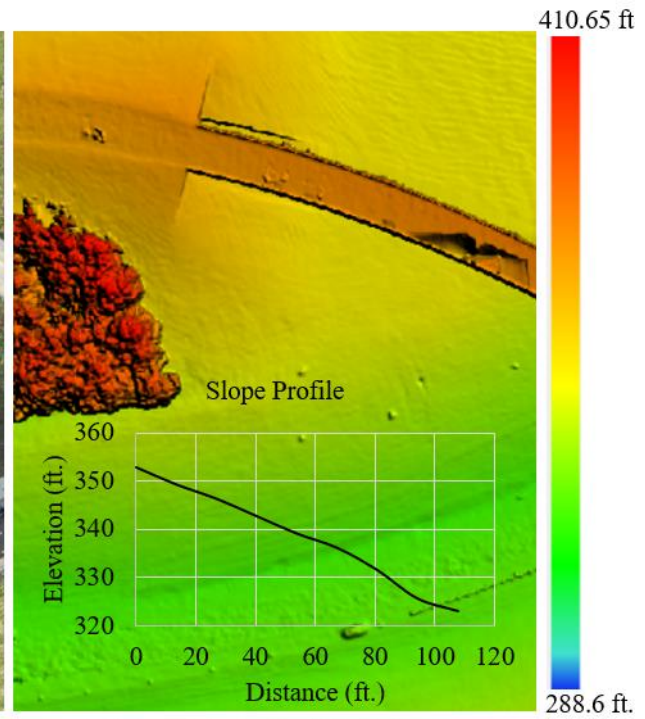
The results from the drone testing for instrumented Slope 1 are presented in Figure 4.4 to Figure 4.7. The images were captured during different seasons, beginning in 2021, and were imported into correlator 3D software. The coordinate system was set to the State Plane Coordinate System Mississippi US-West, and an aerial triangulation was performed with multiple tie points to stitch the images together and develop a digital elevation model (DEM) and digital terrain model (DTM). Ground control points (GCPs) with coordinates that had been identified on the field were used to georeference the DEM. The images were orthorectified and stitched to create an orthomosaic representation of the entire slope site, and 3D models were developed for selected seasonal surveys.

Profile views of the slope were developed using two methods. The views that were captured of the slope in the summer of 2021 were extracted, and a profile was created manually, as shown in Figure 4.4. Images captured by the drone in spring 2022 and fall 2022, georeferenced DEMs, were imported into Civil 3D and surface profiles were created using the kriging interpolation method. The surface profile of the slope was created using the alignment and surface profile tools within Civil 3D. Figure 4.6 and Figure 4.7 show the 3D model, surface topography of the slope, and the surface profile views obtained in spring 2022 and fall 2022, respectively.

Summer 2021



3D Digital Model



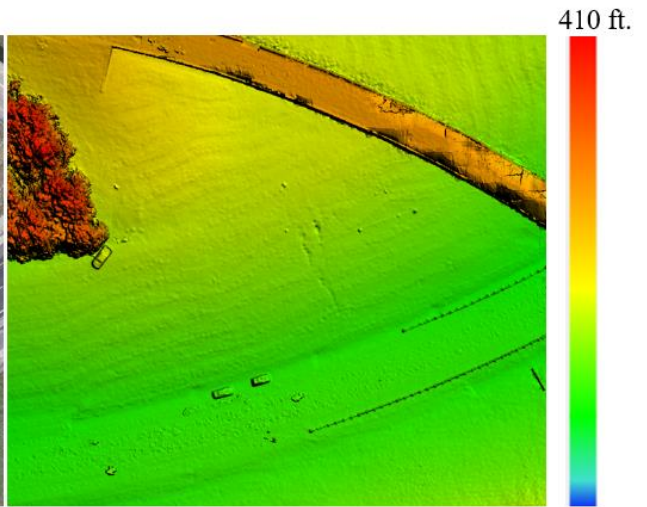
Digital Terrain Model

Figure 4.4 Site 1 Drone Image (Summer 2021)

Fall 2021



3D Digital Model



Digital Elevation Model

Figure 4.5 Site 1 Drone Image (Fall 2021)

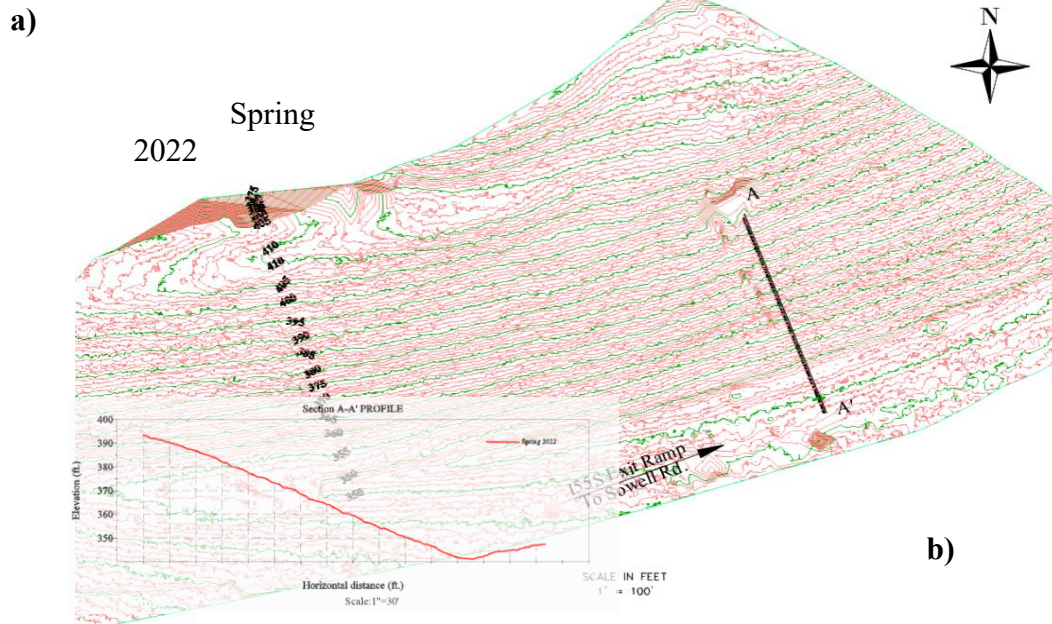
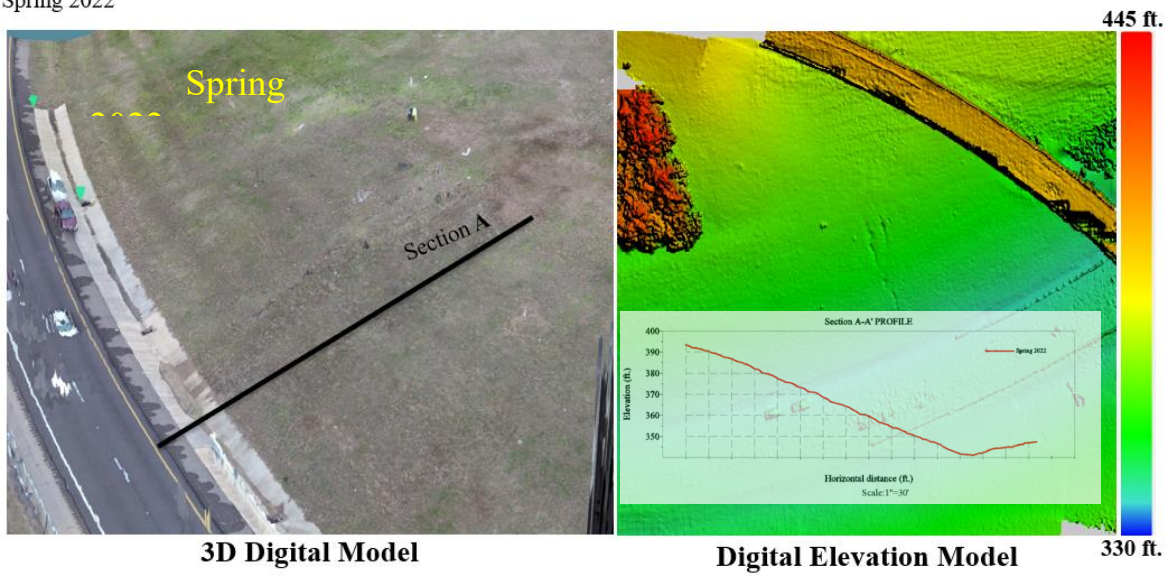
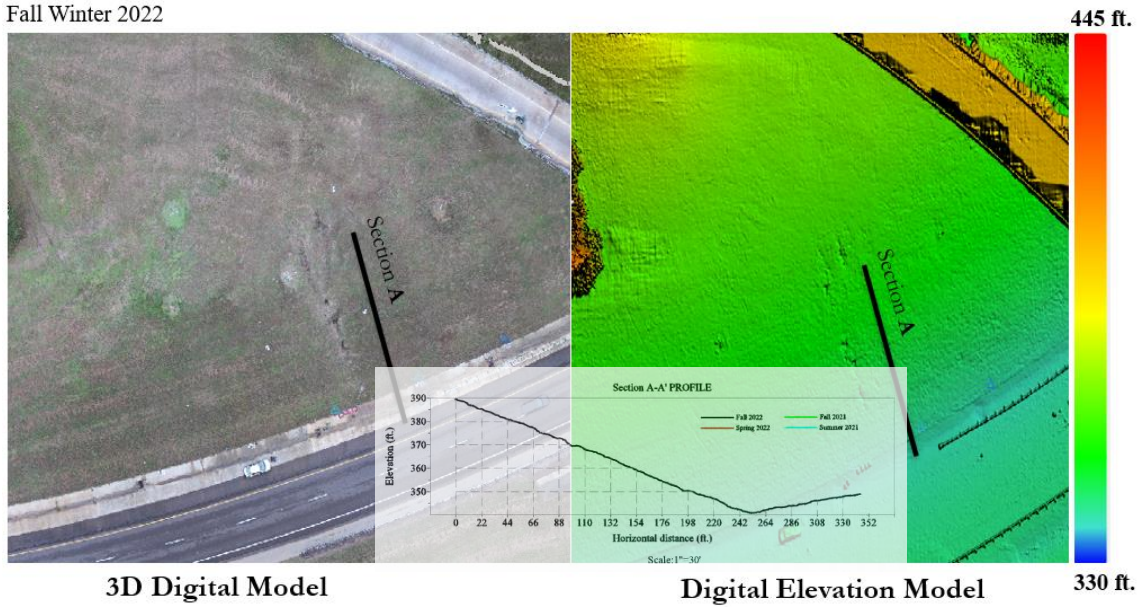
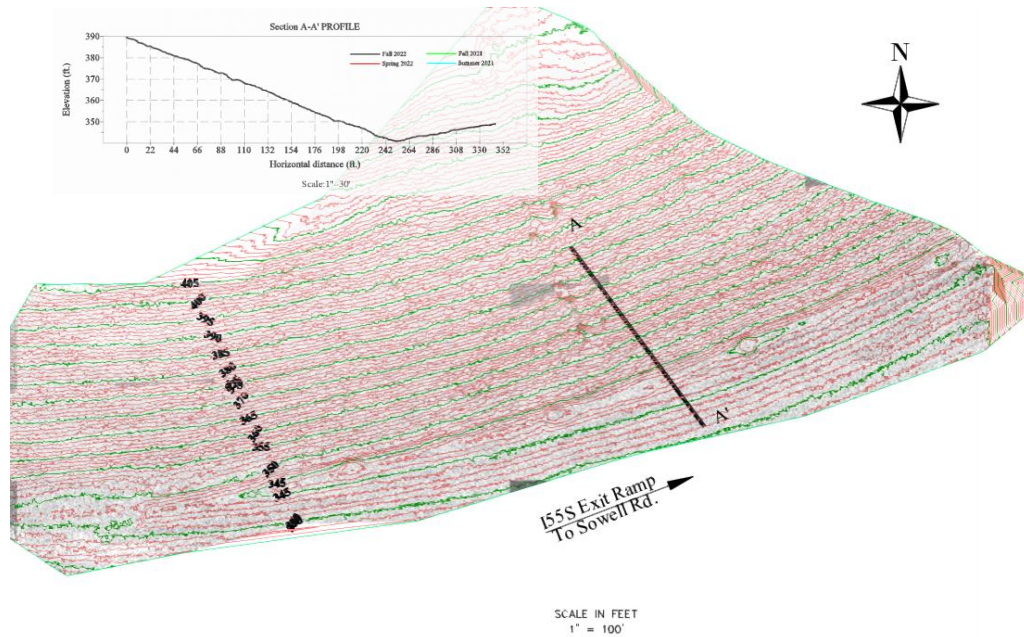


Figure 4.6 Slope 1 Drone Images: (a) DEM, (b) Topography (Spring 2022)

Fall Winter 2022



a)



b)

Figure 4.7 Slope 1 Drone Images: (a) DEM, (b) Topography (Fall 2022)

4.1.1.4 LiDAR

Dense point cloud data from the LiDAR scan was collected to develop 3D surface and generate topography of the slope surface. Subsequently, profile views of the slopes were generated, and field scan data was collected multiple times over the span of several years. Profiles from scans captured at different time intervals can be compared to perform time-dependent

surficial slope movement and deformation analyses. Topography and profile views of Slope 1 obtained from the captured scan data during different seasons are presented in this section. LiDAR scans were acquired at 5 stations on Slope 1 to gather overlapping point cloud data. The field-collected data was digitally post-processed and a single-point cloud group was formed, with over 12 million points for each scan. Point cloud data was collected for four different seasons, namely, summer 2021, fall 2021, spring 2022 & fall/winter 2022. The point clouds were processed with Trimble Realworks software. The bare ground points were extracted.

The point clouds were georeferenced using five ground control points (GCPs) with known coordinates. First, the drone images were ortho-mosaicked and then georeferenced, using the GCPs identified on the field. Other GCPs were then identified on the georeferenced drone imagery mosaic. The GCPs extracted from the drone were incorporated in Trimble RealWorks to georeference the LiDAR point clouds. Georeferencing of the point clouds was done by either selecting points and assigning them to the known GCPs obtained either from pre-identified GCPs on the field or from georeferenced drone orthomosaics. The georeferenced point cloud was then processed, using a ground extraction algorithm to extract the lowest ground surface scan points. This method eliminated unwanted scan points such as vegetation, vehicles, buildings, and similar items. Only the bare ground point clouds were extracted.

The bare ground point clouds collected for all seasons were imported into Civil 3D, and surfaces were generated using the kriging interpolation method. Topographic surface views were generated at 1 ft. major and 5 ft. minor contour intervals and are presented in Figure 4.8(a – d). The surfaces from all seasons were overlaid, and alignments were created along the slope. Surface profiles were then created, using the alignments. Surface profiles along Sections A-A and B-B are presented in Figure 4.8 (e) & (f). Overlaying the surface topographies of different seasons presented the opportunity to stack the surface profiles and create accurate representations of temporal variations in the slope’s surface.

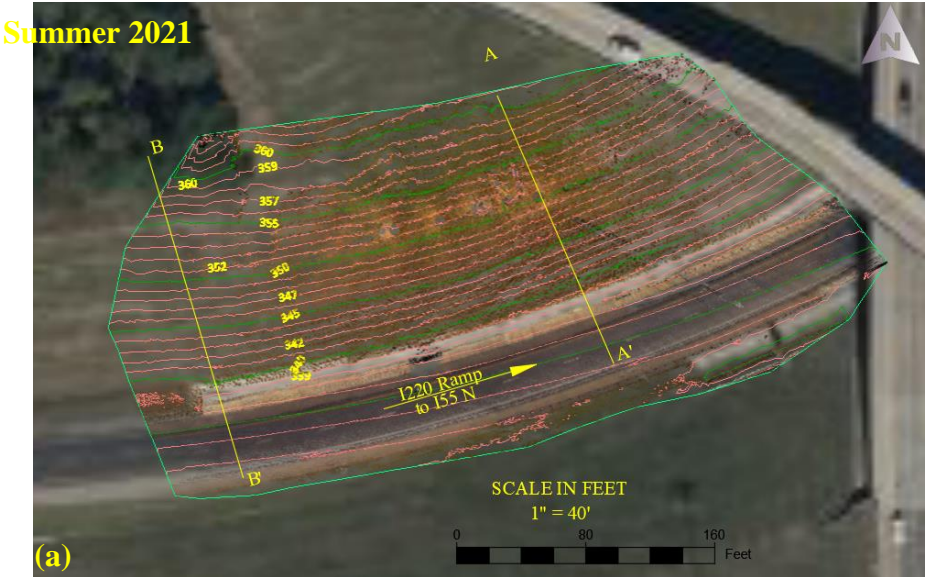


Figure 4.8 (Continued)

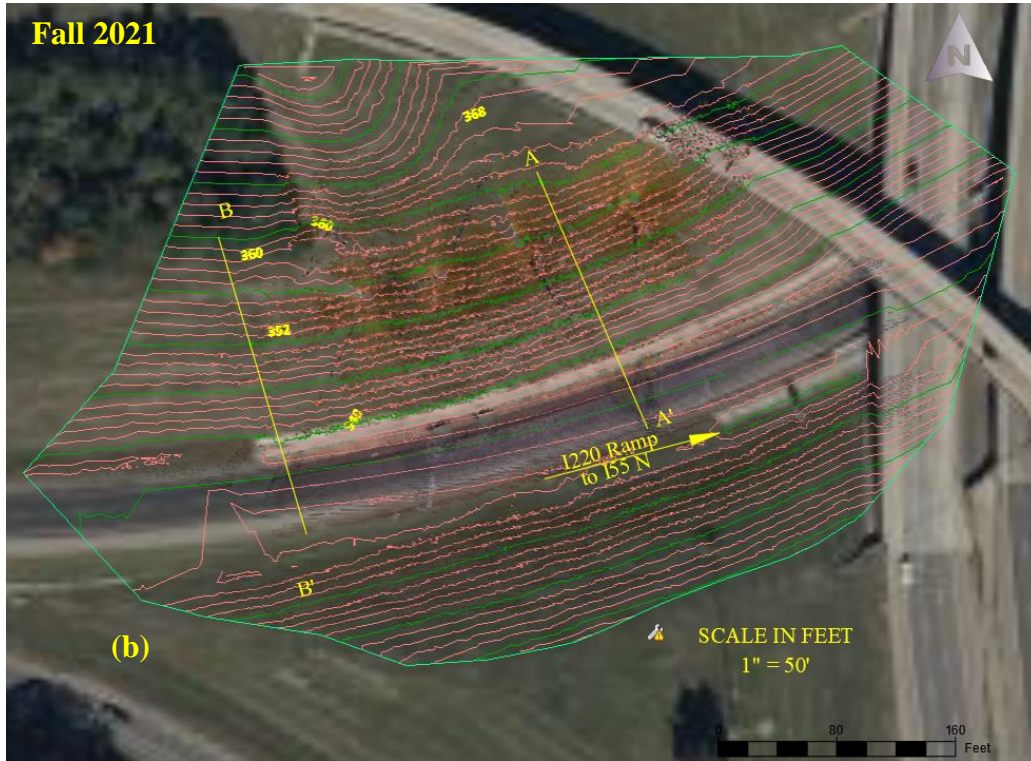


Figure 4.8 (Continued)

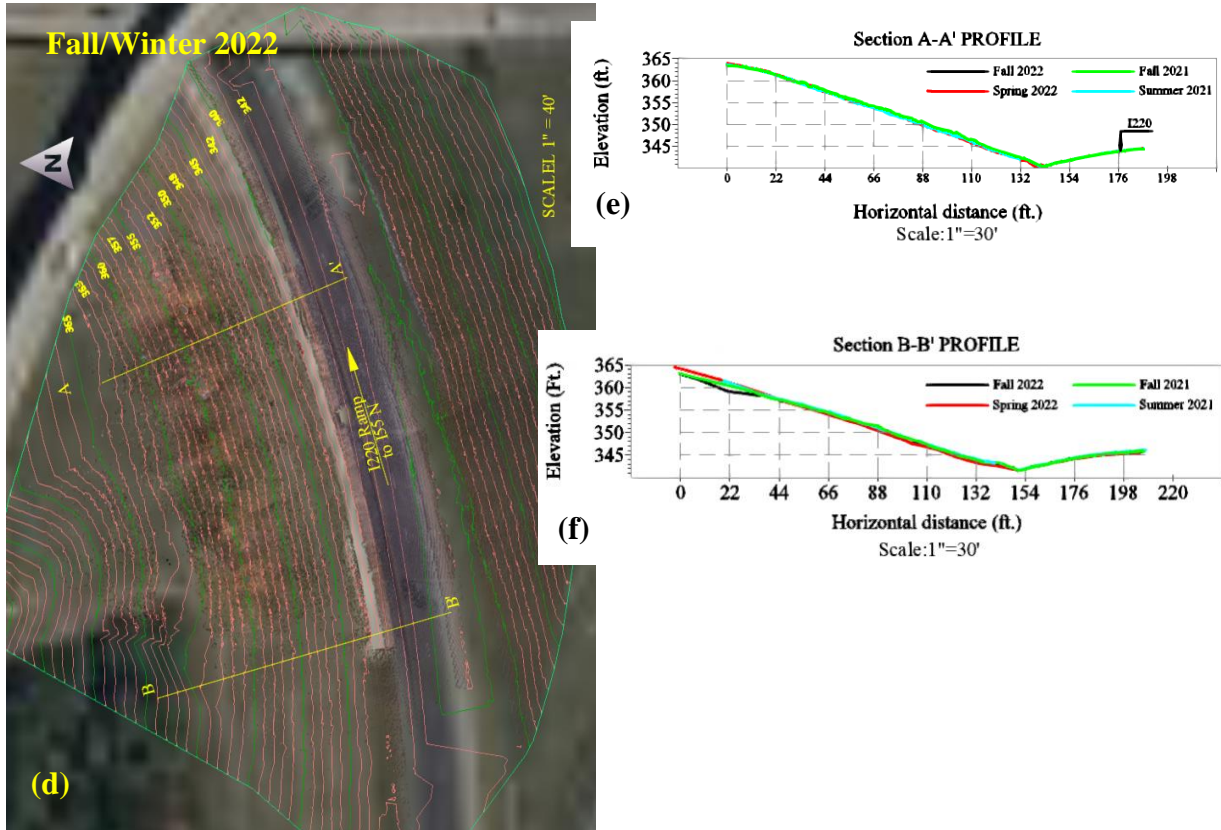


Figure 4.8 LiDAR Point Cloud Surface Topography Instrumented Slope 1: I220 - I55N (a) Summer 2021 (b) Fall 2021 (c) Spring 2022 (d) Fall/Winter 2022 Section (e) Overlaid Surface Profile A-A' (f) Overlaid Surface Profile B-B'

4.1.2 Instrumented Slope 2: MetroCenter Highway Slope

The location of Instrumented Slope 2 is presented in Figure 4.9. I-Slope 2, located near the Metrocenter mall along I220 N over the ramp from US 80E, is 23ft. high with a grade of 3H:1V. A portion of the slope had previously experienced failure and was subsequently repaired with H-piles installed at the crest of the slope. ERI testing was conducted at different seasonal intervals at both the repaired and as-built sections of the slope; the results are presented in Figure 4.10 (a-e).

4.1.2.1 ERI

The ERI test was conducted along a length of 220 ft. (67m) and two lines (A and B) at the crest and midway of the slope, respectively. The ERI test line and slope location are presented in Figure 4.9. ERI results for Line A from the testing conducted from spring 2021 through fall/winter 2022 are presented in Figure 4.10 (a – e).

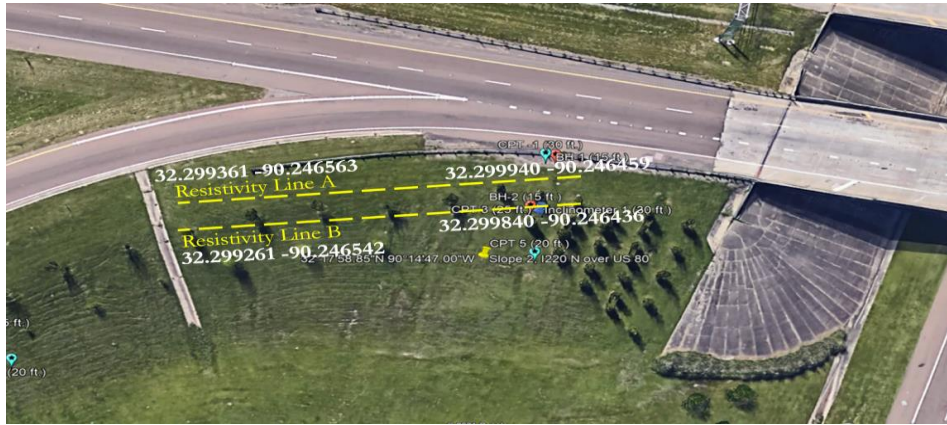


Figure 4.9 Location of Slope 2

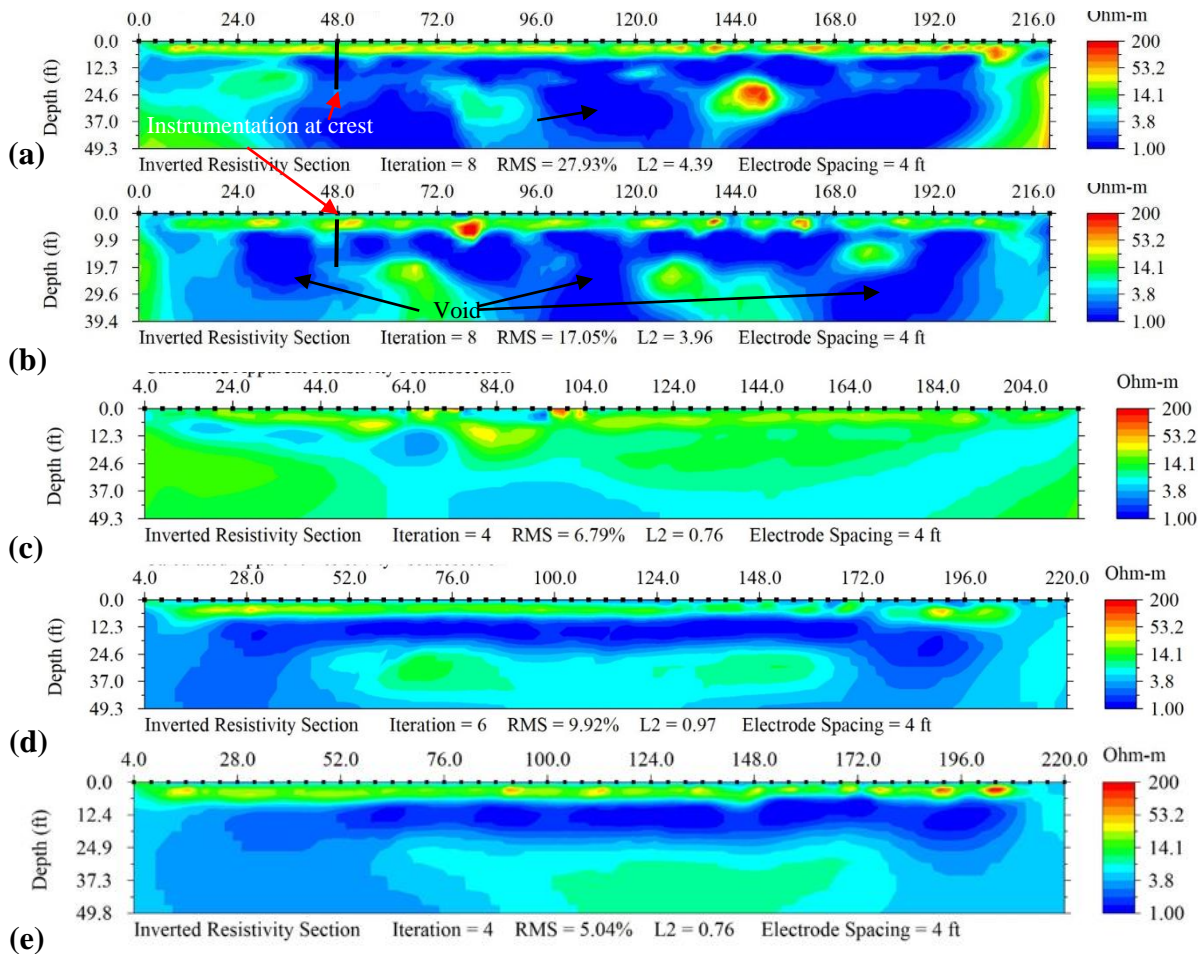


Figure 4.10 Slope 2 ERI Line A: (a) Spring 2021, (b) Summer 2021, (c) Fall 2021, (d) Winter 2021/Spring 2022, (e) Fall/Winter 2022

ERI results for Line B from testing conducted during different seasons are presented in Figure 4.11(a-e). The ERI images demonstrate that resistivity is greatest at shallow depths (more than 6 ft. [2m]) and decreases dramatically at lower depths in the saturated soil zone. There are perched water zones directly below the unsaturated soil zones.

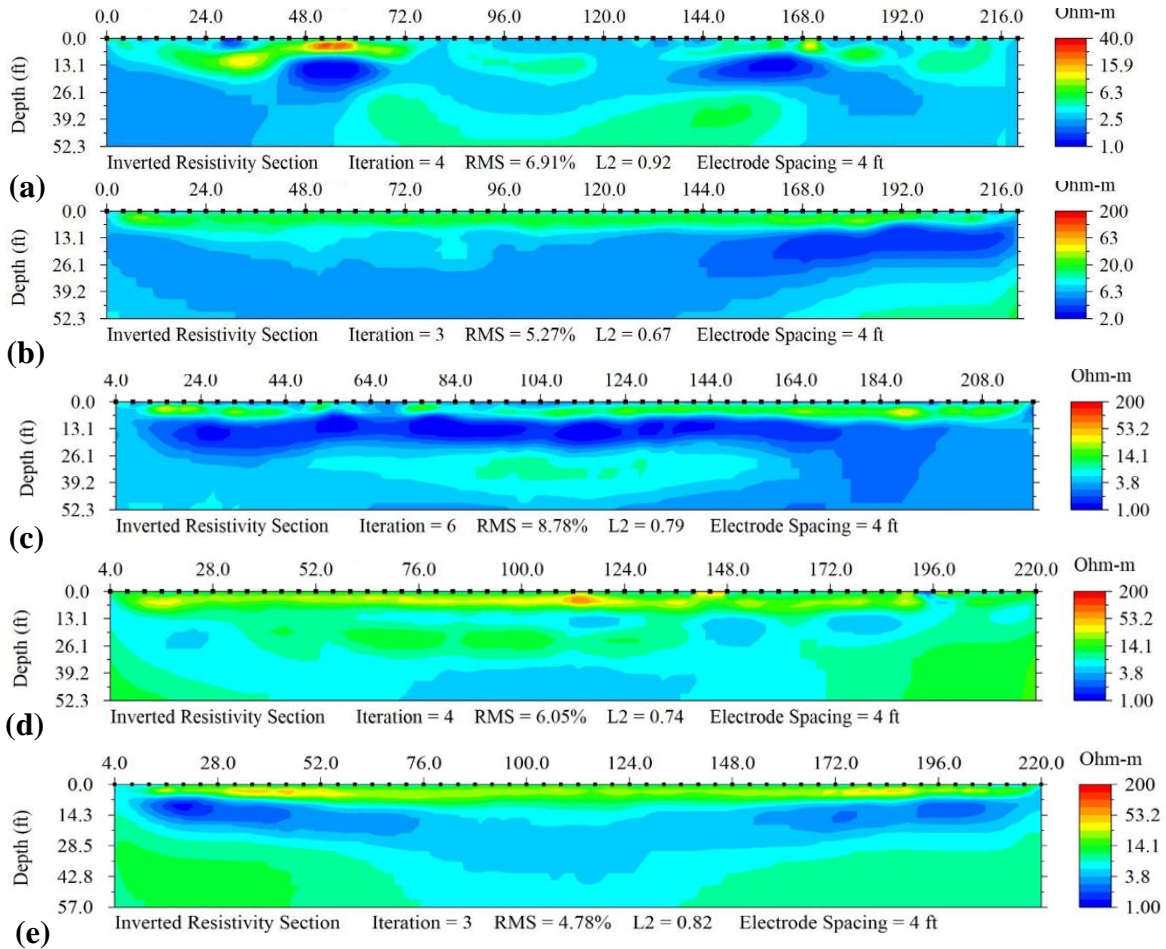


Figure 4.11 Slope 2 ERI Line B: (a) Spring 2021, (b) Summer 2021, (c) Fall 2021, (d) Winter 2021/Spring 2022, (e) Fall/Winter 2022

4.1.1.2 Drone

Multiple drone surveys were taken during different seasons from summer 2021 through fall 2022. The images were post-processed using specialized software, with the coordinates set to the State Plane Coordinate System Mississippi US-West. An aerial triangulation was performed with multiple tie points to stitch the images together and develop digital elevation models (DEMs) and digital terrain models (DTMs). Ground control points (GCPs) with known coordinates pre-identified on the field were used to georeference the DEMs. Images were orthorectified and stitched to create an orthomosaic representation of the entire slope site. DEM representations for different seasons are presented in Figure 4.12 - Figure 4.14. The imagery captured by the drone in fall 2021 had high-quality overlapping, which enabled the development of a high-quality 3D model, as presented in Figure 4-13.

The profile views of the slope were developed using two methods. Figure 4.12 shows one that was created manually, using the elevations extracted in summer 2021. For the drone imagery

collected in fall 2021, the georeferenced DEM was imported into Civil 3D, and the profile was created using the kriging interpolation method and the surface profile tools within Civil 3D.

Figure 4.13 (b) shows the 3D model, surface topography of the slope, and the surface profile views for fall 2021. The DEMs of different seasons make the changes experienced near the bridge abutment at the crest evident and show that the voids at the toe of the slope have grown larger over time.

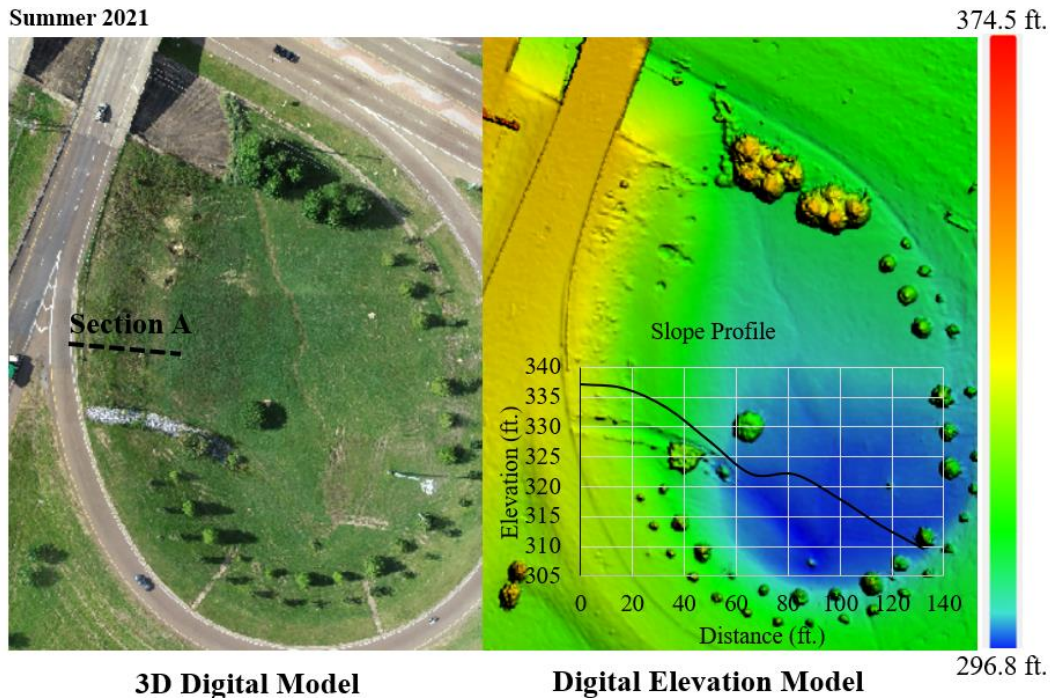


Figure 4.12 Image Taken by Drone of Slope 2 (Summer 2021)

4.1.2.3 LiDAR

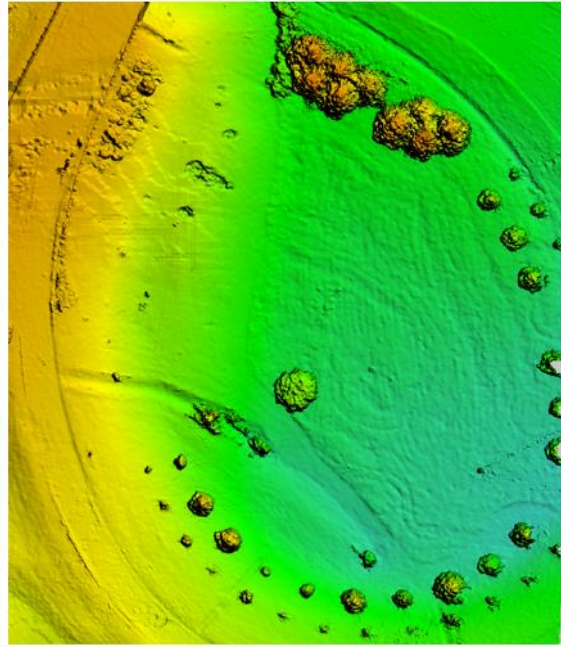
Topography and profile views of Slope 2, obtained from the scan data captured from summer 2021 through fall/winter 2022, are presented in Figure 4.15(a-d) and Figure 4.16. Terrestrial LiDAR scanning was performed at 5 or 6 stations in the middle of the slope to collect overlapping point cloud data. The field-collected data was digitally post-processed and registered together to form a single-point cloud group with more than 20 million points.

The point cloud was then georeferenced by ground control points with known coordinates, and a ground extraction algorithm was used to extract the low surface points and create bare ground point clouds. The bare ground point clouds collected for all seasons were imported into Civil 3D, and the surfaces were generated using the kriging interpolation method. The topographic surface views were generated at 1 ft. major and 5 ft. minor contour intervals and are presented in Figure 4.16(a-d).

Fall 2021

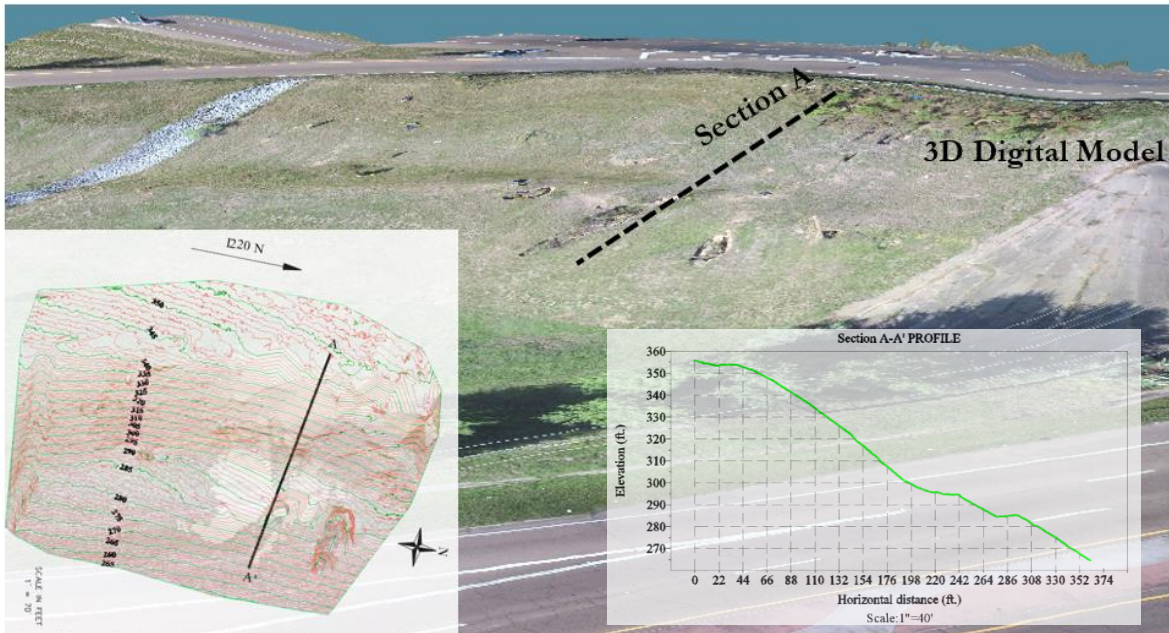


(a) 3D Digital Model



Digital Elevation Model 296.8 ft. 374.5 ft.

Fall 2021



Surface Profile from Drone Point Cloud

(b)

Figure 4.13 Drone Image of Slope 2 in Fall 2021: (a) DEM, (b) 3D Model and Surface Profile

b)

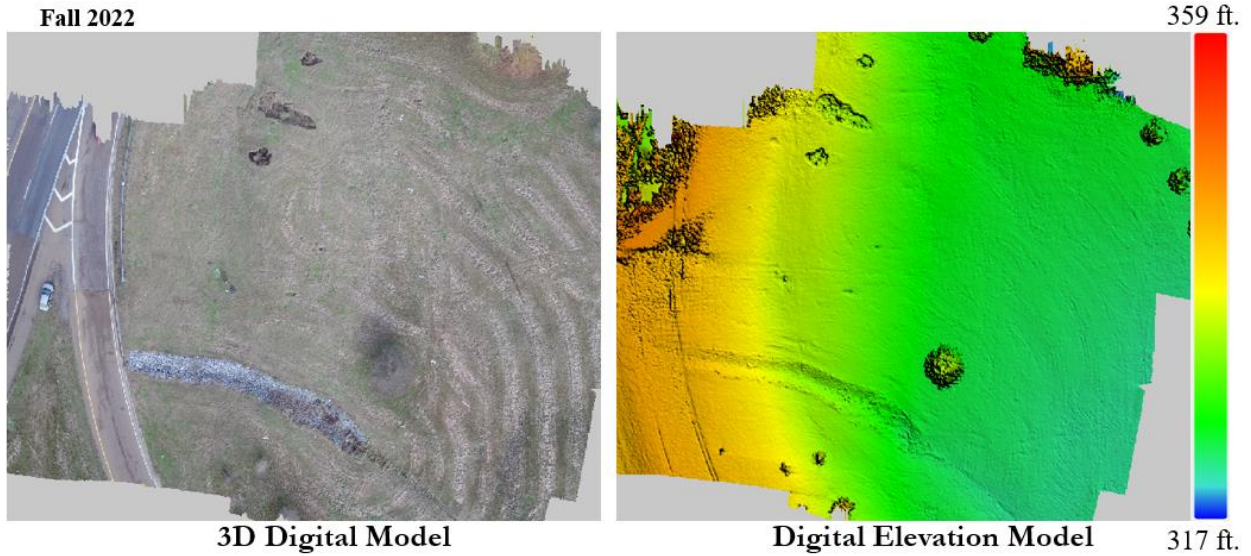


Figure 4.14 Drone Image DEM of Slope 2 (Fall 2022)

Surfaces from all of the seasons were overlaid, and alignments were created along the slope. Stacked surface profiles were created, using the alignments along Sections A-A,' B-B' & C-C'. Surface profile variations during the different seasons along the three sections are presented in Figure 4.16 (a, b, and c). Section C-C' in Figure 4.16 (c) reveal that there are considerable seasonal variations at the crest of the slope and at the void (sinkhole), located between elevations of 340 and 345 ft.

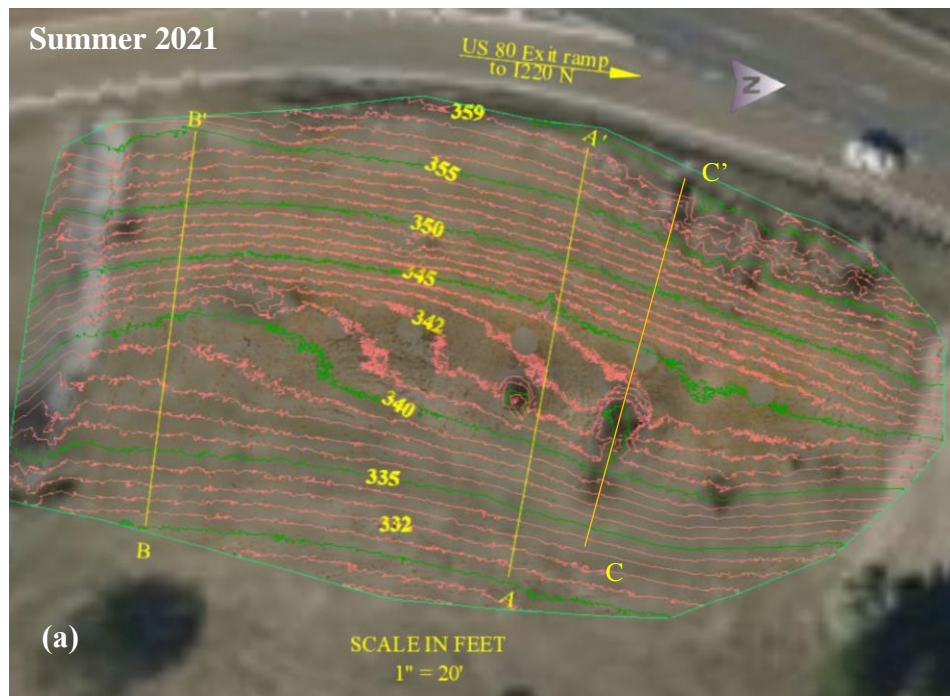


Figure 4.15 (Continued)

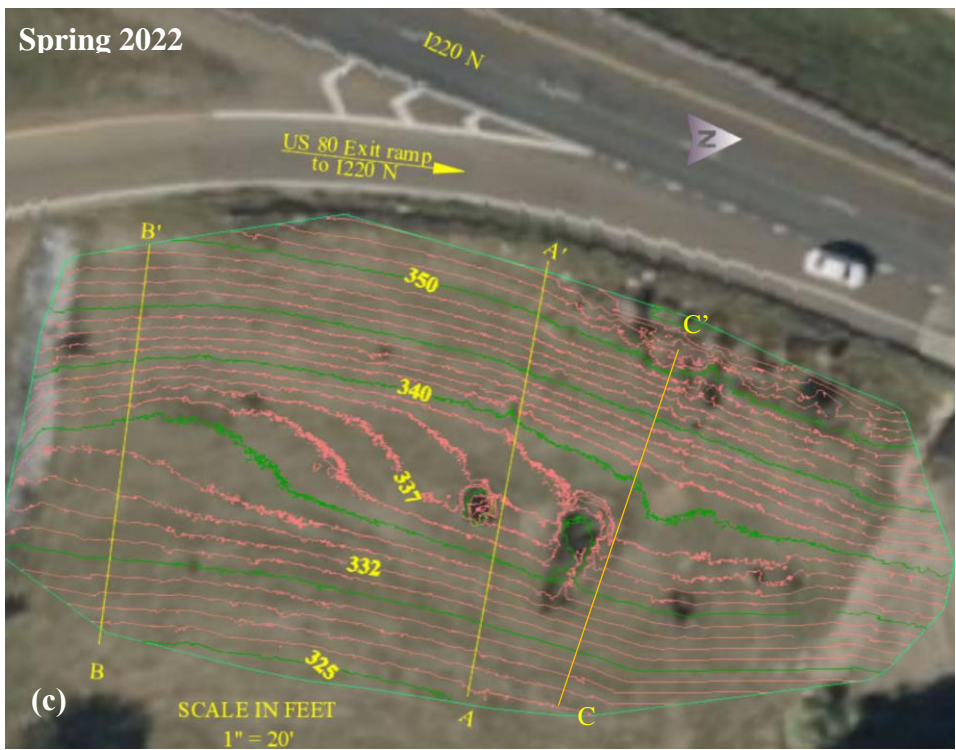
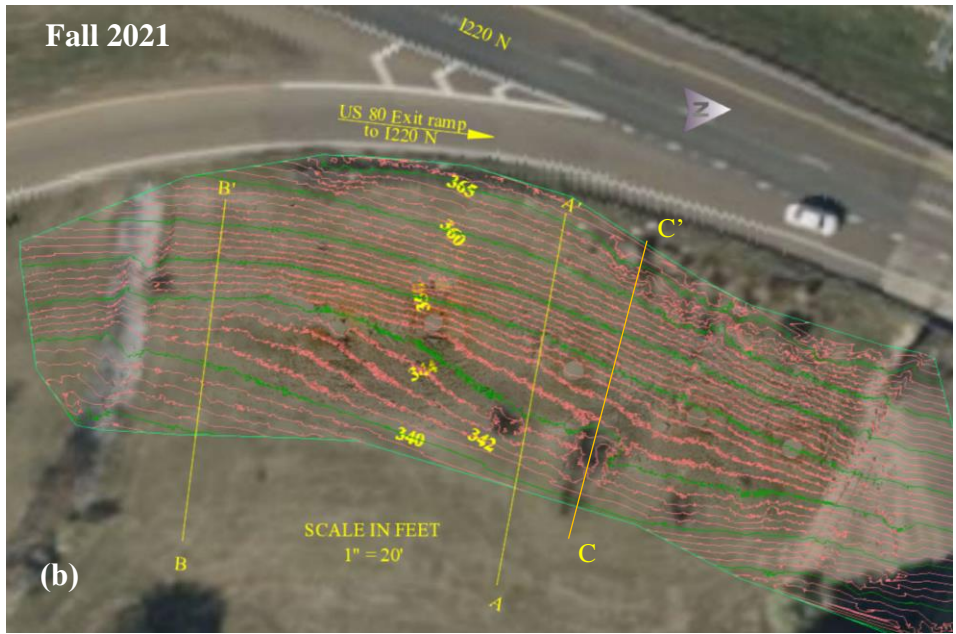


Figure 4.15 (Continued)

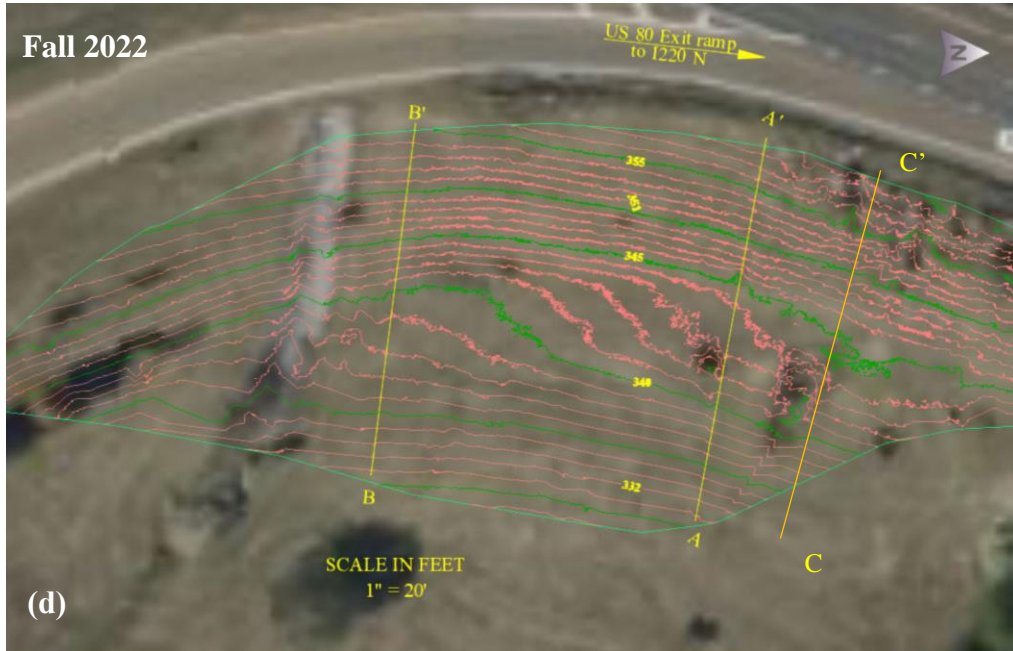


Figure 4.15 Season Variations in Slope 2's LiDAR Point Cloud Surface Topography: (a) Summer 2021, (b) Fall 2021, (c) Spring 2022, and (d) Fall 2022

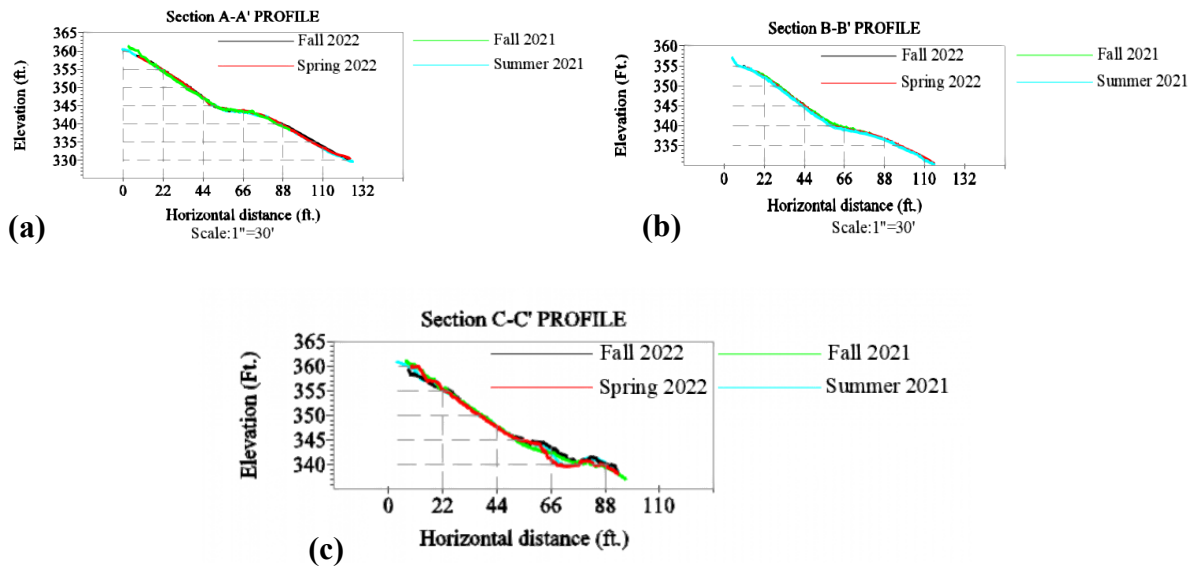


Figure 4.16 Seasonal Variations in Slope 2's LiDAR Point Cloud Surface Profiles: (a) Section A-A', (b) Section B-B', (c) Section C-C'

4.1.3 Instrumented Slope 3: Terry Road Highway Slope

ERI testing results for multiple sections of instrumented Slope 3 are presented below for different seasons, beginning in 2021.

4.1.3.1 ERI

The ERI test for Instrumented Slope 3 was conducted along a 165-foot (50-meter) length of the crest and middle (lines A and B) of the slope. The test line and slope location are presented in Figure 4.17. The results obtained from testing Line A during different seasons from spring 2021 through fall/winter 2022 are presented in Figure 4.18 (a – e).



Figure 4.17 Location of Slope 3 and ERI Test Lines

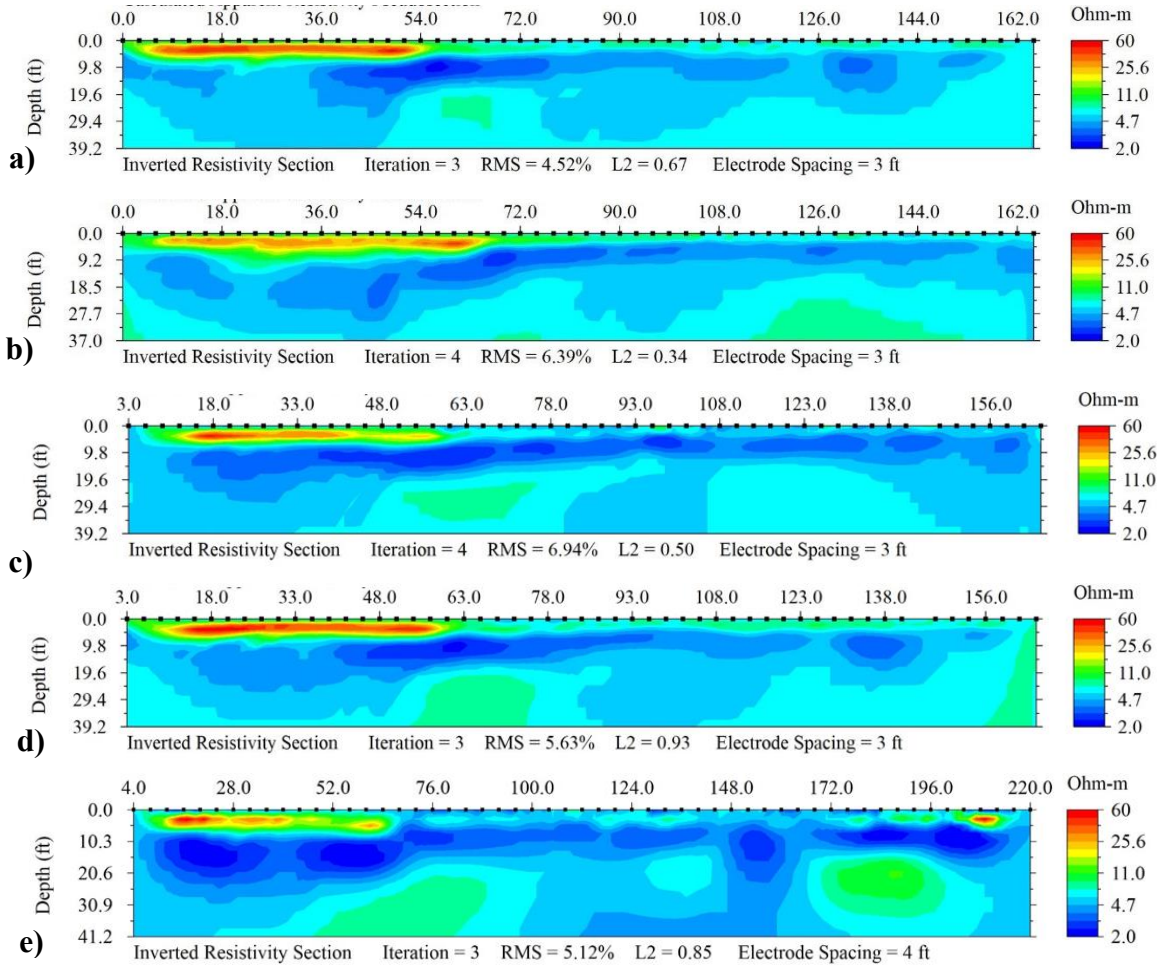


Figure 4.18 ERI Line A of I-Slope 3: (a) Spring 2021, (b) Summer 2021, (c) Fall 2021, (d) Winter 2021/Spring 2022, (e) Fall/Winter 2022

Figure 4.19 (a-e) depicts the ERI results for Line B from testing performed during different seasons and shows the presence of a high resistivity zone, indicating soil movement, at shallow depths (between 5 ft. [1.5m] and 54 ft. [16.5m], and up to a depth of 6 ft. (2m). Resistivity is extremely low (less than 5 Ohm-m) beyond 6 ft. at the crest and middle of the slope (Line A and Line B), just below the unsaturated soil zone at the 54 ft. (16.5m) horizontal distance mark. These low resistivity zones could be attributed to the development of perched water zones.

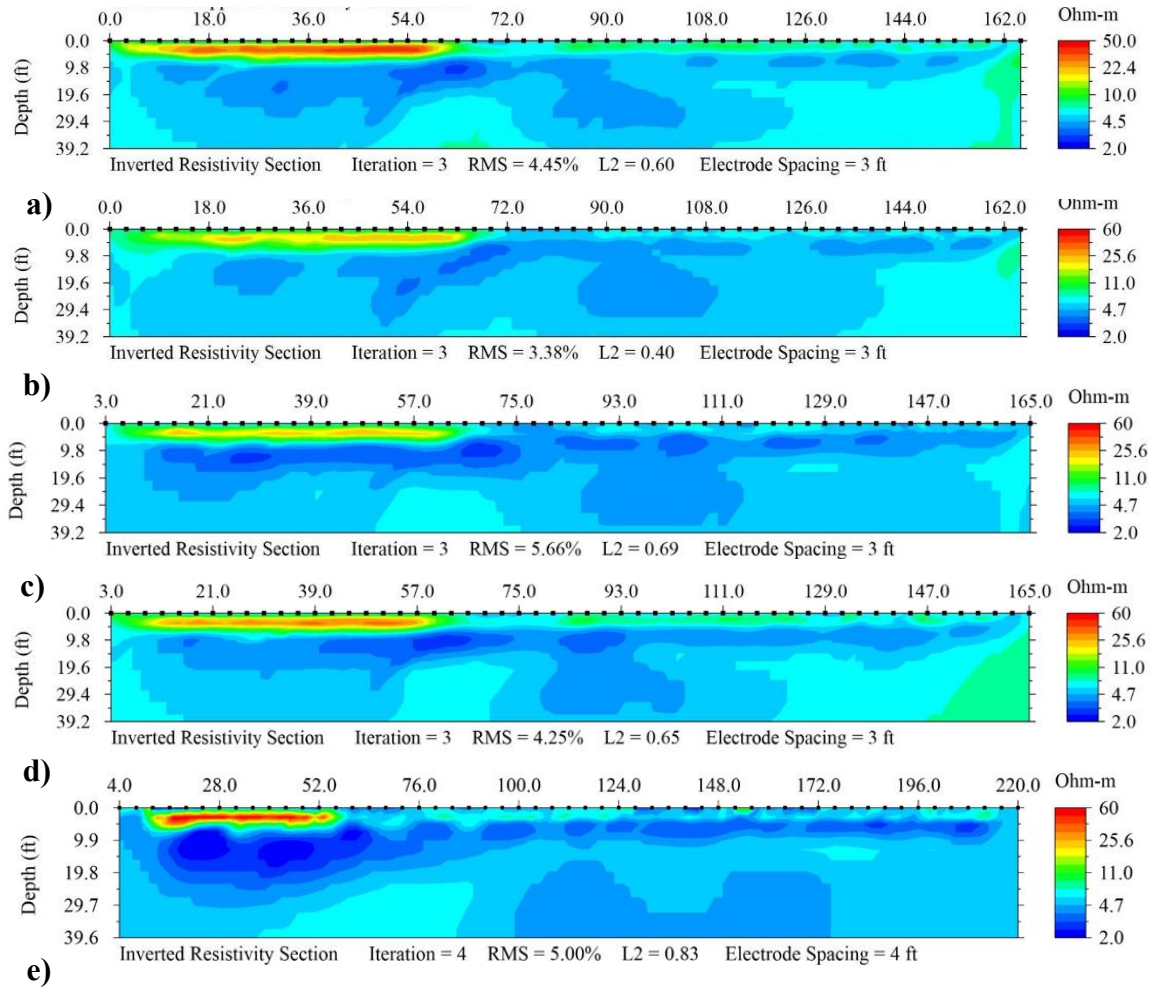


Figure 4.19 ERI Line B of I-Slope 3: (a) Spring 2021, (b) Summer 2021, (c) Fall 2021, (d) Winter 2021/Spring 2022, (e) Fall/Winter 2022

4.1.3.2 Drone

A drone survey was carried out at I-Slope 3 in different seasons from summer 2021 through fall 2022, and the aerial imagery captured was processed using specialized software. The coordinate system for the imagery was set to the State Plane Coordinate System Mississippi US-West. Aerial triangulation was performed with multiple tie points to stitch the images together and develop a digital elevation model (DEM), digital terrain model, (DTM), and mosaics. DEM and orthomosaic digital image representations for different seasons are presented in Figure 4.20 - Figure 4.22. The overlapping imagery data from fall 2021 and fall 2022 enabled the development of a 3D model (see Figures 4.21 and 4.22.)

Profile views were developed using two methods. Elevations were extracted and the profile shown in Figure 4.21 was created manually from the imagery captured in summer 2021. For imagery collected in fall 2021 and fall/winter 2022, georeferenced DEMs were imported into Civil 3D, surfaces were created using the kriging interpolation method, and surface profiles were created by using the alignment and surface profile tools in Civil 3D. Figure 4.21(b) and Figure 4.22 show the 3D model and surface profiles for fall 2021 and fall 2022, respectively.

Summer 2021

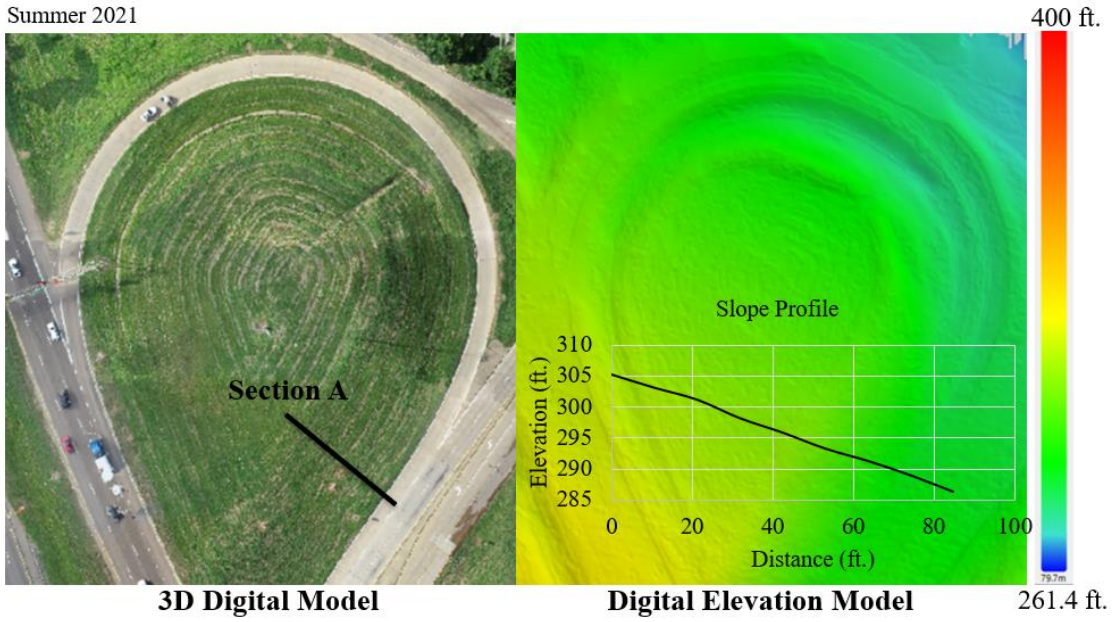
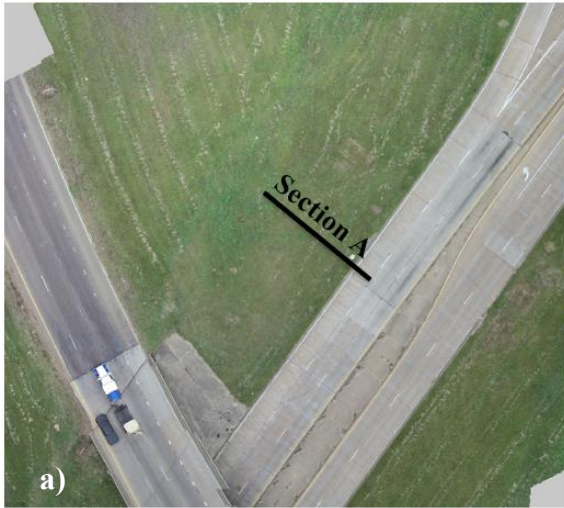
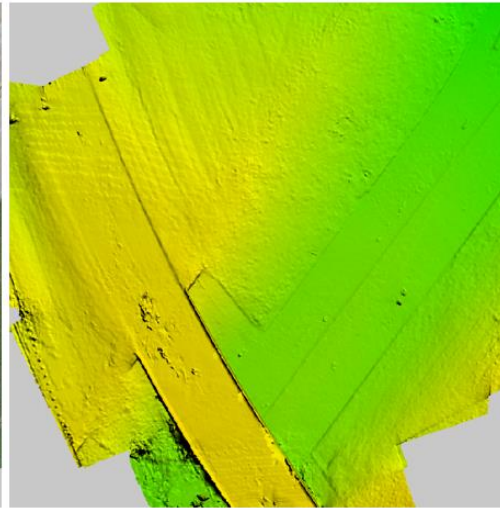


Figure 4.20 Digital Elevation Model based on Drone Imagery of Instrumented Slope 3 (Summer 2021)

Fall 2021



3D Digital Model

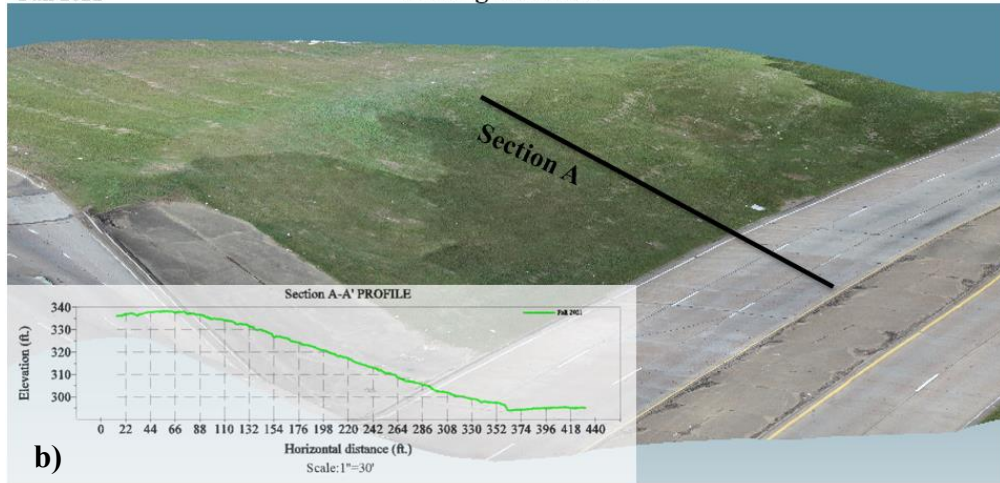


Digital Elevation Model

259 ft.

Fall 2021

3D Digital Model



b)

Figure 4.21 Drone Imagery of Slope 3: (a) Digital Elevation Model, (b) 3D Model, and Surface Profile (Fall 2021)

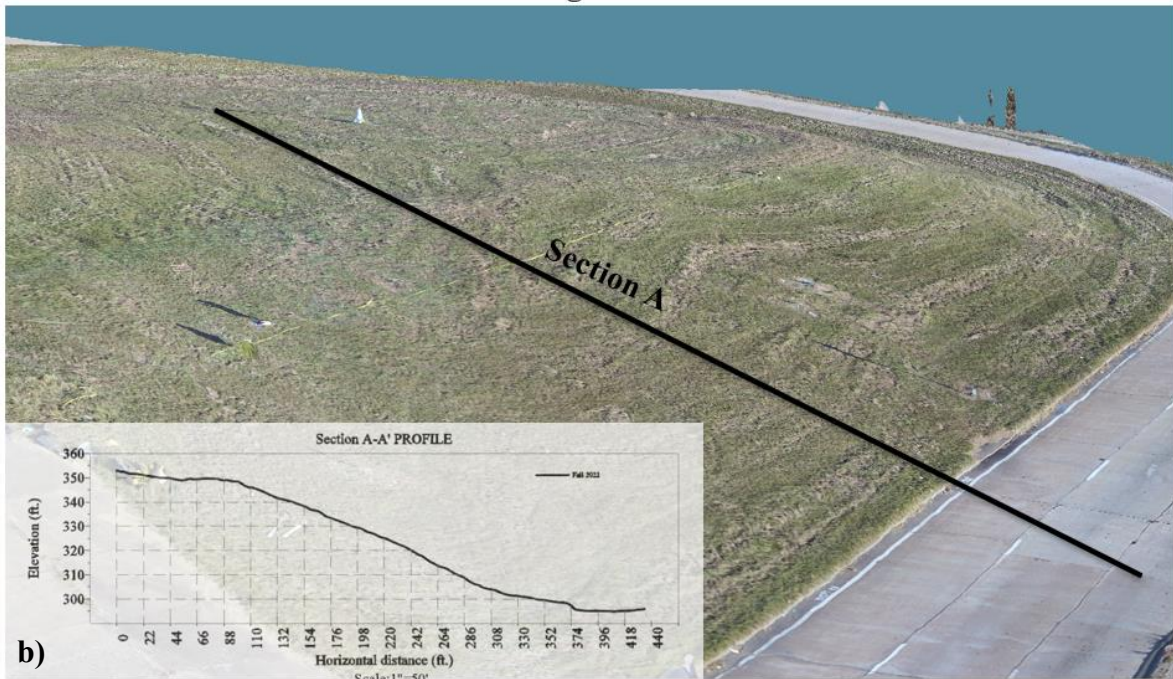
Fall 2022



a)

Fall 2022

3D Digital Model



b)

Figure 4.22 Drone Imagery of Slope 3: (a) Digital Elevation Model, (b) 3D Model, and Surface Profile (Fall 2021)

4.1.3.3 LiDAR

Topography and profile views of Slope 3 developed from Terrestrial LiDAR scanning data collected during different seasons from summer 2021 through fall/winter 2022 are presented in Figures 4.23 a-d. Scanning was performed at several stations, and the overlapping point cloud

data was collected, post-processed on a computer and registered together to form a single point cloud. In the summer of 2021, about 12 scan stations were used in a grid pattern that generated over 300 million scan points. The combined point cloud was then georeferenced, using field ground control points with known coordinates. The low surface points were extracted to create bare ground point clouds, using a ground extraction algorithm. The bare ground point clouds for all seasons collected were imported into Civil 3D, and surfaces were generated using the kriging interpolation method. Topographic surface views were generated at 1 ft. major and 5 ft. minor contour intervals and are presented in Figure 4.23 (a-d). The surfaces from all seasons were overlaid, and alignments were created along the slope. Stacked surface profiles were then created using the alignments along Sections A-A' and B-B,' as presented in Figures 4.24 a & b, respectively.

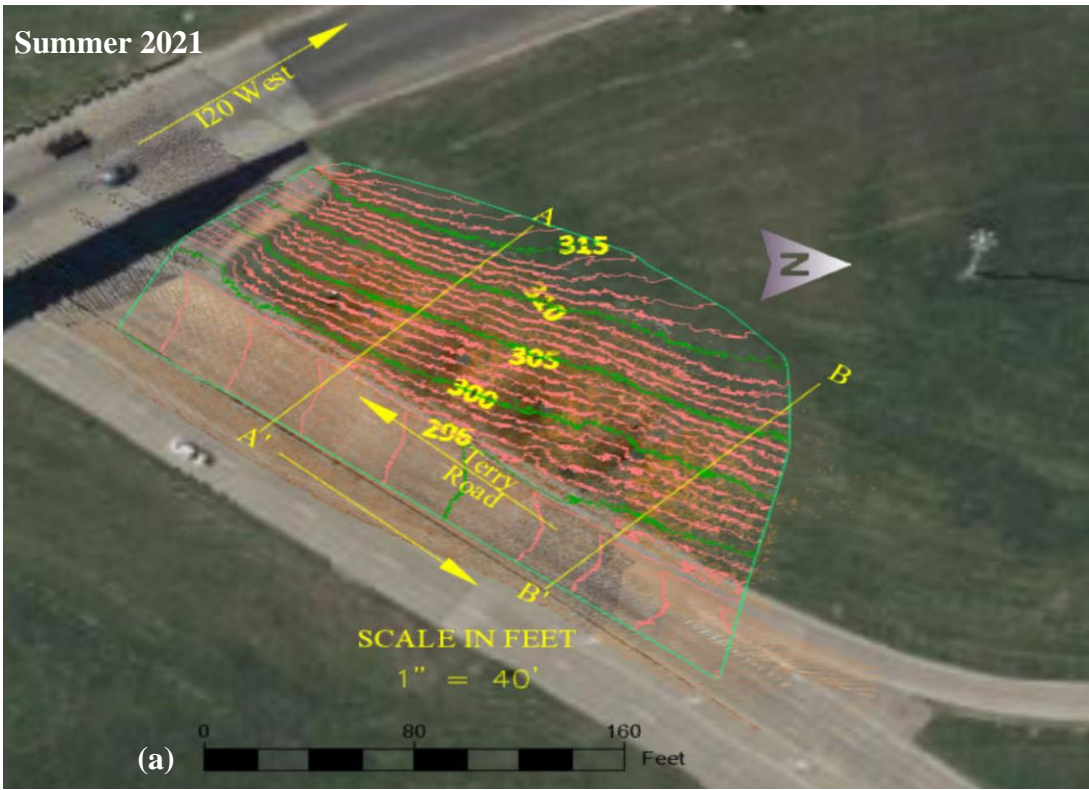


Figure 4.23 (Continued)

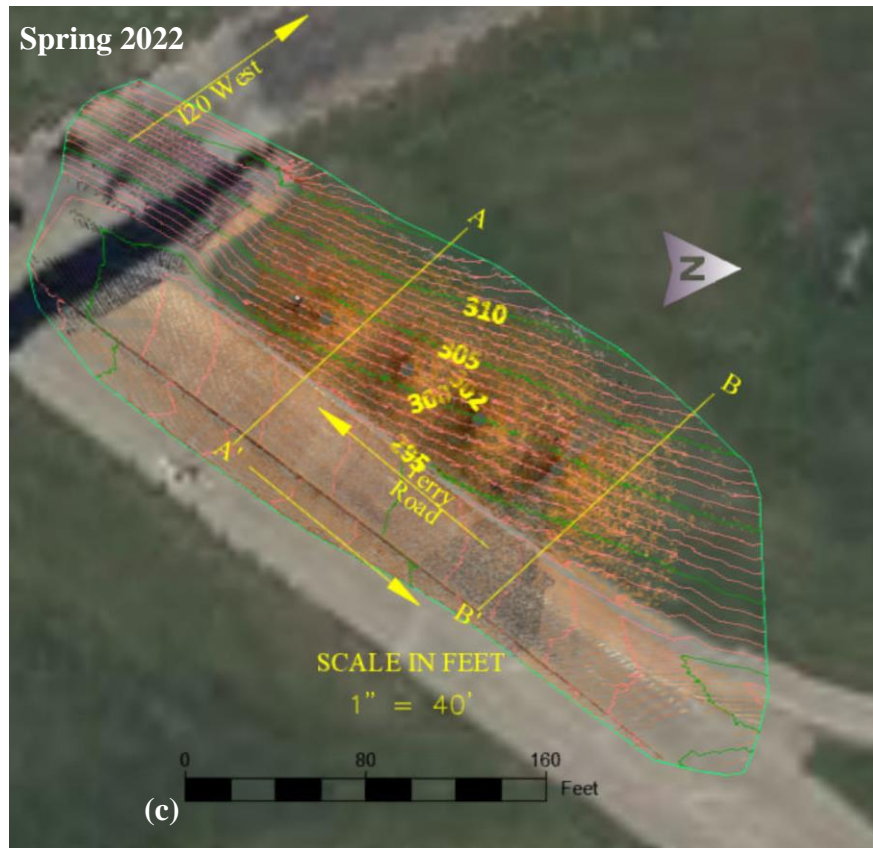
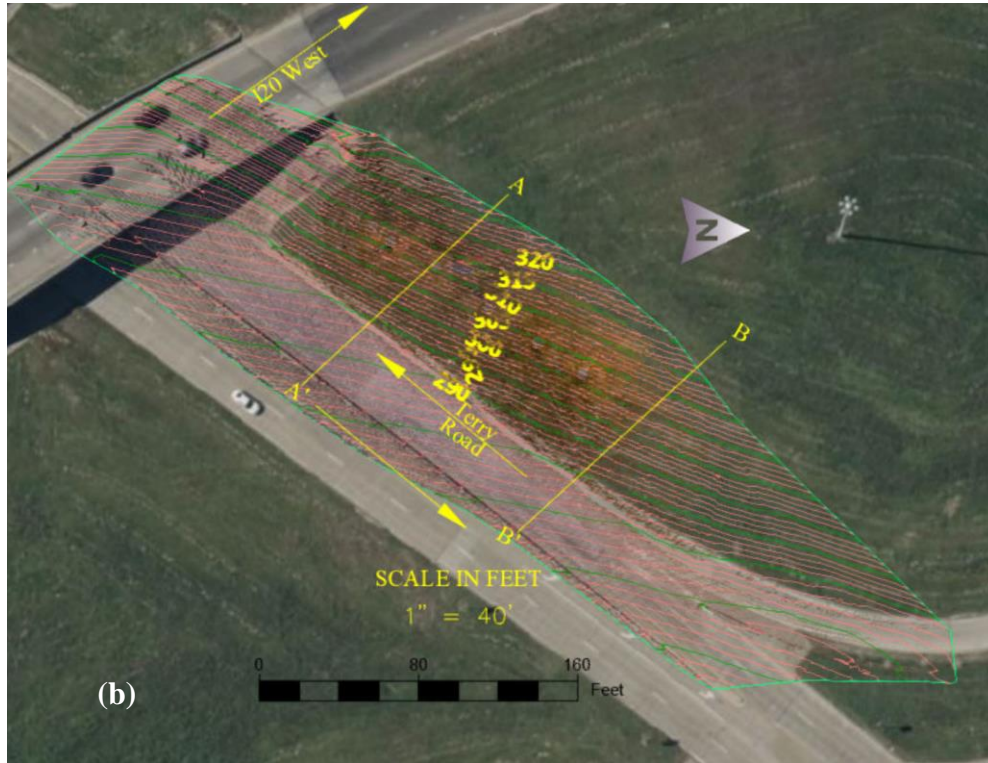


Figure 4.23 (Continued)

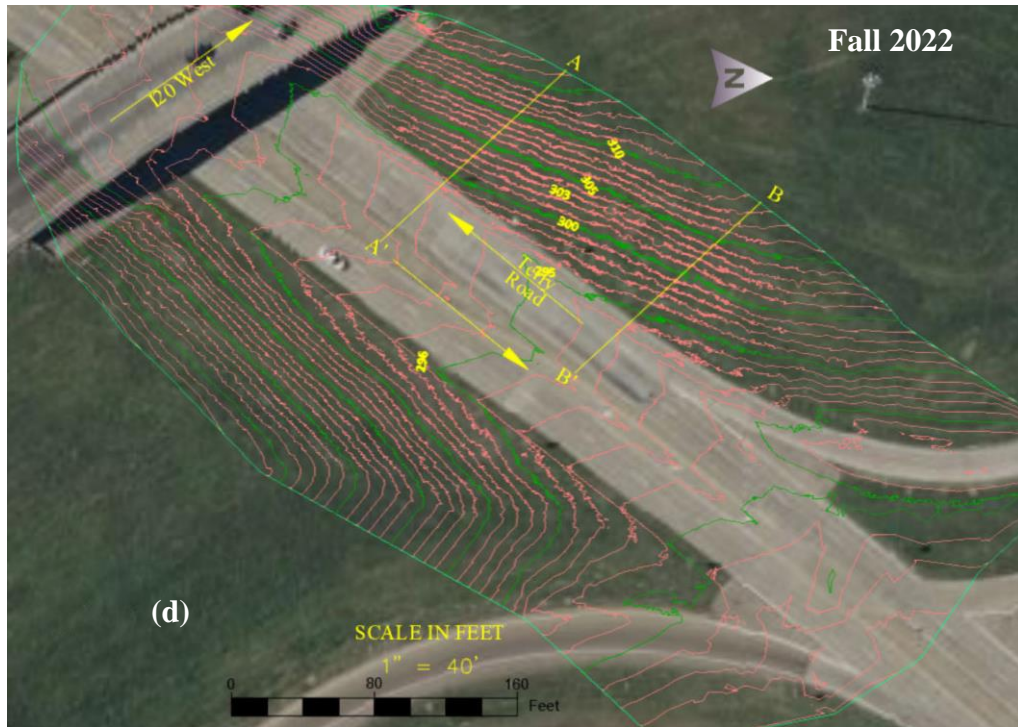


Figure 4.23 LiDAR Point Cloud Surface Topography of Slope 3 Depicting Seasonal Variations: (a) Summer 2021, (b) Fall 2021 (c) Spring 2022 (d) Fall 2022

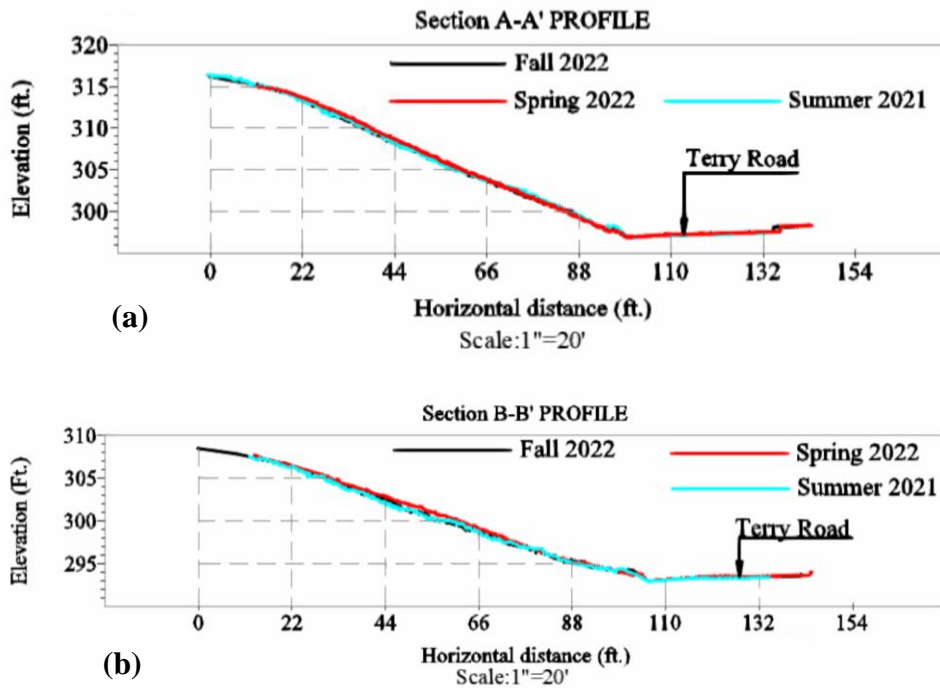


Figure 4.24 LiDAR Point Cloud Surface Profiles of Slope 3 with Seasonal Variations: (a) Section A-A', (b) Section B-B'

4.1.4 Instrumented Slope 4: Highland Drive Highway Slope

Results of ERI testing of instrumented Slope 4 during different seasons beginning in 2021 are presented below.

4.1.4.1 ERI

An ERI test was performed along 162 feet (49.5m) of Slope 4, between the crest and the middle (Lines A and B). The location of the slope and the ERI test lines are presented in Figure 4.25. The results for Line A from testing conducted from spring 2021 through fall/winter 2022 are presented in Figure 4.26 (a – e). The results of the Line B testing are presented in

Figure 4.27 (a-e). Very high resistivity zones were discovered in both the crest (Line A) and middle (Line B) of the slope, at the 84 ft. (25.6m) horizontal mark and 6 ft. (1.83m) depth. In general, high resistive areas were found at the surface, with moisture pockets found deeper.



Figure 4.25 Location of Slope 4, with ERI Test Lines

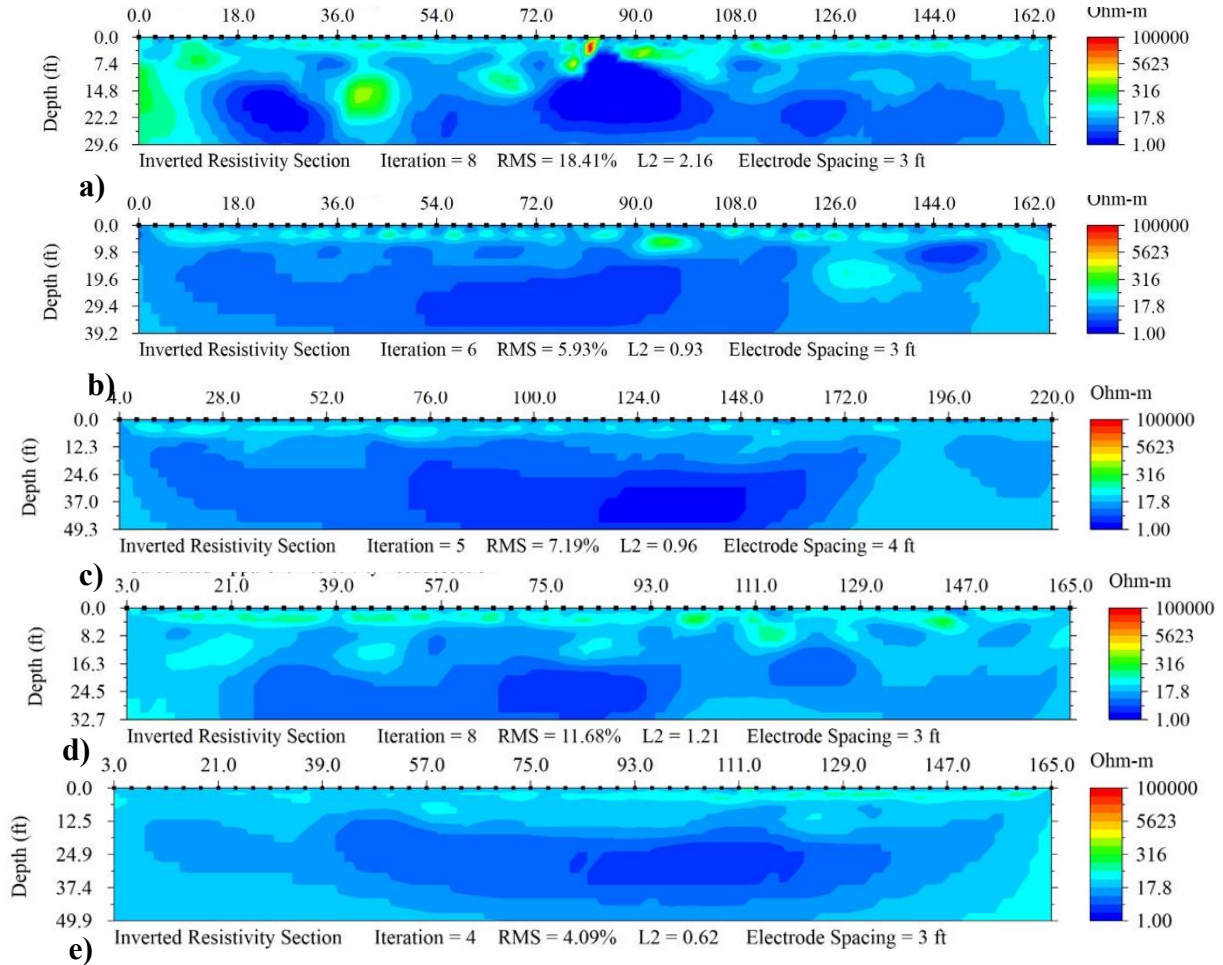


Figure 4.26 Line A of Slope 4: (a) Spring 2021, (b) Summer 2021. (c) Fall 2021, (d) Winter 2021/Spring 2022, (e) Fall/Winter 2022

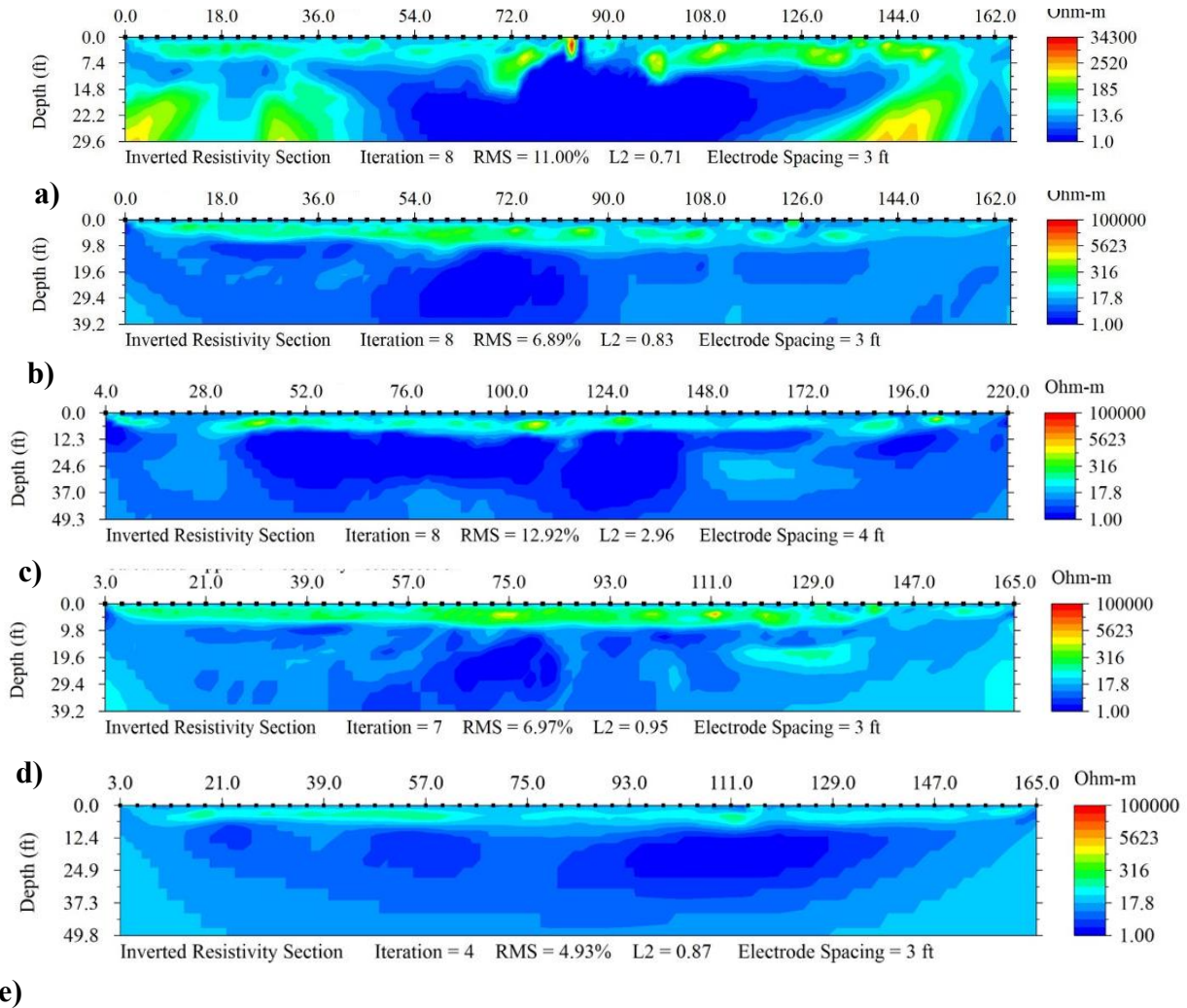


Figure 4.27 Line B of Slope 4: (a) Spring 2021, (b) Summer 2021, (c) Fall 2021, (d) Winter 2021/Spring 2022, (e) Fall/Winter 2022

4.1.4.2 Drone

Drones surveyed instrumented Slope 4 during different seasons from summer 2021 through fall 2022, and the captured aerial imagery was processed using specialized software. The coordinate system for the imagery was set to the State Plane Coordinate System Mississippi US-West. Aerial triangulation was performed with multiple tie points to stitch the images together and develop a digital elevation model (DEM), digital terrain model (DTM), and mosaics. DEM and orthomosaic digital images for different seasons are presented in Figure 4.28 to Figure 4.31

For the drone imagery collected in fall/winter 2022, the georeferenced DEM was imported into Civil 3D, and the surface was created using the kriging interpolation method. The surface profiles were created by using the alignment and surface profile tools within Civil 3D. Figure 4.31 (b) and (c) show the slope 3D model and the surface profile views for fall 2022, respectively.

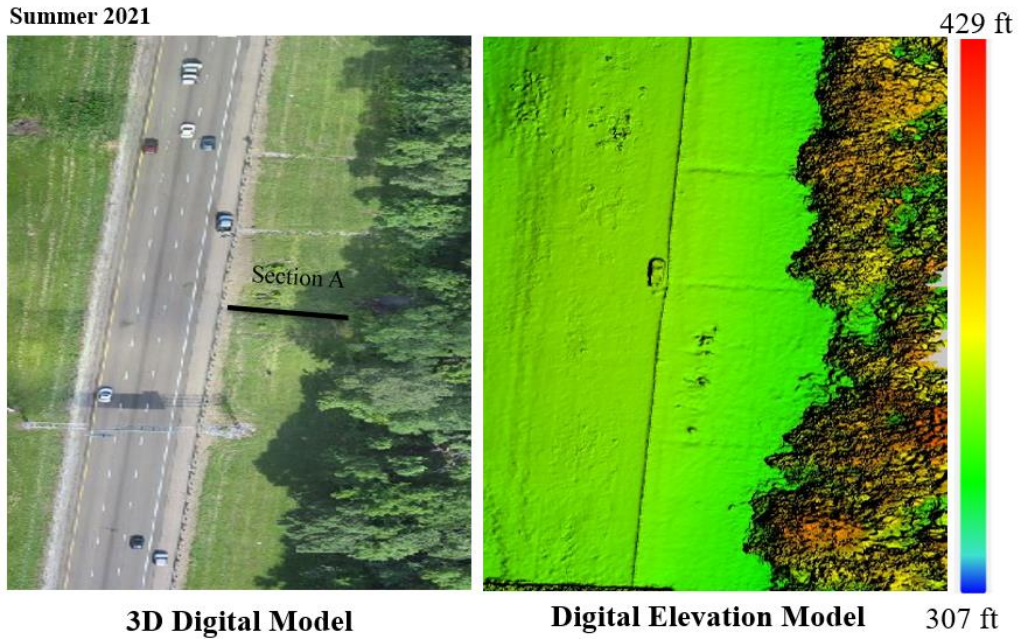


Figure 4.28 Digital Representation Derived from Drone Imagery of Slope 4 (Summer 202)

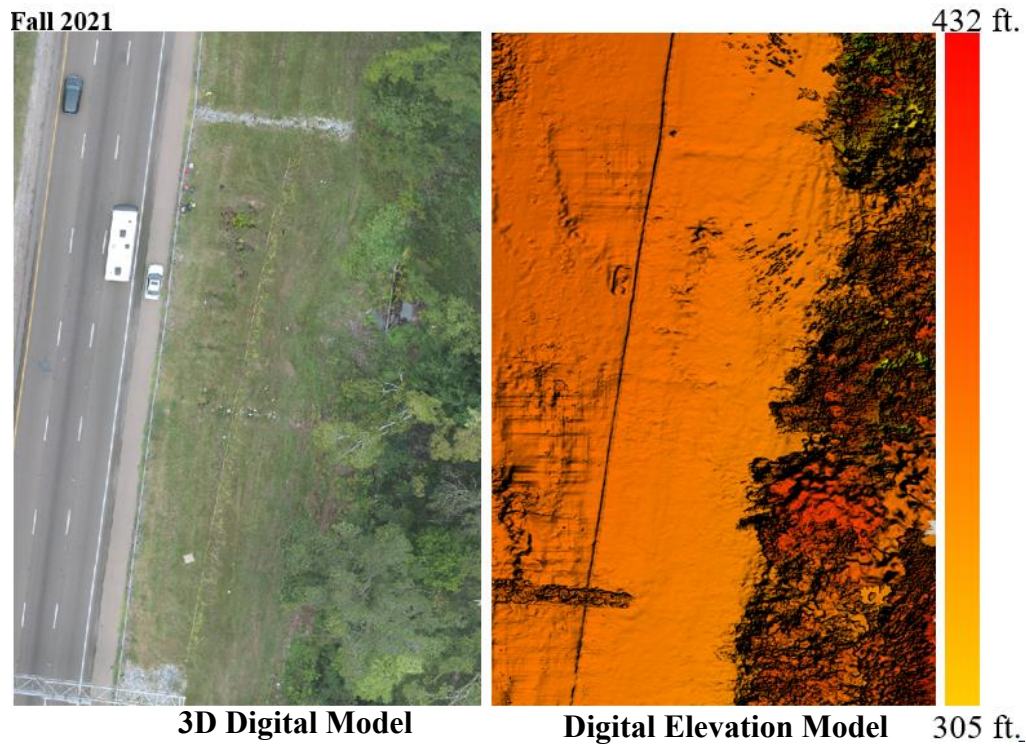
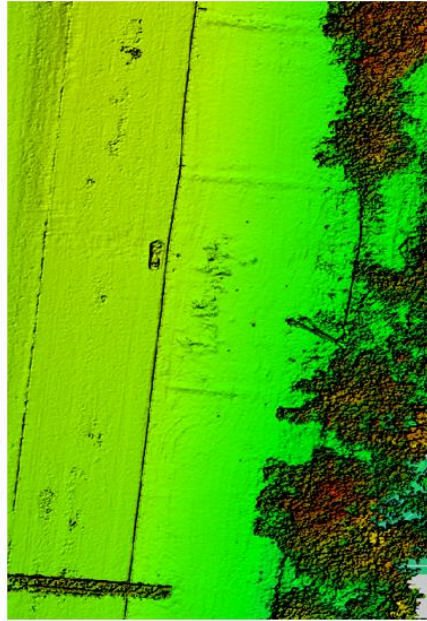


Figure 4.29 Digital Representation of Slope 4 Derived from Drone Imagery (Fall 2021)

Spring 2022



3D Digital Model



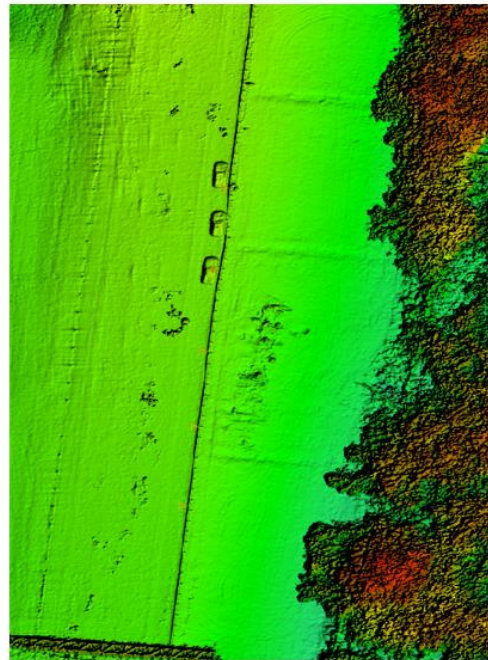
Digital Elevation Model 429 ft.
290 ft.

Figure 4.30 Digital Representation of Slope 4 Derived from Drone Imagery (Spring 2022)

Fall/Winter 2022



(a) 3D Digital Model

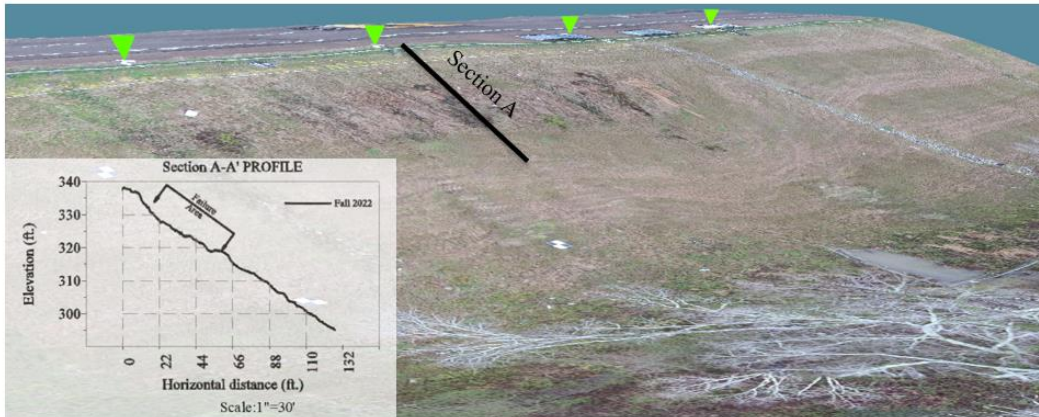


Digital Elevation Model 429 ft.
307 ft.

Figure 4.31 (Continued)

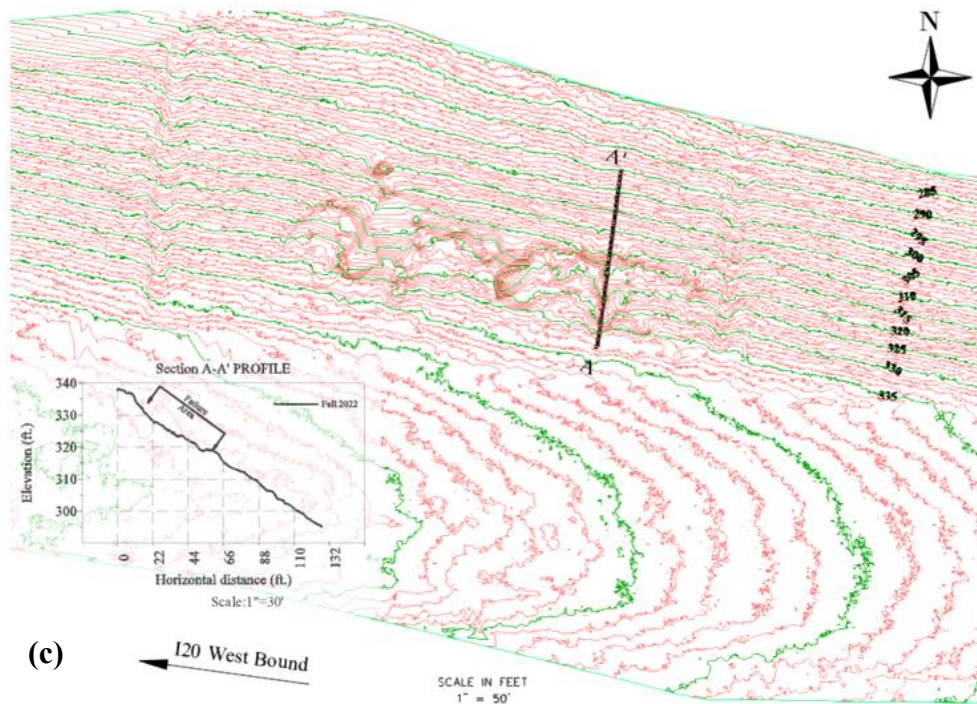
Fall/Winter 2022

3D Model



(b)

Fall/Winter 2022



(c)

Figure 4.31 Drone Imagery of Slope 4 in Fall/Winter 2022: (a) Digital Elevation Model, (b) 3D Model and Surface Profile, (c) Surface Topography

4.1.4.3 LiDAR

Topography and profile views of Slope 4 developed from the Terrestrial LiDAR scanning data collected during different seasons from summer 2021 through fall/winter 2022 are presented in **Figure 4.32**. Laser scanning was performed at several stations, and the overlapping point cloud data were collected. The point clouds were post-processed on a computer and registered together to form a single point cloud that was georeferenced, using field ground control points with known coordinates. The low surface points were extracted, using a ground extraction algorithm, to create the bare ground point clouds. The bare ground point clouds were imported into Civil 3D, and

surfaces were generated using the kriging interpolation method. Topographic surface views were generated at 1 ft. major and 5 ft. minor contour intervals and are presented in Figure 4.32 (a-d).

Surfaces from all seasons were overlaid, and alignments were created along the slope. Stacked surface profiles were created using the alignments along Sections A-A' and B-B' and are presented in Figure 4.33 (a) and (b), respectively. No significant variations were observed along A'A,' but there were observable variations along the toe of the slope, along section B-B'.

Summer 2021



Fall 2021

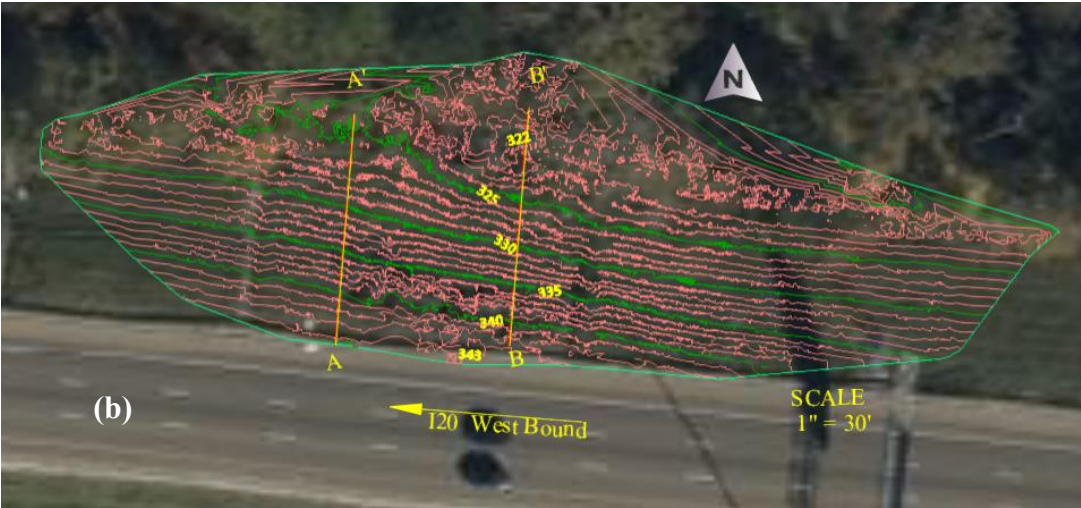


Figure 4.32 (Continued)

Spring 2022



Fall 2022

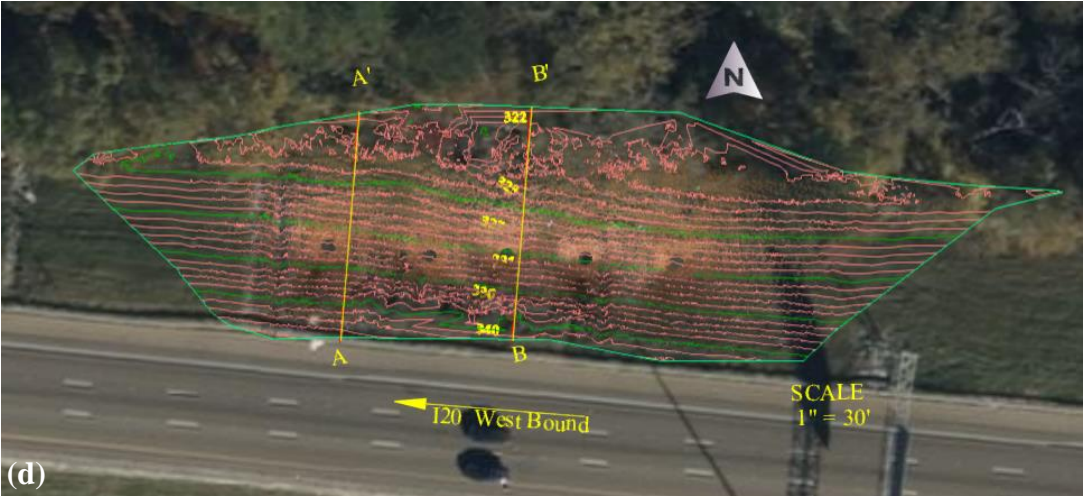


Figure 4.32 LiDAR Point Cloud Surface Topography Seasonal Variations in Slope 4: (a) Summer 2021, (b) Fall 2021, (c) Spring 2022, (d) Fall 2022

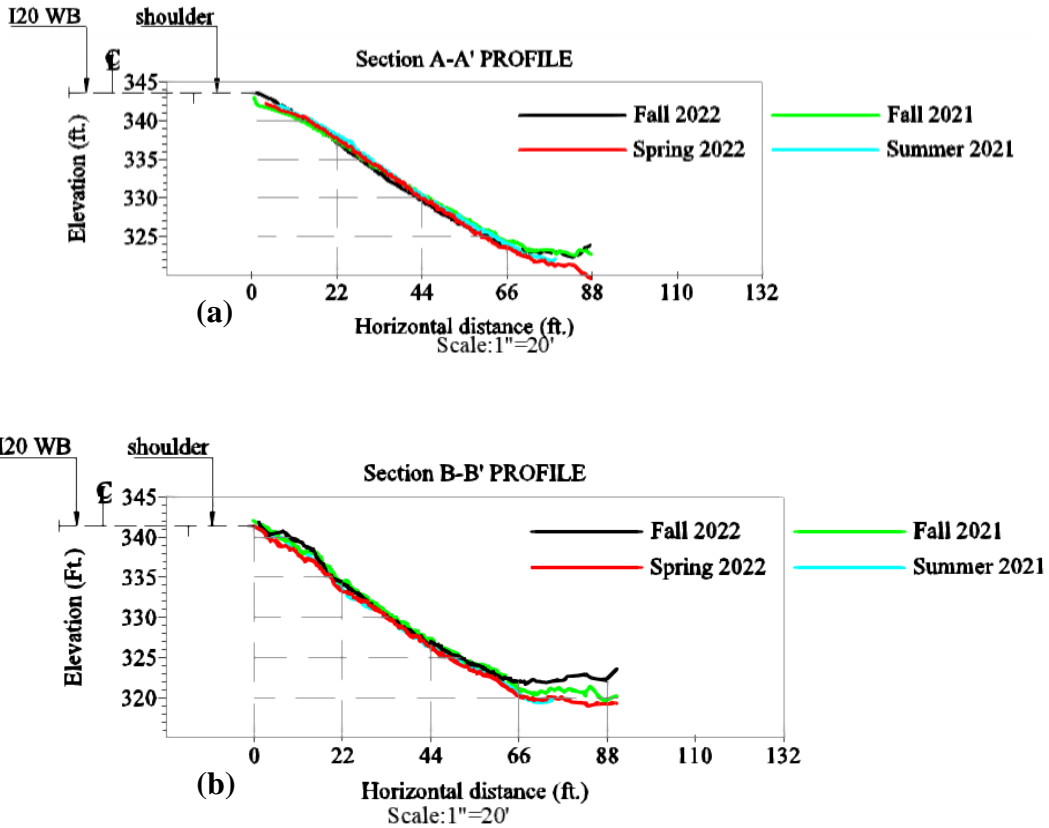


Figure 4.33 LiDAR Point Cloud Surface Profiles of Seasonal Variations for Slope 4: (a) Section A-A', (b) Section B-B'

4.1.5 Instrumented Slope 5: Sowell Road Highway Slope

4.1.5.1 ERI

An ERI test was conducted of 270 feet between the crest and the middle (Lines A and B) of Slope 5. The test lines and slope location are presented in Figure 4.34. The results obtained for Line A during different seasons from spring 2021 through fall/winter 2022 are presented in Figure 4.35 (a-e).



Figure 4.34 Slope 5 ERI Test Lines Location

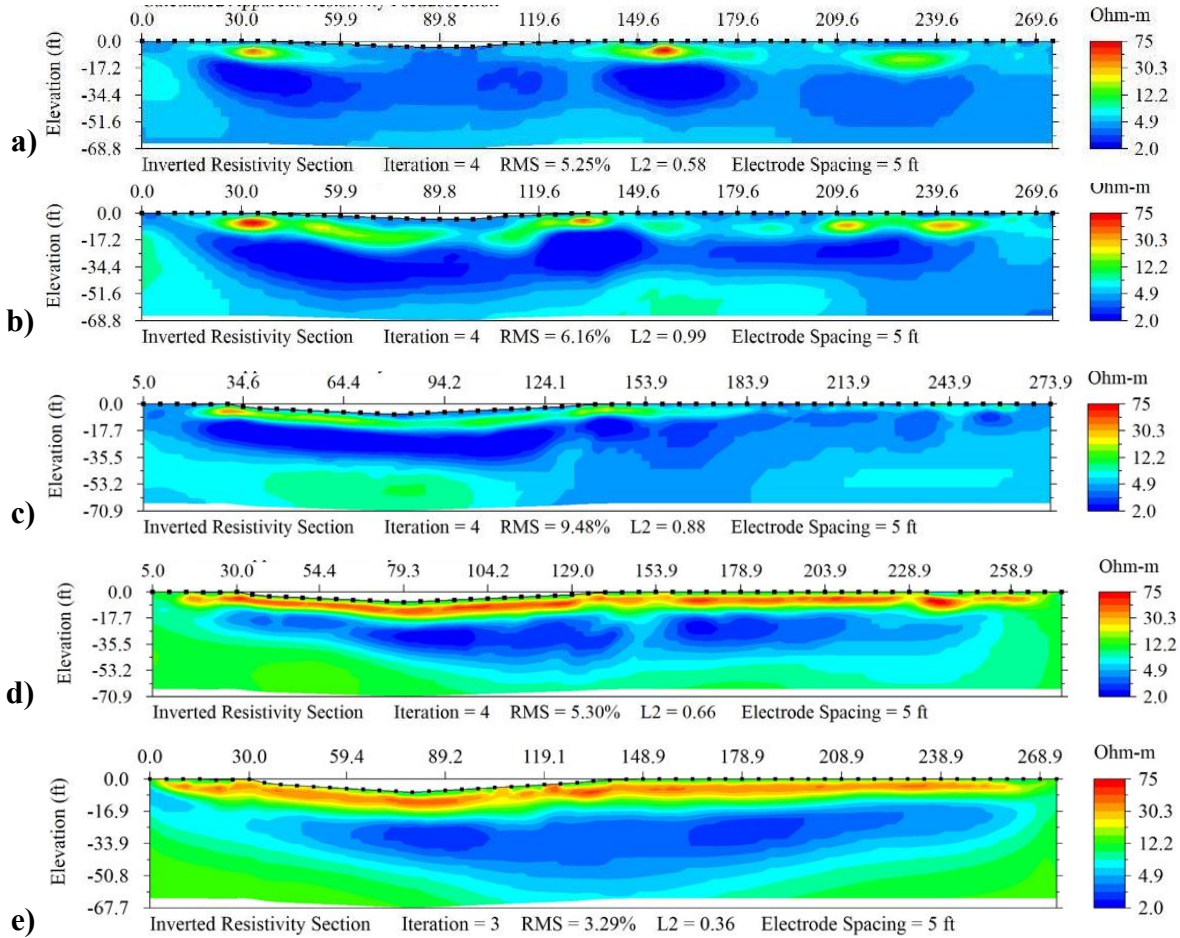


Figure 4.35 Results from ERI testing of Line A of Slope 5: (a) Spring 2021, (b) Summer 2021, (c) Fall 2021, (d) Winter 2021/Spring 2022, (e) Fall/Winter 2022

The resistivity in the layers up to 8' depth throughout the width of the slope crest gradually increased from fall 2021 to fall/winter 2022, indicating soil deformation. The deformation was more clearly defined in the ERI profiles from spring 2022 and fall/winter 2022, as seen in Figure 4.35 (d) & (e), respectively.

ERI results for Line B from testing performed during different seasons are presented in

Figure 4.36 (a-e). In general, shallow levels (up to 5 ft. [1.5m] depths) have higher resistivity values (up to 75 Ohm-m). Perched water zones are found at depths greater than 15 feet (5m).

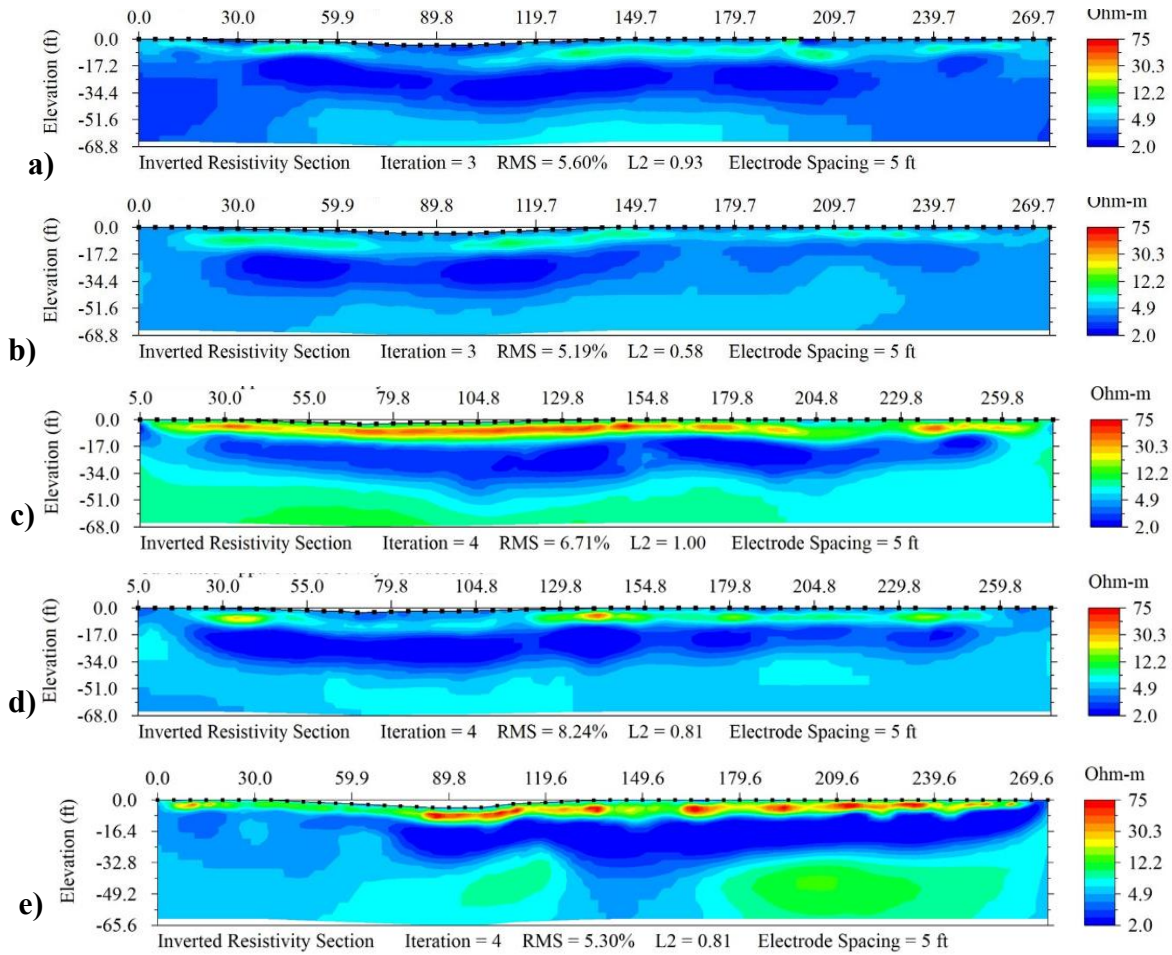


Figure 4.36 Line B of Slope 5: (a) Spring 2021, (b) Summer 2021, (c) Fall 2021, (d) Winter 2021/Spring 2022, (e) Fall/Winter 2022

4.1.5.2 Drone

Drone surveys for Slope 5 were conducted during different seasons from summer 2021 through fall 2022, and the aerial imagery was processed using specialized software. The coordinates were set to the State Plane Coordinate System Mississippi US-West. Aerial triangulation was performed with multiple tie points to stitch the images together and develop a digital elevation model (DEM), digital terrain model (DTM), and mosaics. The DEM and orthomosaic digital image representations are presented in Figure 4.34 to Figure 4.36.

The profile views of the slope were developed using two methods. The elevations were extracted, and a profile was created manually from the imagery obtained in summer 2021 and fall 2021, as shown in Figures 4.37 & Figure 4.38 respectively. For the drone imagery collected in fall/winter 2022, the georeferenced DEM was imported into Civil 3D, and the surface was created using the kriging interpolation method. The alignment and surface profile tools in Civil 3D were used to create the surface profile.

Figure 4.36 (b) and (c) shows the 3D model of the slope and the surface profile views for fall/winter 2022. The Orthomosaic failed for spring 2022 due to the light quality of the images and is therefore not included in this report.

Summer 2021

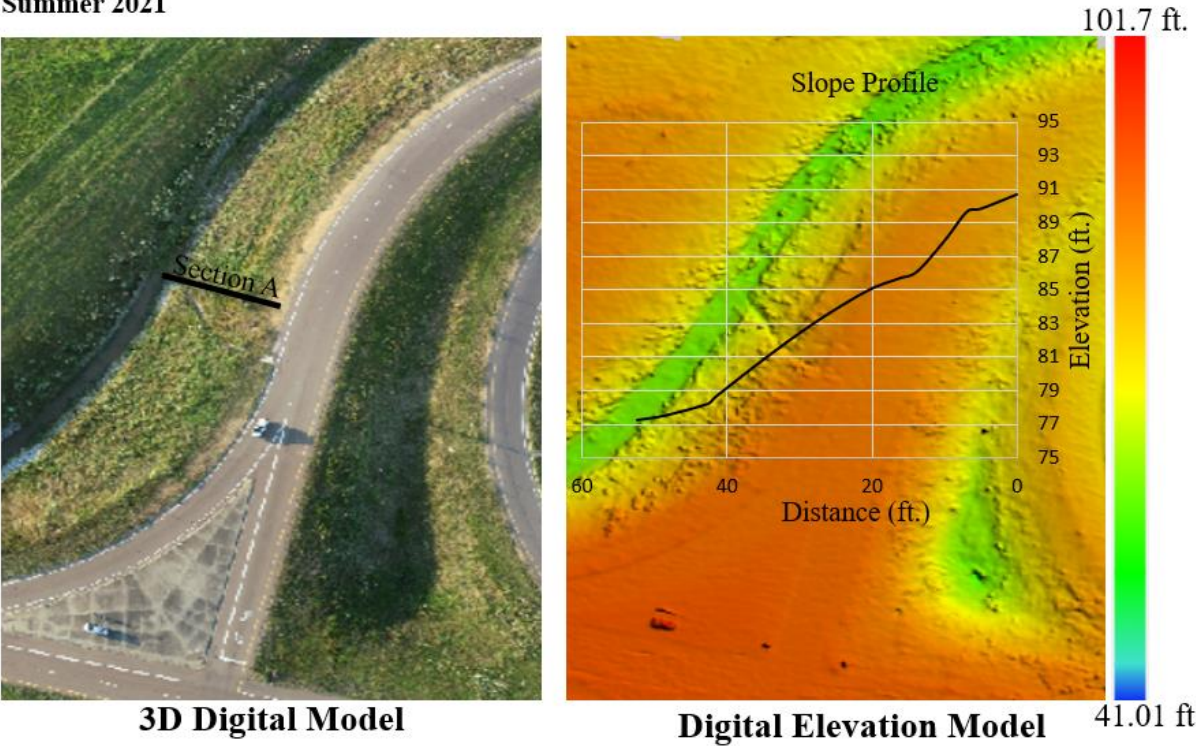


Figure 4.37 Slope 5 Drone Image (Summer 2021)

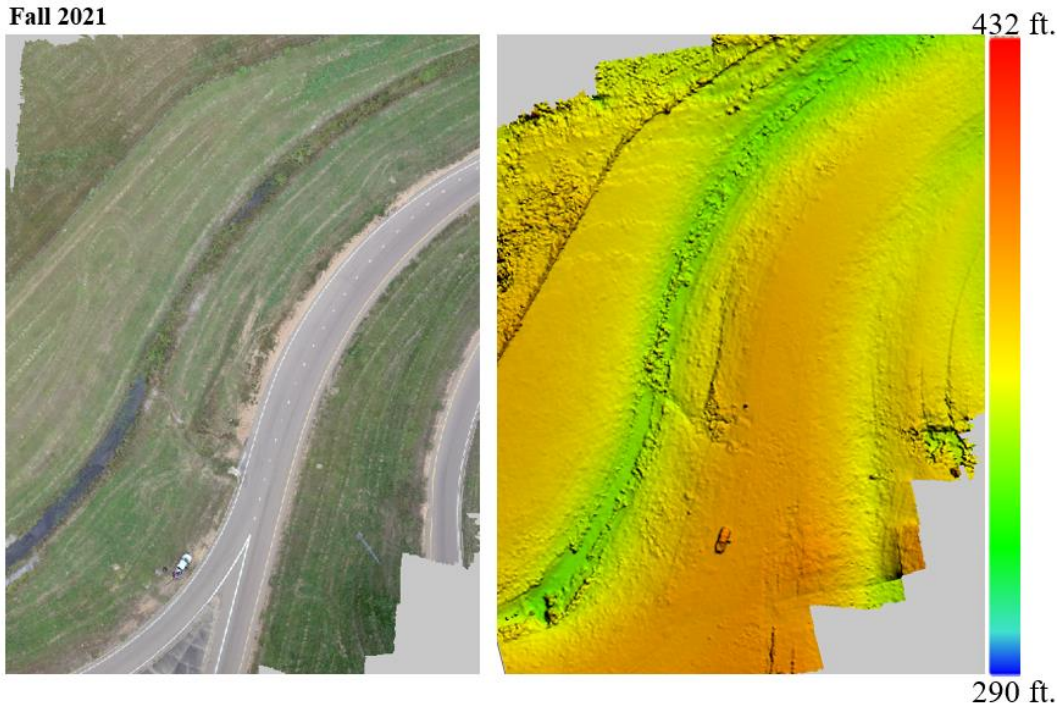


Figure 4.38 Drone Image of Slope 5 (Fall 2021)

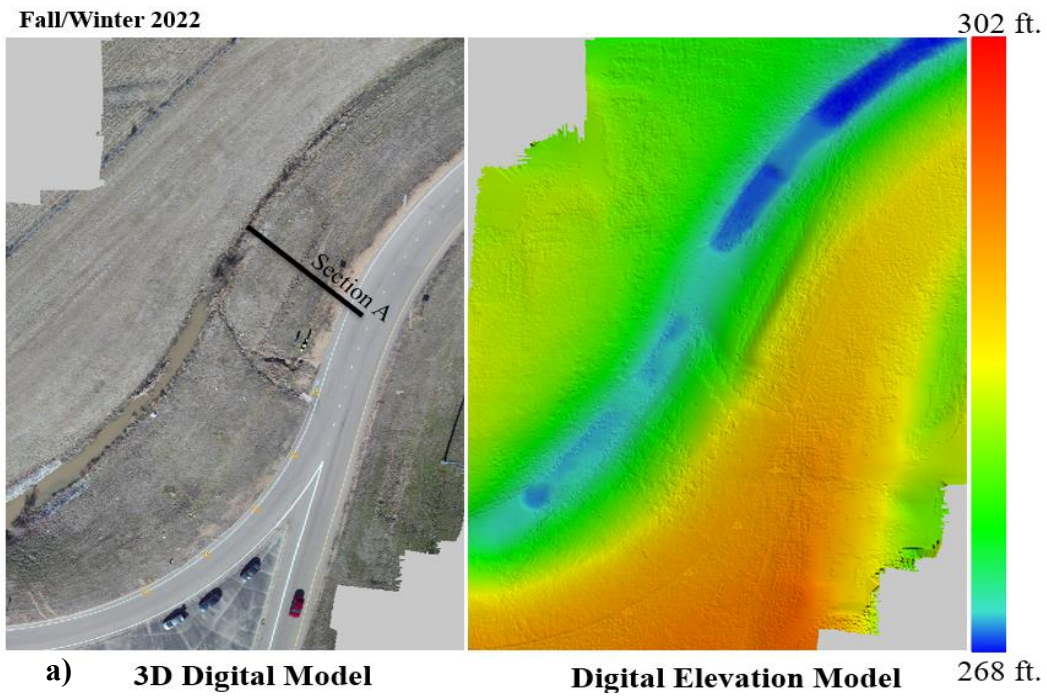


Figure 4.39 (Continued)

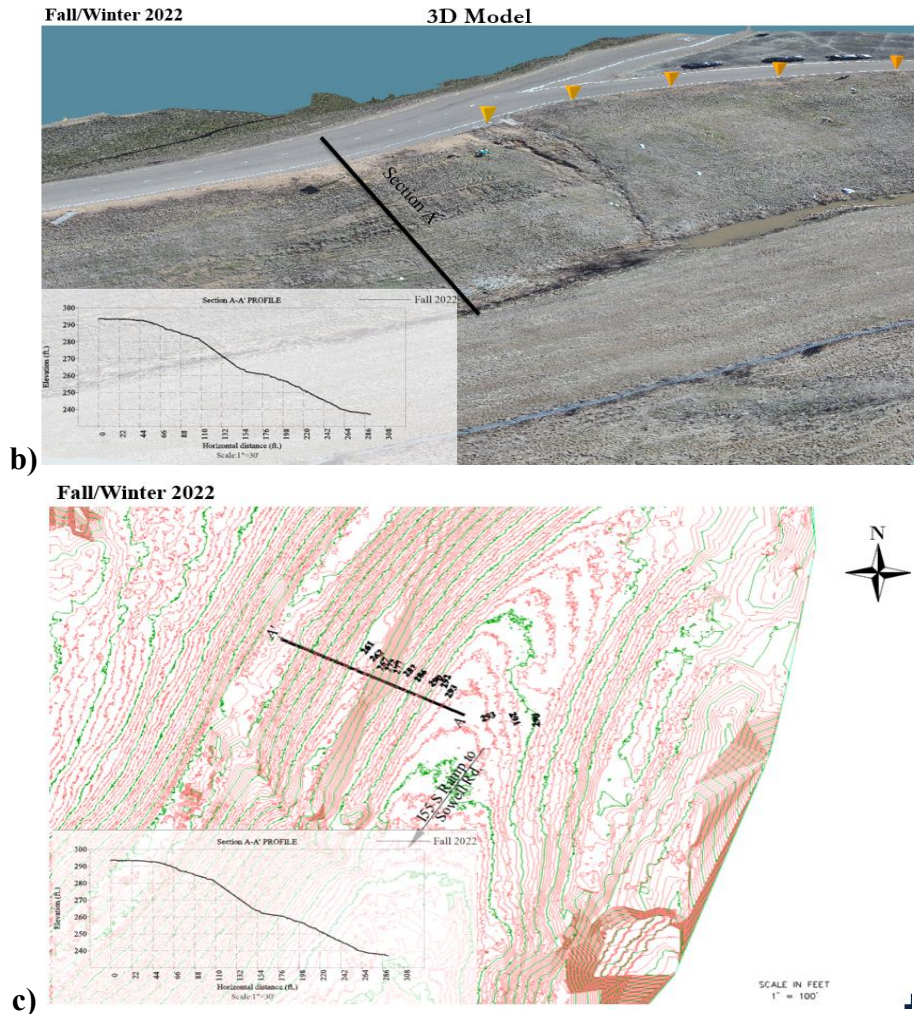


Figure 4.39 Slope 5 Drone Image Fall/Winter 2022: (a) Digital Elevation Model, (b) 3D Model & Surface Profile, and (c) Surface Topography

4.1.5.3 LiDAR

Topography and profile views of Slope 5 developed from the terrestrial LiDAR scanning data collected during different seasons from summer 2021 through fall/winter 2022 are presented in Figure 4.40. Laser scanning was performed at several stations, and the overlapping point cloud data was collected, post-processed on a computer and registered together to form a single point cloud. The combined point cloud was then georeferenced using field ground control points with known coordinates. Low surface points were extracted to create the bare ground point clouds, using a ground extraction algorithm. The bare ground point clouds for all seasons collected were imported into Civil 3D, and digital elevation model surfaces were generated using the kriging interpolation method. Topographic surface views were generated at 1 ft. major and 5 ft. minor contour intervals and are presented in **Figure 4.40** (a-d).

Surfaces from all seasons were overlaid, and alignments were created along the slope. Stacked surface profiles were then created using the alignments along Sections A-A' and B-B' and are presented in Figure 4.3841 (a) & (b), respectively.

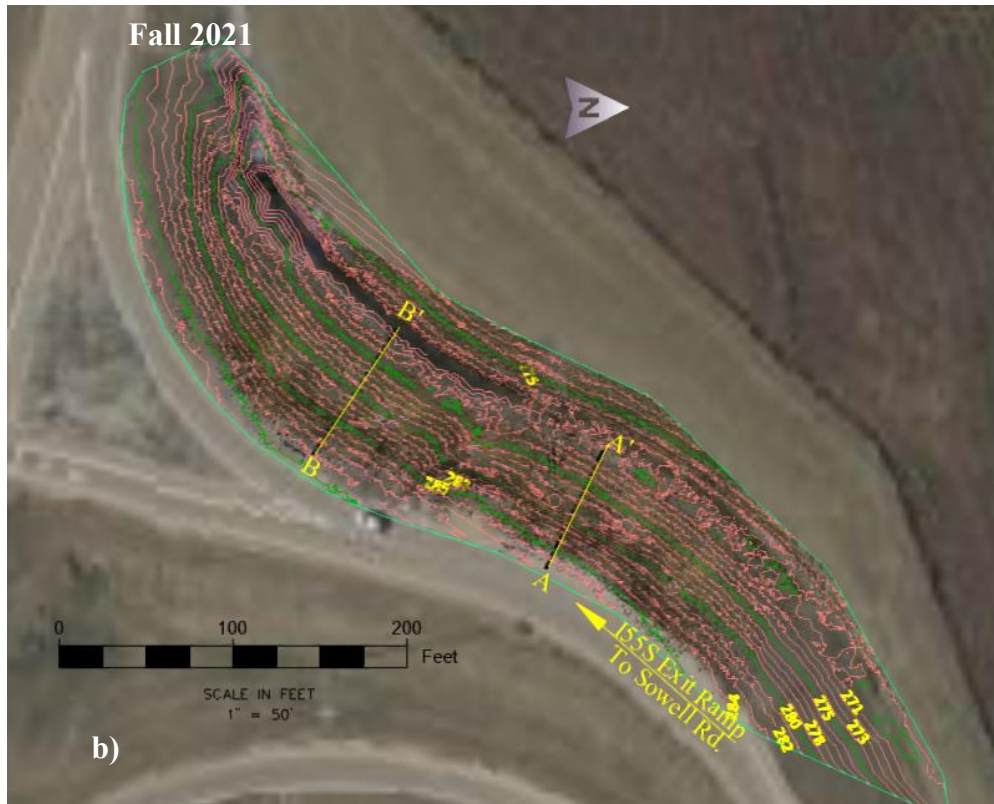
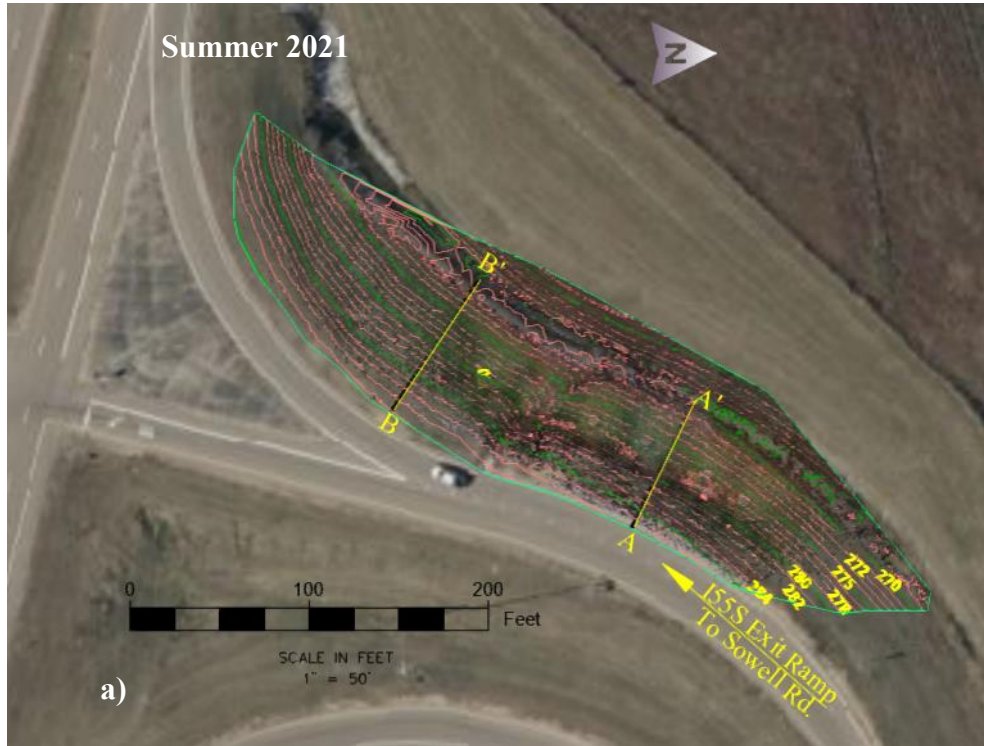


Figure 4.40 (Continued)

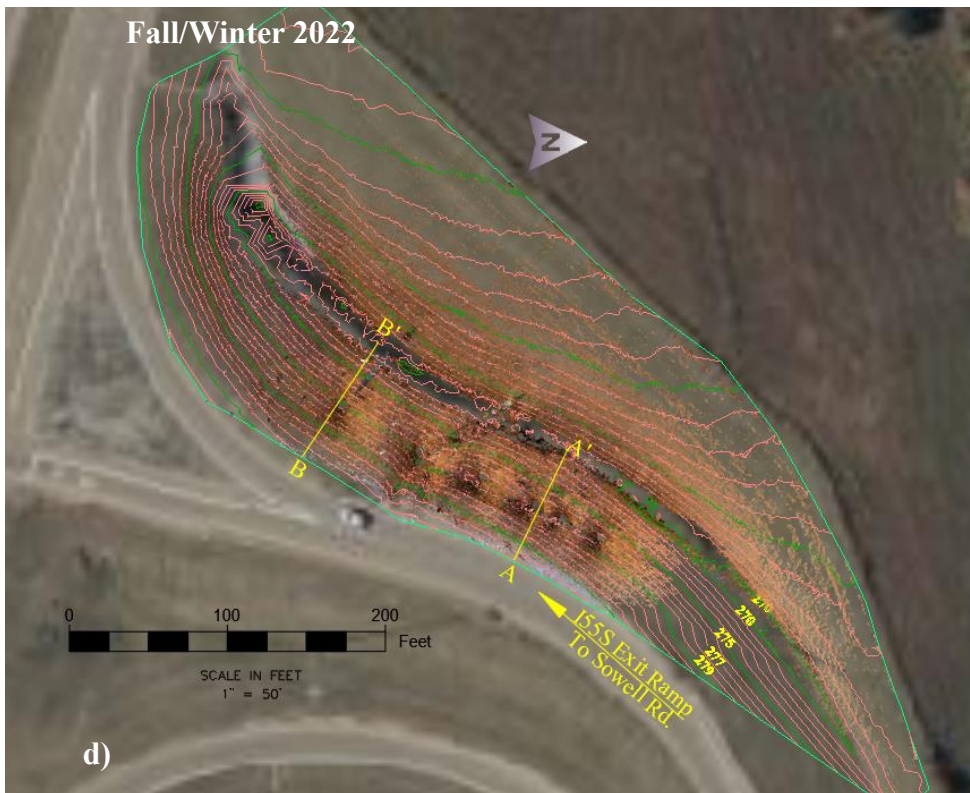


Figure 4.40 LiDAR Point Cloud Surface Topography Seasonal Variations in Slope 5: (a) Summer 2021, (b) Fall 2021, (c) Spring 2022, (d) Fall 2022

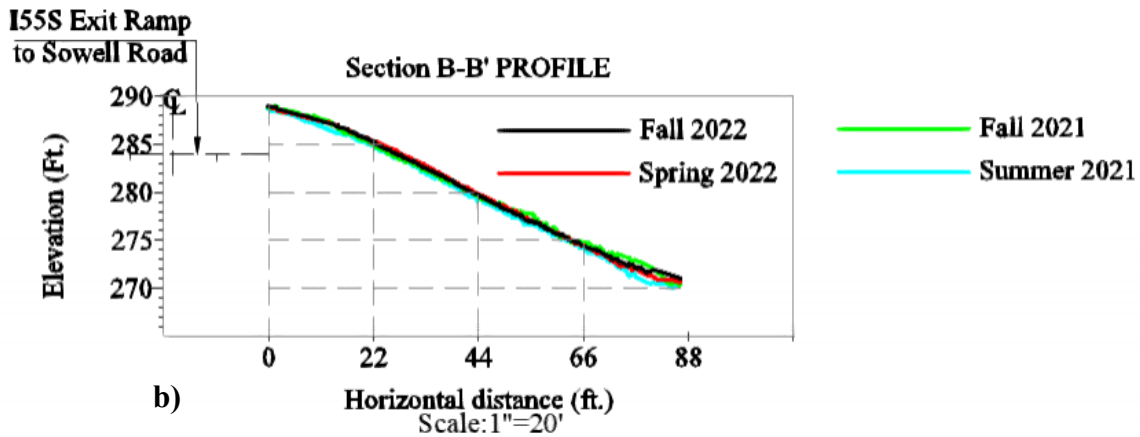
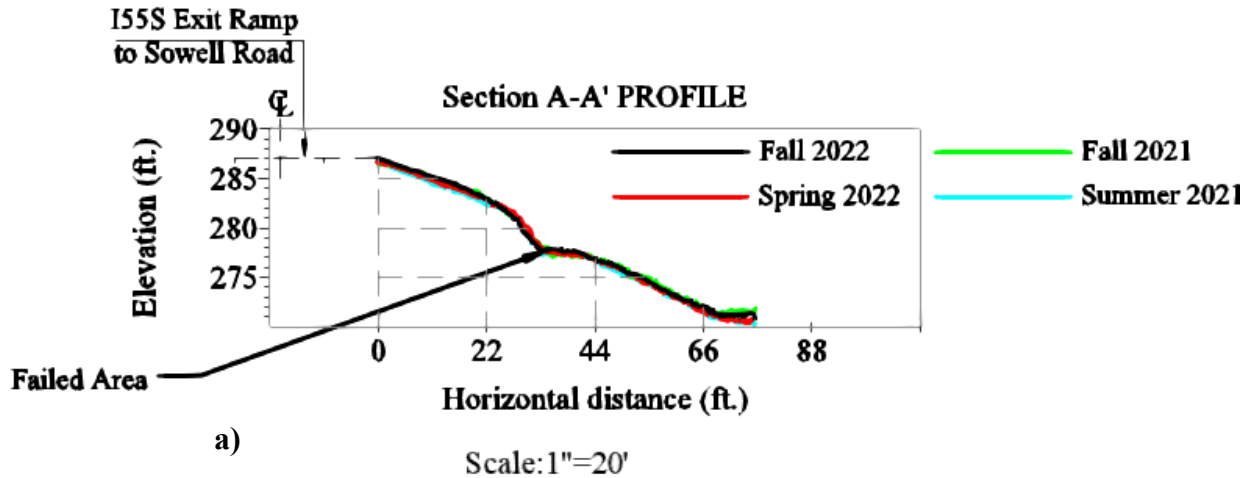


Figure 4.41 LiDAR Point Cloud Surface Profiles Seasonal Variations for Slope 5: (a) Section A-A' and (b) Section B-B'

4.1.6 Instrumented Slope 6: McRaven Road Highway Slope

4.1.6.1 ERI

An ERI test was performed for 220 feet between the crest and the middle (Lines A and B) of Slope 6. The test lines and slope location are presented in Figure 4.42. The results of the testing for Line A, performed during different seasons from spring 2021 through fall/winter 2022 are presented in Figure 4.43 (a – e). Results for Line B are presented in Figure 4.44 (a-e). The test results showed patches of high resistivity (4- Ohm-m) at shallow depths (up to 5 ft. [1.5 m]) in both Line A and Line B. These sections, shown in red, are quickly followed by a length of low resistivity between 10 ft. (3m) and 25 ft. (7.6m), indicating a high moisture zone. The resistivity increases somewhat above the 35 ft (10.7m) level, indicating that the soil is slightly less saturated at those depths.



Figure 4.42 Location of ERI Test Lines in Slope 6

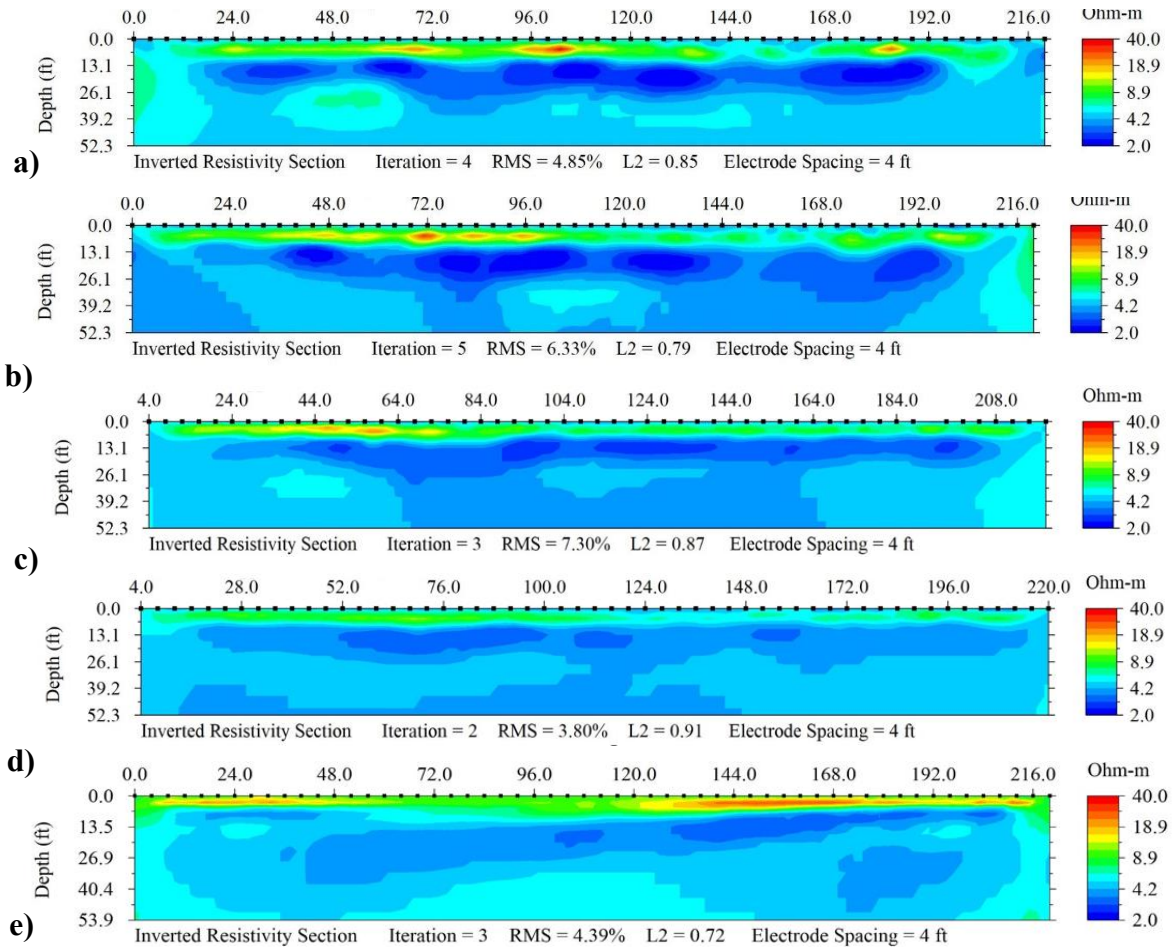


Figure 4.43 Slope 6 ERI Line A: (a) Spring 2021, (b) Summer 2021, (c) Fall 2021, (d) Winter 2021/Spring 2022, and (e) Fall/Winter 2022

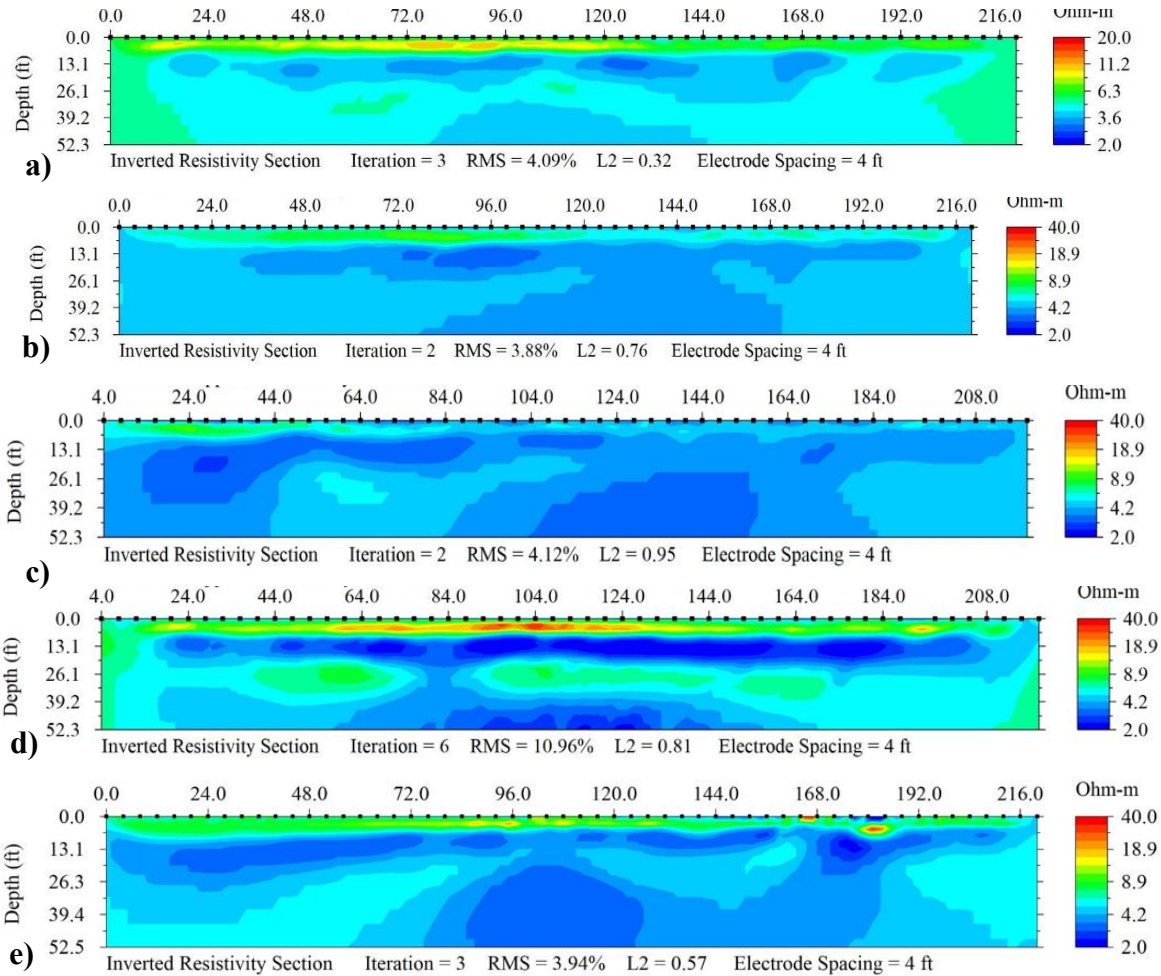


Figure 4.44 Slope 6 ERI Line B: (a) Spring 2021, (b) Summer 2021, (c) Fall 2021, (d) Winter 2021/Spring 2022, and (e) Fall/Winter 2022

4.1.6.2 Drone

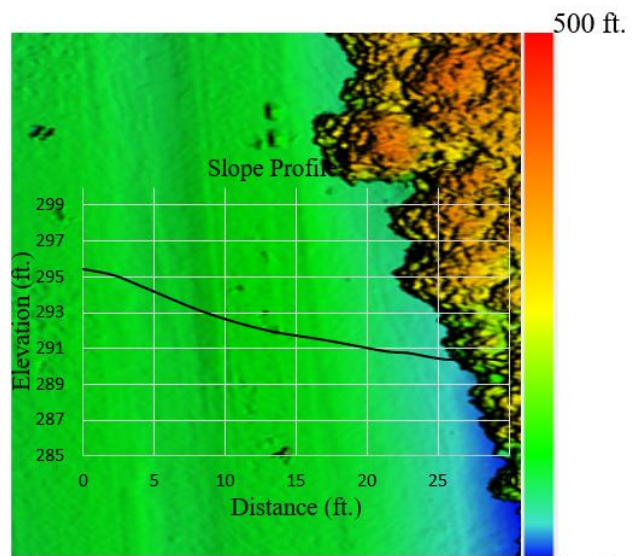
Drone surveys were conducted during the various seasons from summer 2021 through fall 2022, and the aerial imagery captured was processed using specialized software. The coordinates for the imagery were set to the State Plane Coordinate System Mississippi US-West. Aerial triangulation was performed with multiple tie points to stitch the images together and develop a digital elevation model (DEM), digital terrain model (DTM), and mosaics. The DEM and orthomosaic digital image representations are presented in Figure 4.415 to Figure 4.47.

The profile views of the slope were developed using two methods. The elevations were extracted, and a profile was created manually for the imagery captured in summer 2021, as shown in Figure 4.41. A georeferenced DEM was imported into Civil 3D for the imagery collected in fall/winter 2022, and the surface was created using the kriging interpolation method. Then, a surface profile was created along the slope, using the alignment and surface profile tools in Civil 3D. Figure 4.437 (b) & (c) show the 3D model of the slope and the surface profile views for fall/winter 2022. The orthomosaic failed for spring 2022 and could not be included in this report.

Summer 2021



3D Digital Model



Digital Elevation Model

Figure 4.45 Drone Image of Slope 6 (Summer 2021)

Fall 2021

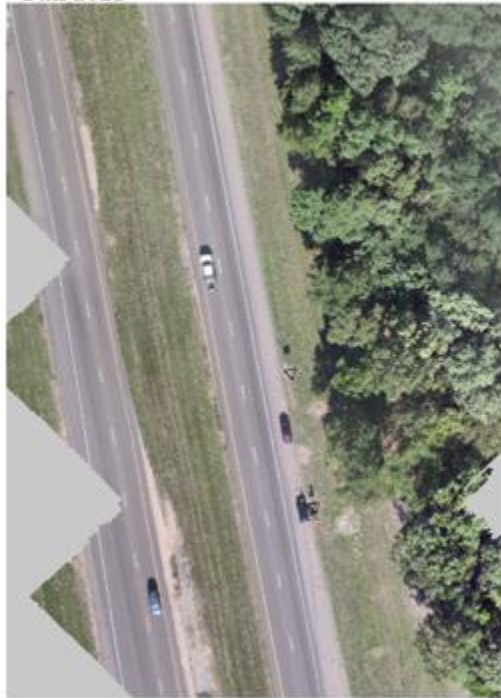
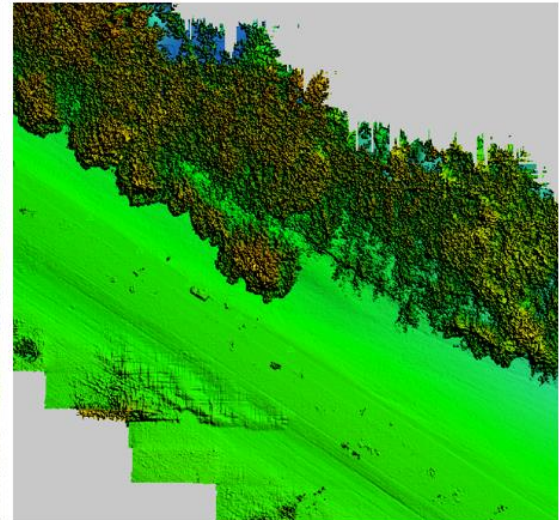


Figure 4.46 Drone Image of Slope 6 (Fall 2021)

Fall/Winter 2022



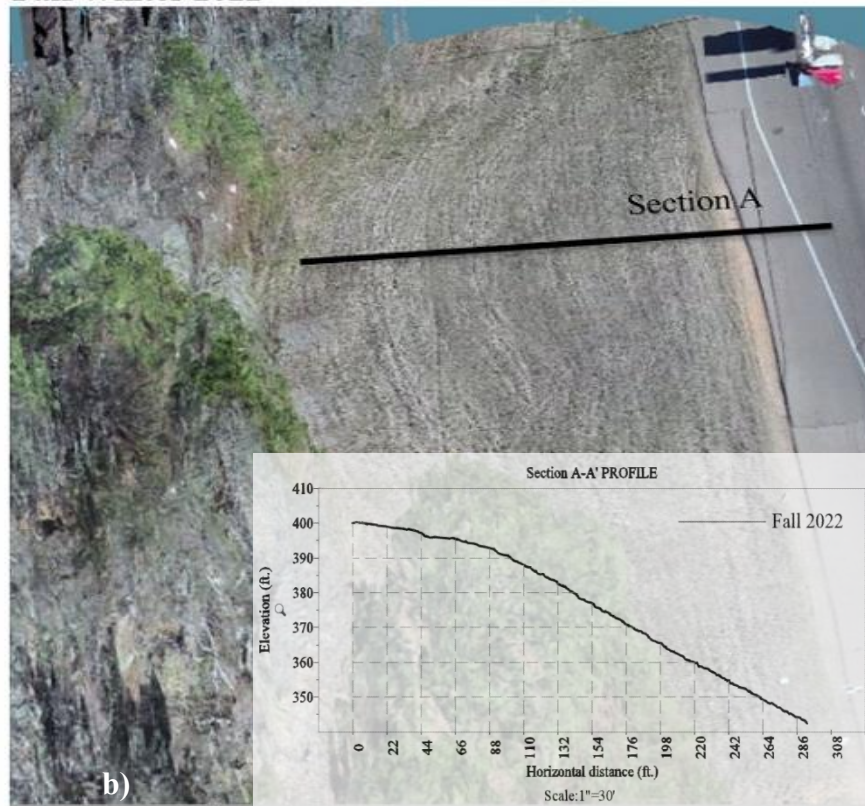
a) 3D Digital Model



Digital Elevation Model 358 ft. 486 ft.

Fall/Winter 2022

3D Model



b)

Figure 4.47 (Continued)

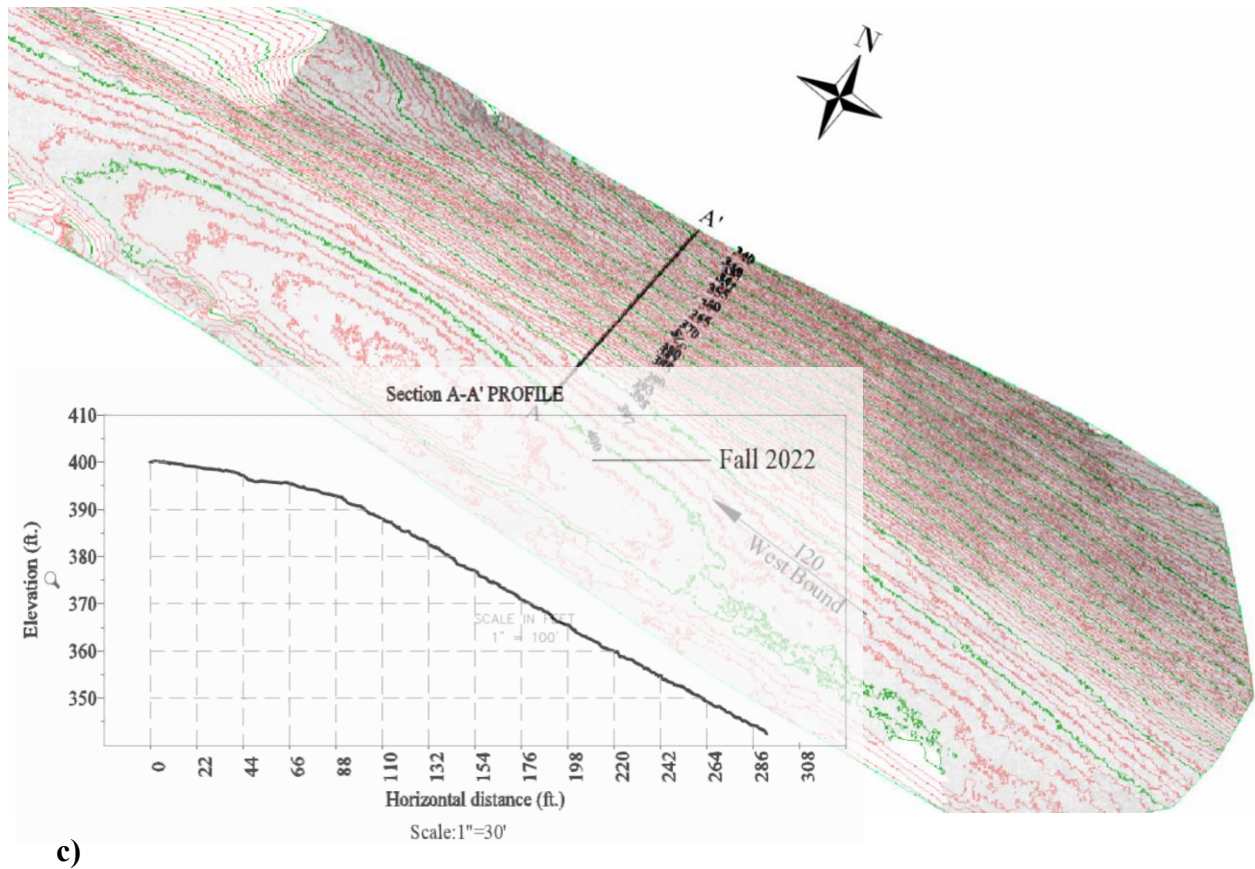


Figure 4.47 Drone Images of Slope 6 (Fall/Winter 2022): (a) Digital Elevation Model, (b) 3D Model & Surface Profile, (c) Surface Topography & Profile

4.1.6.3 LiDAR

Topography and profile views of Slope 6 developed from the terrestrial LiDAR scanning data collected during different seasons from summer 2021 through fall/winter 2022 are presented in Figure 4.448. Laser scanning was performed at several stations to collect point cloud data, which was then processed on a computer and registered to form a single point cloud. The combined point cloud was then georeferenced using field ground control points with known coordinates. Low surface points were extracted using a ground extraction algorithm to create the bare ground point clouds imported into Civil 3D. Digital elevation model surfaces were generated using the kriging interpolation method. Topographic surface views were generated at 1 ft. major and 5 ft. minor contour intervals and are presented in Figure 4.448 (a-d).

Surfaces from all seasons were overlaid, and alignments were created along the slope. Stacked surface profiles were then created using the alignments along Sections A-A' and B-B' and presented in Figure 4.49 (a) & (b). Minor elevation changes were observed on the slope surface, with more pronounced ones appearing at the toe of the slope along both profile sections. A comparison between the DEMs generated by drone images and LiDAR point cloud for I-slope 6 is presented in Figure 4.50. Although the drone DEM provides good results for the surface elevations, terrestrial LiDAR scanning provides substantially better results for the surface elevation variation and surrounding features, such as trees and signposts.

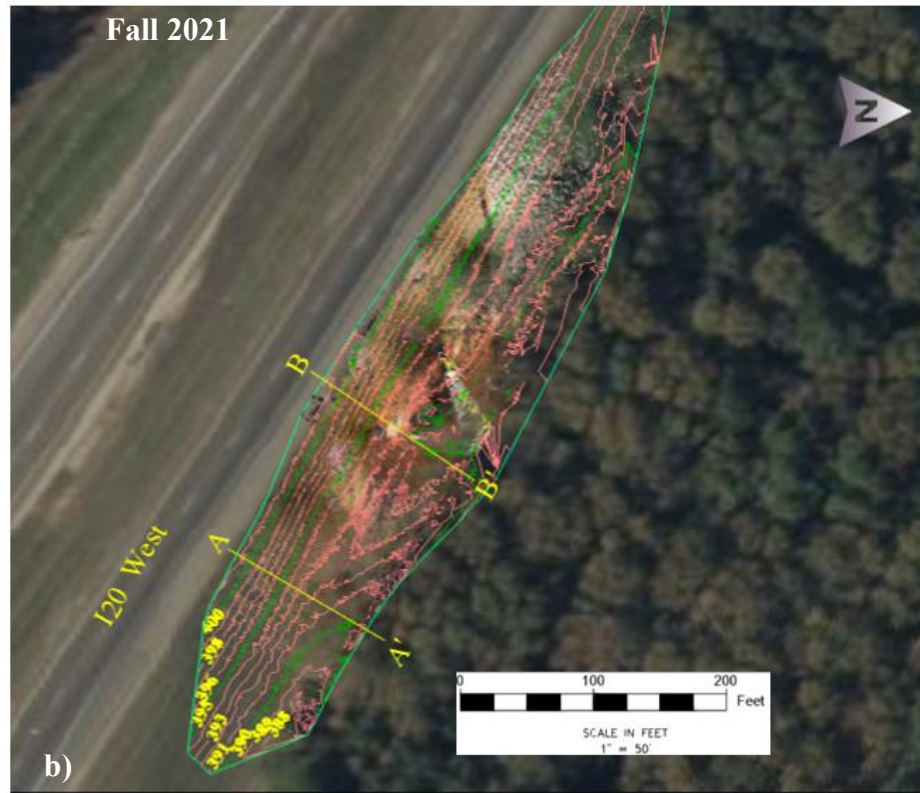


Figure 4.48 (Continued)

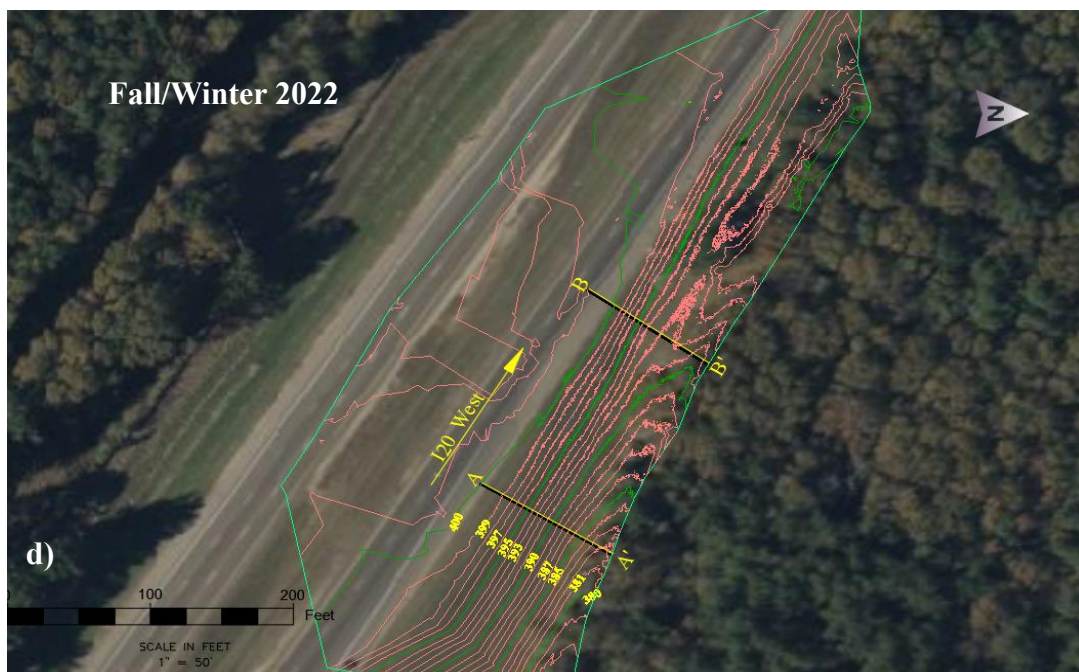
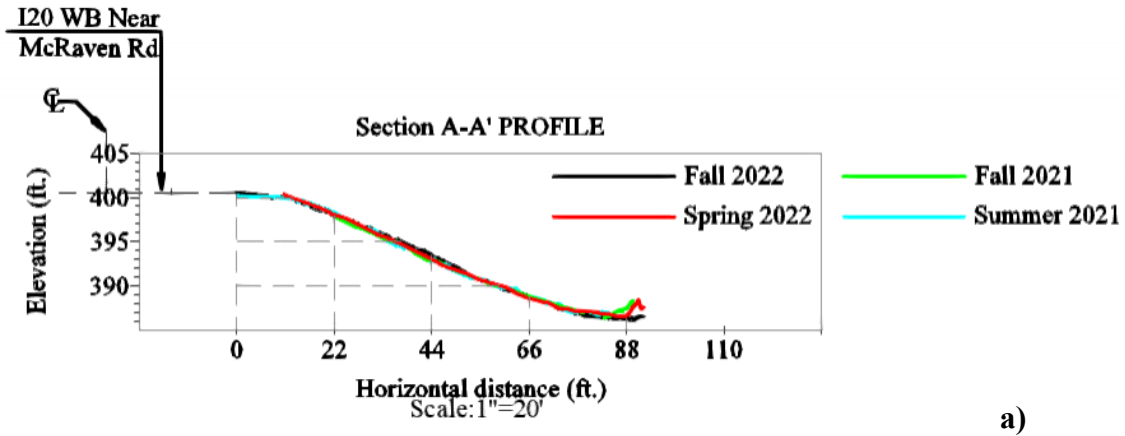
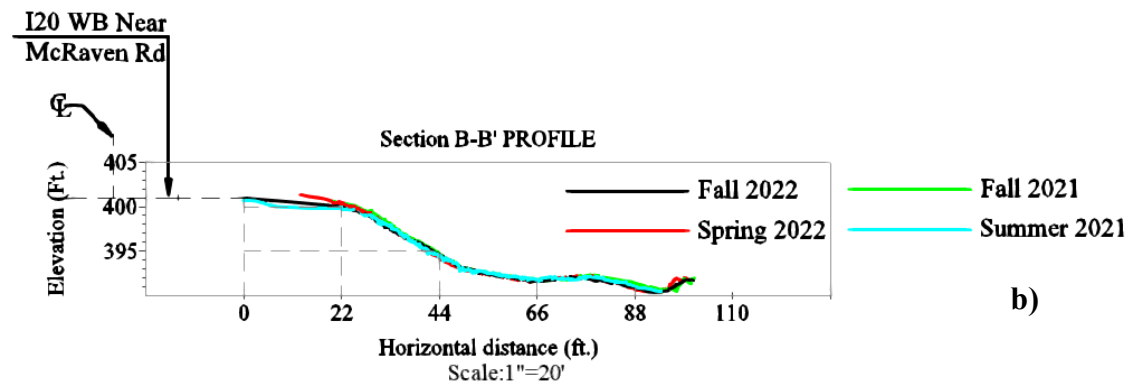


Figure 4.48 LiDAR Point Cloud Surface Topography Seasonal Variations of Slope 6: (a) Summer 2021, (b) Fall 2021, (c) Spring 2022, and (d) Fall/Winter 2022



a)



b)

Figure 4.49 LiDAR Point Cloud Surface Profiles of Seasonal Variations in Slope 6: (a) Section A-A', (b) Section B-B'

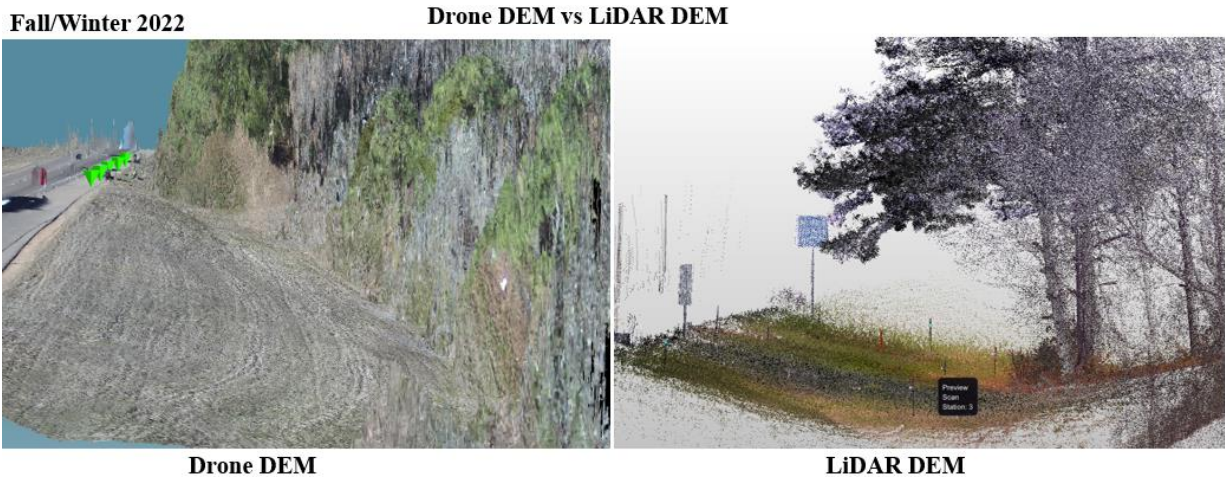


Figure 4.50 Drone 3D Model and LiDAR 3D Model of Slope 6

4.2 Advanced Evaluation of the Failed Slope Sites

4.2.1 Failed Slopes Site Selection

A list of all the failed site slopes with their slope coordinates is presented in Table 4.2 and the location of each is presented on a map in Figure 4.51.

Table 4.2 Location of Failed Highway Slopes

Slope #	Failed Slope Names	Slope Coordinates
1	Not Used	
2	I-20 Slide repair near exit 100	32.329587° -89.295857°
3	SR 25 Southbound 1.0 mile north of the Rankin/Scott Co Line	32.556351° -89.756880°
4	SR 25/43 interchange	Slope along SR25 SB
		Left Abutment
		Right Abutment
5	Black River	Section 1
		Section 2
		Section 3
6	Metrocenter ERI Test Site	32.302328° -90.246606°
7	US 49 South Slope	32.767579° -90.372679°
8	178 Union Slide	34.426984° -88.947275°
9	Dogwood	32.341764° -90.057848°
10	US 49 North Slope	32.791746° -90.371784°
11	Not Used	
12	Big Black River I20 Eastbound Slope	32.351763° -90.622673°
13	US 51 South near Gallatin St.	32.277564° -90.193766°
14	US 49 Slope in Simpson County (Vetiver site)	31.700006° -89.615546°
15	Slope Along US 27	32.092452° -90.618008°
16	SR 13 NB Approx 500 Feet North of SR 481 Along Eastern 3:1 Fill Slope of the NB Lane – Not used	32.358823° -89.668809°
17	I-20 EB Approx 1 Mile E of SR 481 East of MP 81 Along Mainline Inside Slope	32.319949° -89.598560°
18	I-55 NB Exit Ramp at Wynndale Rd Interchange Along Outside Backslope	32.130873° -90.287300°
19	Mannsdale Rd HW 463 NB (Madison Site)	32.497542° -90.180010°
20	Mannsdale Rd HW 463 SB (Madison Site)	32.497387° -90.180216°

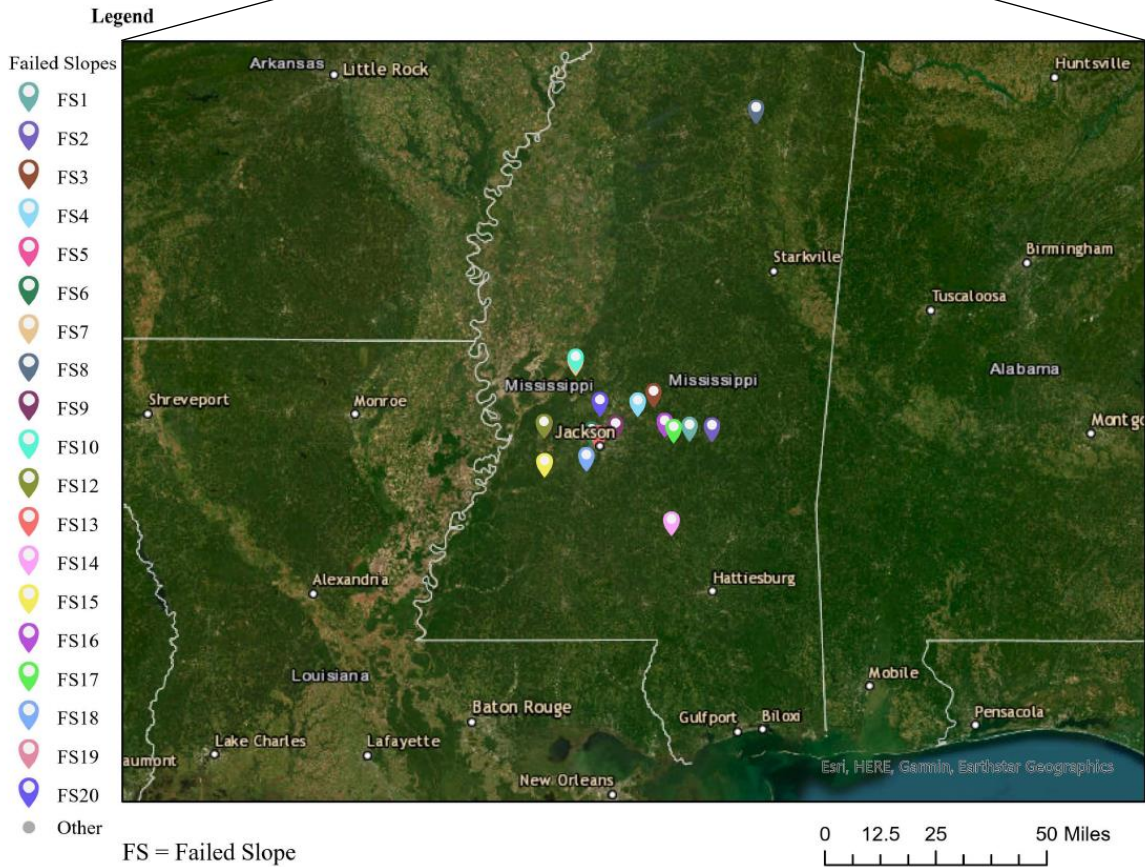


Figure 4.51 Geo-location of Failed Slopes

4.2.2 Failed Slope 2: I-20 Slide Repair Near Exit 100

4.2.2.1 ERI

An ERI test was performed for failed Slope 2, along two lines spanning 270 feet between the crest and the middle (Lines A and B). The test lines and slope location are presented in Figure 4.52. The results for Lines A & B presented in Figure 4.53 (a) & (b) for summer 2021 show that low resistivity areas exist below 8 ft. of depth, indicating wet soil along the whole span, likely caused by rainfall infiltration. The resistivity increases somewhat at 35 ft. (10.7 m), indicating that the soil is slightly less saturated at those depths.



Figure 4.52 Location of Failed Slope 2

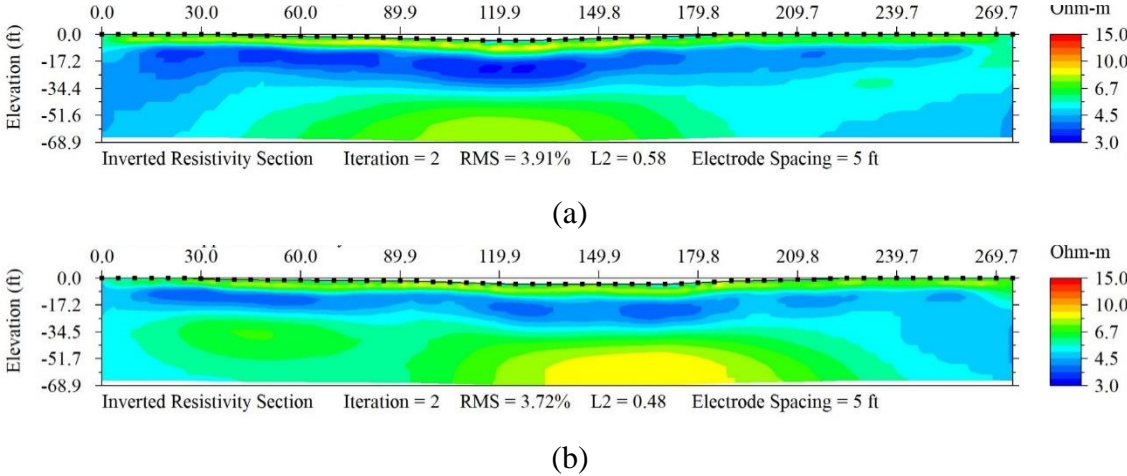


Figure 4.53 ERI Test Results of Failed Slope 2: (a) Line A and (b) Line B

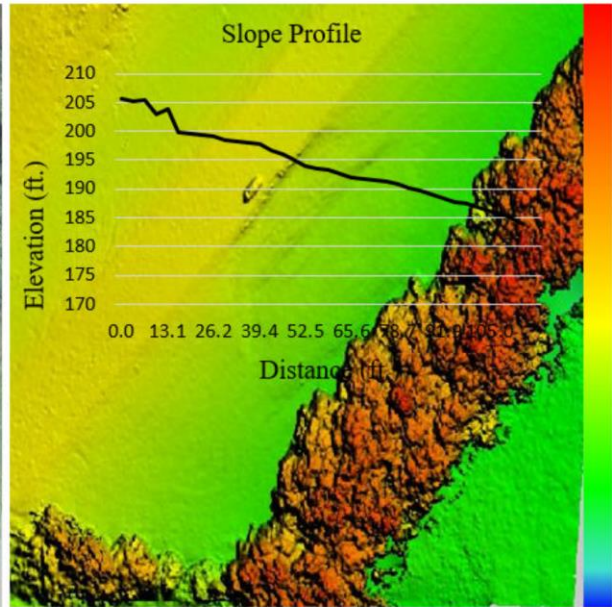
4.2.2.2 Drone

A drone survey of failed Slope 2 commenced in summer 2021, and the aerial imagery captured by the drone was processed using specialized image processing software. Aerial triangulation was performed with multiple tie points to stitch the images together and develop a digital elevation model (DEM), digital terrain model (DTM), and mosaics. DEM and orthomosaic digital image representations of the failed slope are presented in Figure 4.53. The elevations from the DEM along section A were extracted, and a profile was created manually, as shown in Figure 4.54.

Summer 2021



3D Digital Model



Digital Elevation Model

145.7 ft.

Figure 4.54 Drone Images of Failed Slope 2

4.2.2.3 LiDAR

Laser scanning was performed at several stations, and the overlapping point cloud data were collected. The collected point clouds were then post-processed on a computer and registered together to form a single point cloud. The combined point cloud was then georeferenced using field ground control points with known coordinates. Using a ground extraction algorithm, low surface points were extracted to create the bare ground point clouds. The bare ground point cloud was processed in Civil 3D. The topographic surface view was generated at 1 ft. major and 5 ft. minor contour intervals and is presented in **Figure 4.55(a)**. Using alignments created on the surface, a surface profile view was generated along section A-A, as presented in **Figure 4.55 (b)**.

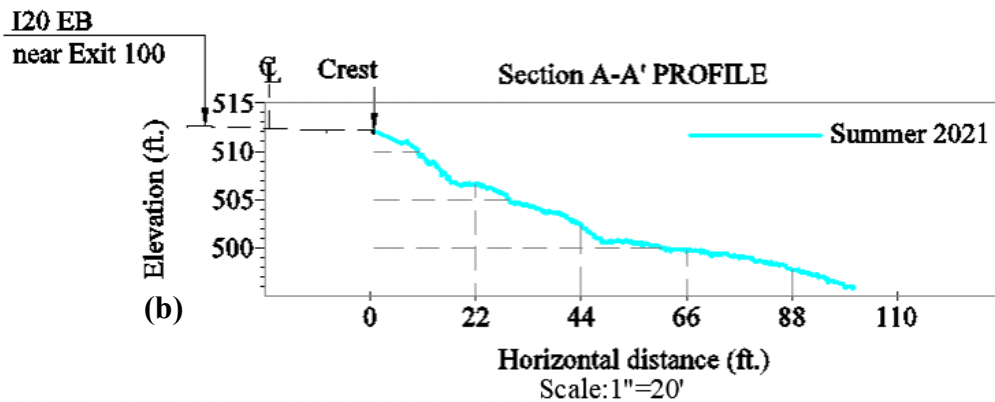
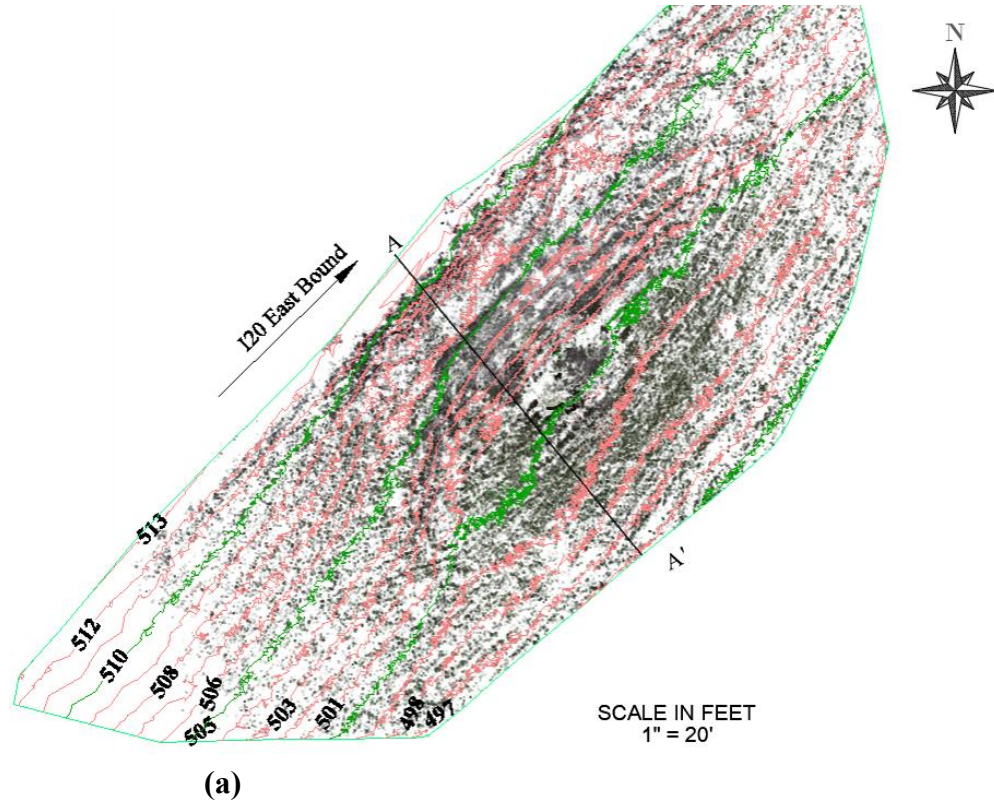


Figure 4.55 Failed Slope 2: (a) Surface Topography and (b) Surface Profile

4.2.3 Failed Slope 3: SR 25 Southbound 1.0-mile North of the Rankin/Scott Co Line

4.2.3.1 ERI

An ERI test for failed Slope 3 was conducted along two lines spanning 220 feet at the crest and middle (Lines A and B). The test line and slope location are presented in Figure 4.56. The results of the test conducted in summer 2021 for Lines A & B are presented in Figure 4.57 (a) & (b). At Line A, the results indicated that soil deformation exists at the shallow levels, at

horizontal distances of 52 ft., 78 ft., 100 ft., and 148 ft. Just below the deformations, there are wet zones that are perched water zones formed most likely due to surface water infiltration through deformed soil. A similar phenomenon was also observed at the middle of the slope (Line B), where surficial deformations are followed by perched water zones, but to a lesser degree than those found in the crest of the slope.



Figure 4.56 ERI Location in Failed Slope 3

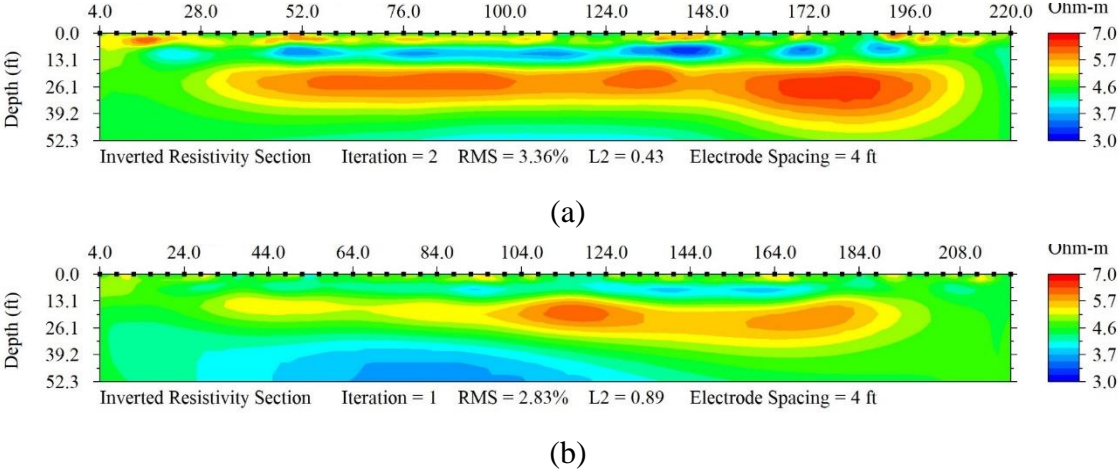


Figure 4.57 ERI Test Results of Failed Slope 3

4.2.4 Failed Slope 4: SR 25/43 Interchange.

4.2.4.1 ERI

In the summer of 2021, an ERI test was conducted for failed Slope 4 at three locations: along the slope of SR25 southbound, and along the left and right bridge abutments of the SR25/43 interchange. On the slope of SR25 southbound, the test was done along three lines spanning 323 feet at the crest, middle and toe of the slope (Lines A, B and C). The test lines and slope location

are presented in Figure 4.58, and the results are presented in Figure 4.59 (a) and (b). The highest level of wet soil below 15 ft. depth is in Line B. Between 144 and 179 ft. horizontal distance, the soil deformation is clear by the sag in the resistivity profile. At the middle line (4.58 (b)), the high resistivity at the surficial level at the 144' horizontal distance indicates soil deformation. Lines A and C also show high resistivity zones at the surficial level, followed by low resistivity zones at depths under 15 ft., indicating the presence of wet soil.

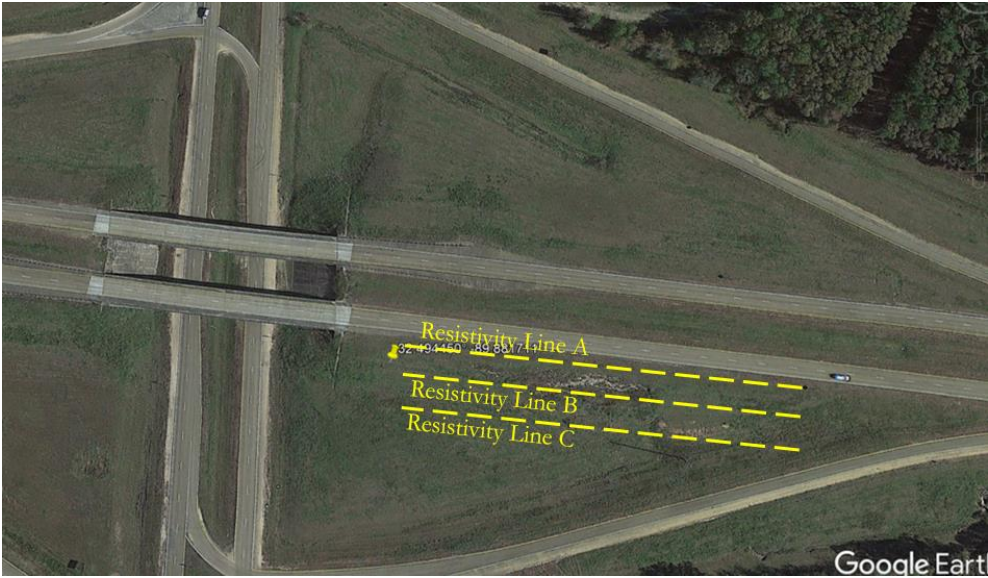


Figure 4.58 Failed Slope 4: Slope along SR25 SB SR 25/43 Interchange

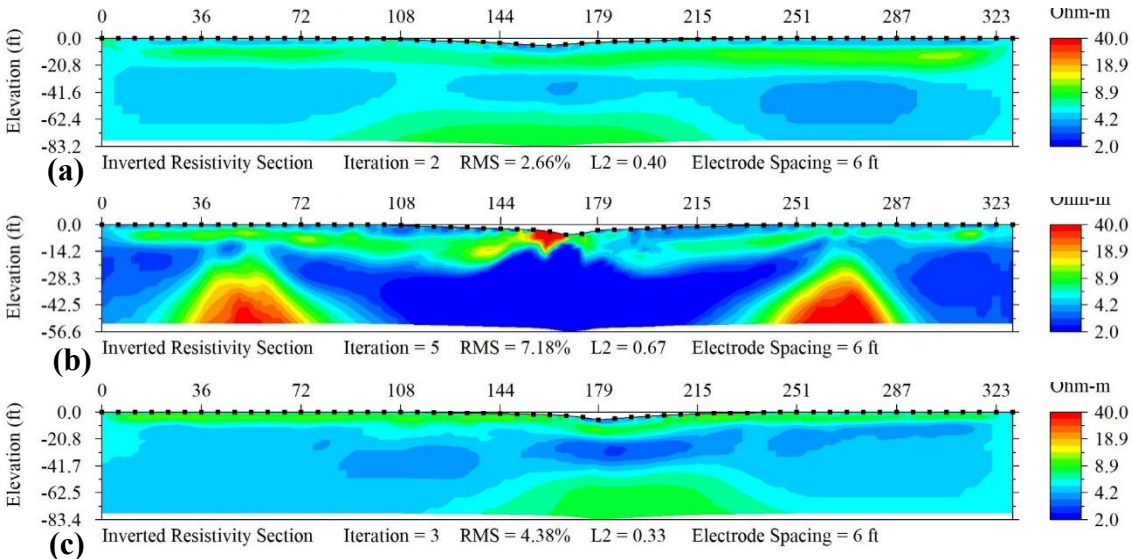


Figure 4.59 ERI Test Results of Failed Slope 4 -Slope along SR25 SB: (a) Line A, (b) Line B, (c) Line C

Left Abutment: The ERI test was performed along two lines spanning 81 ft. (Lines D and E) at the left bridge abutment. The ERI test lines and slope location are presented in Figure 4.60; the results for Lines D & E are presented in Figure 4.61 (a) & (b).



Figure 4.60 Location of ERI Lines at Failed Slope 4 - SR25/43 Interchange Left Abutment

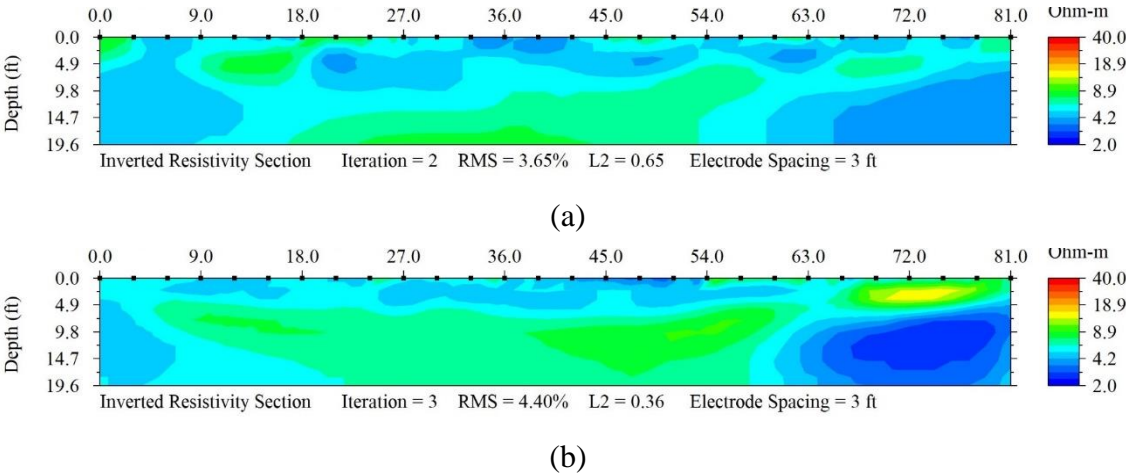


Figure 4.61 ERI Test Results of Failed Slope 4 at Left Abutment: (a) Line D and (b) Line E

Right Abutment: At the right bridge abutment of the SR25/43 interchange, the ERI test was completed along two lines spanning 81 feet (Lines F and G). The ERI test lines and slope location are presented in Figure 4.62. The results for Lines F & G are presented in Figure 4.63 (a) & (b).



Figure 4.62 ERI Test Location of Failed Slope 4- SR25/43 Interchange Right Abutment

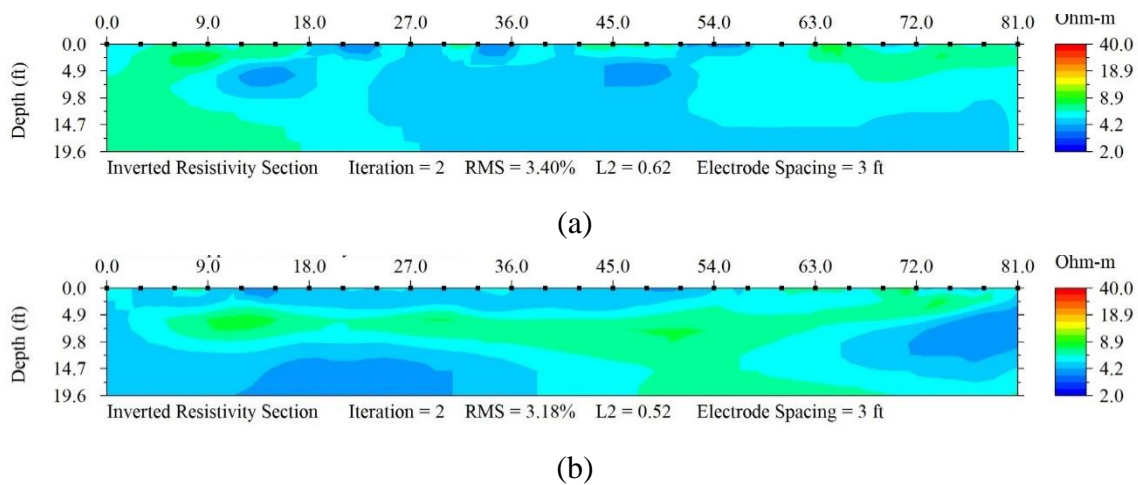


Figure 4.63 Failed Slope 4 ERI Test Results - SR25/43 Interchange Right Abutment (a) Line F and (b) Line G

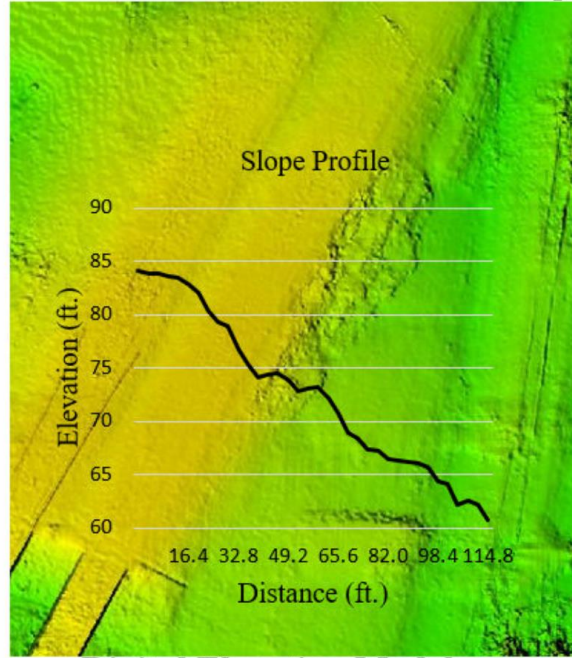
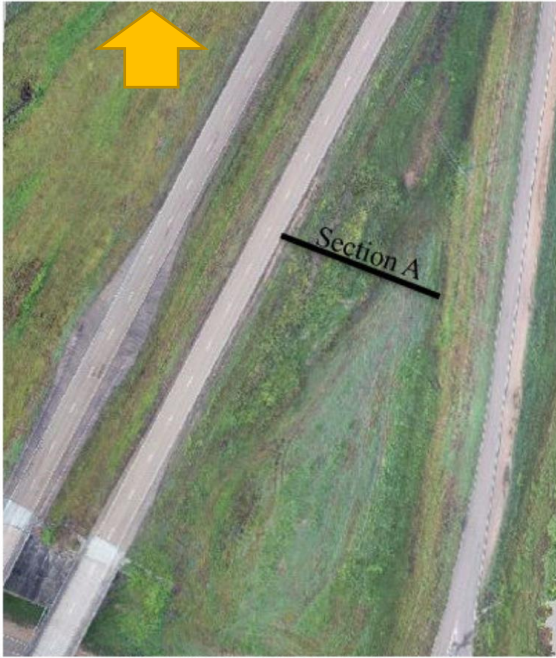
4.2.4.2 Drone

In summer of 2021, a drone survey mission commenced at three locations: along the slope of SR25 southbound, and along the left and right bridge abutments of the SR25/43 interchange. The aerial imagery captured by the drone was processed using specialized image processing software. Aerial triangulation was performed with multiple tie points to stitch the images together and develop a digital elevation model (DEM), digital terrain model (DTM), and mosaics. The elevations along Section A of the DEM were extracted, and surface profile views were manually created. DEM and orthomosaic 3D digital image representations of the failed slope are presented in Figure 4.64 (a-c). The slide failure along SR25 southbound is presented in Figure 4.64 (a); failures of the left and right bridge abutments of the SR25/43 interchange are presented in Figure 4.64 (b) & (c), respectively.

Summer 2021

Slope Failure along HWY25

148.6 ft.



(a) 3D Digital Model

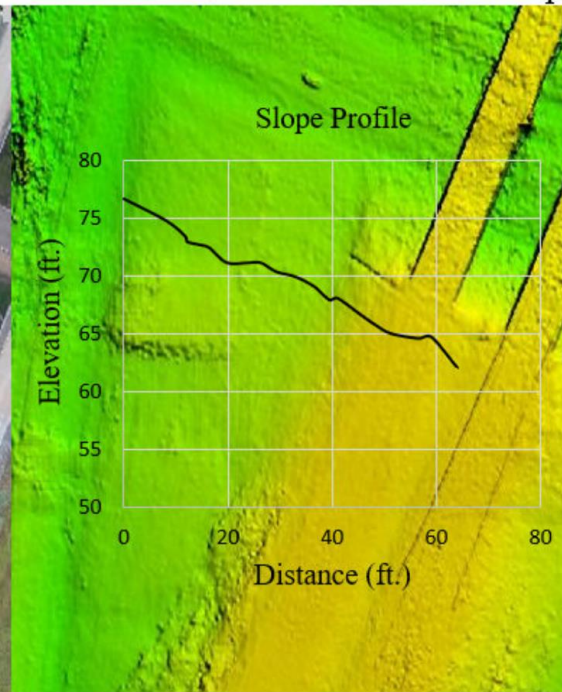
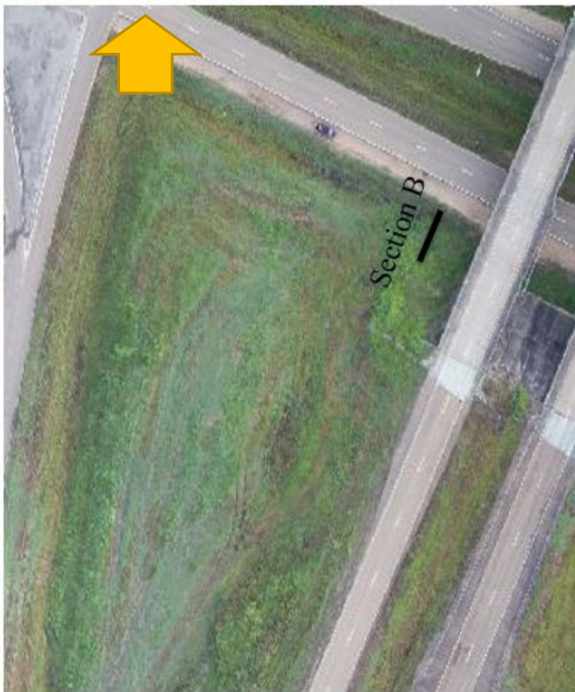
Digital Elevation Model

23 ft.

Summer 2021

HWY25/MS43 Interchange Left Abutment

148.6 ft.



(b) 3D Digital Model

Digital Elevation Model

23 ft.

Figure 4.64 (Continued)

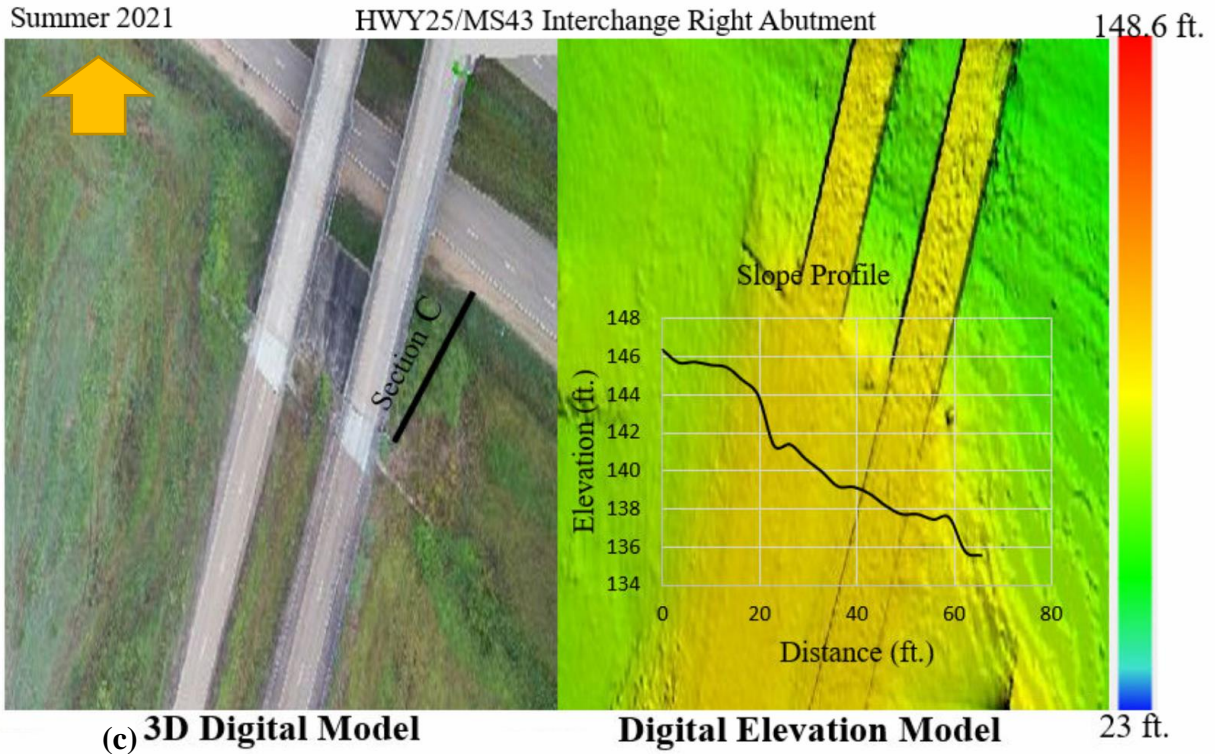
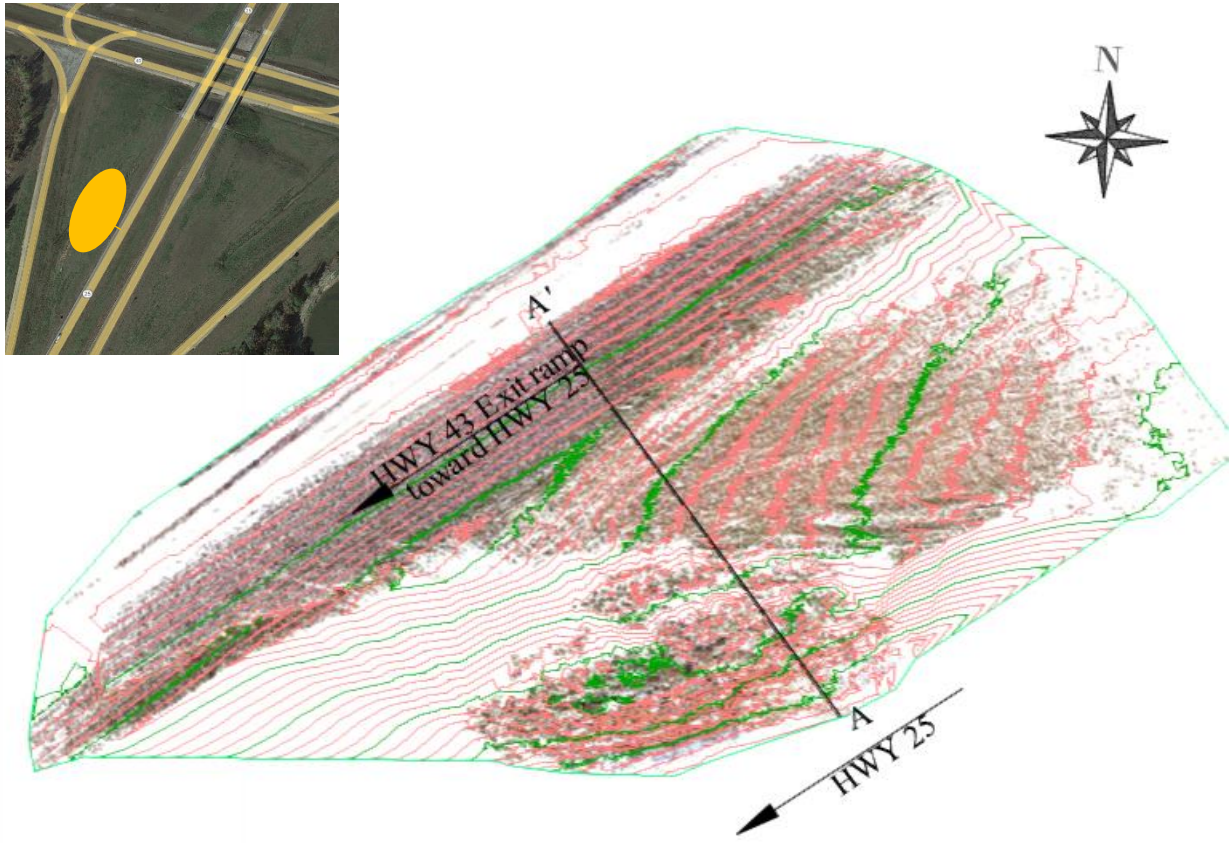


Figure 4.64 Slope 4 Failures: (a) Failure along SR25, (b) Failure of Left Abutment, (c) Failure of Right Abutment

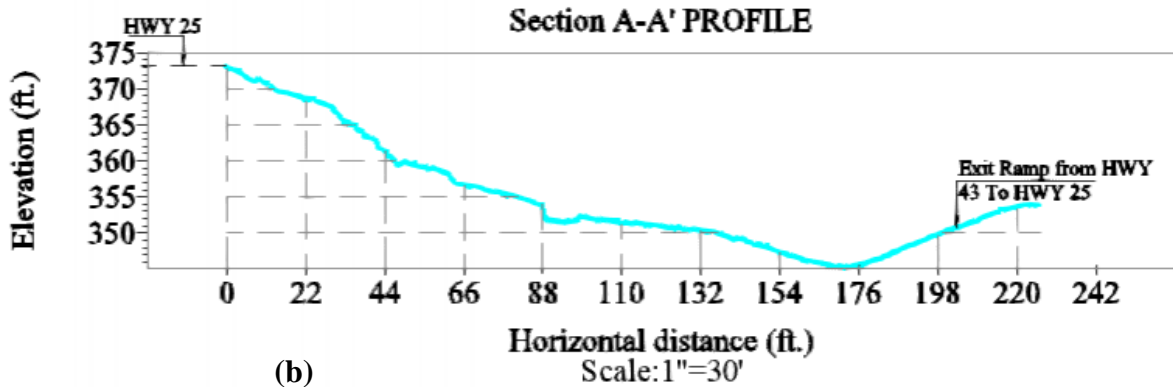
4.2.4.3 LiDAR

Terrestrial scanning was performed at three locations: along the slope of SR25 southbound and along the left and right bridge abutments of the SR25/43 interchange. The laser scanner was placed at four or five stations, and the overlapping point cloud data were collected. The point clouds were then post-processed on a computer and registered together to form a single point cloud. The combined point cloud was then georeferenced using field ground control points with known coordinates. Using a ground extraction algorithm, low surface points were extracted to create the bare ground point clouds. The bare ground point clouds for all seasons collected were imported into Civil 3D, and digital elevation model surfaces were generated using the kriging interpolation method. Topographic surface views were generated at 1 ft. major and 5 ft. minor contour intervals. The topographic and surface profile views of the SR25 slope slide failure are presented in Figure 4.65. The uneven slope surface along the failed area is clearly visible from the surface profile view in Figure 4.65 (b).



(a)

SCALE IN FEET
1" = 50'



(b)

Figure 4.65 Slope 4 Slide Failure: (a) LiDAR Point Cloud Surface Topography, (b) Surface Profile

The topographic contour view of the left bridge abutment of the SR25-43 interchange is presented in Figure 4.66 (a). The surface profile views along two lines (A-A') and (B-B') are presented in Figure 4.66 (b) & (c), respectively.

SR2543Left Abutment

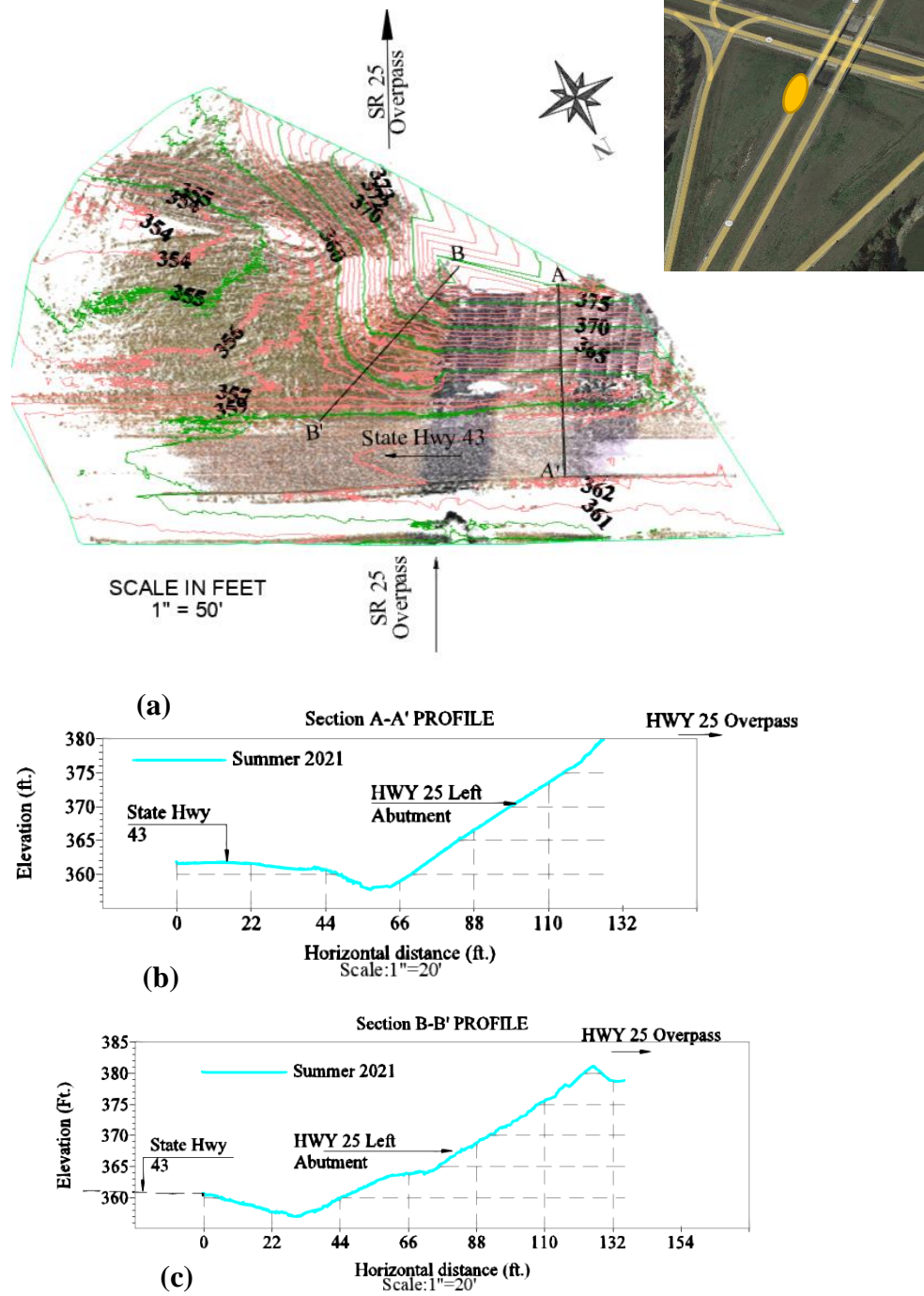


Figure 4.66 Failed Left Abutment of Slope 4: (a) LiDAR Point Cloud Surface Topography, (b) Surface Profile Section A-A', (c) Surface Profile Section B-B'

A topographic contour view of the right bridge abutment of the SR25-43 Interchange is presented in Figure 4.67 (a). A surface profile views along two lines (A-A') and (B-B') are presented in Figure 4.67 (b) and (c), respectively.

SR25/43 Right
abutment

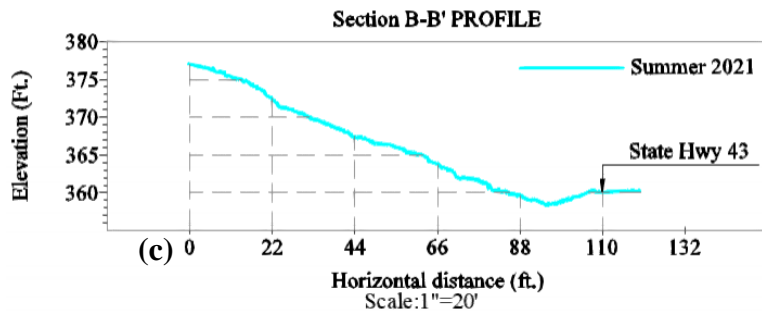
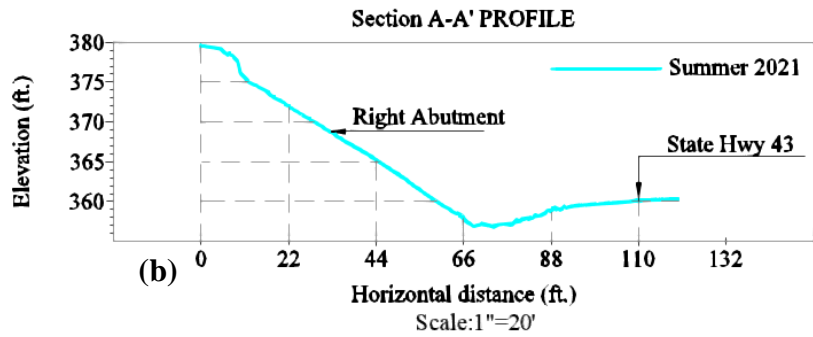
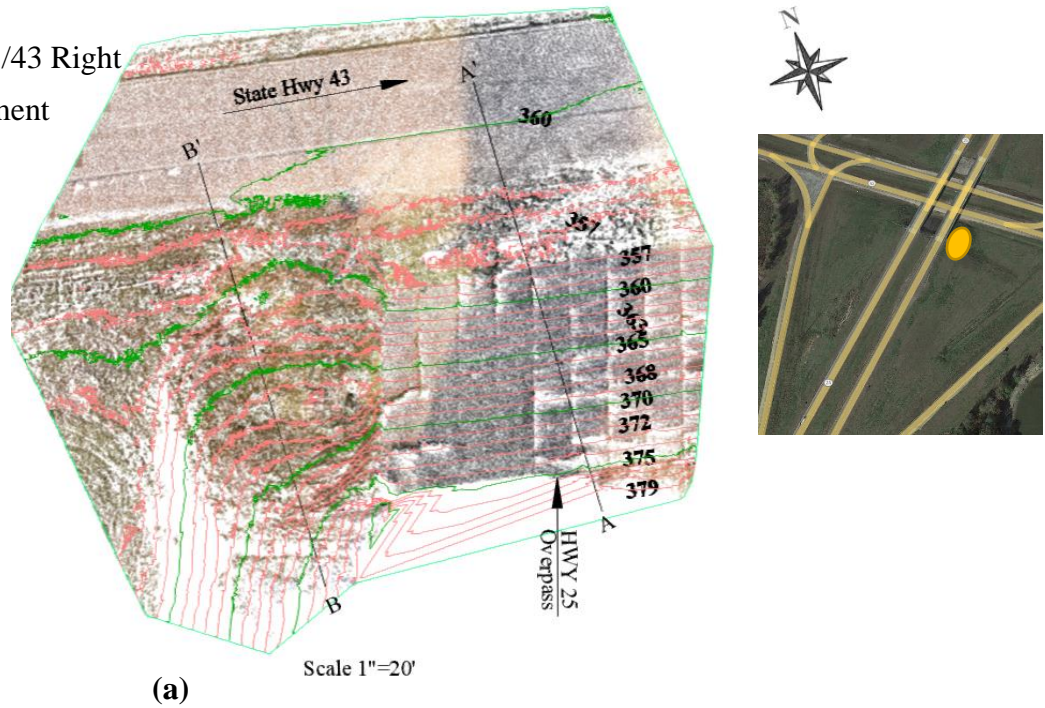


Figure 4.67 Failed Right Abutment in Slope 4: (a) LiDAR Point Cloud Surface Topography, (b) Surface Profile Section A-A', (c) Surface Profile Section B-B'

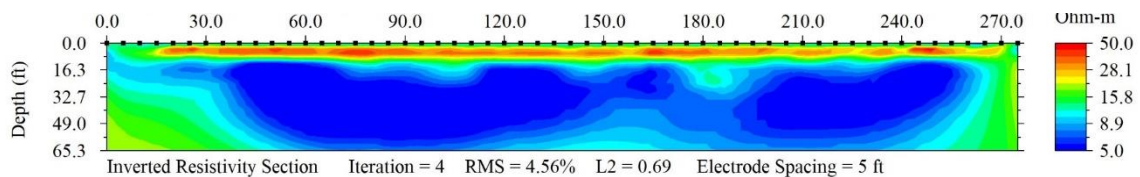
4.2.5 Failed Slope 5: Big Black River

4.2.5.1 ERI

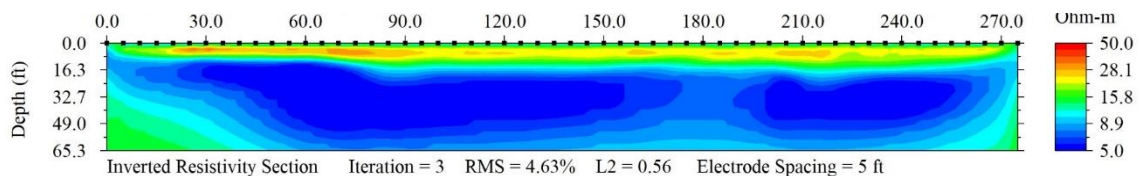
ERI tests for failed Slope 5 were carried out in the summer of 2021 at the three locations identified in Figure 4.68 as Sections 1, 2 and 3. In Section 1, the ERI test was conducted along two test lines (Lines A & B) over a span of 323 ft., and the results are presented in Figure 4.69 (a) and (b). In Section 2, the ERI test was conducted along Lines C & D over a span of 270 ft., and the results are presented in Figure 4.70 (a) and- (b). In Section 3, the ERI test was conducted along Lines E and F, over a span of 108 ft., and the results are presented in Figure 4.71 (a) and (b). The results for Sections 1 and 2 show high resistivity zones along the whole test span up to 10 ft. depth. Wet soil zones are present below the deformed soil, up to 65 ft. depth. The higher resistivity shown by the ERI profiles for Section 3 is probably because the images were taken at a depth of 26 ft. and the wet zones are below that depth.



Figure 4.68 Location of ERI Test Lines in Failed Slope 5 (Big Black River)



(a)



(b)

Figure 4.69 ERI Test Results of Section 1 of Failed Slope 5: (a) Line A, (b) Line B

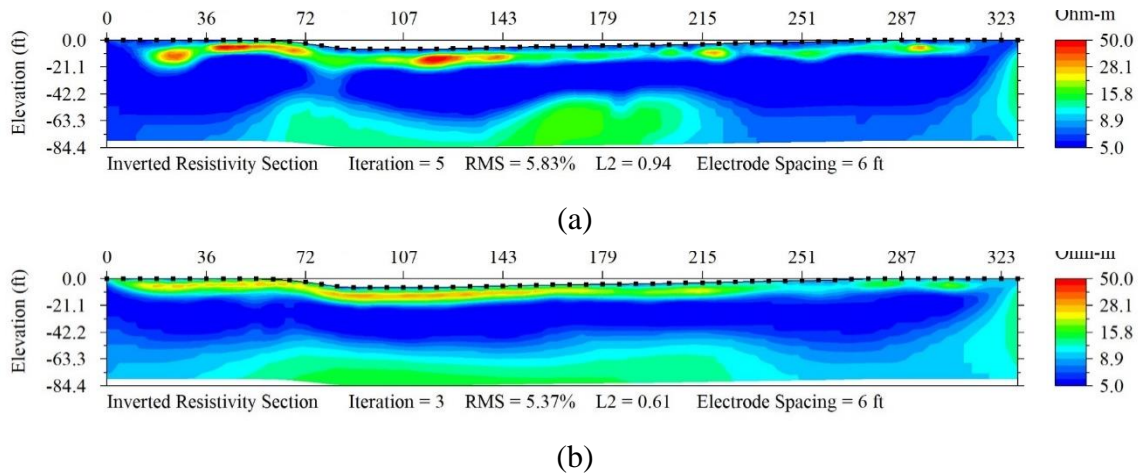


Figure 4.70 ERI Test Results of Section 2 of Failed Slope 5: (a) Line C, (b) Line D

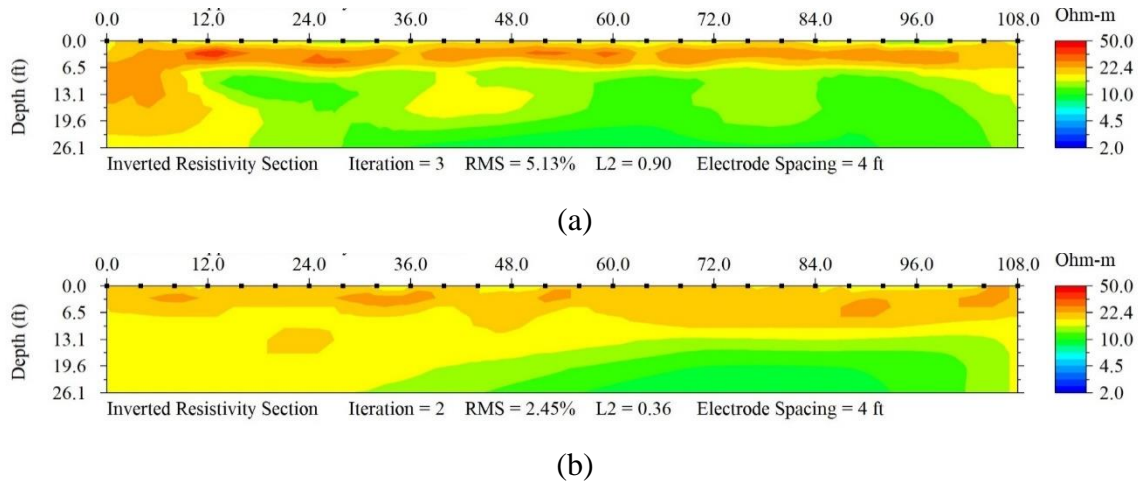


Figure 4.71 ERI Test Results of Failed Slope 5, Section 3: (a) Line E (b) Line F

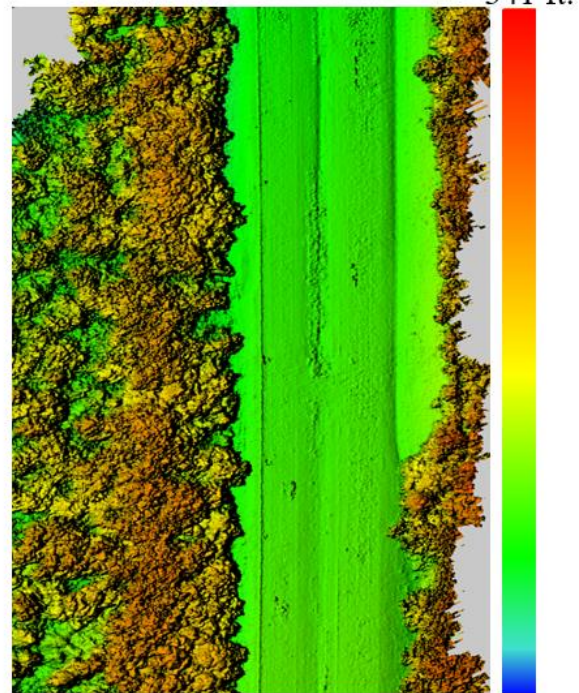
4.2.5.2 Drone

A drone survey mission was conducted for failed Slope 5 (Big Black River Slope) in the Summer of 2021 at three locations designated as Sections 1, 2 and 3 in Figure 4.6872. The aerial imagery captured by the drone was processed using specialized image processing software. Aerial triangulation was performed with multiple tie points to stitch the images together and develop a digital elevation model (DEM), digital terrain models (DTM), and mosaics. DEM was imported into Civil 3D, and the surface was created using the kriging interpolation method. Alignment along the slope was created, and a surface profile view was generated. Figure 4.72 (a) and (b) show the 3D model of the slope and the surface profile views.

Summer 2021

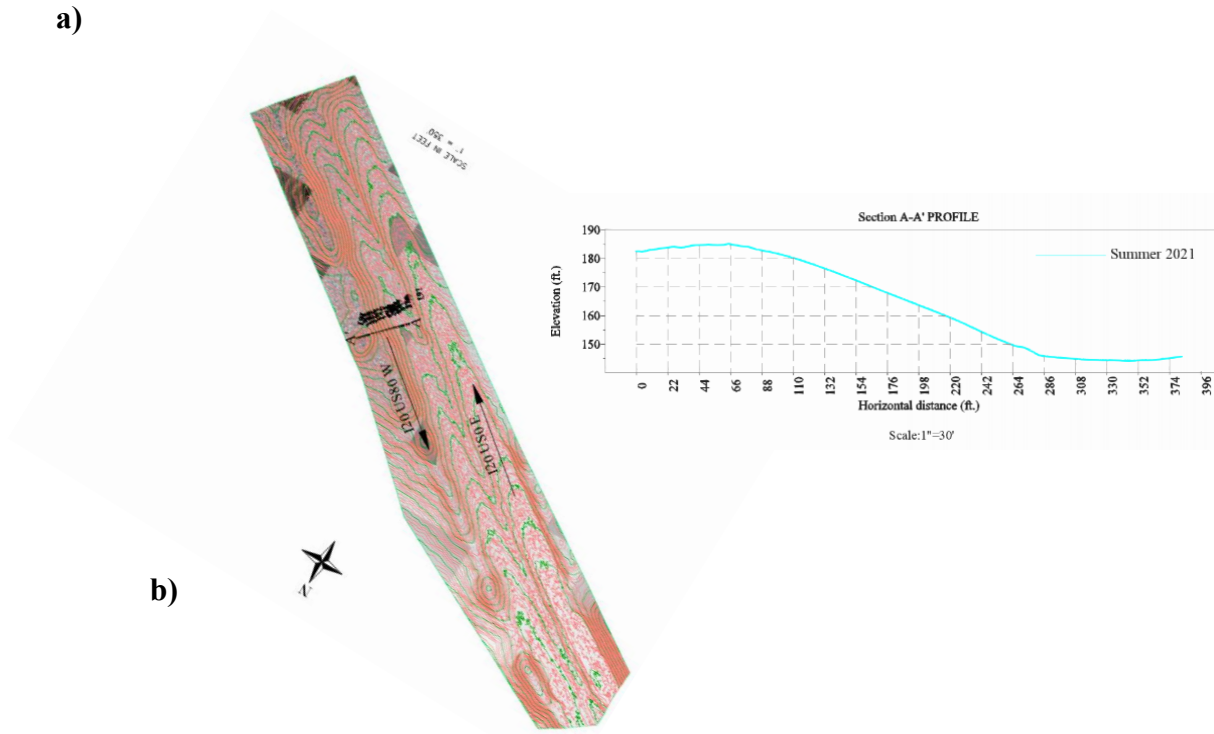


3D Digital Model



Digital Elevation Model 105 ft. 341 ft.

a)



b)

Figure 4.72 Drone Images of Failed Slope 5: (a) Digital Elevation Model, (b) Surface Topography and Profile (Summer 2021)

4.2.5.3 LiDAR

Terrestrial LiDAR scanning was performed at three locations designated as Sections 1, 2 and 3 of Slope 5, as shown in Figure 4.6873. The laser scanner was placed at four or five stations in each section of the slope, and the overlapping point cloud data were collected. The point clouds were then post-processed on a computer and registered together to form a single point cloud. The combined point cloud was then georeferenced using field ground control points with known coordinates. The low surface points were extracted to create the bare ground point clouds, using a ground extraction algorithm. The bare ground point clouds for all seasons collected were imported into Civil 3D, and digital elevation model surfaces were generated using the kriging interpolation method. Topographic surface views were generated at 1 ft. major and 5 ft. minor contour intervals, then surface profile views were generated, using alignments. The topographic and surface profile views of Section 1 of the Big Black River Slope are presented in Figure 4.73.

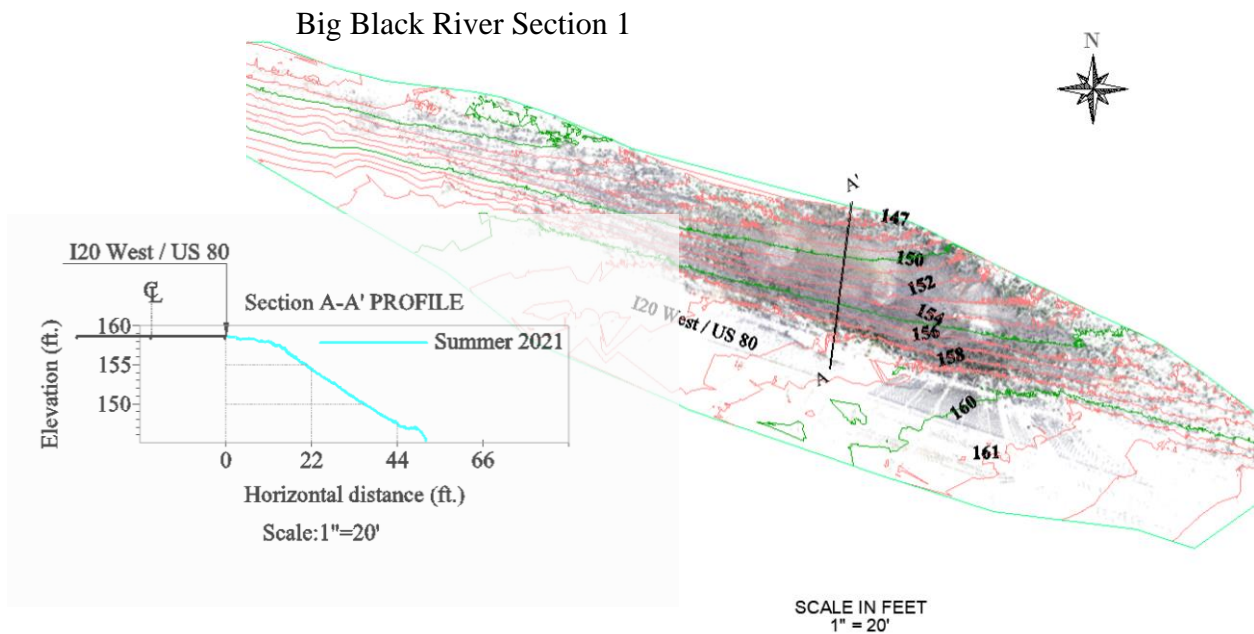


Figure 4.73 LiDAR Point Cloud Surface Topography and Profile of Section 1 of Big Black River

The topographic and surface profile views of Section 2 and Section 3 of the Big Black River Slope are presented in Figure 4.74 and Figure 4.75, respectively.

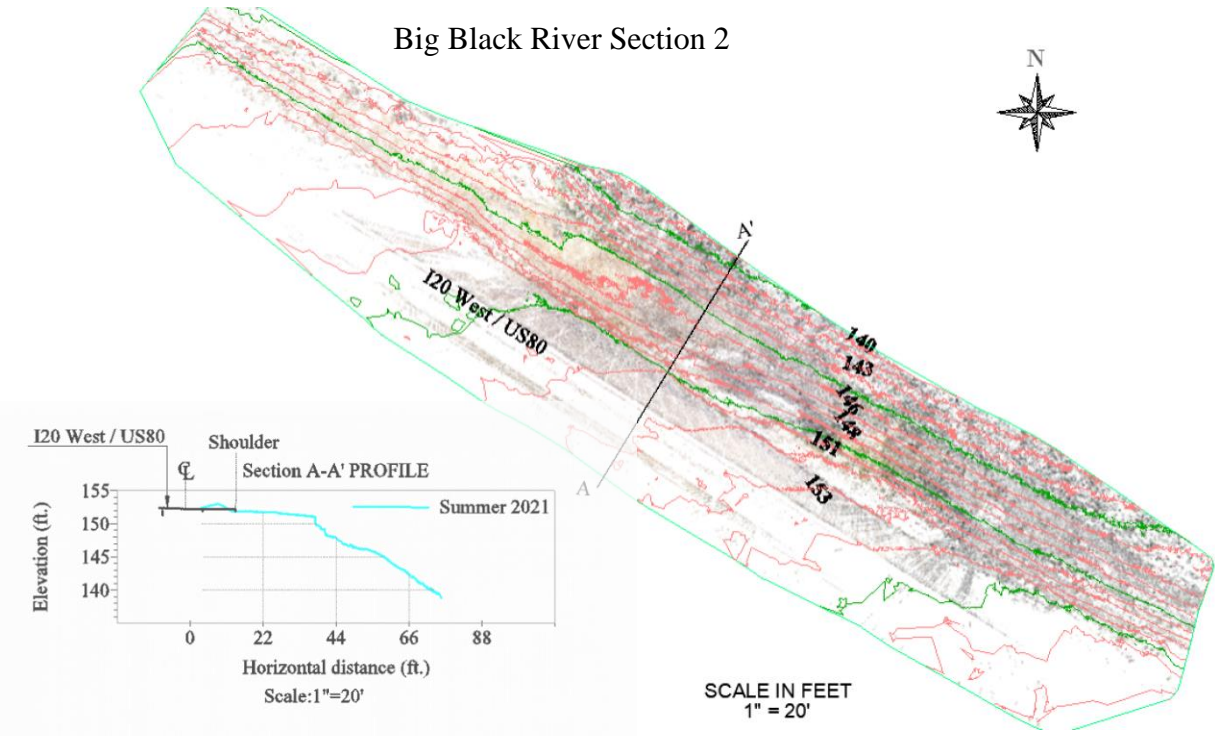


Figure 4.74 LiDAR Point Cloud Surface Topography and Profile of Section 2 of Big Black River

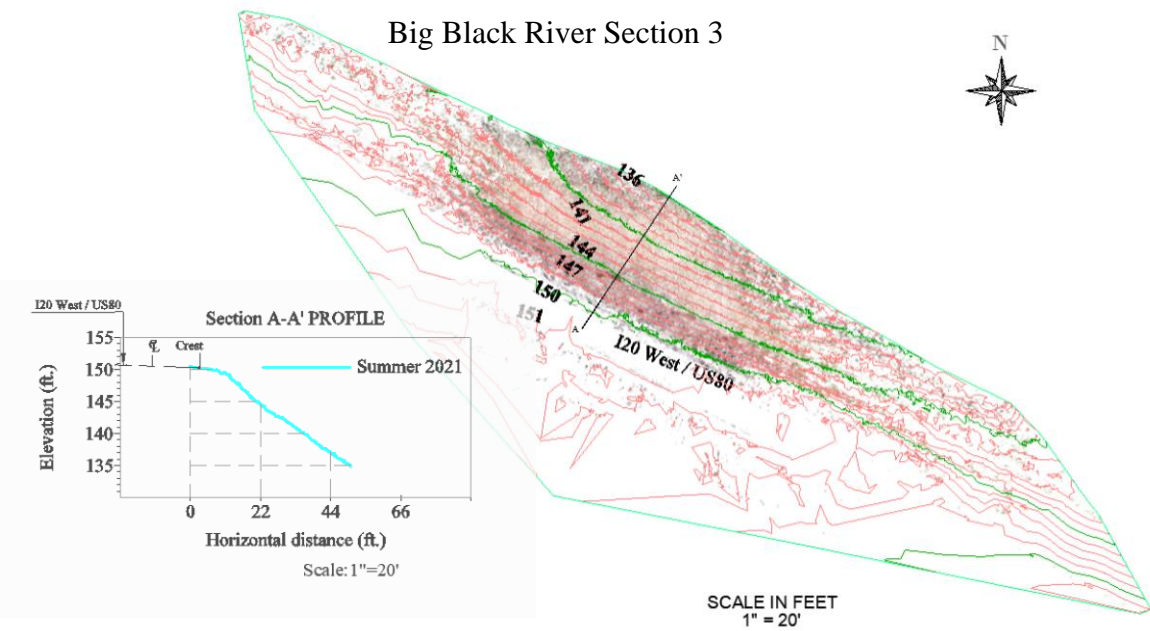


Figure 4.75 LiDAR Point Cloud Surface Topography and Profile of Section 3 of Big Black River Site

4.2.6 Failed Slope 6: Metrocenter ERI Test Site

4.2.6.1 ERI

The ERI test for the Metrocenter test site was performed at lines A, B, C, and D, spanning 270 feet between the crest and the toe of Slope 6 after it failed in the fall of 2021. The location of the slope and the test lines are presented in Figure 4.76. ERI results for all four lines are presented in Figure 4.77 (a -d). High resistivity is probably the cause of the surface deformation that exists at Lines A, B and C between the 10 ft. and 70 ft. horizontal distances. At lower depths, lower resistivity indicates that the soil is wet, probably because of rainfall infiltration. ERI test results indicate surface deformation at the surficial level between the 10' – 70' horizontal distances.

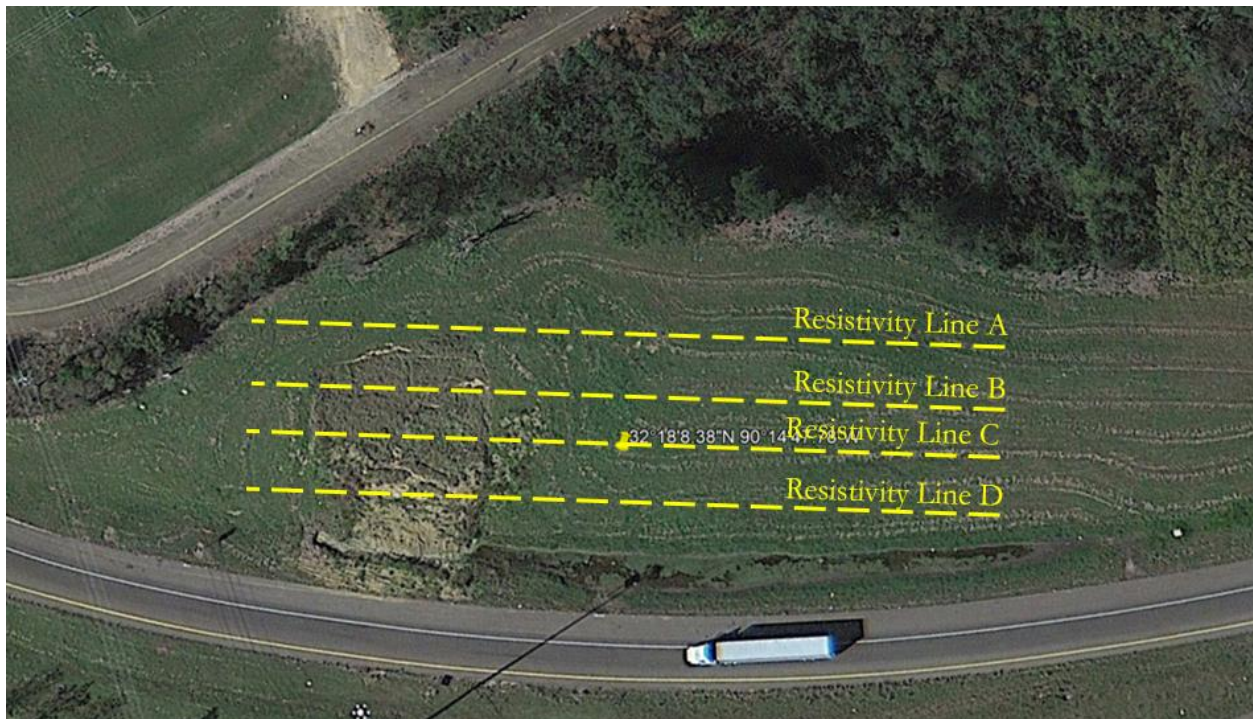


Figure 4.76 Location of Test Lines for Failed Slope 6

4.2.6.2 Drone

A drone survey mission was performed for failed Slope 6 in summer 2021 and fall/winter 2022. The aerial imagery captured by the drone was processed using specialized image processing software. Aerial triangulation was performed with multiple tie points to stitch the images together and develop a digital elevation model (DEM), digital terrain model (DTM), and mosaics. DEM and orthomosaic digital image representations for different seasons are presented in Figure 4.78 and Figure 4.79

DEMs were imported into Civil 3D, and the surface was created using the kriging interpolation method. Alignment along the slope was created, and a surface profile view was generated along Line A, shown in Figure 4.78 (a) and Figure 4.79 (a). The summer 2021 and fall/winter 2022 DEM and orthomosaic 3D models are presented in Figure 4.78(a), Figure 4.79(a) and Figure 4.79 (b), respectively. The topographic contour views and surface profile views along

Line A for summer 2021 and fall/winter 2022 are presented in Figure 4.78 (b) and Figure 4.79 (c), respectively.

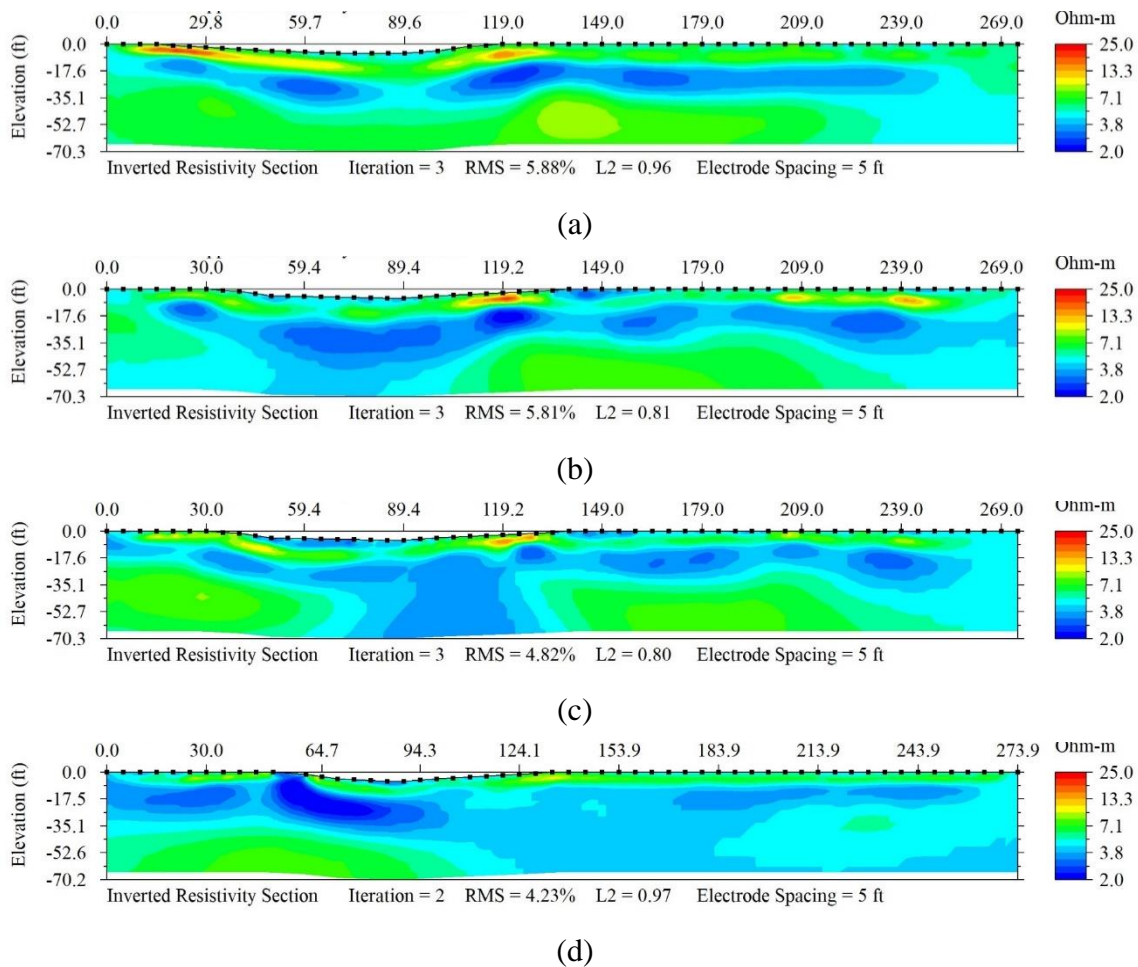


Figure 4.77 ERI Test Results for Failed Slope 6: (a) Line A, (b) Line B, (c) Line C, (d) Line D

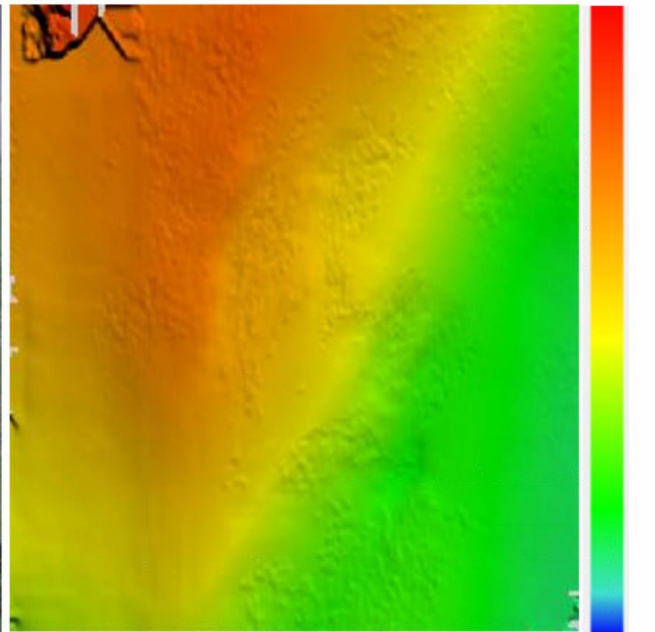
4.2.6.3 LiDAR

Terrestrial LiDAR scanning data was collected in the summer of 2021 after the slope failed and then again in the fall of 2022 after it was stabilized. Laser scanning was performed at several stations, and the overlapping point cloud data were collected, processed, and registered together to form a single point cloud. The combined point cloud was then georeferenced using field ground control points with known coordinates. Using a ground extraction algorithm, low surface points were extracted to create the bare ground point clouds. The bare ground point clouds for all seasons collected were imported into Civil 3D, and digital elevation model surfaces were generated using the kriging interpolation method. Topographic surface views were then generated at 1 ft. major and 5 ft. minor contour intervals for summer 2021 and fall 2022 and are presented in Figure 4.80 (a) and (b), respectively.

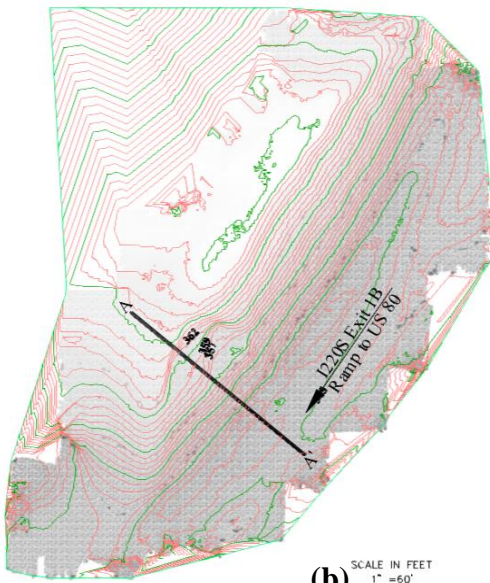
Summer 2021



3D Digital Model



Digital Elevation Model



(b)

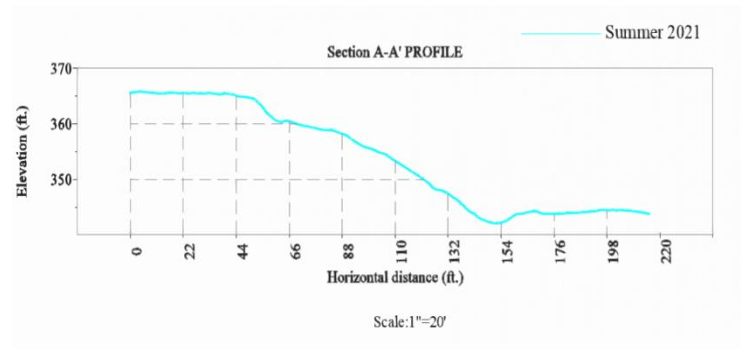
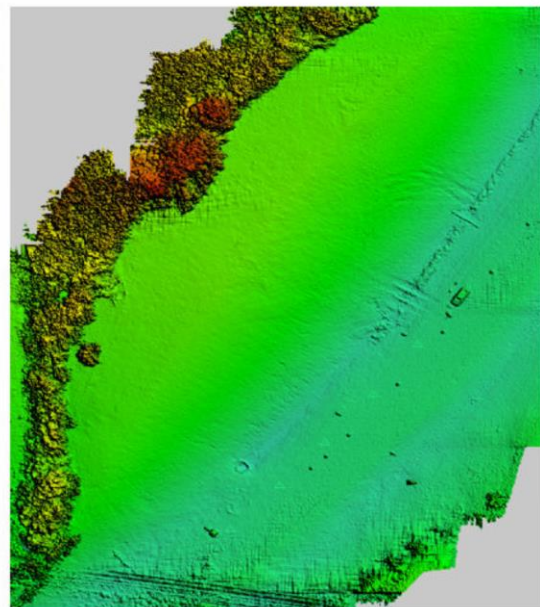


Figure 4.78 Drone Images for Failed Slope 6: (a) Digital Elevation Model, (b) Surface Topography and Profile (Summer 2021)

Fall/Winter 2022



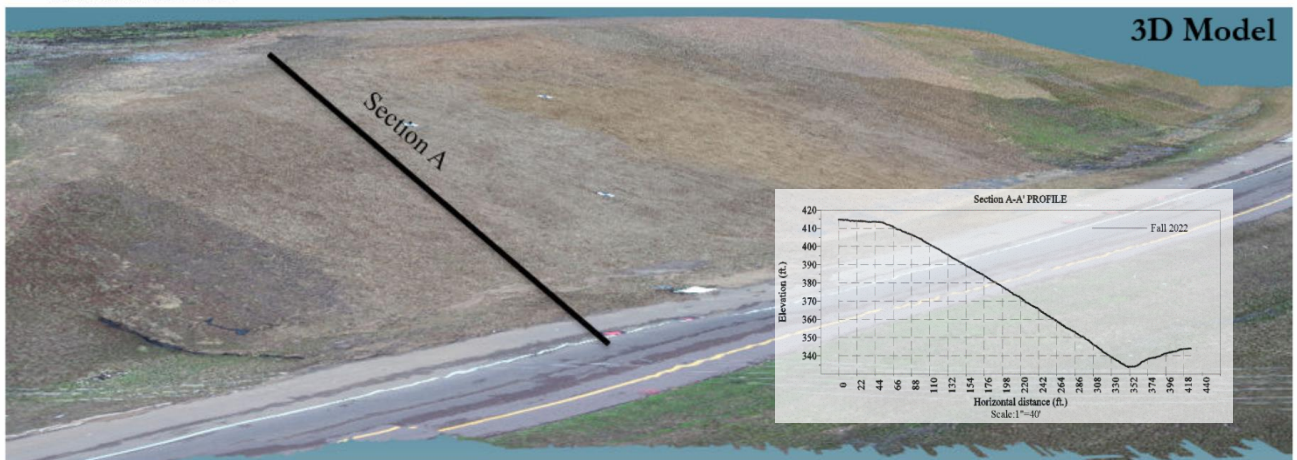
3D Digital Model



Digital Elevation Model

a)

Fall/Winter 2022



b)

Figure 4.79 (Continued)

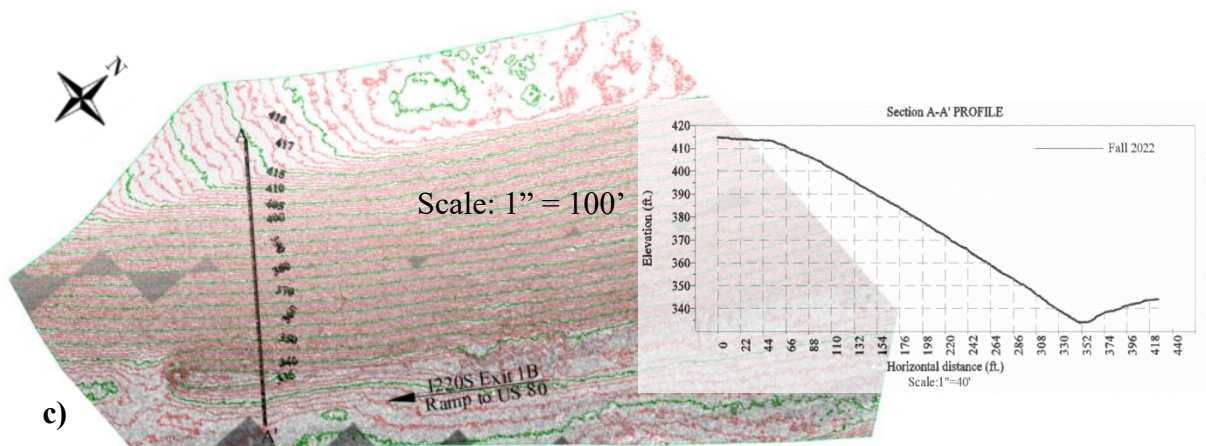


Figure 4.79 Drone Images for Failed Slope 6: (a) DEM, (b) 3D Model View, (c) Surface Topography and Profile (Fall/Winter 2022)

The surfaces from the two seasons were overlaid, and alignments were created along the slope. Stacked surface profiles were created using the alignments along Sections A-A' and are presented in Figure 4.80 (c). The rugged slope profile of summer 2021 is indicative of the terrain after the failure of the slope, which is unlike the smooth profile captured in fall 2022.

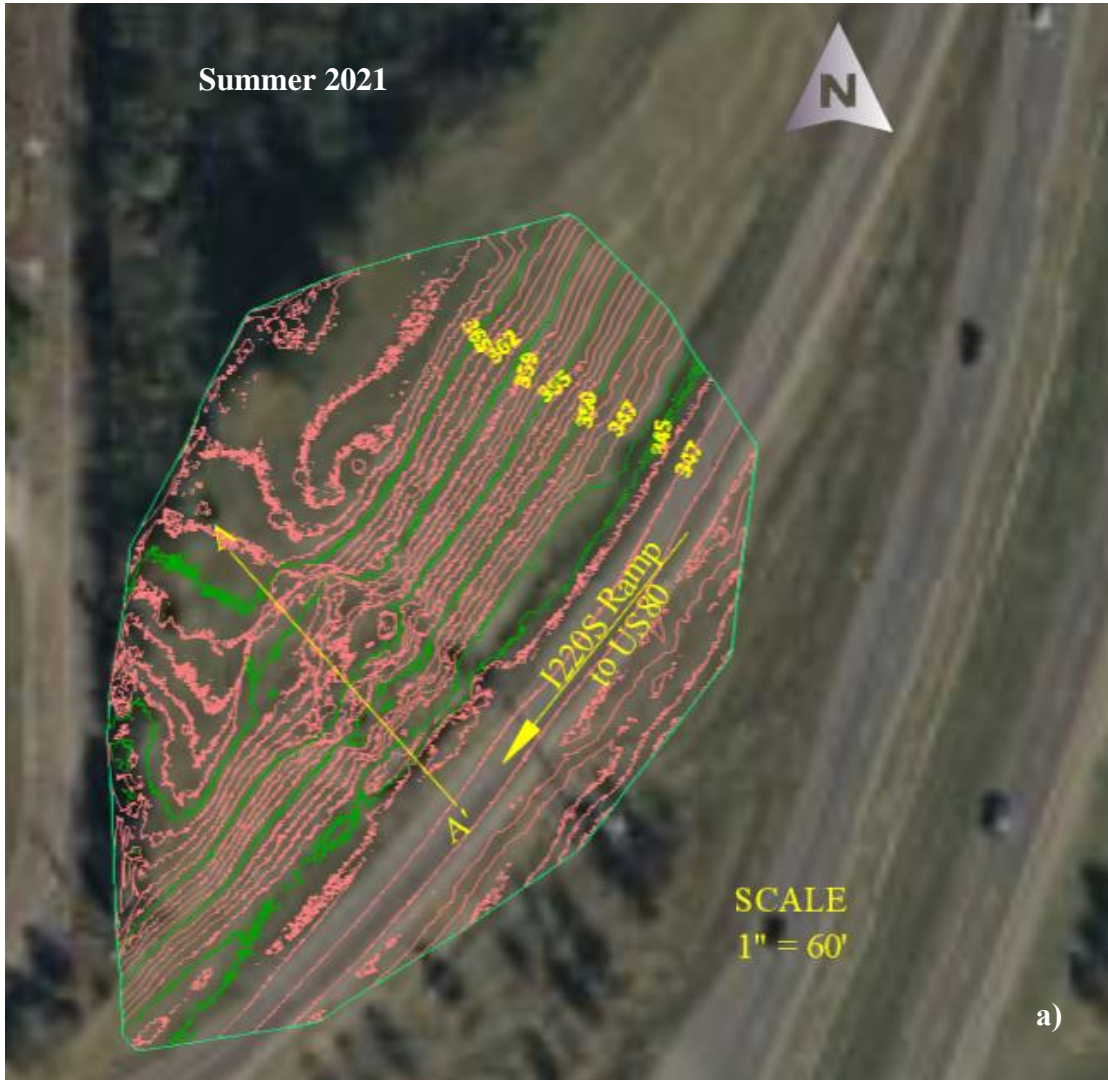


Figure 4.80 (Continued)

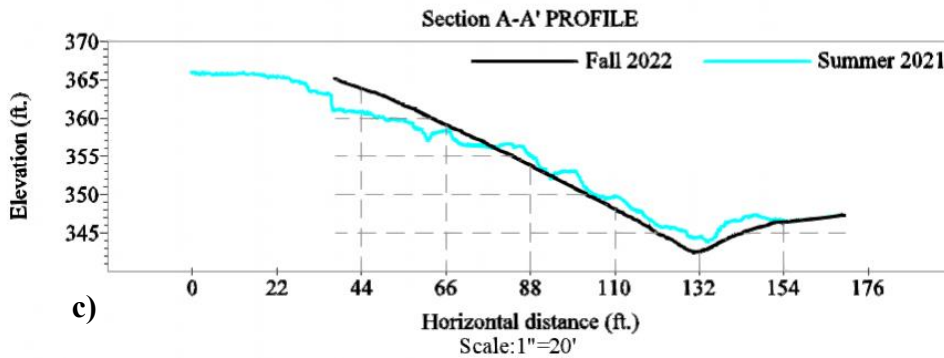
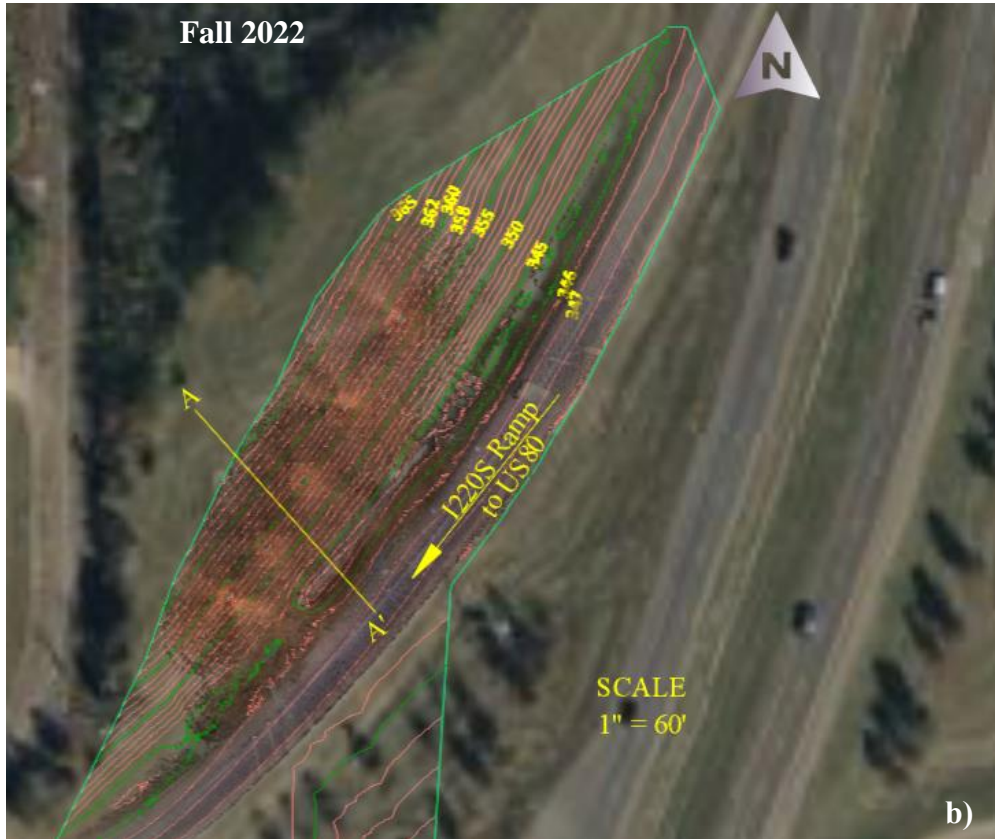


Figure 4.80 LiDAR Point Cloud Surface Topography of Failed Slope 6: (a) Summer 2021, (b) Fall 2021, (c) Overlaid Surface Profile

4.2.7 Failed Slope 7: US 49 South Slope

4.2.7.1 ERI

The ERI test for failed Slope 7 was conducted along three lines: Lines A & B, which spanned 270 feet at the crest and middle, and Line C, which spanned approximately 82 ft. at the toe of the slope. The location of the slope and test lines are presented in Figure 4.81. The ERI results for Lines A & B for summer 2021 are presented in Figure 4.82 (a), (b) and (c). The ERI results indicated that from the surface of the crest up to a depth of 15 ft., there are high resistivity layers that indicate loose soil with air voids. Low resistivity areas exist below the loose soil,

indicating wet soil along the entire span, likely caused by rainfall infiltration. Line B in the middle of the slope has lower resistivity than the crest. The soil at Line C is wetter from the surficial levels to the surveyed depth of 13 ft.



Figure 4.81 Location of ERT Test Lines for Failed Slope 7

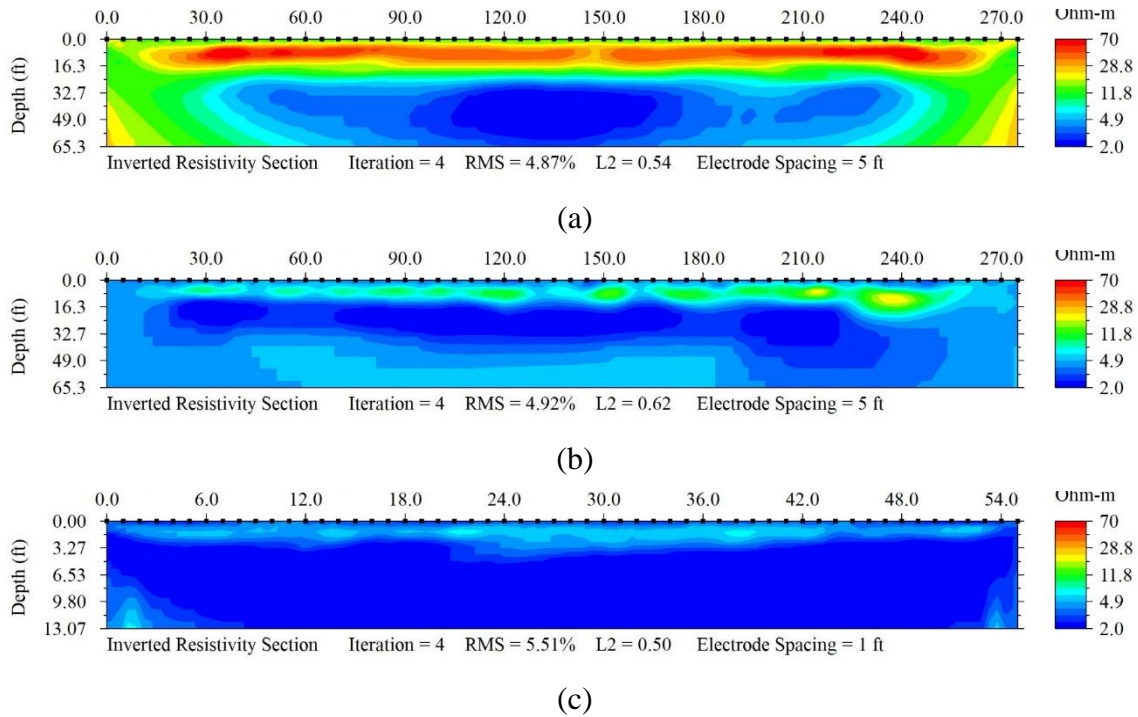


Figure 4.82 ERI Test Results of Failed Slope 7: (a) Line A, (b) Line B, (c) Line C

4.2.7.2 Drone

A drone survey mission in summer 2021 captured aerial imagery that was processed using specialized image processing software. Aerial triangulation was performed with multiple tie points to stitch the images together and develop a digital elevation model (DEM), digital terrain model (DTM), and mosaics. DEM and orthomosaic digital image representations of the failed slope are presented in Figure 4.83. The elevations along line A were extracted, and the profile shown in Figure 4.83 was created manually.

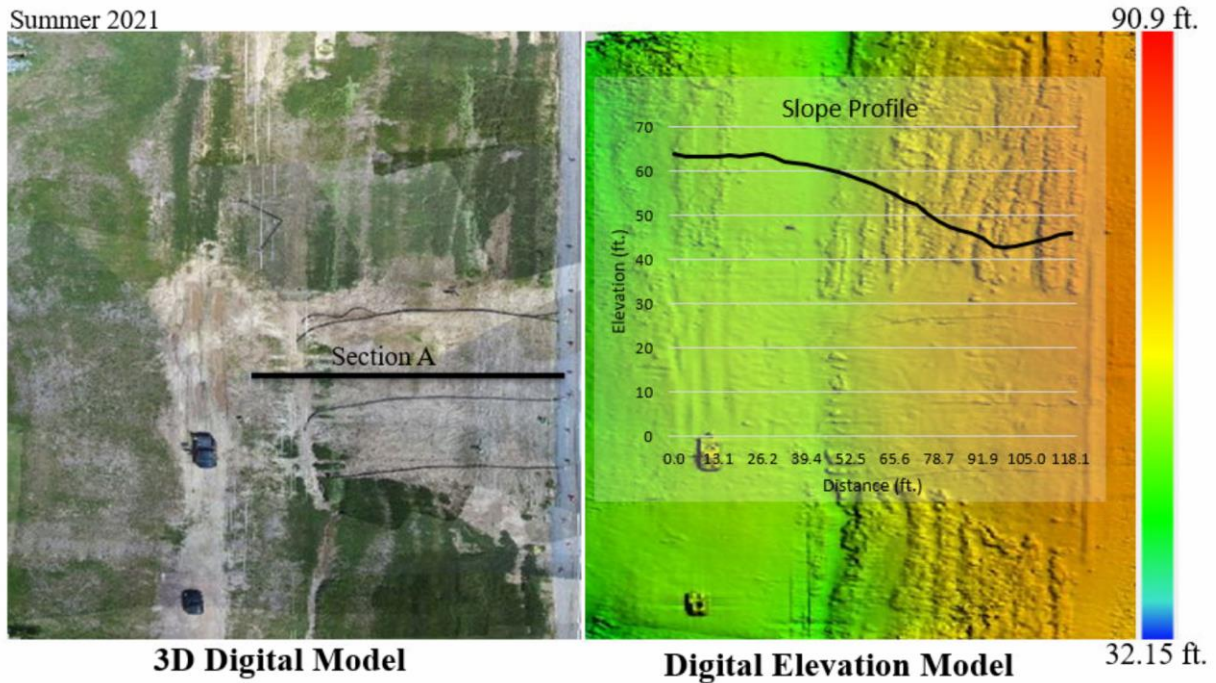


Figure 4.83 Drone images of Failed Slope 7 (Summer 2021)

4.2.8 Failed Slope 8: 178 Union Slide

4.2.8.1 ERI

ERI tests were performed along three lines, Lines A, B & C, for failed Slope 8, all spanning 378 feet. The location of the slope and the test lines are presented in Figure 4.84. The results for Lines A, B & C are presented in Figure 4.865 (a), (b) and (c). The results showed the presence of high resistivity layers, indicating loose soil with air voids, from the surface of the crest (Line A) down to 6 ft. and also below 47 ft. Low resistivity areas are below the loose soil, indicating wet soil along the entire span, likely caused by rainfall infiltration.



Figure 4.84 Location of ERI Test Lines in Failed Slope 8

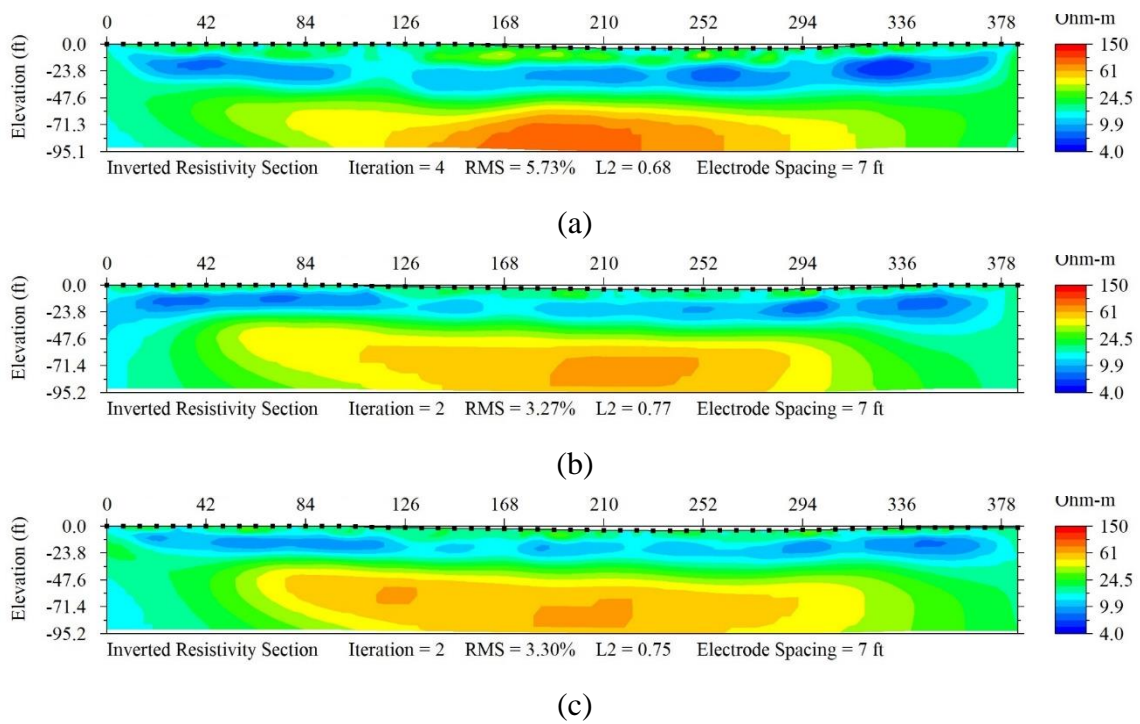


Figure 4.85 Results of ERI Test Results for Failed Slope 8: (a) Line A, (b) Line B, (c) Line C

4.2.9 Failed Slope 9: Dogwood

4.2.9.1 ERI

ERI tests were performed along three lines, A, B & C, of failed Slope 9, each spanning 378 feet. The locations of the slope and ERI test lines are presented in Figure 4.86. ERI results for Lines A, B & C are presented in Figure 4.87 (a), (b) and (c). The results showed that high resistivity layers exist up to a depth of 20 ft. at the crest line (Line A), between a horizontal distance of 40 and 65 ft., indicating deformed soil. Low resistivity areas are directly below the loose soil, indicating perched water conditions from rainfall infiltration. Lines B & C, shown in Figure 4.87 (b) and (c) indicate a similar pattern but to a lesser degree than that in Line A.

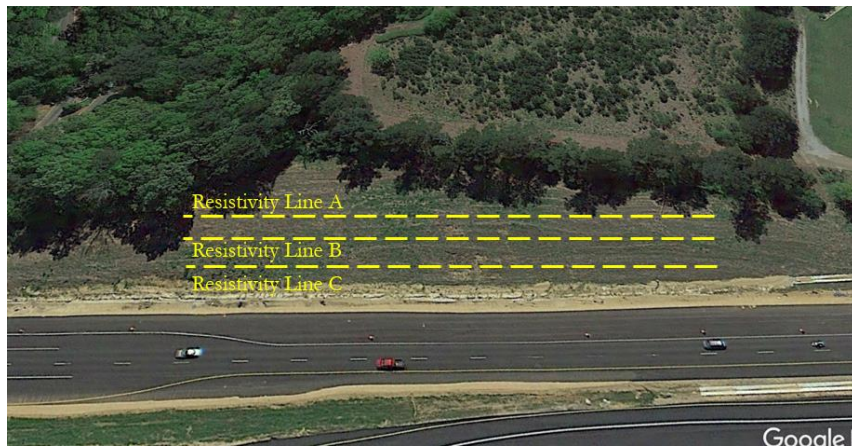


Figure 4.86 Location of ERI Test Lines in Failed Slope 9

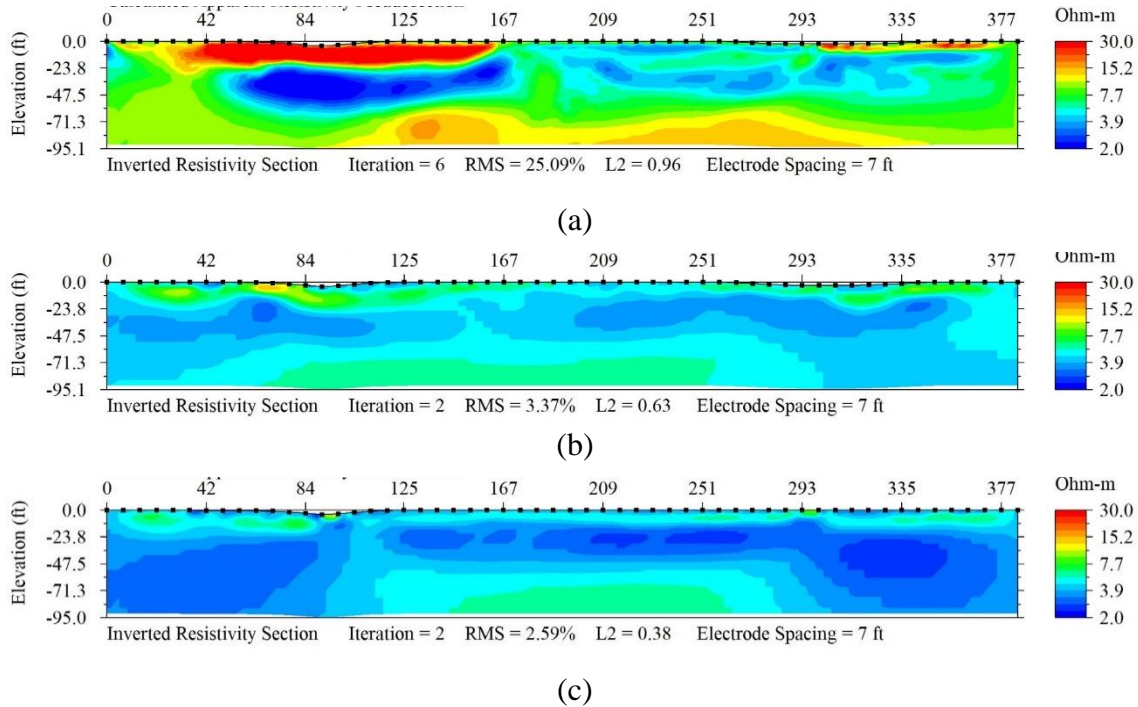


Figure 4.87 ERI Test Results for Failed Slope 9 -Dogwood Slope: (a) Line A, (b) Line B, (c) Line C

4.2.9.2 Drone

A drone survey mission was conducted in the summer of 2021 of the failed Flowood Dogwood Slope (Slope 9), and the aerial imagery captured by the drone was processed using specialized image processing software. Aerial triangulation was performed with multiple tie points to stitch the images together and develop a digital elevation model (DEM), digital terrain model (DTM), and mosaics. The DEM and orthomosaic digital image representations are presented in Figure 4.88. The elevations from the DEM along Line A were extracted, and a profile was created manually, as shown in Figure 4.88.

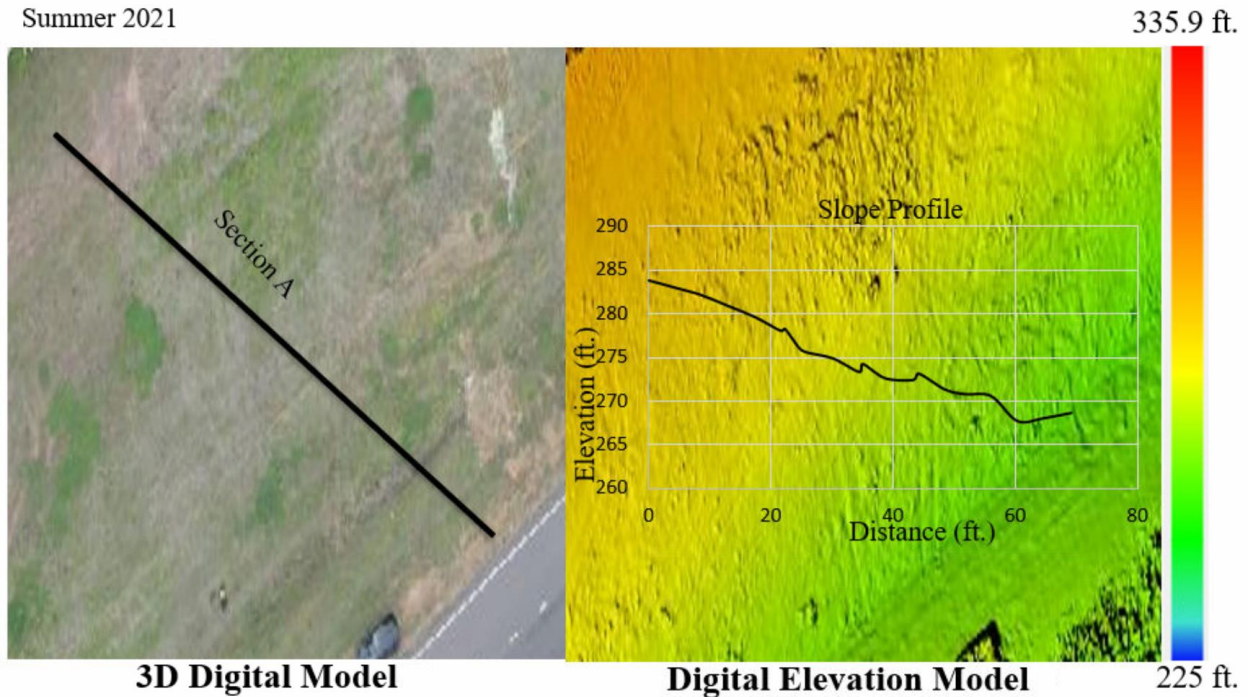


Figure 4.88 Drone Images of Failed Slope 9 (Summer 2021)

4.2.9.3 LiDAR

Terrestrial LiDAR scanning data was collected in the summer of 2021. Laser scanning was performed at several stations, and the overlapping point cloud data were collected. The point clouds were then post-processed on a computer and registered together to form a single point cloud. Using a ground extraction algorithm, low surface points were extracted to create the bare ground point clouds, which were processed in Civil 3D. The topographic surface view was generated at 1 ft. major and 5 ft. minor contour intervals, then a surface profile view was generated, using alignments. The topographic contour view is presented in Figure 4.89(a). The surface profile view along section A-A' is presented in Figure 4.89 (b).

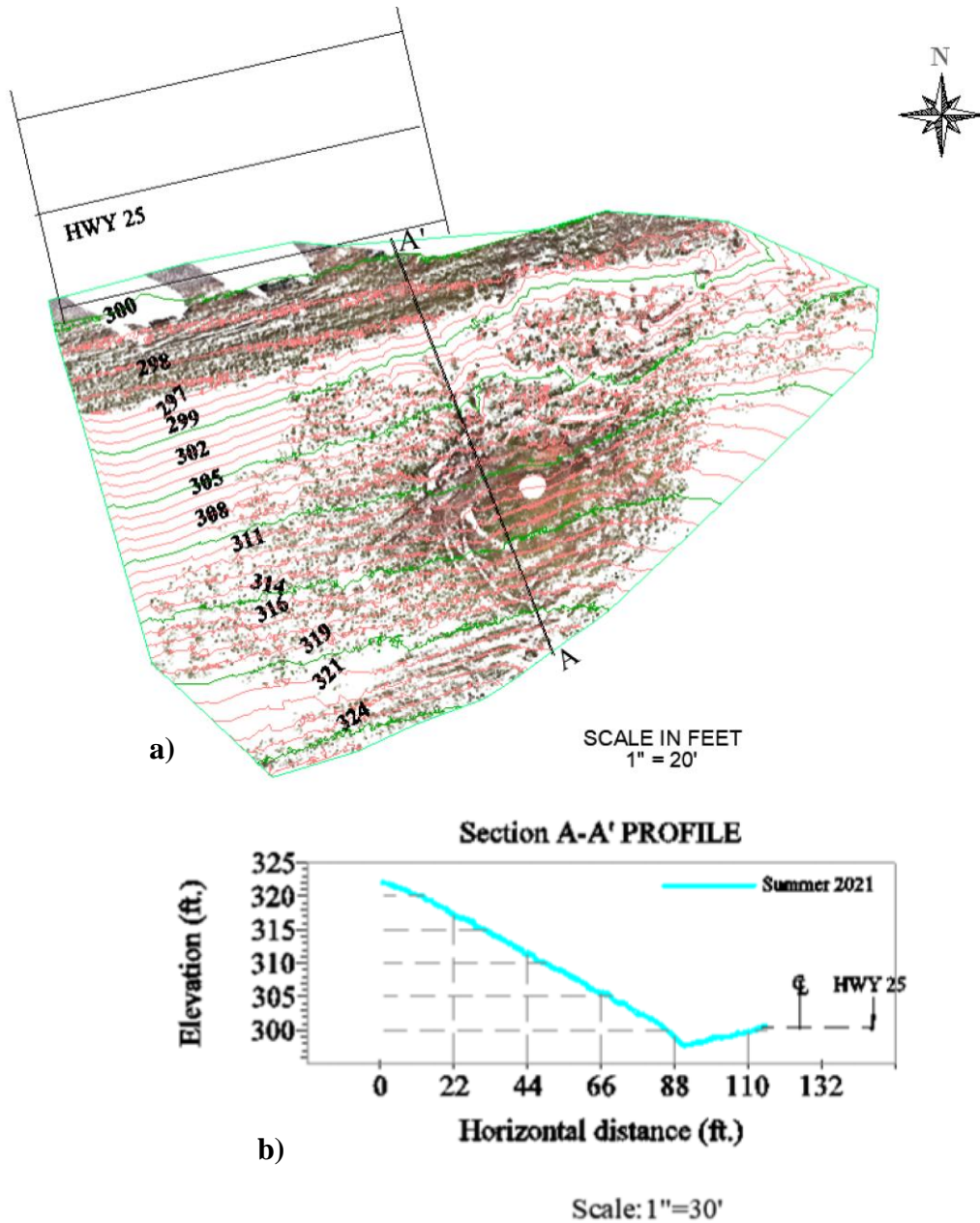


Figure 4.89 LiDAR Point Cloud Surface of Failed Slope 9: (a) Topography and (b) Profile View

4.2.10 Failed Slope 10: US 49 North Slope Profile Summer 2021

4.2.11.1 ERI

ERI tests were conducted for failed Slope 10 along three lines, A, B & C, each spanning 486 feet, with electrodes spaced at intervals of 9 ft. The location of the slope and the test lines are presented in Figure 4.90. The results for Lines A, B & C are presented in Figure 4.91 (a), (b) and (c). The results revealed high resistivity layers at all three lines up to approximately 25 ft. depth, indicating deformed soil. Low resistivity areas exist directly below the loose soil, indicating perched water conditions caused by rainfall infiltration.



Figure 4.90 Location of ERI Test Lines in Failed Slope 10

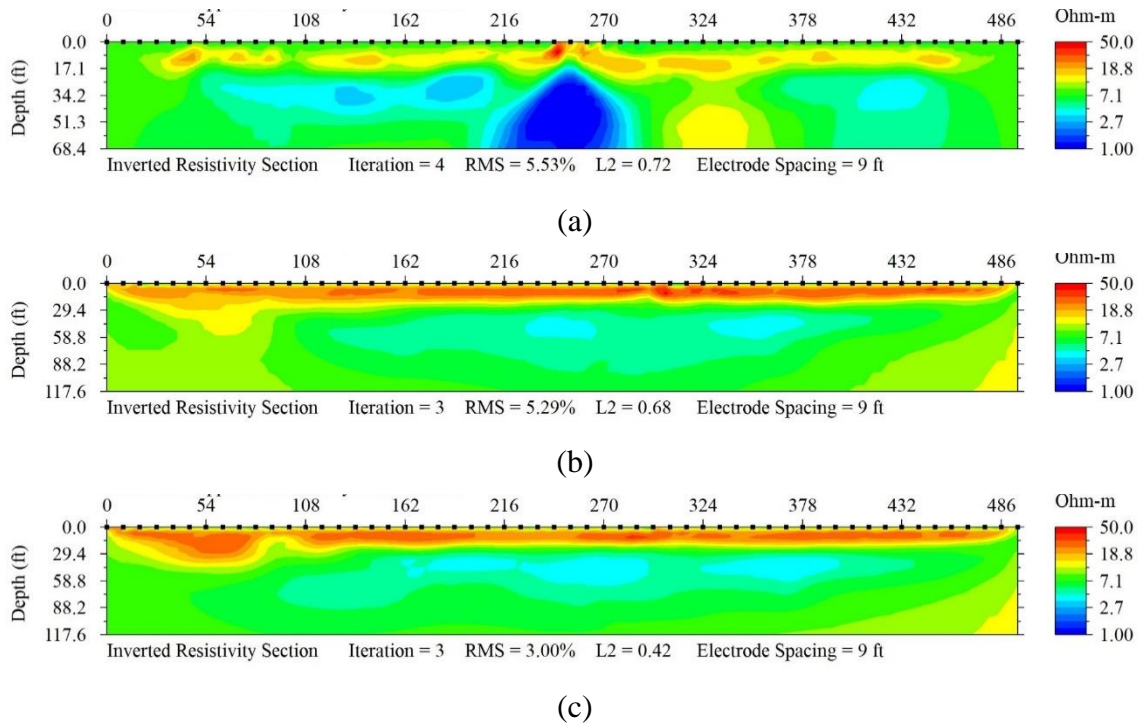


Figure 4.91 ERI Test Results for Failed Slope 10: (a) Line A, (b) Line B, (c) Line C

4.2.10.1 Drone

A drone survey mission in summer 2021 captured aerial imagery that was processed using specialized image processing software. Aerial triangulation was performed with multiple tie points to stitch the images together and develop a digital elevation model (DEM), digital terrain model (DTM), and mosaics. The DEM and orthomosaic digital image representations are

presented in Figure 4.92. The elevations were extracted from the DEM along Line A, and a profile was created manually, as shown in Figure 4.92.

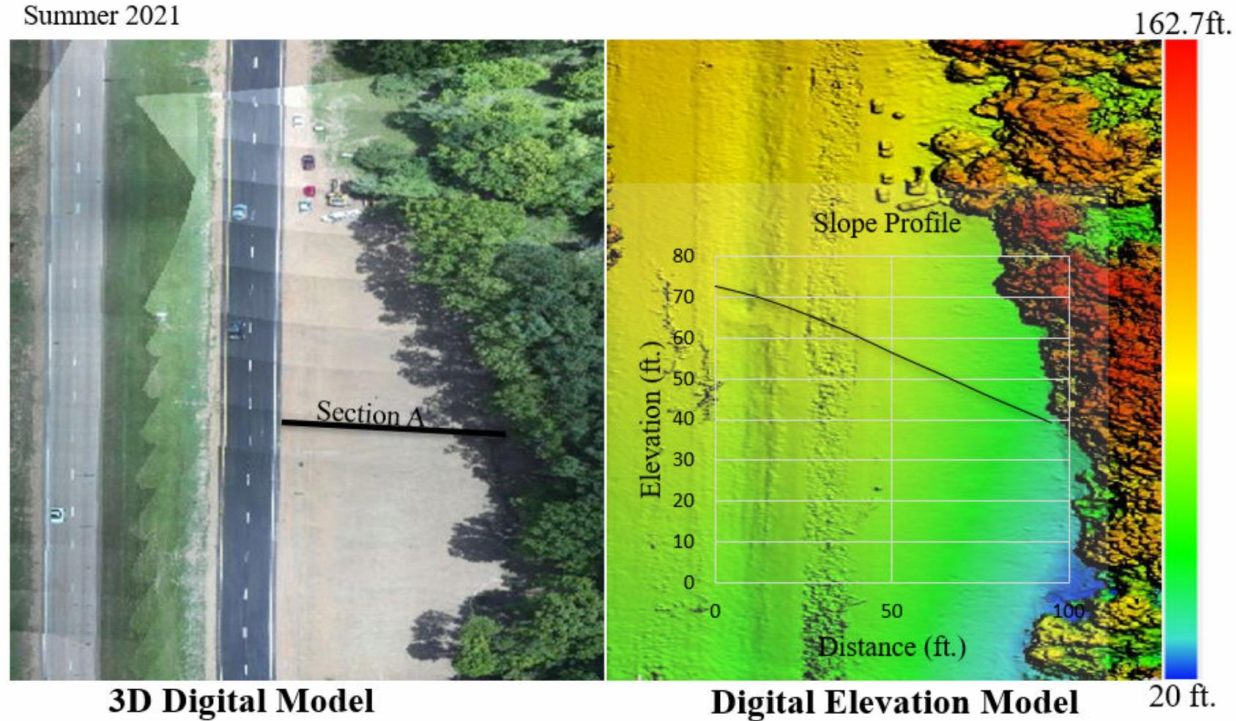


Figure 4.92 Drone Images of Failed Slope 10 (Summer 2021)

4.2.10.2 *LiDAR*

Terrestrial LiDAR scanning data was collected in the summer of 2021 for failed Slope 10. Laser scanning was performed at several stations, and the overlapping point cloud data were collected, post-processed on a computer, and registered together to form a single point cloud. Using a ground extraction algorithm, low surface points were extracted to create the bare ground point clouds, which were processed in Civil 3D. The topographic surface view was generated at 1 ft. major and 5 ft. minor contour intervals, then a surface profile view was generated, using alignment. The slope’s topographic contour view and surface profile view along section A-A’ are presented in Figure 4.93.

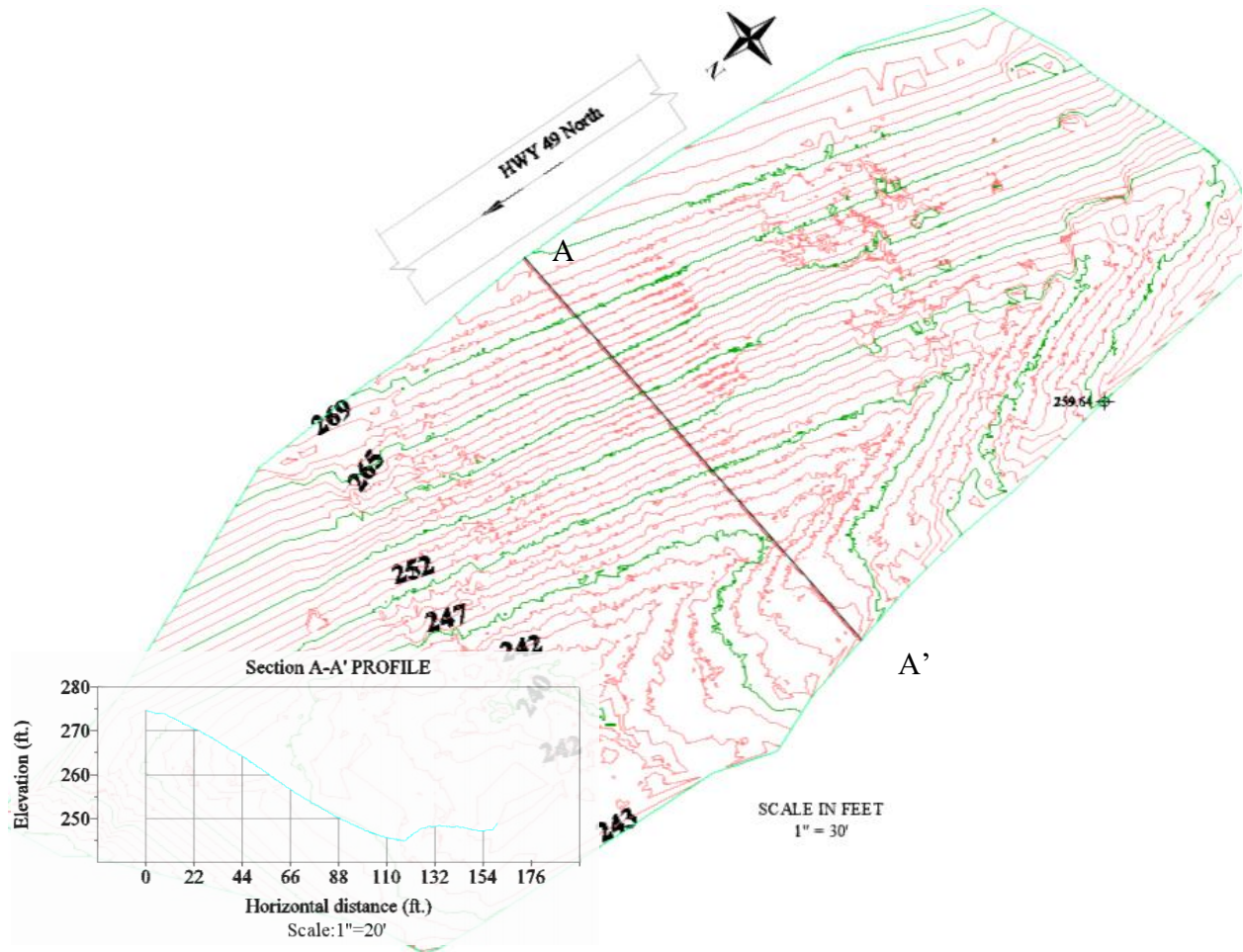


Figure 4.93 LiDAR Point Cloud Surface Topography and Profile View of Failed Slope 10

4.2.11 Failed Slope 12: Big Black River I20 Eastbound Slope

4.2.11.1 ERI

ERI tests for failed Slope 12 were performed along the A and B lines that span approximately 220 ft. and are equipped with electrodes spaced at 5 ft. intervals. The location of the slope and test lines are presented in Figure 4.94. The ERI results for Lines A & B are presented in Figure 4.95 (a) & (b) and show that high resistivity layers are present up to approximately 8 ft. depth, indicating deformed soil. Low resistivity areas exist directly below the loose soil, indicating perched water conditions from rainfall infiltration.



Figure 4.94 ERI Test Lines in Failed Slope 12

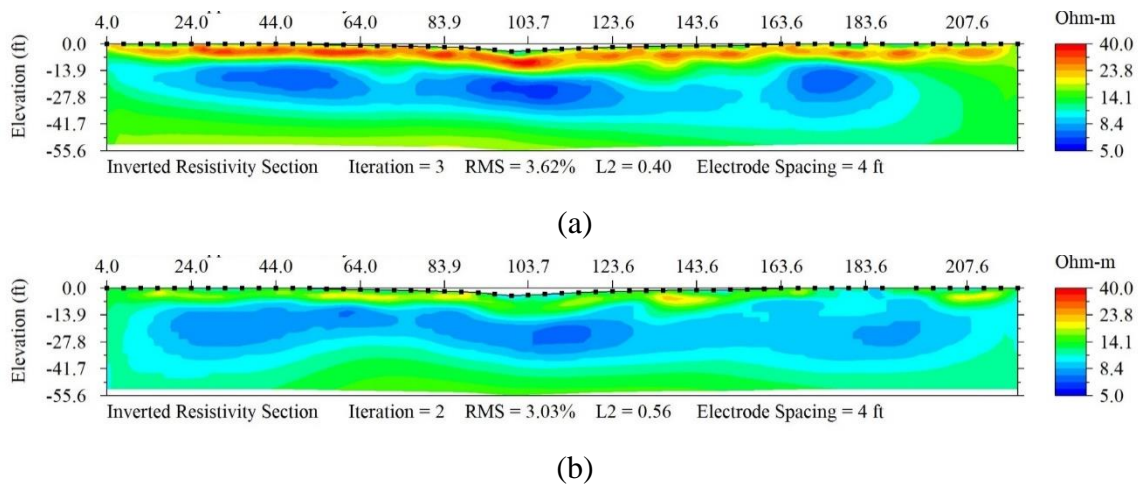


Figure 4.95 ERI Results of Failed Slope 12: (a) Line A (b) Line B

4.2.11.2 Drone

A drone survey mission was conducted for failed Slope 12 in the summer of 2021, and the aerial imagery captured was processed using specialized image processing software. Aerial triangulation was performed with multiple tie points to stitch the images together and develop a digital elevation model (DEM), digital terrain model (DTM), and mosaics. The DEM and orthomosaic digital image representations are presented in Figure 4.96 (a). The DEMs were imported into Civil 3D, and the surface was created using the kriging interpolation method. Alignment was created along the slope, and a surface profile view was generated along Line A,

as shown in Figure 4.96 (a). The topographic contour views and surface profile view along line A for summer 2021 are presented in Figure 4.96 (b).

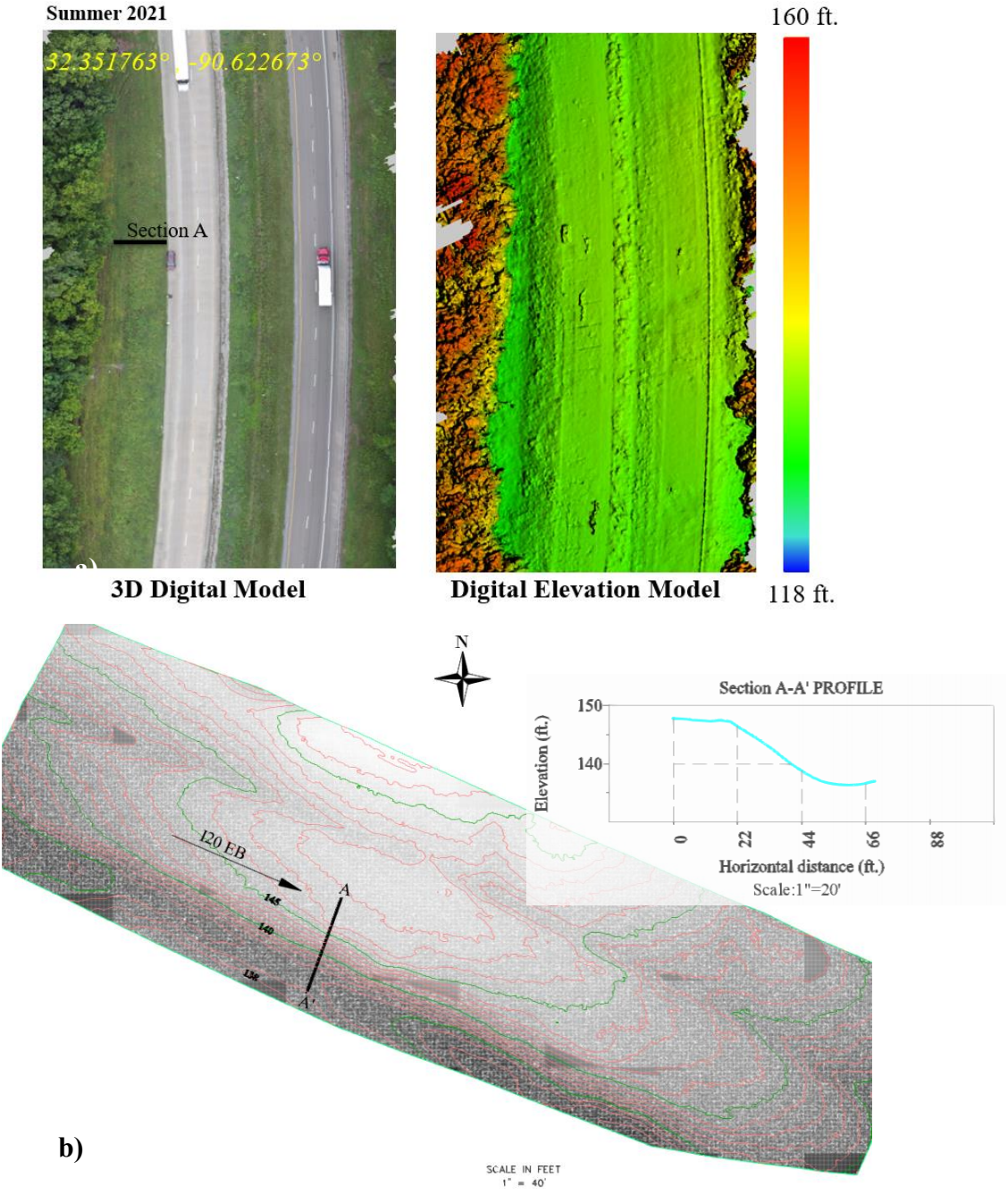


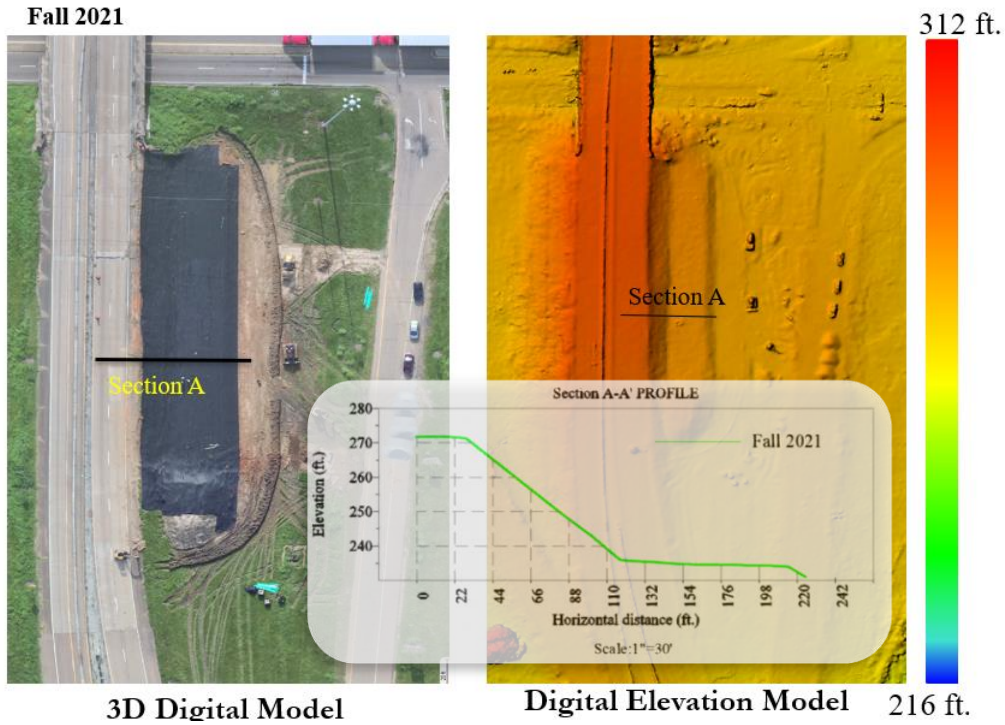
Figure 4.96 Drone Images of Failed Slope 12 Captured in Summer 2021: (a) Digital Elevation Model, (b) Surface Topography and Profile

4.2.12 Failed Slope 13: US 51 South near Gallatin St.

The Gallatin St. slope was an active construction site at the time of reconnaissance, so it was only accessible by a drone. The drone imagery processing results are presented in 4.2.12.1.

4.2.12.1 Drone

A drone survey mission was conducted for Slope 13 in the fall of 2021, after its failure. The captured aerial imagery was processed using specialized image processing software. Aerial triangulation was performed with multiple tie points to stitch the images together and develop digital elevation models (DEMs), digital terrain models (DTMs), and mosaics. The DEM and orthomosaic digital image representations are presented in Figure 4.97 (a). The DEM was imported into Civil 3D, and the surface was created using the kriging interpolation method. Alignment along the slope was created, and a surface profile view was generated along Section A, identified in Figure 4.97(a). The topographic contour views and surface profile view along Section A for fall 2021 are presented in Figure 4.97 (b).



a)

Figure 4.97 (Continued)

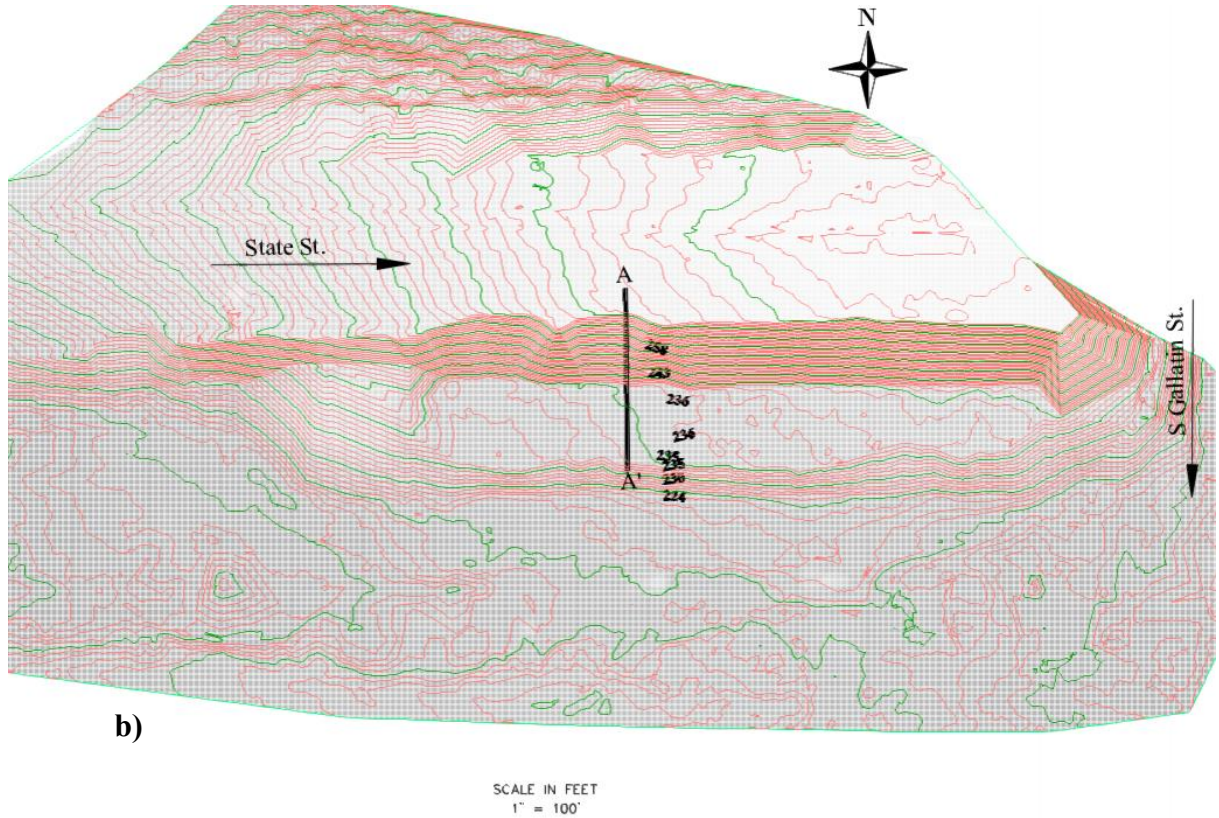


Figure 4.97 Drone Images of Failed Slope 13: (a) Digital Elevation Model, (b) Surface Topography (Summer 2021)

4.2.13 Failed Slope 14: US 49 Slope in Simpson County (Vetiver Site).

4.2.13.1 ERI

ERI tests were conducted for failed Slope 14 across two lines, A & B, spanning 320 ft. and equipped with electrodes spaced at 5 ft. intervals. The location of the slope and test lines are presented in Figure 4.98. The ERI results are presented in Figure 4.99 (a) and (b).



Figure 4.98 Location of ERI Test Lines in Failed Slope 14

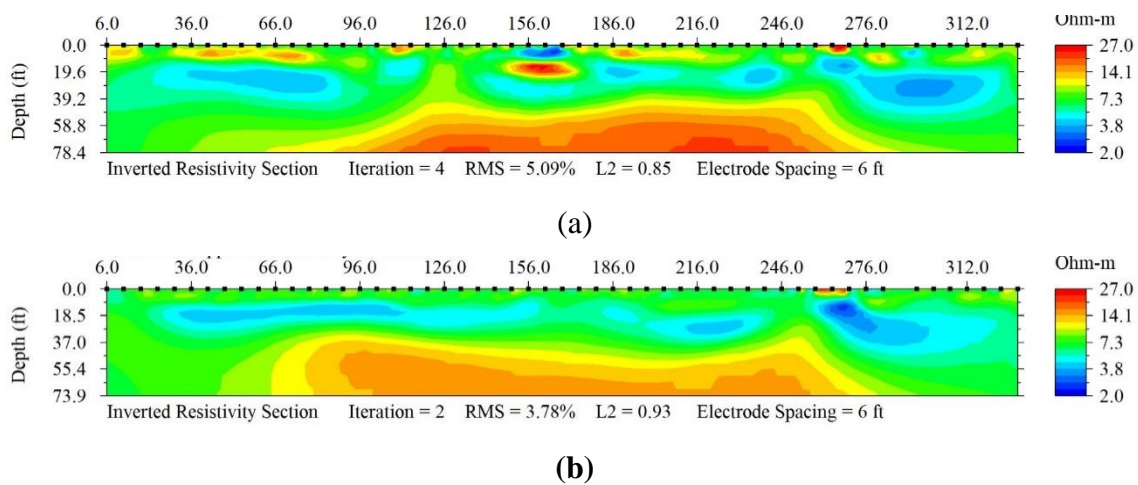


Figure 4.99 ERI Test Results of Failed Slope 14: (a) Line A (b) Line B

4.2.13.2 Drone

Drone survey missions were conducted over failed Slope 14 in spring 2022 and fall 2022, and the aerial imagery captured was processed using specialized image processing software. Aerial triangulation was performed with multiple tie points to stitch the images together and develop digital elevation model (DEMs), digital terrain models (DTMs), and mosaics. The DEM and orthomosaic digital image representations are presented in Figure 4.100 (a) & Figure 4.101 (a).

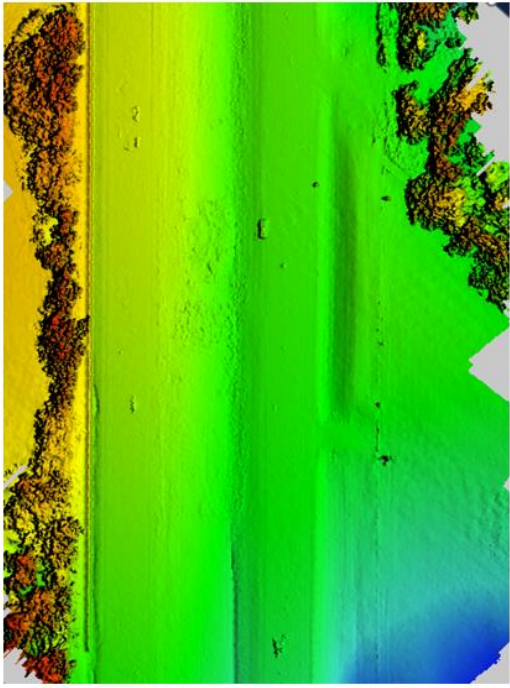
The DEMs were imported into Civil 3D, and surfaces were created using the kriging interpolation method. Alignments along the slope were created, and surface profile views were generated along the slope. The topographic contour views and surface profile views for spring 2022 and fall 2022 are presented in Figure 4.100 (b) & Figure 4.101 (b) respectively. The 3D

model representation of the slope and surface profile views for spring 2022 and fall 2022 are presented in Figure 4.100 (c) and Figure 4.101 (c) respectively.

Spring 2022



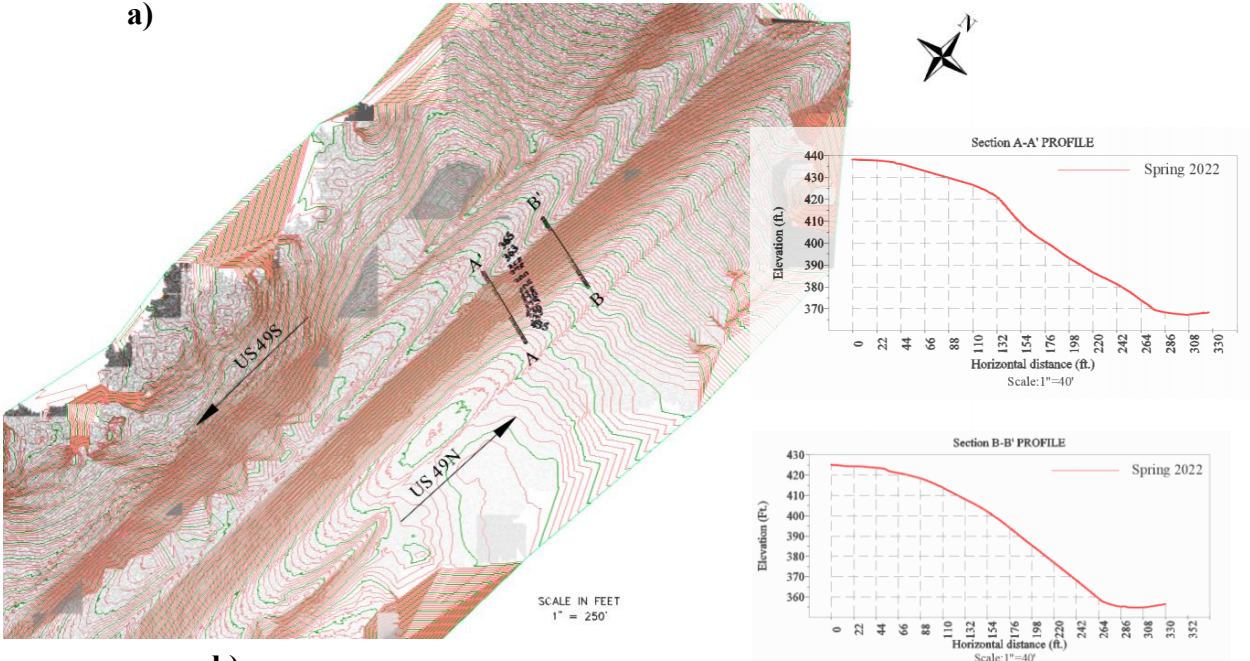
3D Digital Model



Digital Elevation Model 331 ft.

466 ft.

a)



b)

Figure 4.100 (Continued)

Spring 2022

3D Model

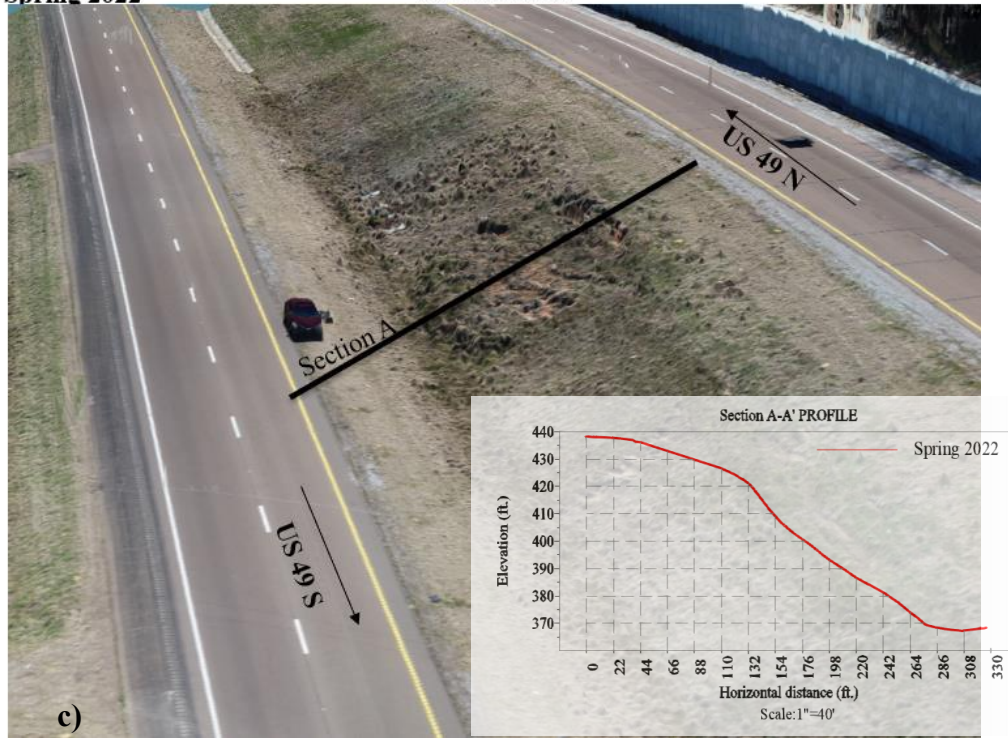
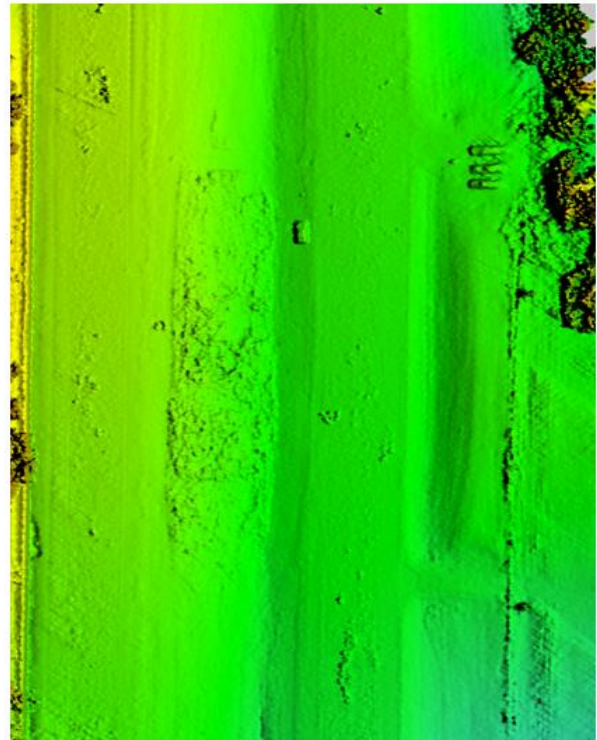


Figure 4.100 Drone Images of Failed Slope 14: (a) Digital Elevation Model, (b) Surface Topography & Profiles, (c) 3D Model & Surface Profile (Spring 2022)

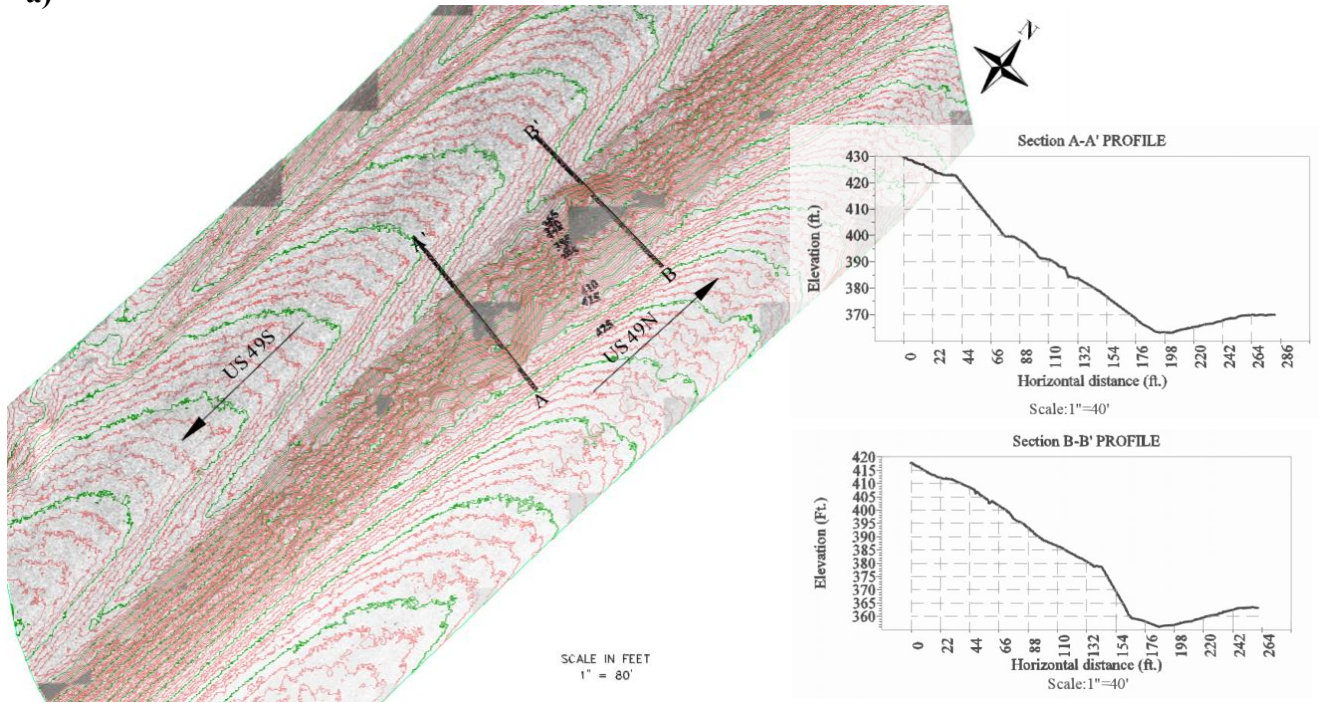
Fall/Winter 2022

482 ft.



a) 3D Digital Model

Digital Elevation Model 331 ft.



b)

Figure 4.101 (Continued)

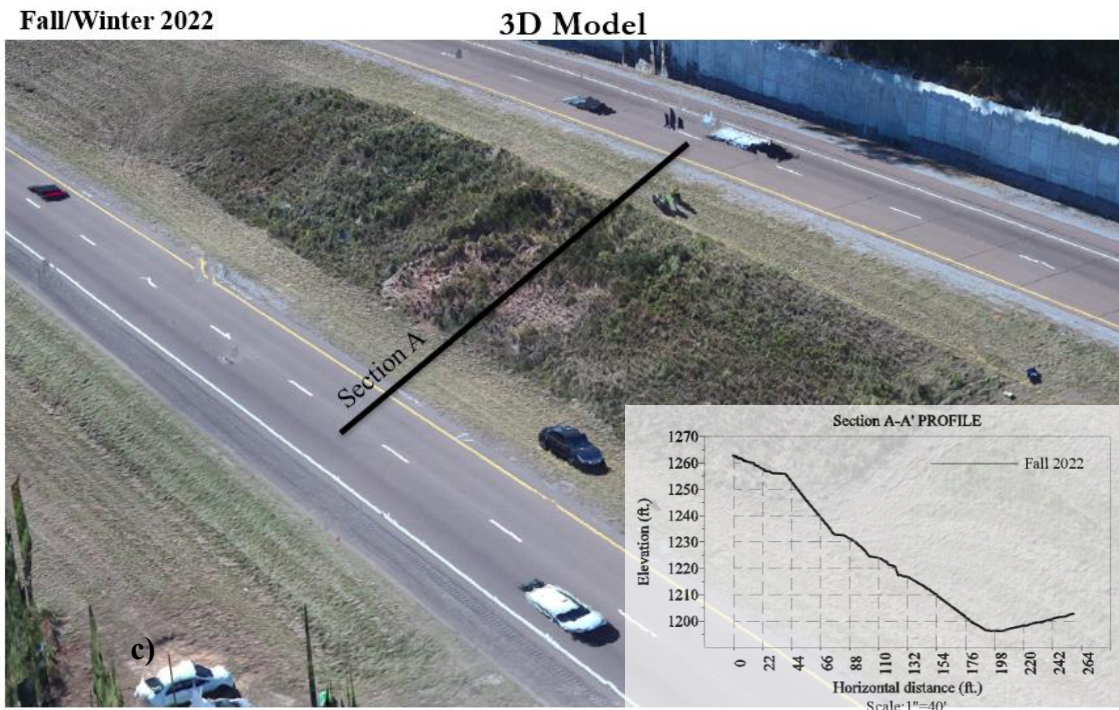


Figure 4.101 Drone Images of Failed Slope 14: (a) Digital Elevation Model, (b) Surface Topography & Profiles, (c) 3D Model & Surface Profile (Fall 2022)

4.2.13.3 *LiDAR:*

Terrestrial LiDAR scanning data was collected after the failure of Slope 14 in spring 2022 and then again in Fall 2022 after the slope was stabilized with vetiver grass. Laser scanning was performed at several stations, and the overlapping point cloud data were collected, then post-processed and registered together to form a single point cloud, which was then georeferenced using field ground control points with known coordinates. Using a ground extraction algorithm, low surface points were extracted to create the bare ground point clouds. The bare ground point clouds for all seasons collected were imported into Civil 3D, and digital elevation model surfaces were generated using the kriging interpolation method. Topographic surface views were generated at 1 ft. major and 5 ft. minor contour intervals for spring 2022 and fall 2022 and are presented in Figure 4.102 (a) and (b), respectively. The surfaces from the two seasons were overlaid, and alignments were created along the slope. Stacked surface profiles were then created using the alignments along Sections A-A' and B-B' and are presented in Figure 4.103 (a) & (b).

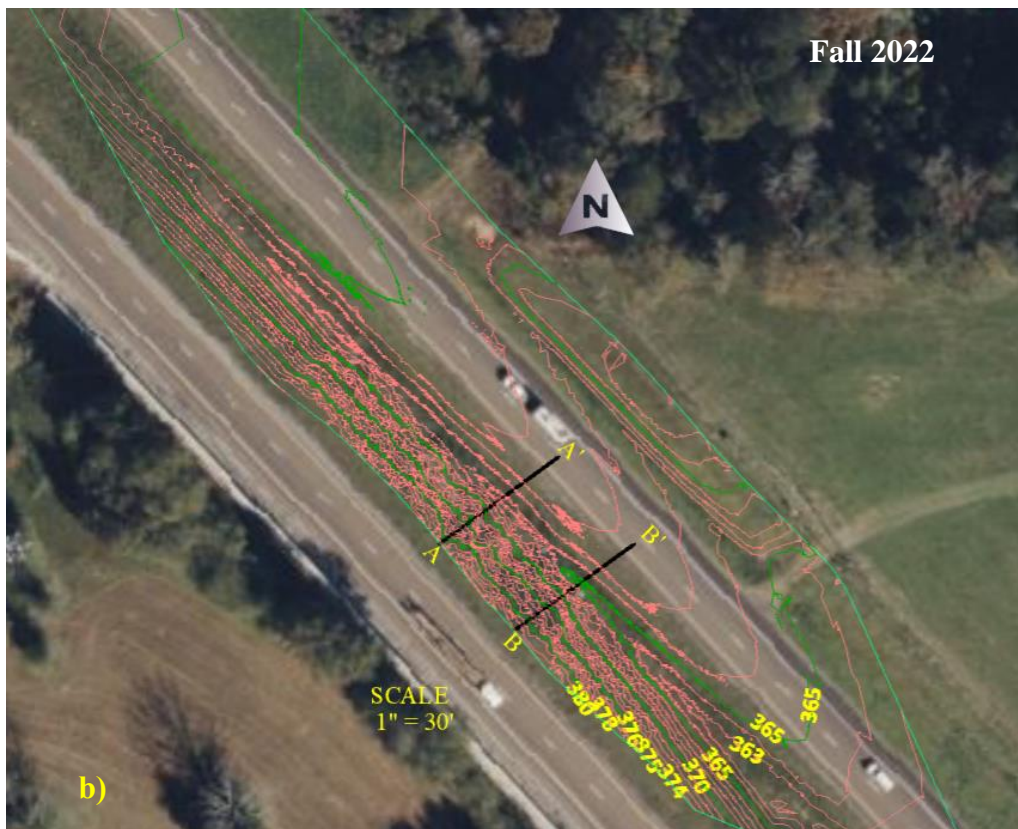
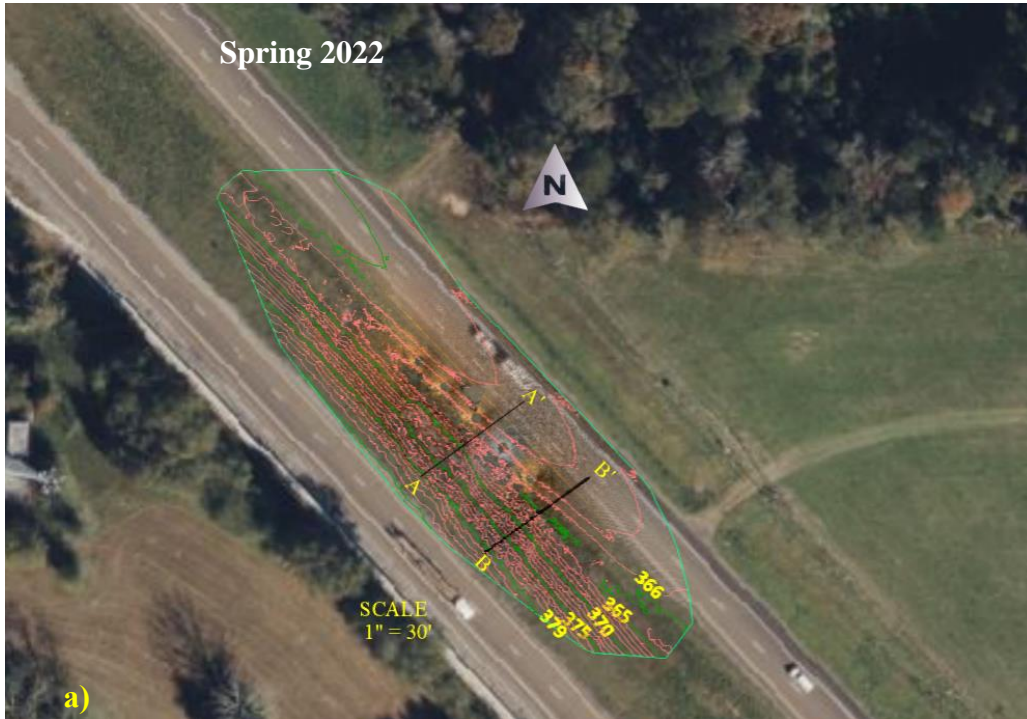
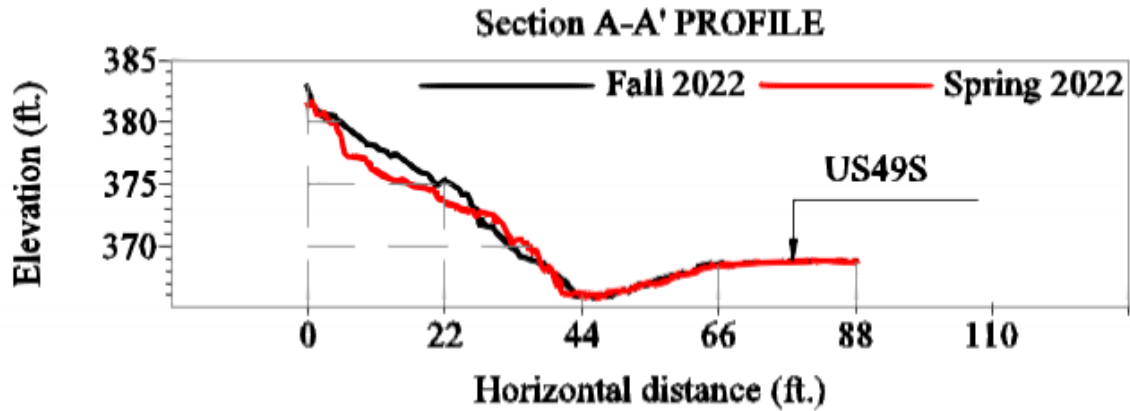
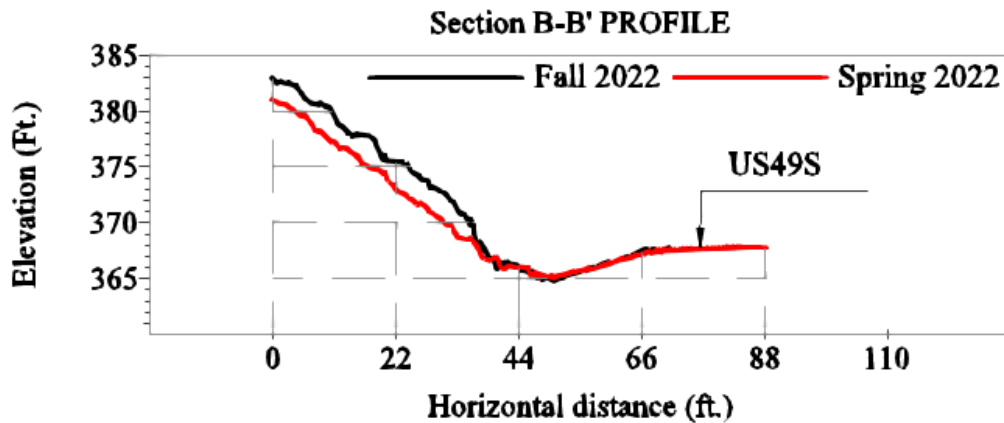


Figure 4.102 LiDAR Point Cloud Surface Topography for Failed Slope 14: (a) Fall 2021, (b) Fall 2022



a)

Scale:1"=20'



b)

Scale:1"=20'

Figure 4.103 LiDAR Point Cloud Overlayed Surface Profiles for Failed Slope 14: (a) Profile Section A-A', (b) Profile Section B-B'

4.2.14 Failed Slope 15: Slope Along US 27

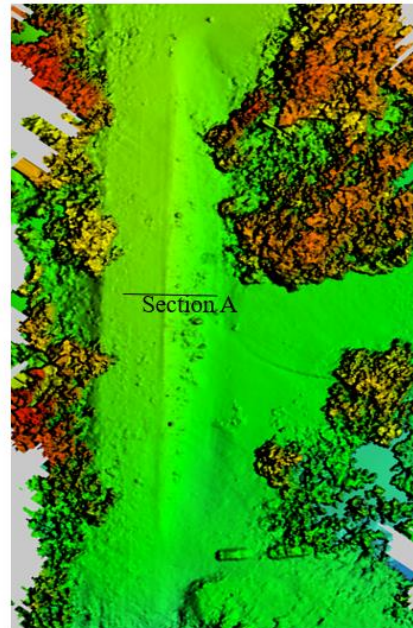
4.2.14.1 Drone

A drone survey mission was conducted over failed Slope 15 in the fall of 2021, and the captured aerial imagery was processed using specialized image processing software. Aerial triangulation was performed with multiple tie points to stitch the images together and develop a digital elevation model (DEM), digital terrain models (DTMs), and mosaics. The DEM and orthomosaic digital image representations are presented in Figure 4.104 (a). The DEM was imported into Civil 3D, and the surface was created using the kriging interpolation method. Alignment along the slope was created, and a surface profile view was generated along Section A. The topographic contour and surface profile for fall 2021 are presented in Figure 4.104 (b).

Fall 2021

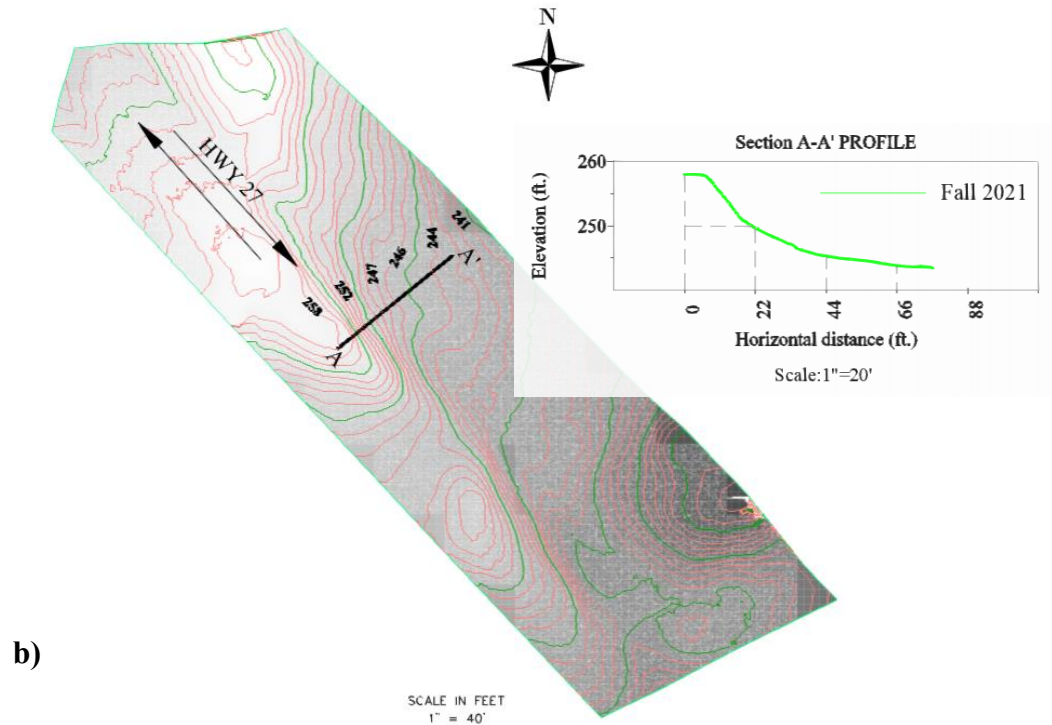


a) 3D Digital Model



349 ft.

Digital Elevation Model 209 ft.



b)

Figure 4.104 Drone Images of Failed Slope 15: (a) Digital Elevation Model (b) Surface Topography and Profile (Fall 2021)

4.2.14.2 LiDAR

Terrestrial LiDAR scanning data was collected of failed Slope 15 in the fall of 2021. Laser scanning was performed at several stations, and the overlapping point cloud data were collected, then post-processed on a computer and registered together to form a single point cloud. Using a ground extraction algorithm, the low surface points were extracted to create the bare ground point cloud, which was processed in Civil 3D. The topographic surface view was generated at 1 ft. major and 5 ft. minor contour intervals, then a surface profile view was generated, using alignment. The slope's topographic contour view and surface profile view along section A-A' are presented in Figure 4.105

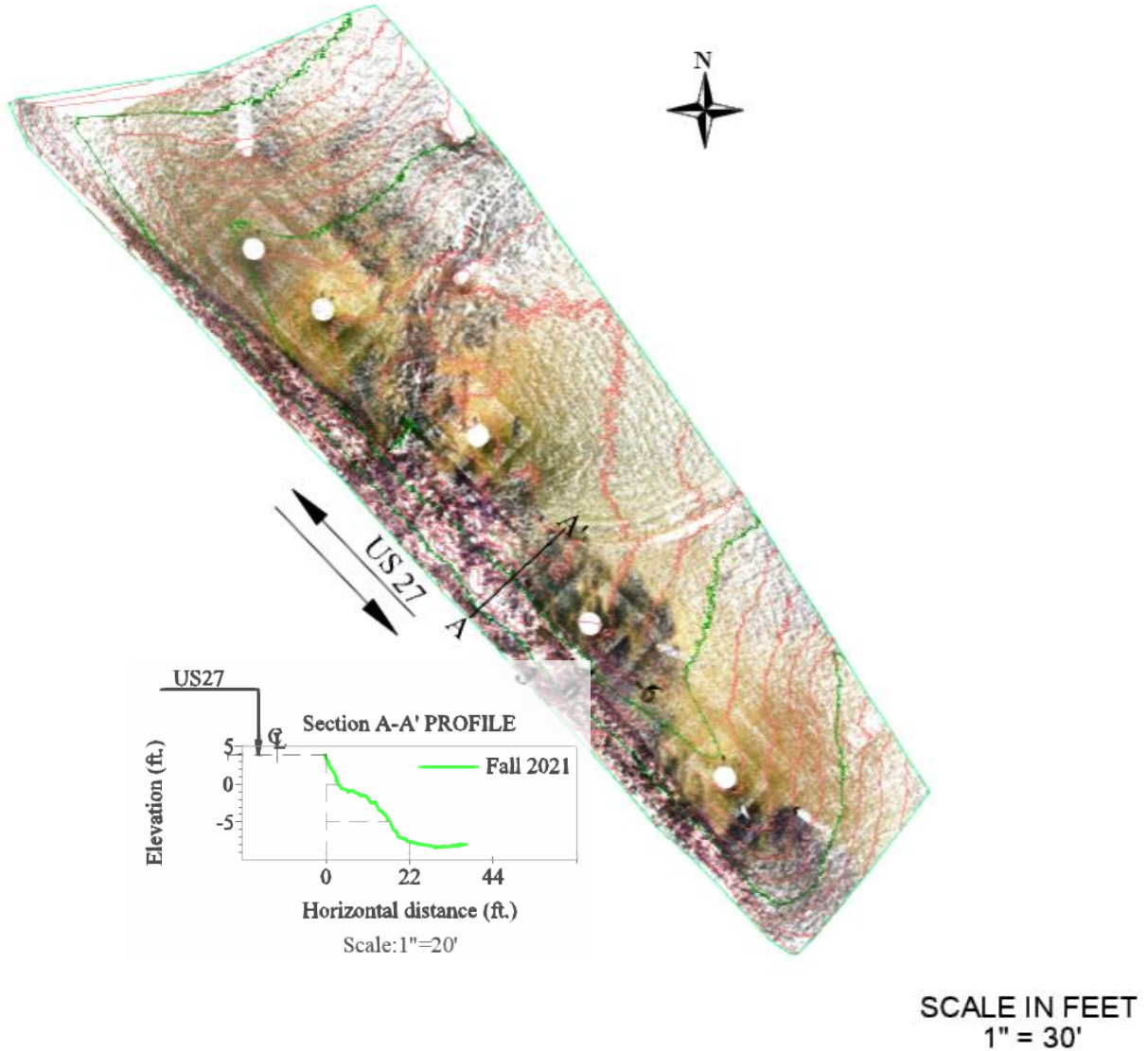


Figure 4.105 LiDAR Point Cloud Surface Topography and Profile View for Failed Slope 15 (Fall 2021)

4.2.15 Failed Slope 17: I-20 EB Approx 1 Mile E of SR 481 at Forrest Near MP 89 Along Mainline Inside Slope

4.2.15.1 ERI

ERI tests were conducted along two lines, A & B, of failed Slope 17, spanning approximately 270 ft. and having electrodes paced at 5 ft. intervals. The slope of the location and the ERI test lines are presented in Figure 4.106. The results, presented in Figure 4.107 (a) & (b), show the presence of high resistivity layers up to approximately 15 ft. depth at Line A, between 30 ft. and 230 ft. horizontal distance, indicating deformed soil. Low resistivity areas are directly below the loose soil, indicating perched water conditions from rainfall infiltration. Line B has a similar ERI pattern but has lower resistivity.



Figure 4.106 ERI Test Lines at Failed Slope 17

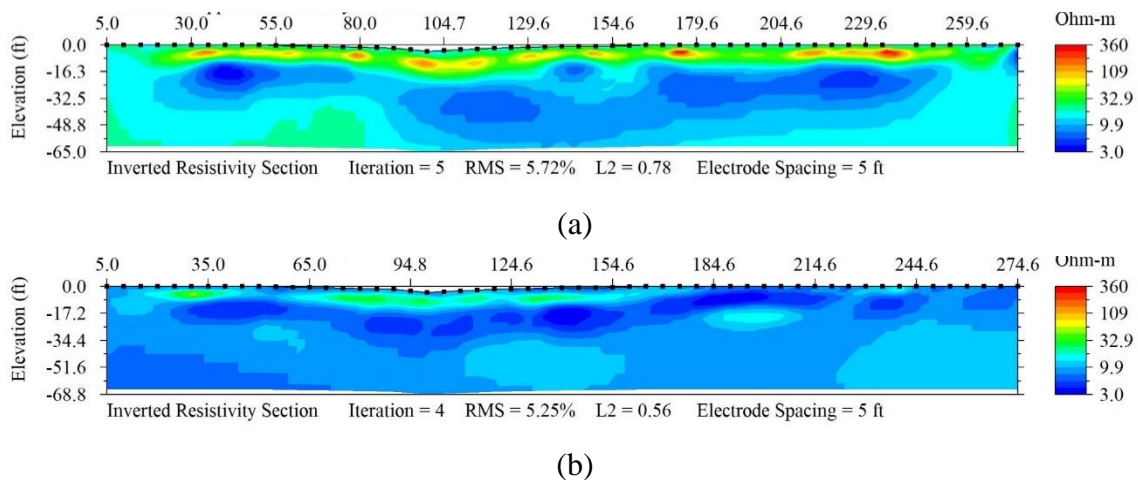


Figure 4.107 ERI Test Results of Failed Slope 17: (a) Line A (b) Line B

4.2.15.2 *Drone*

Drone survey missions were carried out over failed Slope 17 in fall 2021 and fall/winter 2022, and the captured aerial imagery was processed using specialized image processing software. Aerial triangulation was performed with multiple tie points to stitch the images together and develop a digital elevation model (DEM), digital terrain model (DTM), and mosaics. The DEM and orthomosaic digital image representations for Fall 2021 and Fall/Winter 2022 are presented in Figure 4.108 (a) & Figure 4.109 (a). DEMs were imported into Civil 3D, and surfaces were created using the kriging interpolation method. Alignments along the slope were created, and surface profile views were generated along the slope. The topographic contour views and surface profile views for Fall 2021 and Fall/Winter 2022 are presented in Figure 4.108 (b) and Figure 4.109(b). The 3D model representation of the slope and surface profile views for Fall 2021 and Fall/Winter 2022 are presented in Figures Figure 4.108 (c) and Figure 4.109 (c).

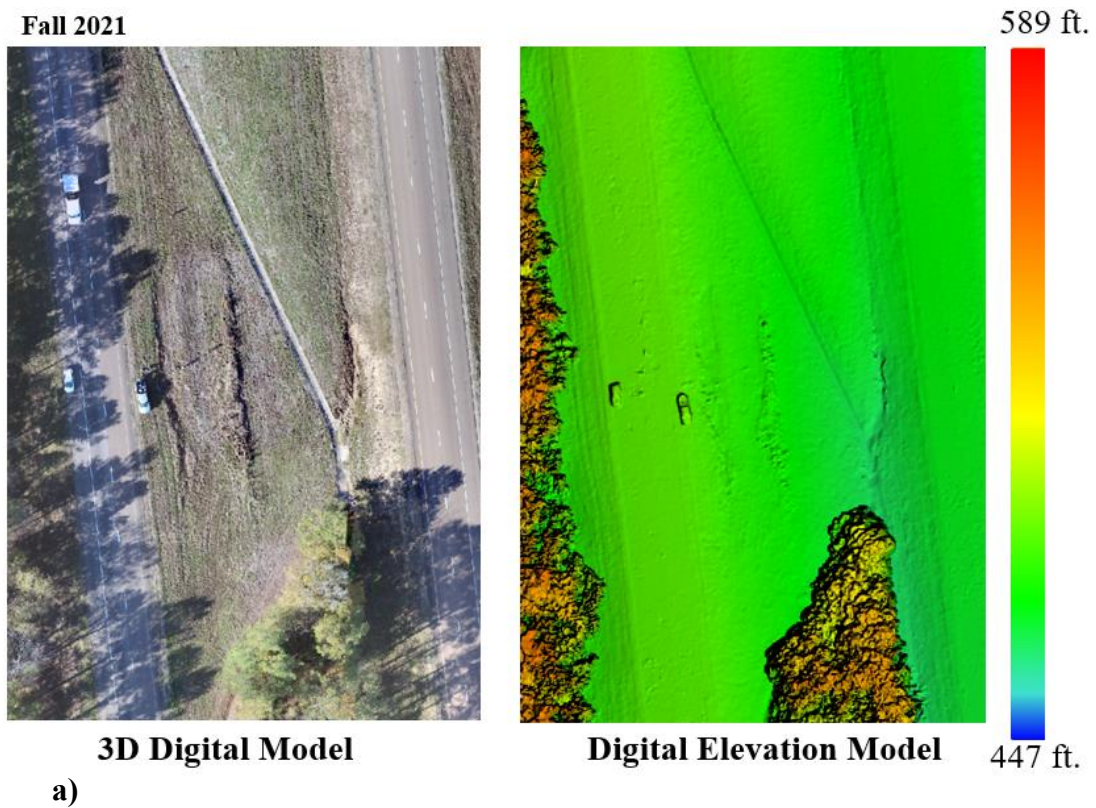


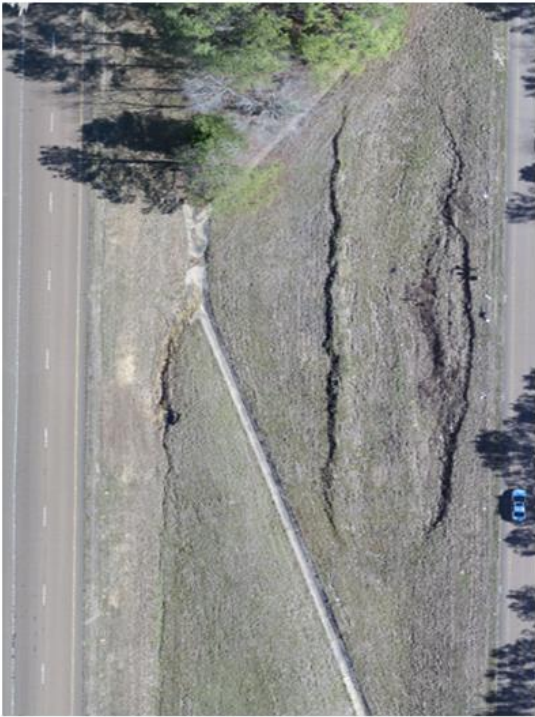
Figure 4.108 (Continued)



Figure 4.108 Drone Images of Failed Slope 17 from Fall 2021: (a) Digital Elevation Model and (b) Surface Topography and Profile

Fall/Winter 2022

589 ft.

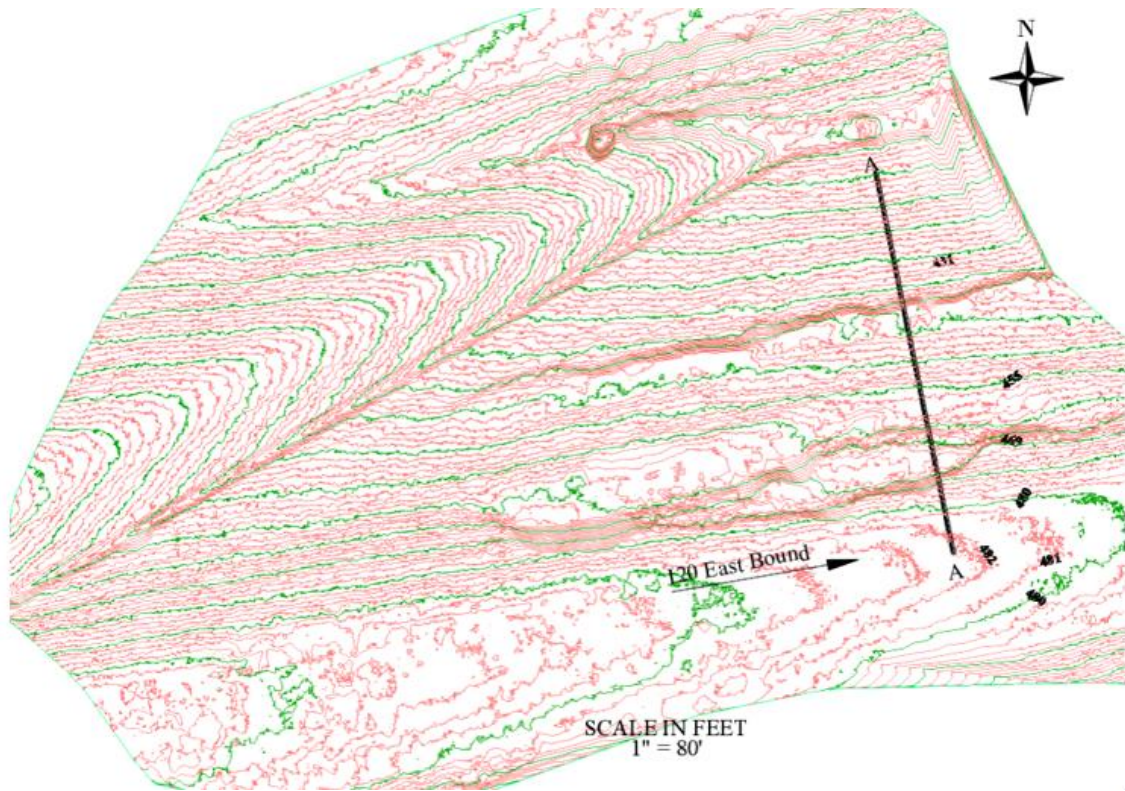


3D Digital Model

Digital Elevation Model

447 ft.

a)



b)

Figure 4.109 (Continued)

Fall/Winter 2022

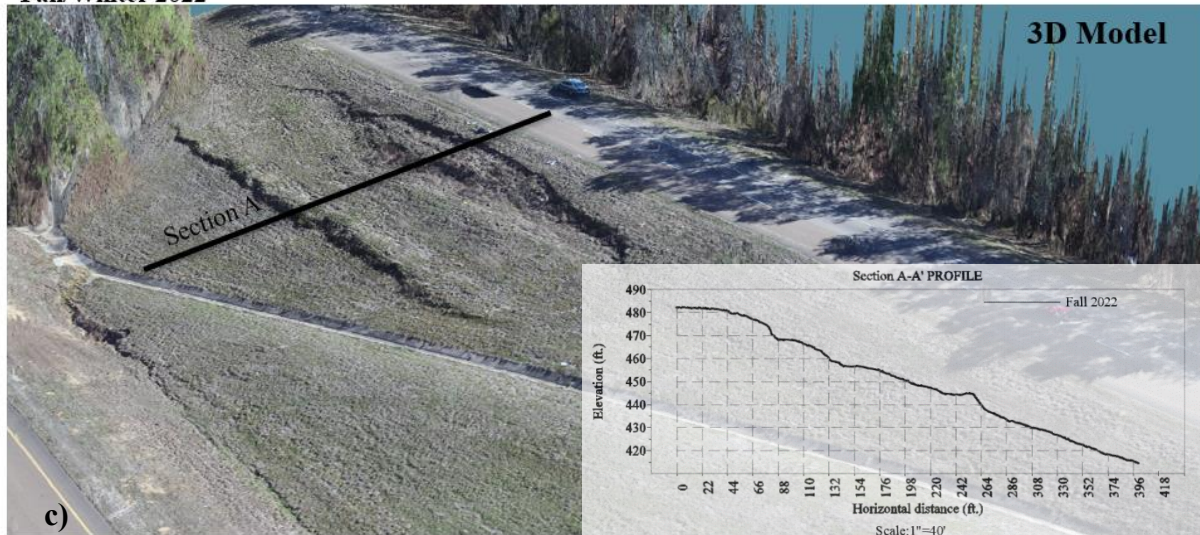
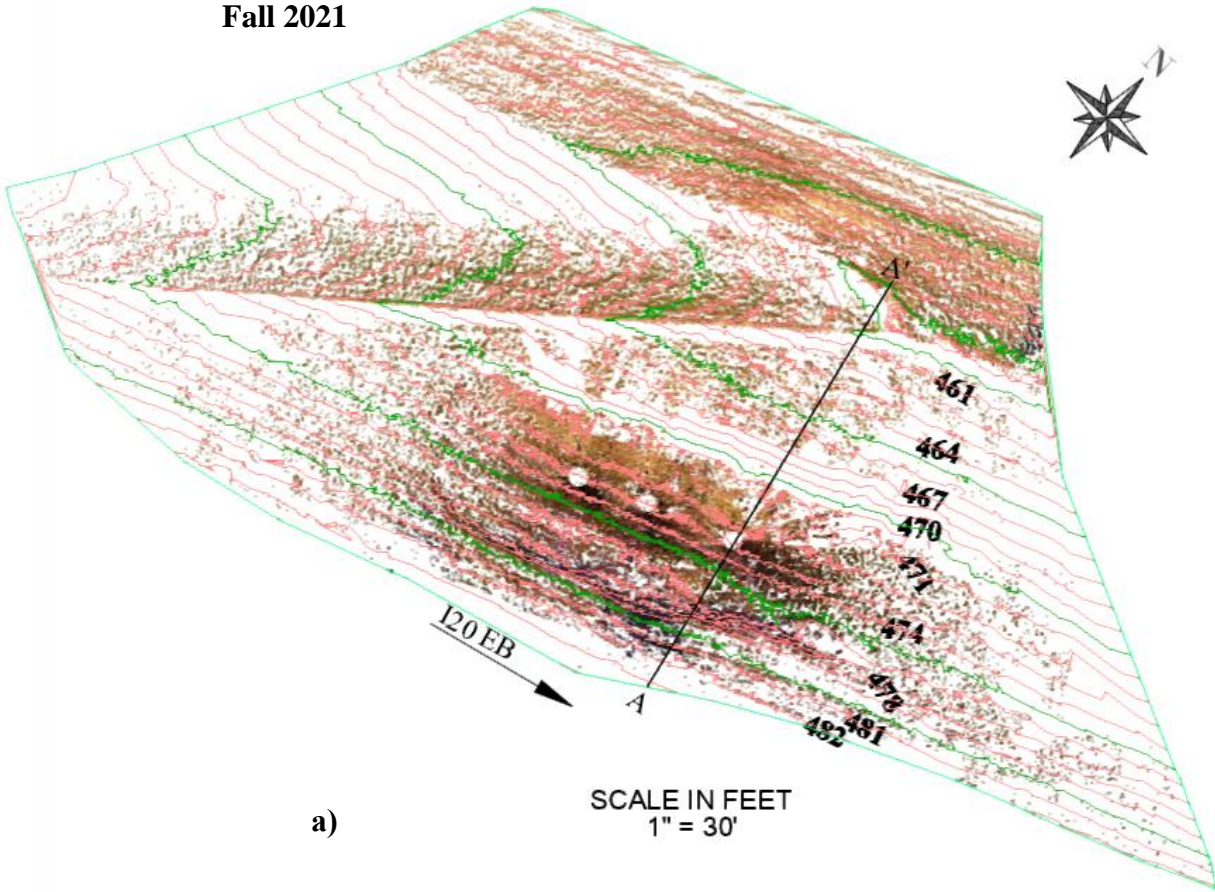


Figure 4.109 Drone Images of Failed Slope 17: (a) Digital Elevation Model, (b) Surface Topography, (c) 3D Model & Surface Profile (Fall 2022)

4.2.15.3 *LiDAR*

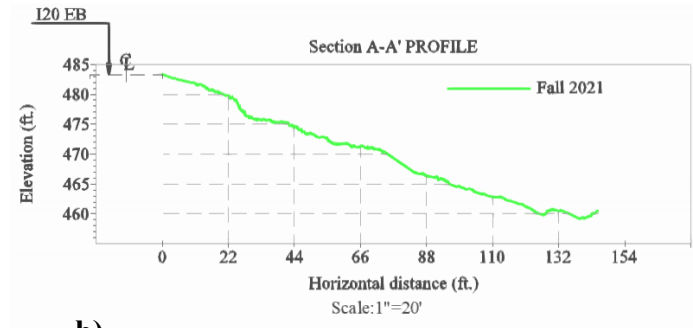
Terrestrial LiDAR scanning data was collected for failed Slope 17 in fall 2021 and fall 2022. Laser scanning was performed at several stations, and the overlapping point cloud data were collected, then post-processed on a computer and registered together to form a single point cloud. The ground control points weren't available for the data collected in fall 2021, so the point cloud wasn't georeferenced; however, the point cloud for fall 2022 was georeferenced using field ground control points with known coordinates. Using a ground extraction algorithm, the low surface points were extracted to create the bare ground point clouds for both seasons, which were imported into Civil 3D, and digital elevation model surfaces were generated using the kriging interpolation method. Topographic surface views for Fall 2021 and Fall/Winter 2022 were generated at 1 ft. major and 5 ft. minor contour intervals and are presented in Figure 4.110 (a) and Figure 4.111 (a), respectively. Surface profile views for Fall 2021 and Fall/Winter 2022 were generated using alignments and are presented in Figure 4.110 (b) and Figure 4.111 (b)

Fall 2021



a)

SCALE IN FEET
1" = 30'



b)

Figure 4.110 LiDAR Point Cloud Surface for Failed Slope 17: (a)Topography, (b) Surface Profile (Fall 2021)

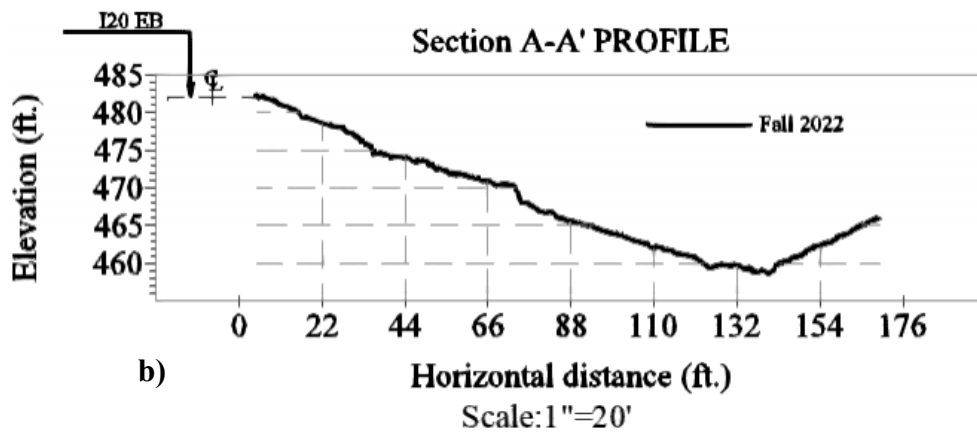
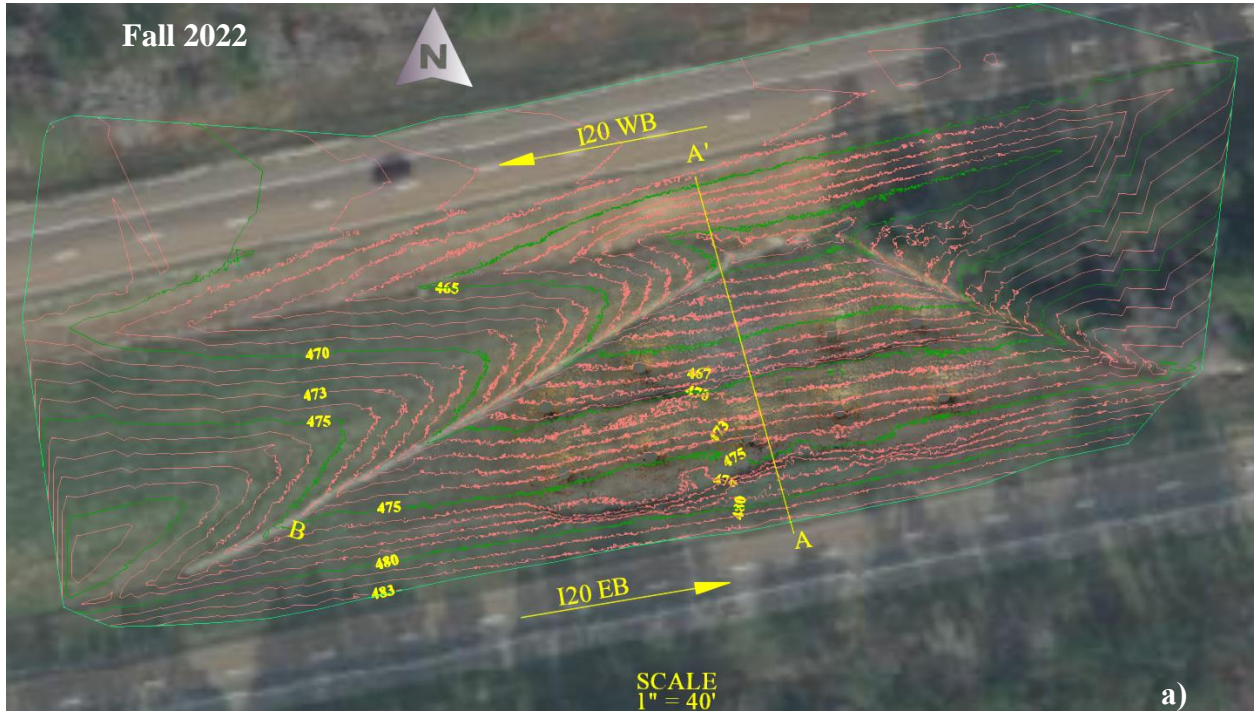


Figure 4.111 LiDAR Point Cloud Surface of Failed Slope 17: (a) Topography, (b) Surface Profile View (Fall 2022)

4.2.16 Failed Slope 18: I-55 NB Exit Ramp at Wynndale Rd Interchange Along Outside Backslope

4.2.16.1 ERI

ERI tests were conducted at failed Slope 18, along Lines A and B spanning approximately 275 ft. and equipped with electrodes spaced at 5 ft. The locations of the slope and test lines are presented in Figure 4.112. The test results are presented in Figure 4.113(a) and (b). The slope is deformed at the surficial level, and there are low resistivity zones at Line A, at shallow depths up to approximately 12 ft., indicating infiltration of water due to surficial soil deformation. High

resistivity layers are present between 155 ft. and 185 ft. horizontal distances, at a depth of 15 ft. to 40 ft..



Figure 4.112 Location of ERI Test Lines in Failed Slope 18

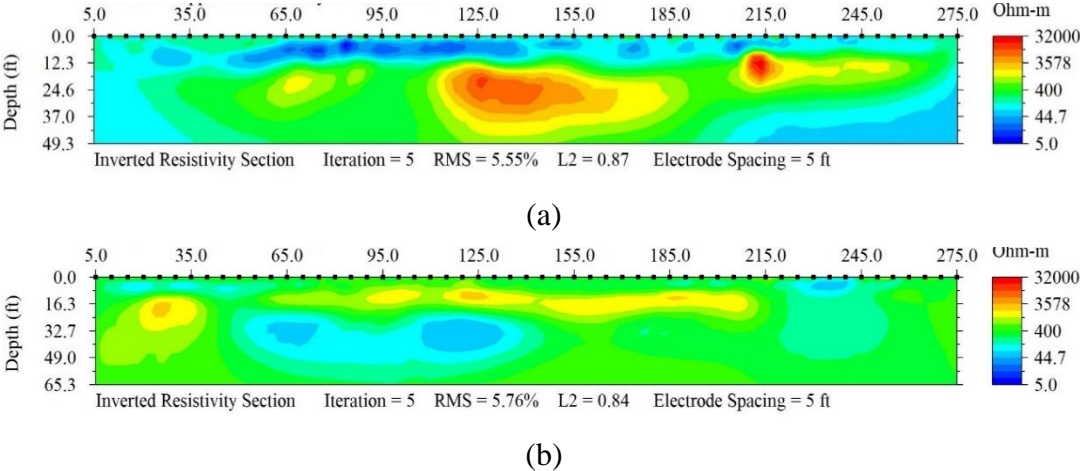


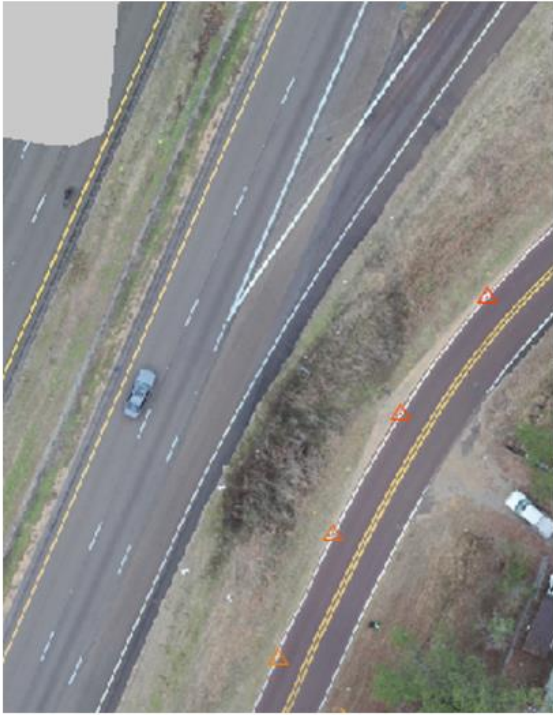
Figure 4.113 ERI Test Results of Failed Slope 18: (a) Line A and (b) Line B

4.2.16.2 *Drone*

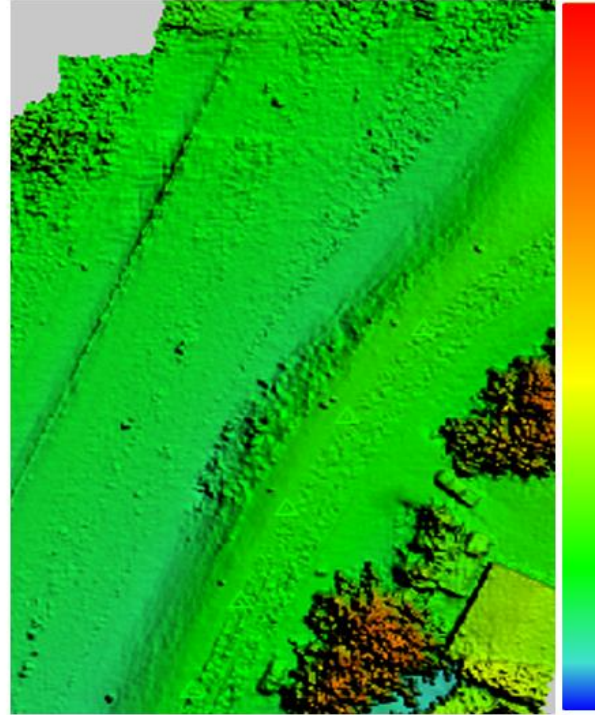
A drone survey mission was carried out over failed Slope 18 in fall/winter 2022, and the aerial imagery captured was processed using specialized image processing software. Aerial triangulation was performed with multiple tie points to stitch the images together and develop a digital elevation model (DEM), digital terrain models (DTMs), and mosaics. The DEM and orthomosaic digital image representations are presented in Figure 4.114 (a). The DEM was imported into Civil 3D, and the surface was created using the kriging interpolation method. Alignment was created and a surface profile view was generated along the slope (section A). The topographic contour is presented in Figure 4.114 (b). The 3D model representation created from the drone imagery, along with the surface profile view, is presented in Figure 4.114(c).

Fall/Winter 2022

471 ft.



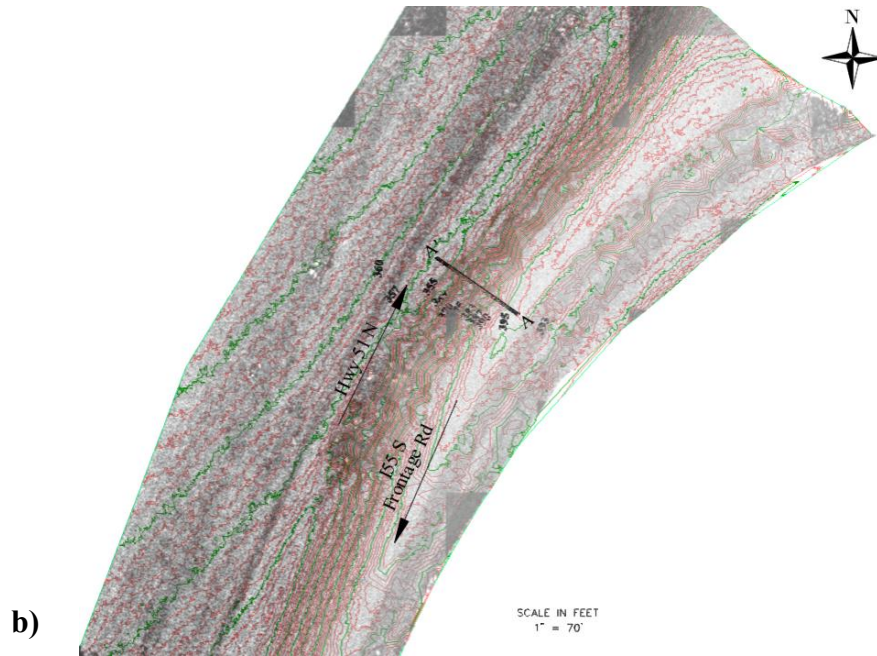
3D Digital Model



Digital Elevation Model

330 ft.

a)



b)

Figure 4.114 (Continued)

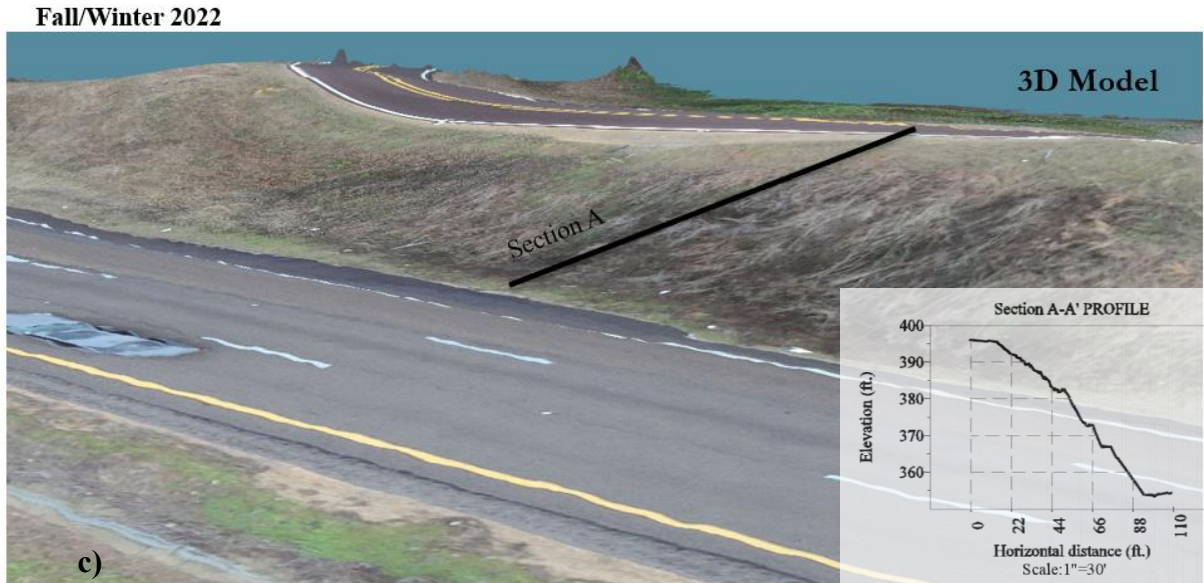
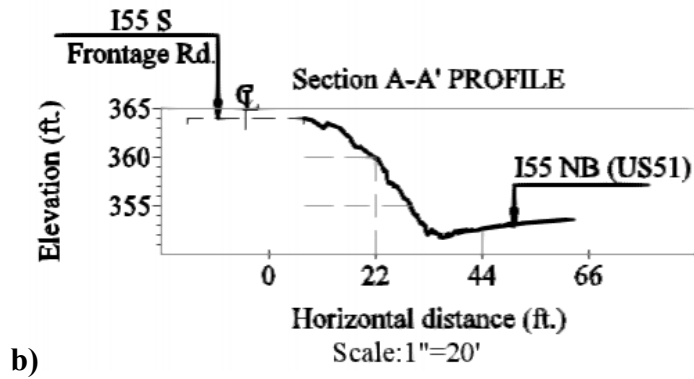
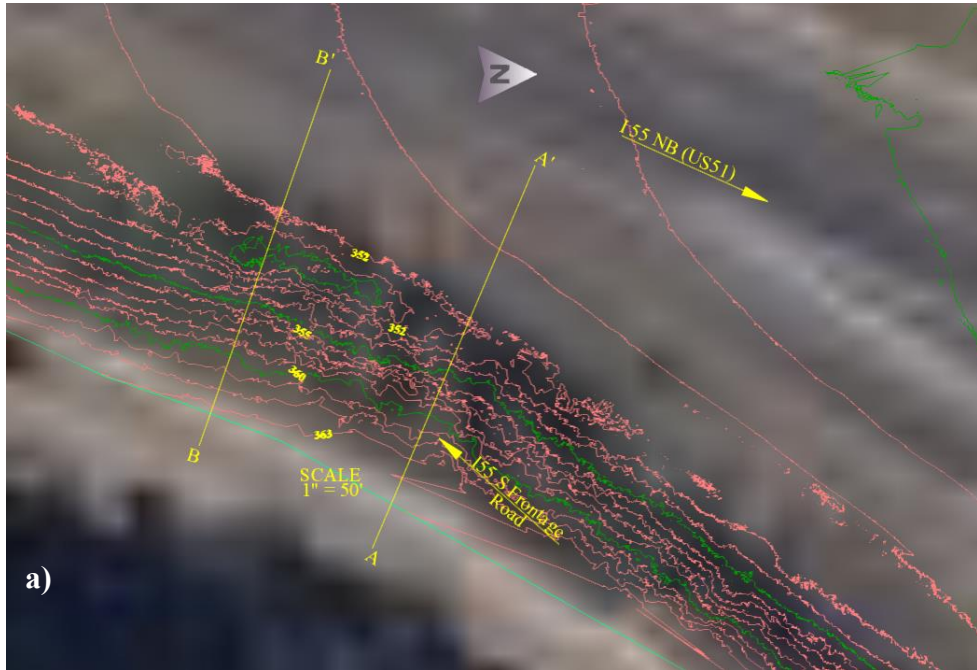


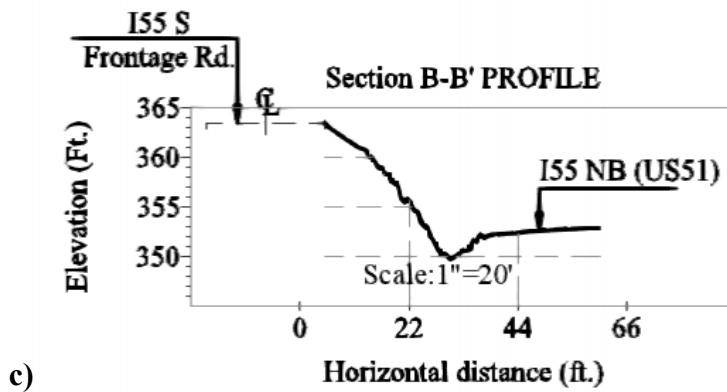
Figure 4.114 Drone Images of Failed Slope 18: (a) Digital Elevation Model, (b) Surface Topography, and (c) 3D Model and Surface Profile (Fall 2022)

4.2.16.3 *LiDAR*

Terrestrial LiDAR scanning was performed at several stations in fall/winter 2022, and overlapping point cloud data were collected, then post-processed on a computer and registered together to form a single point cloud. Using a ground extraction algorithm, low surface points were extracted to create the bare ground point clouds, which were processed in Civil 3D. The topographic surface view was generated at 1 ft. major and 5 ft. minor contour intervals, then a surface profile was generated, using the alignment. The slope's topographic contour view is presented in Figure 4.115 (a), and surface profile views along sections A-A' and B-B' are presented in Figure 4.115 (b) and (c).



b)



c)

Figure 4.115 LiDAR Point Cloud Surface Topography of Failed Slope 18: (a) Surface Topography, (b) Surface Profile Section A-A', (b) Surface Profile Section B-B' (Fall 2022)

4.2.17 Failed Slope 19: Mannsdale Rd HW 463 NB (Madison Site)

4.2.17.1 ERI

ERI tests were conducted for failed Slope 19 along lines A and B that spanned 440 ft. and were equipped with electrodes spaced at 8 ft. intervals. The location of the slope and test lines are presented in Figure 4.116. ERI results for Lines A & B are presented in Figure 4.117 (a) and (b). Patches of low resistivity zones exist at both lines, across the entire horizontal span of the ERI profile, as the slope and road have suffered extensive settlement over the years due to the condition of the soil.



Figure 4.116 Location of ERI Test Lines in Failed Slope 19

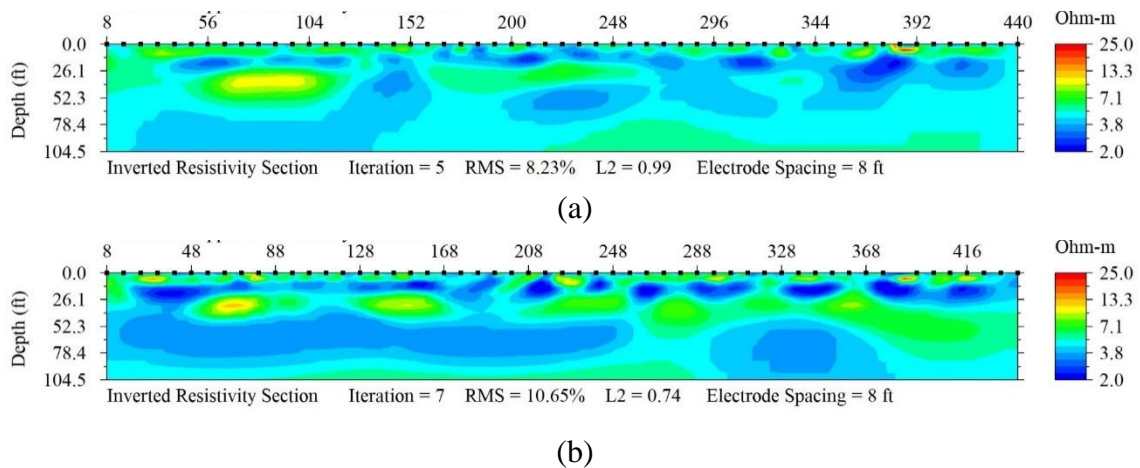


Figure 4.117 ERI Test Results of Failed Slope 19: (a) Line A and (b) Line B

4.2.17.2 Drone

A survey mission was carried out by drone over failed slope 19 in spring 2022, and the aerial imagery captured was processed using specialized image processing software. Aerial triangulation was performed with multiple tie points to stitch the images together and develop a digital elevation model (DEM), digital terrain models (DTMs), and mosaics. The DEM was

imported into Civil 3D, and the surface was created using the kriging interpolation method. Alignment was created along the slope, and a surface profile view was generated along Section A of the slope. The DEM and orthomosaic digital images and the surface profile view are presented in Figure 4.118.

Spring 2022

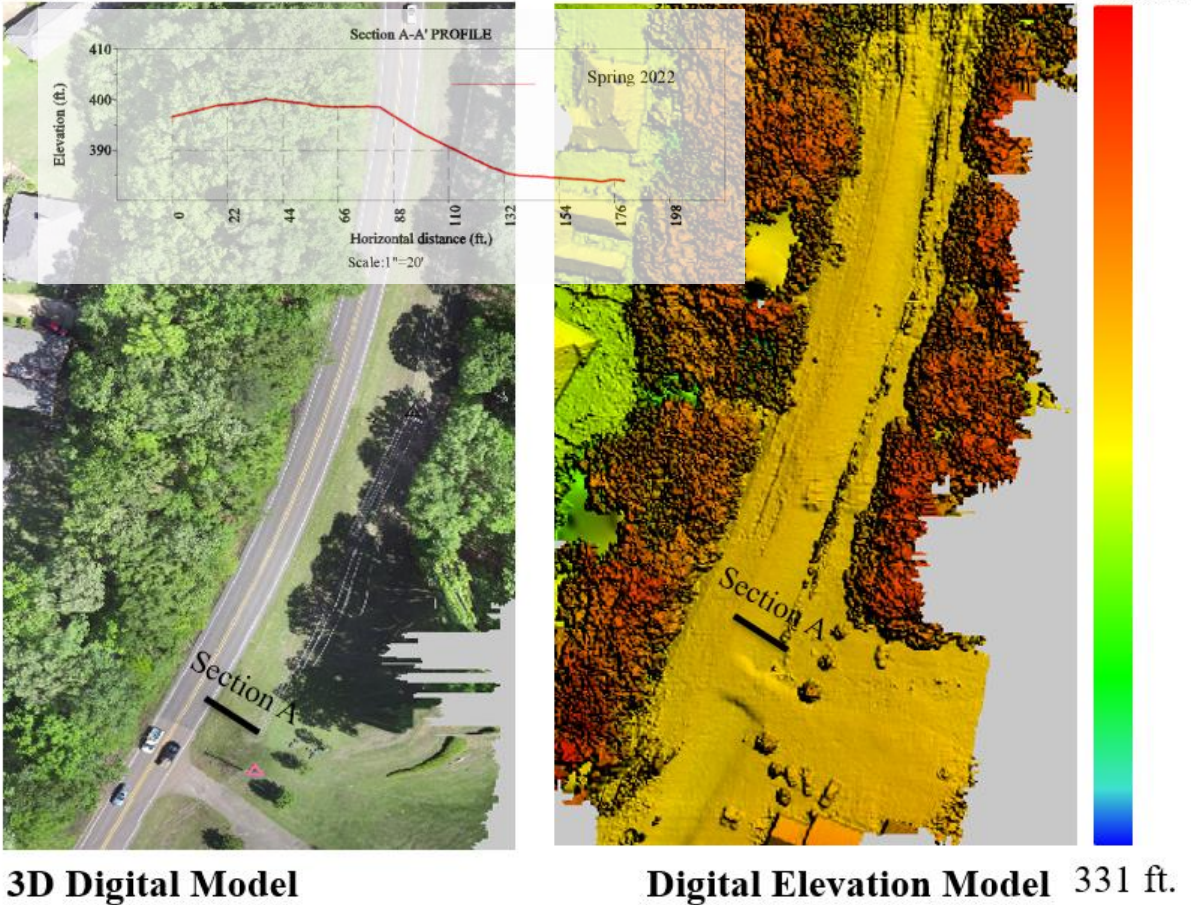


Figure 4.118 Drone Images of the DEM and Surface Profile of Failed Slope 19 (Spring 2022)

4.2.17.3 *LiDAR*

Terrestrial LiDAR scanning was performed at several stations in fall 2021 and spring 2022, and the overlapping point cloud data were collected, then post-processed and registered together to form a single point cloud. The combined point clouds for both seasons were georeferenced using field ground control points with known coordinates. Using a ground extraction algorithm, the low surface points were extracted to create the bare ground point clouds. The bare ground point clouds were imported into Civil 3D, and the digital elevation model surfaces were generated using the kriging interpolation method. Topographic surface views were generated at 1 ft. major and 5 ft. minor contour intervals and are presented in Figure 4.119 (a) and (b), respectively. The surfaces from the two seasons were overlaid, and alignments were created along the slope. Stacked surface profiles were then created using the alignments along Section A-A,' which is presented in Figure 4.120.

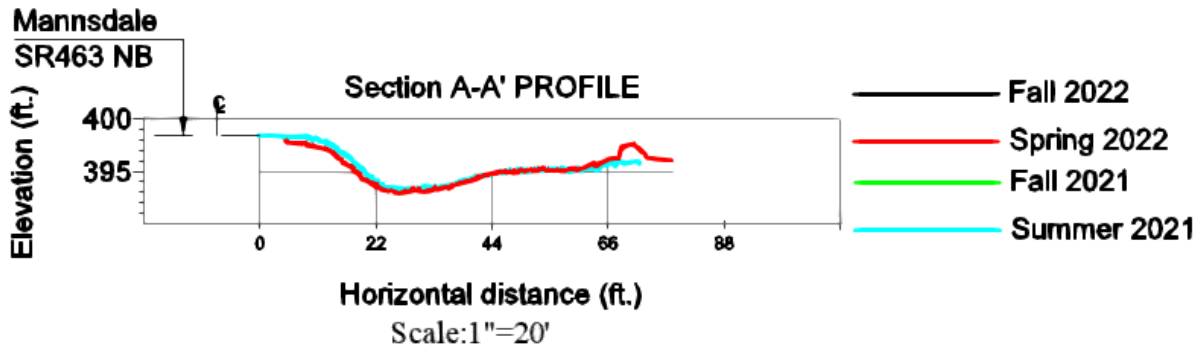


Figure 4.120 LiDAR Point Cloud Overlaid Surface Profiles for Failed Slope 19

4.2.18 Failed Slope 20: Mannsdale Rd HW 463 SB (Madison Site)

4.2.18.1 ERI

ERI tests were performed along Lines A and B of failed slope 20 that spanned 495 ft. and were equipped with electrodes spaced at 9 ft. intervals. The locations of the slope and ERI test lines are presented in Figure 4.121. The ERI results are presented in Figure 4.122 (a) and (b). Patches of high resistivity exist along both lines in the shallow depths, indicating loose or deformed soil. Low resistivity areas exist directly below the loose soil, from 15 to 30 ft. depths, indicating perched water conditions from rainfall infiltration.



Figure 4.121: ERI Test Lines at Failed Slope 20

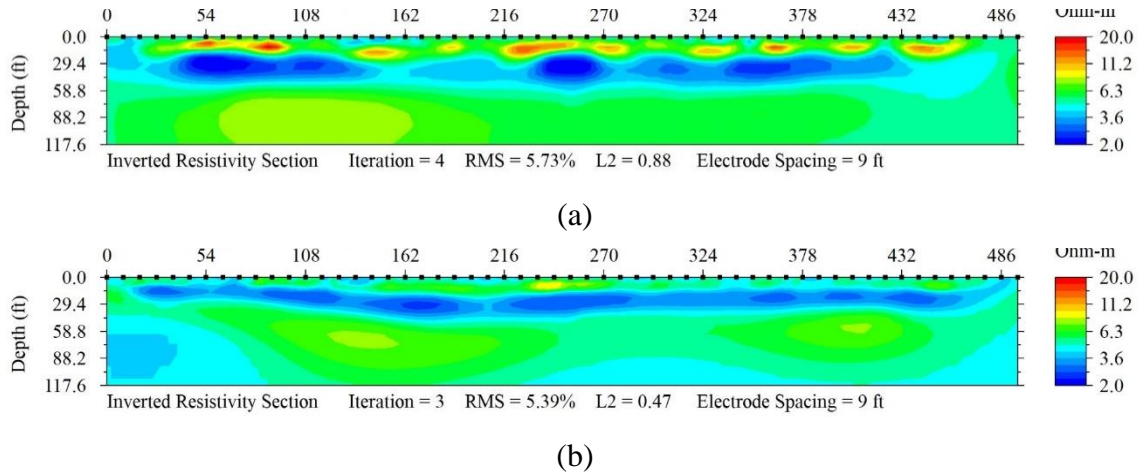


Figure 4.122 ERI Test Results of Failed Slope 20: (a) Line A and (b) Line B

4.2.18.2 *Drone*

A survey mission was carried out by a drone over failed Slope 20 in spring 2022, and the aerial imagery captured was processed using specialized 0

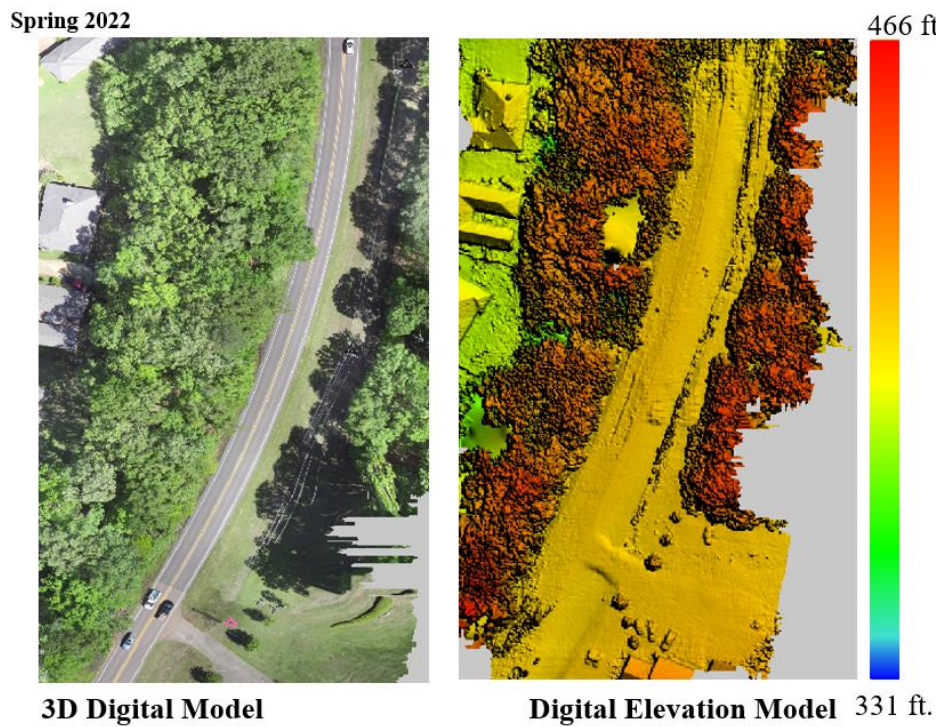


Figure 4.123 Drone Images of DEM for Failed Slope 20 (Spring 2022)

CHAPTER 5 APPLICATION OF ADVANCED LANDSLIDE MONITORING METHODS

5.1 Introduction

This study monitored instrumented slopes and failed slopes using multiple advanced techniques such as instrumentation, electrical resistivity imaging (ERI), drones, and LiDAR. The collected data was analyzed using advanced tools and software for advanced site characterization and to understand the slope's behavior over time. Examples of slope monitoring applications are provided in this chapter.

5.1.1 Instrumentation

Six highway slopes in the Jackson, MS area, were instrumented with sensors to monitor various soil parameters. The soil parameters include soil moisture content, matric suction, soil temperature, air temperature, and rainfall intensity. Industrial-grade sensors such as GS-1 moisture sensors, Meter Teros 21 soil water potential sensors, ECRN-50 tipping bucket rain gauges, EM50 data loggers, and RT-1 air temperature sensors were installed at each slope. Additionally, two 30 ft. long inclinometer casing pipes were installed at each slope to track and assess slope movement along the grade. The sensors were connected to data loggers through cables of approximately 150 ft. in length, enabling the collection of continuous and real-time measurements. Data loggers were programmed to gather readings from the various sensors hourly, providing valuable information about moisture levels, temperature, and rainfall intensity.

5.1.2 Electrical Resistivity Imaging (ERI)

ERI surveys enable the creation of subsurface resistivity profiles, which offer insights into an area's geological composition and moisture distribution. The collected resistivity data from the field investigation, obtained through AGI's Super-Sting R8/IP equipment, was processed using EarthImager-2D software. This software facilitated the construction of an initial model based on the resistivity information. Then the software performed ERI inversion to transform the field data into color-coded 2D image profiles. The observed voltage and current measurements were used to rebuild the subsurface resistivity distribution during the ERI inversion process.

5.1.3 LiDAR

In this study, 3D laser scanning was performed using Trimble X7 terrestrial LiDAR equipment. Dense point cloud data were acquired from an embankment that had previously experienced extreme surficial deformations and failure. Topographical surfaces were developed using the dense point cloud data, and the bare ground was extracted. Temporally spaced surface profiles of the failed and undamaged areas of the slopes were created for comparative analysis, and the surface profiles were matched against the resistivity imaging profiles collected during the same time period.

This study utilized Trimble X7 terrestrial LiDAR equipment for 3D laser scanning of a previously failed embankment. Dense point cloud data was acquired and used to develop topographical surfaces, followed by the extraction of bare ground. The comparative analysis

involved creating surface profiles of both the failed and undamaged areas of the slopes, which were then matched with resistivity imaging profiles collected concurrently.

5.1.4 UAV

Aerial imagery for this study was captured using the DJI Matrice 200 Professional Quadcopter, referred to as a drone or UAV. Weighing 9.986 lb., including the camera payload, and with an endurance of approximately 24 minutes, the UAV features an integrated 3-axis gimbal system to stabilize the camera during flight. This minimizes vibration-induced blur in the aerial images. The gimbal allows for a pitch range of -90° (nadir) to $+30^{\circ}$, adjustable in-flight using the DJI GO and COPTERUS mobile application. Aerial images were captured in daylight using the UAV-mounted FLIR's Zenmuse XT2 payload unit featuring a 1/1.7" CMOS 12.4 megapixel camera. The UAV was operated both manually and automatically by a remote FAA-licensed small unmanned aerial system (sUAS) pilot. UAV flights were carried out at elevations ranging from approximately 100 ft. to 300 ft. over the areas of interest. The airborne photography was completed at each slope site location (shown in Figure 5.1) in approximately 10 to 20 minutes.

5.2 ERI, LiDAR and UAV for Site Characterization

5.2.1 Site Description & Methodology

Data collected from UAV, LiDAR, and ERI investigations for the four slopes in central Mississippi listed below were used to evaluate their current conditions. The methodology schematic is presented in Figure 5.2

- Highway Slope at I220S exit 1B Ramp
- Highway Slope at I20E near Exit 100
- Highway Slope at US 49S toward Jackson
- Highway Slope at SR 25S/43 Interchange

5.2.2 Data Collection

Resistivity data at the slope sites were collected using multiple ERI survey lines with 56 electrodes configured in a dipole-dipole array on each slope. The collected data were processed through EarthImager software to obtain resistivity image profiles.

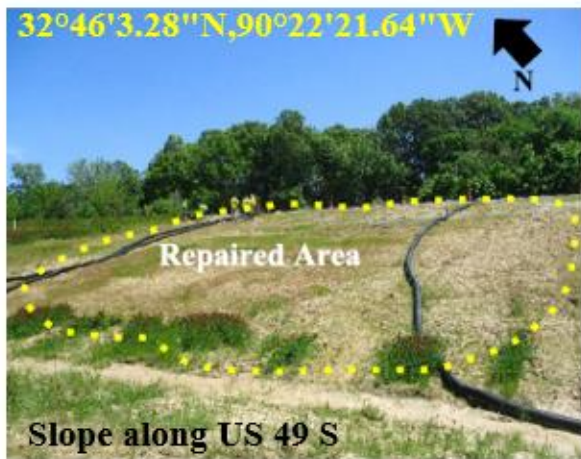


Figure 5.1 Sites Selected for Comparing Results of Geophysical and Remote Sensing Investigations

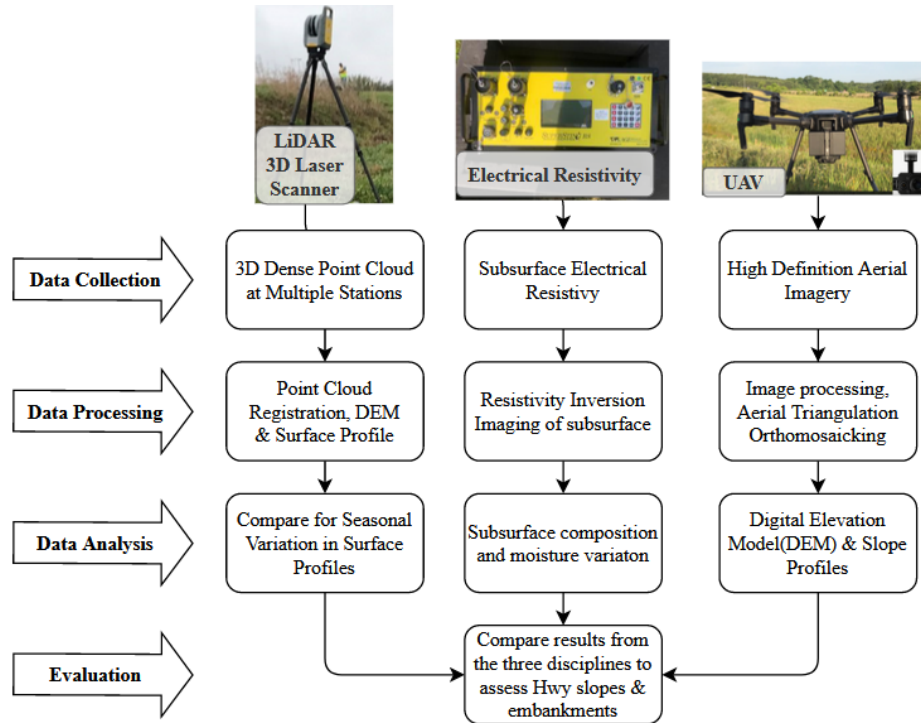


Figure 5.2 Schematic of Methodology (Nobahar et al., 2023)

UAV Field Test Data Collection: Aerial images were obtained from a DJI Matrice 200 Professional Quadcopter (UAV or drone). The drone imagery was processed by specialized image processing software, and a DEM and DSMs were created using well-established photogrammetry procedures.

LiDAR: Trimble X7 terrestrial LiDAR scanner was deployed at five stations on the slope for surveying, and point cloud data was collected during the scanning process. Additionally, 10 spherical targets were positioned 4 ft. above the ground around the slope to assist with the registration of the point cloud data obtained from each station.

5.2.3 Data Analysis & Results

5.2.3.1 Slope along Metrocenter, I220S Exit 1B Ramp to US 80W

The failed slope was investigated by conducting ERI testing, LiDAR, and drone surveys.

ERI Results

The results of the ERI analysis for embankment lines A, B, C, and D at the Metrocenter site indicate the presence of multiple low-resistivity areas within the embankment. (See Figure 5.3.) The ERI profiles show areas characterized by low resistivity in blue. These regions exhibit resistivity values ranging from 2 to 6 Ohm-m. The presence of low resistivity indicates a high degree of soil saturation and the presence of water accumulation zones, known as perched water zones, within the embankment. Areas with high resistivities, indicated by yellow and red colors, are relative, depending on the nature of the soil. High resistivity areas are denoted by deformed and loosely packed soil that tends to have larger air voids. The extent of a failed area can be

identified based on high resistivity areas (red-colored zones) and by the sag in the ERI profile, as seen in Figure 5.3.

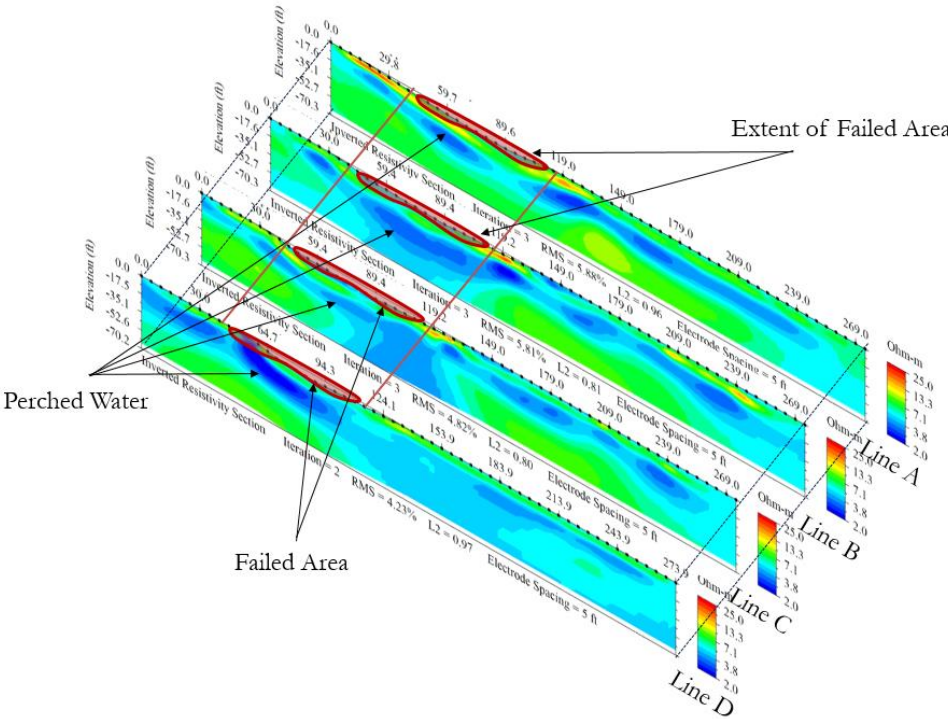


Figure 5.3 ERI Test Results of Line A, B, C & D for Slope along I220N and I55 N Interchange

Drone Results

After collecting the data, the images were processed using specialized software, and digital elevation models (DEM) were created, using the principles of photogrammetry. The DEMs were further classified into digital surface models (DSMs) and digital terrain models (DTMs). DSMs capture the elevation of all objects such as vegetation; DTMs eliminate all artificial and natural features and retain only the natural surface of the earth. DTMs provide more precise information about elevation changes than DSMs, as they capture both natural and artificial features of the slope failure and provide more detailed information about the soil profile settlement. The elevation changes were calculated by measuring the slope of each pixel. The DTM, DSM, and 3D output data created using the results of UAV surveying are presented in Figure 5.4 and help clearly identify the characteristics of the slope failure. The failure area can be clearly delineated from the drone DSM, and the area of soil that moved was estimated as 10522 sq. ft.; the volume of soil that moved was estimated as 4550 cu. ft.

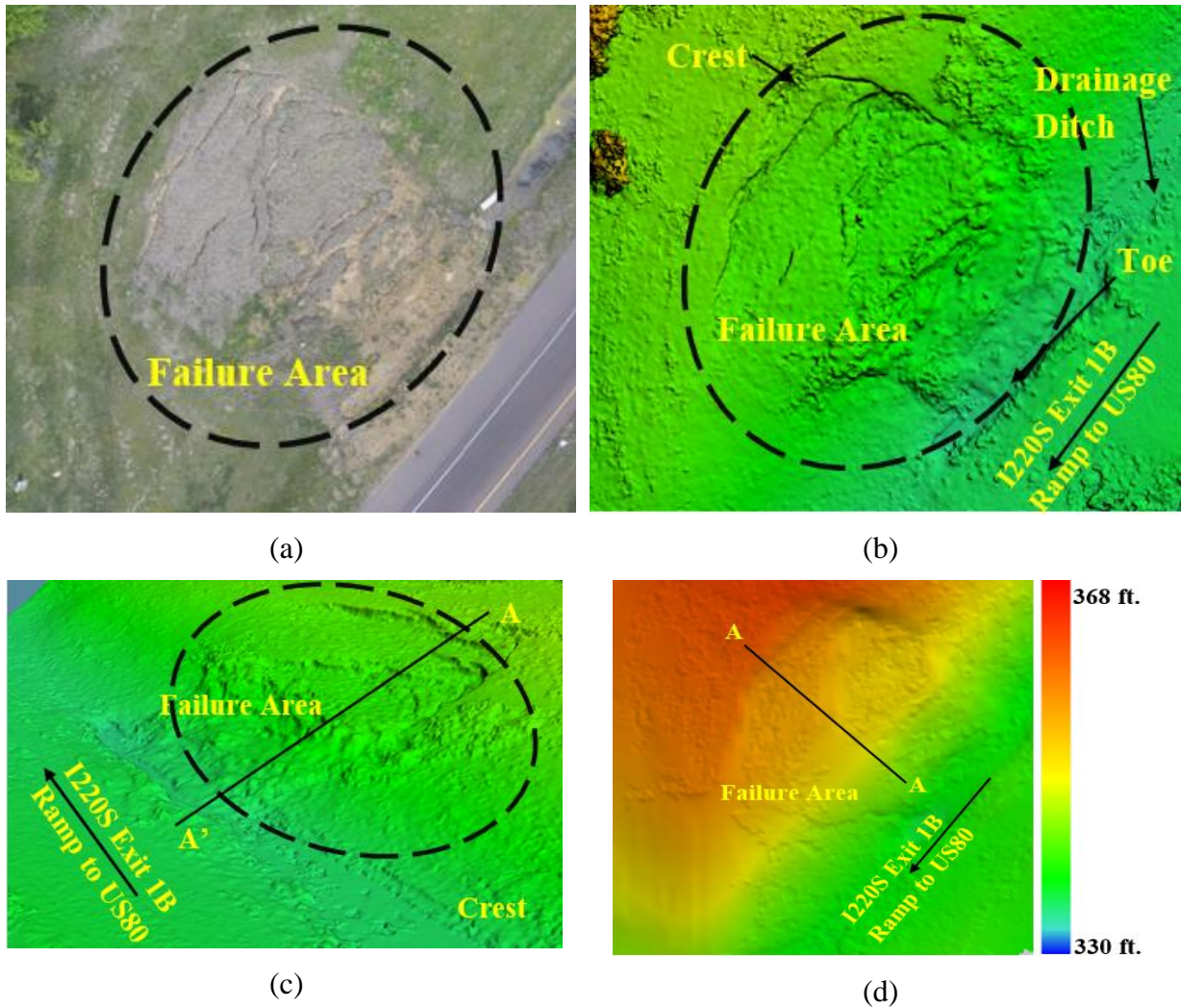
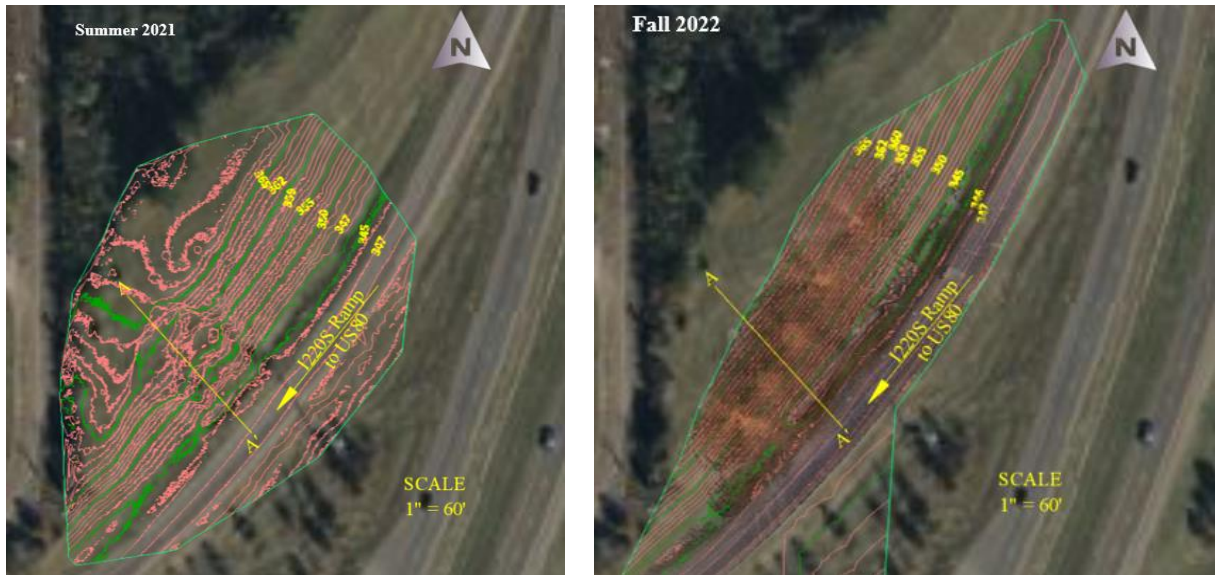


Figure 5.4 ERI Test Site for Slope at Metrocenter (I220S Exit 1B Ramp Toward US80): (a) UAV Orthomosaic Image, (b) UAV DSM, (c) UAV 3D DSM, (d) UAV DTM, (e) UAV Surface Profile

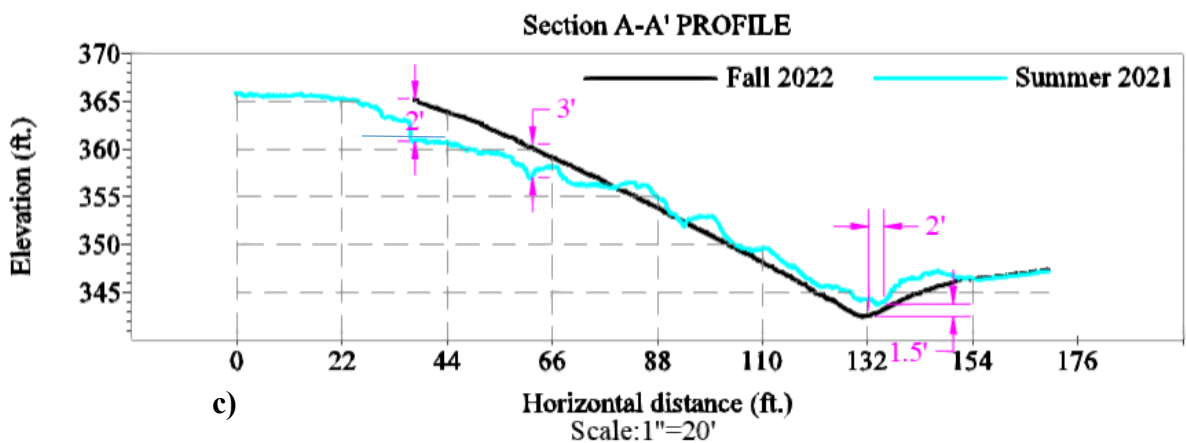
LiDAR Results

The point cloud data collected during the summer of 2021 and the fall/winter of 2022 were processed and analyzed following the workflow described in Section 5.1.3. The resulting surface profiles, obtained at different time intervals, are shown in Figure 5.5. The point clouds from both seasons were registered independently. The temporally spaced point clouds were georeferenced and stacked on each other to compare them and detect any changes that occurred. The slope surface profiles for different seasons were extracted from the same locations on both point clouds. Comparing the pre-failure profile with the post-repair surface profile revealed crucial information. From Figure 5.5(c), it is evident that the crest of the slope is 2 ft. higher than the collapsed part of the slope. Near the middle of the slope, the elevation had to be raised 3 ft. from the failed level. At the toe of the slope, the excess dirt had to be removed, and as a result, the repaired slope at toe was about 1.5 ft. lower than that of the collapsed slope.



(a)

(b)



(c)

Figure 5.5 ERI Test Site for Slope at Metrocenter (I220S Exit 1B Ramp Toward US80): (a) LiDAR Surface Topography Summer 2021, (b) LiDAR Surface Topography Fall/Winter 2022, (c) LiDAR Stacked Surface Profiles

Evaluation

Analysis of LiDAR-captured point cloud data and drone DEM showed variations in the surface profile settlement. The LiDAR output was far more detailed regarding surface variations, but the drone imagery provided excellent visualization, as seen in the DSM and DTM presented in Figure 5.4. The results of the UAV surveying analysis helped identify the characteristics of slope failure. The ERI analysis of embankment lines A, B, C, and D at the Metrocenter site showed the presence of multiple low resistivity areas within the subsurface embankment, which suggests a high level of soil saturation and the existence of water accumulation zones. These perched water zones may have caused the eradication of suction over time in the surficial level and resulted in slide failure. The ERI image profile also confirmed the depth of the slip surface, which was highlighted by areas of high resistivity due to the presence of loose soil with air voids.

5.2.3.2 Slope along I20E Before Exit 100

ERI Results

The ERI analysis of Lines A & B of the failed slope along I20 near exit 100 is presented in Figure 5.6. Several low resistivity areas are located at different points along the embankment profile, suggesting soil saturation and water accumulation (perched water zones) within the embankment. For example, the dark blue area between 90 ft. and 150 ft. on the ERI profile along line A, which has the lowest resistivity value (less than 3 Ohm-m at a depth of 34 ft.), suggests a high potential for soil movement due to high soil saturation.

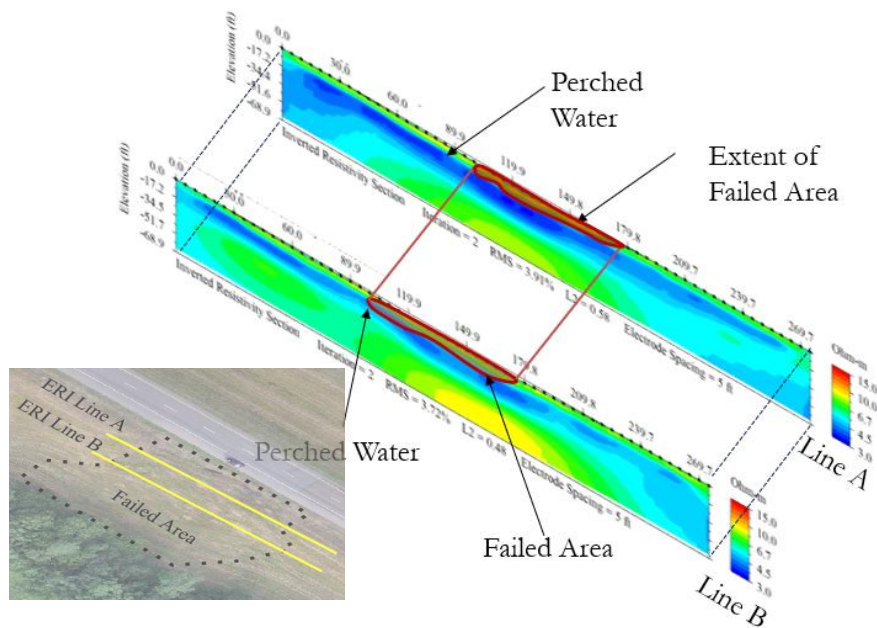


Figure 5.6 ERI Test Results for Lines A & B for Slope along I20E Before Exit 100

Drone Results

The failed slope near Exit 100 on I20 EB was analyzed using imagery captured by the drone. The aerial imagery was processed, the DEM, DSM, and 3D output data were generated, and the surface failure profile was extracted using the DEM model, as shown in Figure 5.7. The profile reveals that the soil has settled 5.14 ft. at 10 ft. from the crest of the embankment and 5.56 ft. at the toe of the embankment. By using DEM, it is possible to create a detailed map of the failure area, accurately define the failure's boundaries, and measure the area of the soil that has moved (15,801.73 sq. ft.) and the amount of dirt that has been displaced (33,270.30 cubic ft.).

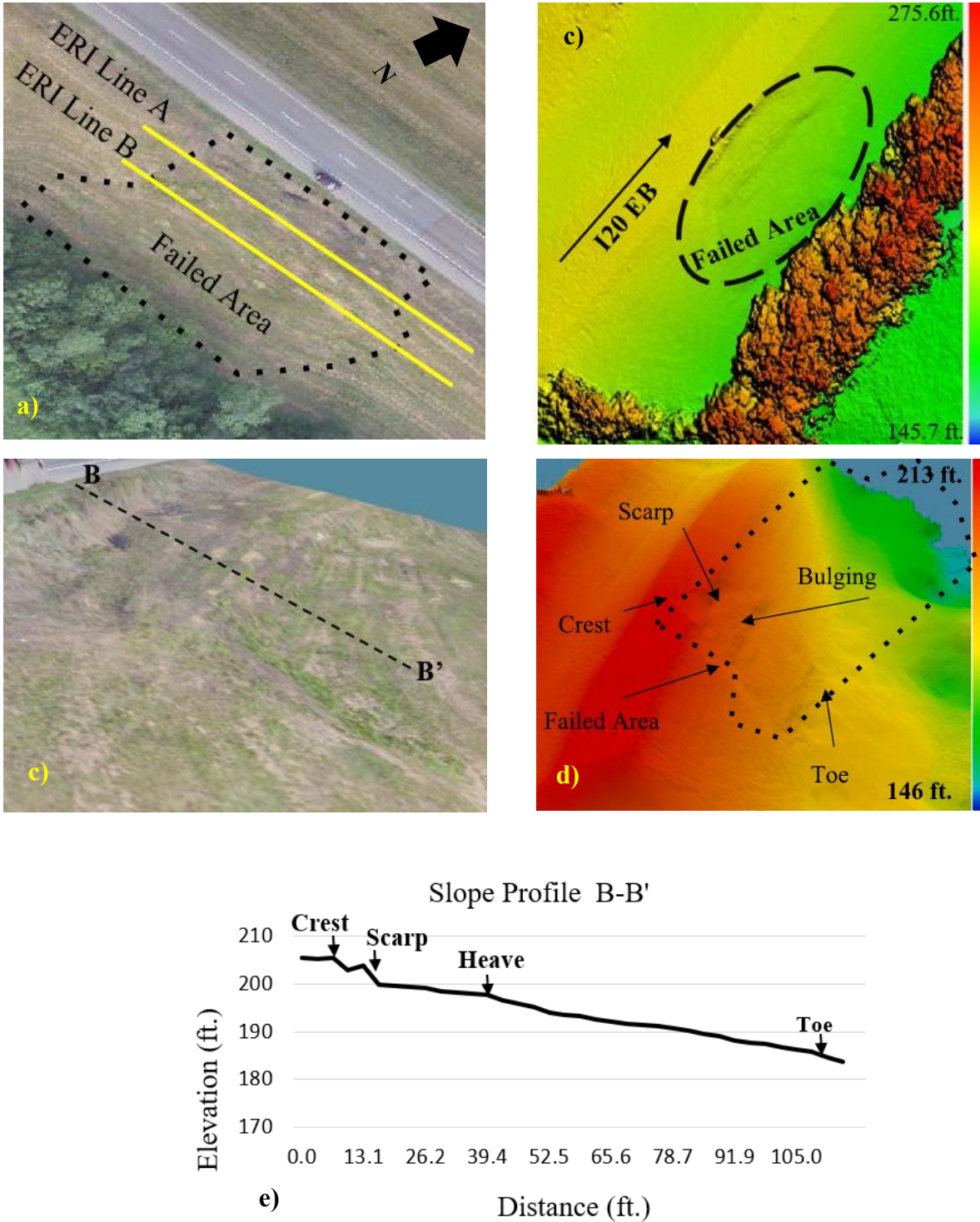


Figure 5.7 Slope at I20 EB Exit 100: (a) UAV Orthomosaic Image, (b) UAV DSM, (c) UAV 3D Model, (d) UAV DEM, (e) UAV Surface Profile

LiDAR Results

The elevations presented below are from the Mississippi State Plane Coordinate System and are different from the drone results, which are in the GPS system. The surface topography and profile obtained from the LiDAR survey are presented in **Figure 5.8**. Regardless of the coordinate system, the surface profile developed from the LiDAR point cloud is similar to that obtained from the drone DEM.

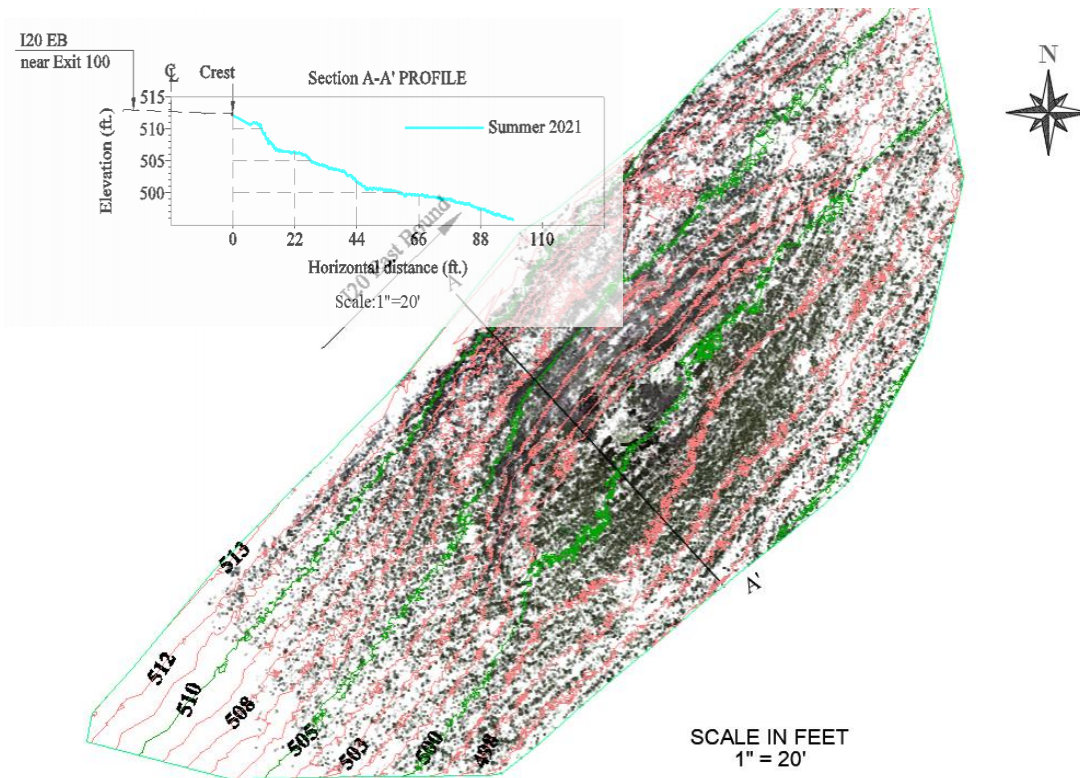


Figure 5.8 LiDAR Results: Surface Topography and Profile View

Evaluation

The location of the slope failure indicated by the drone and LiDAR surface representations coincide with the ERI profile low resistivity areas within the subsurface, indicating zones with excessively wet soil. The surface profiles created from both drone imagery and LiDAR verify the failure dimensions, eliminating the need for manual measurements. The wet zones delineate the depth of the slip surfaces, whereas the surface profile and DEM help characterize the extent of the failure and several morphological aspects such as scarp, heaving, and so forth.

5.2.3.3 Slope along US 49S Toward Jackson

ERI Results

The ERI profiles of the embankment at Lines A, B, and C in Figure 5.9 indicate several zones with low resistivity. The red color in the Line A profile represents high resistivity areas that were covered with a mesh to repair the embankment. The low resistivity blue color in the Line A profile below 10 ft. represents areas with soil saturation and water accumulation, or perched water zones within the embankment. According to the inspection findings of Line C, the

embankment toe has been completely saturated with water due to rainwater infiltration. This suggests that there is a high risk of the embankment failing.

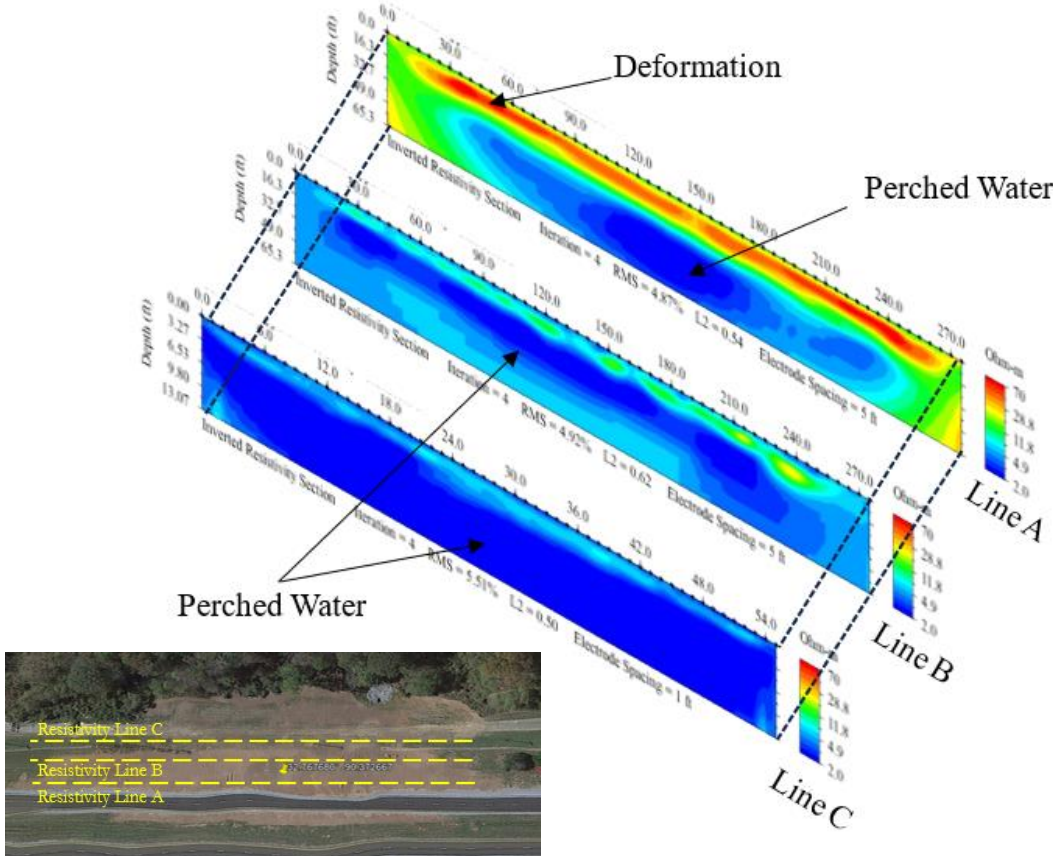


Figure 5.9 ERI Test results for Lines A, B & C for Failed Slope along US49S toward Jackson

Drone Results

The analysis results of the UAV survey imagery for the embankment are presented in Figure 5.10. The images were captured after the slope failure was repaired; therefore, little settlement is visible from the surface profile. The orthomosaic and the DEM are presented in Figure 5.10, and the failure length and width were delineated and measured as 95 ft. long x 145 ft wide. The DSM provides clear boundaries around the failure area and an accurate measurement of the amount of soil moved (12,948.98 sq. ft.).

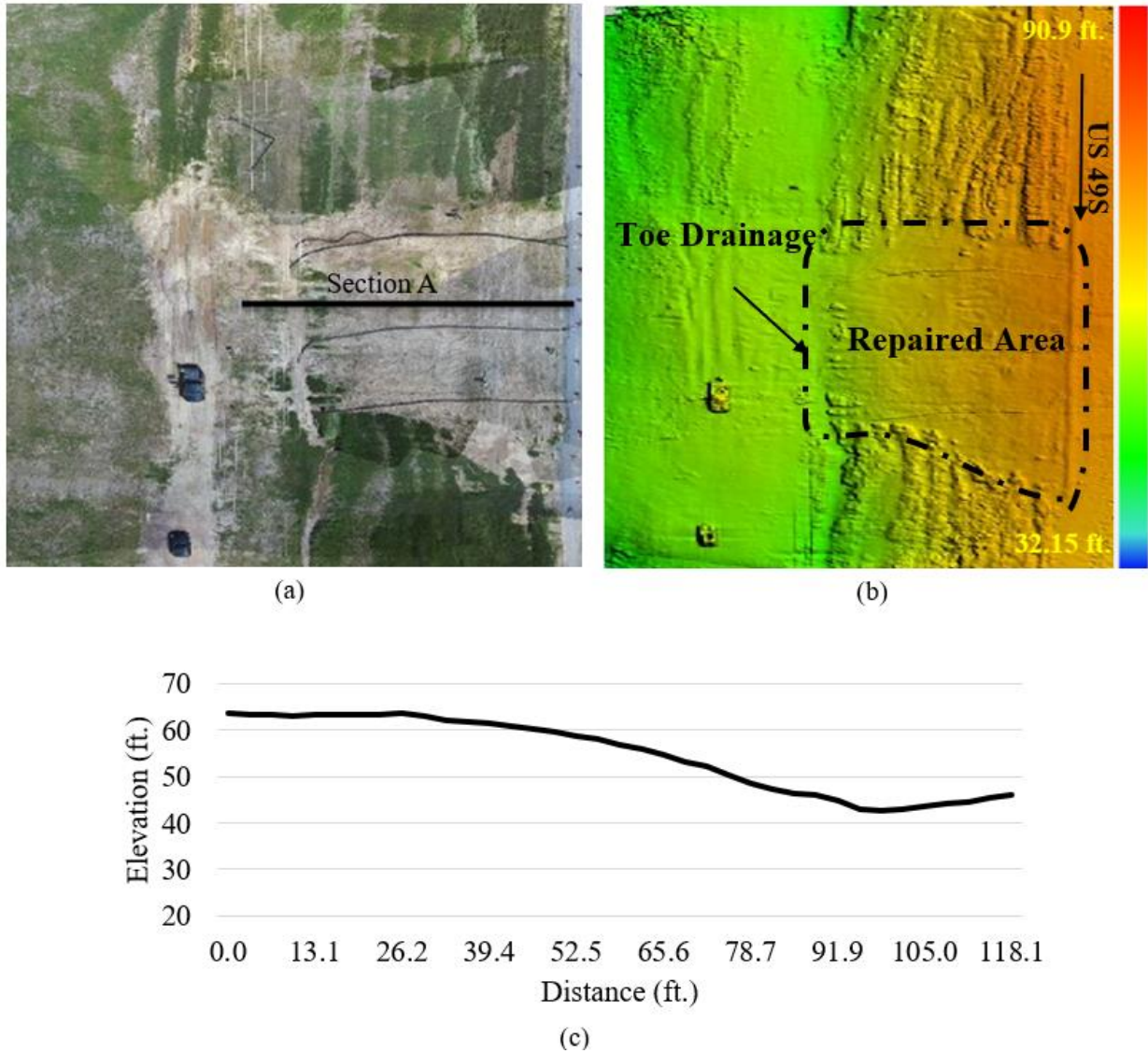


Figure 5.10 Slope at US49S 20 EB Exit 100: (a) UAV Orthomosaic Image, (b) UAV DSM, (c) UAV Surface Profile

Evaluation

Comparing the ERI results of the drone survey results provided much valuable information. For instance, the extent of the repaired area, which is clear from the UAV DEM in Figure 5.10, coincides with the subsurface higher resistivity areas in the ERI profiles in Figure 5.11, thus informing the extent of the repair of the previously failed area in x, y and z directions. The high resistivity zones up to a depth of 16 ft. at Lines A, B & C indicate the depth of the slip surface, which was repaired.

5.2.3.4 Slope along Highway 25S/MS43 Interchange

ERI Results

The ERI profiles for Lines A, B and C at the slope along US HWY 25 are presented in Figure 5.11. Lines A and C have higher resistivity than Line B, indicating that the middle of the slope has high water accumulation that might have weakened the shear strength of the slope soil and caused the failure.

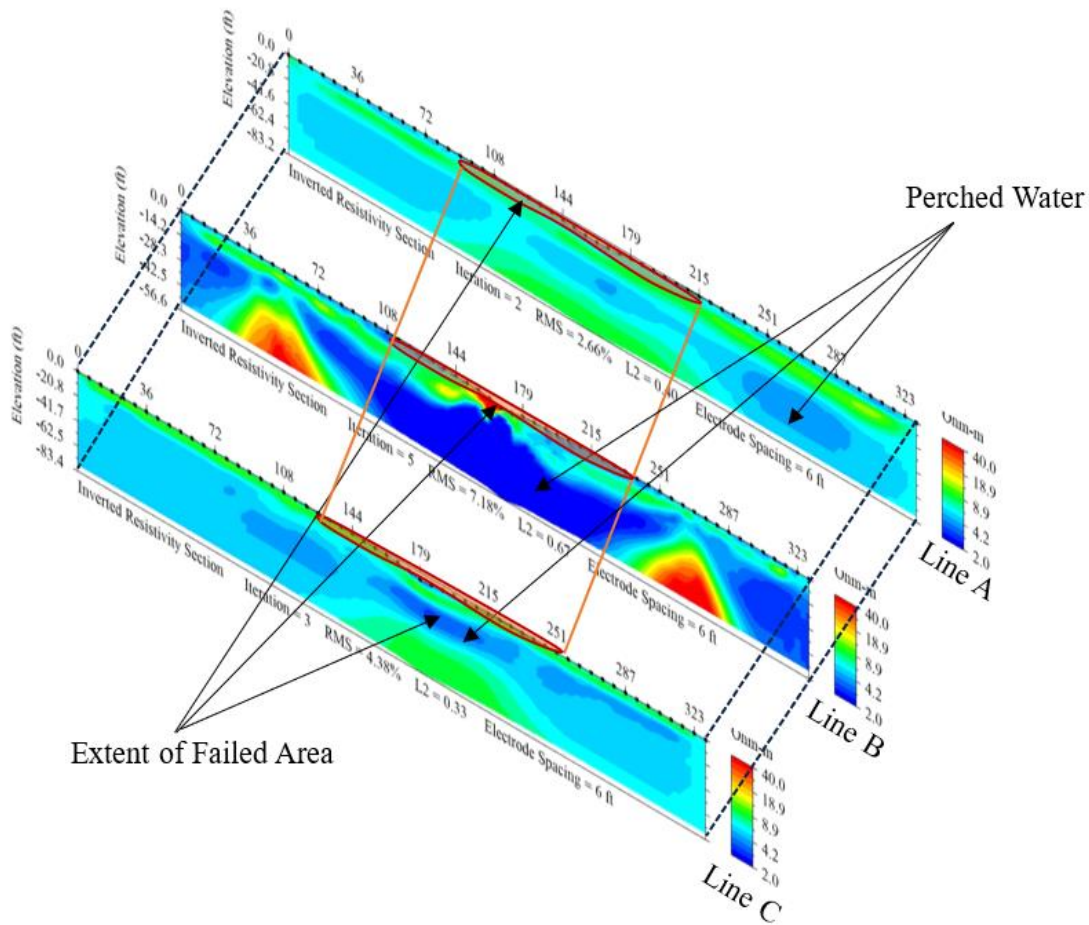
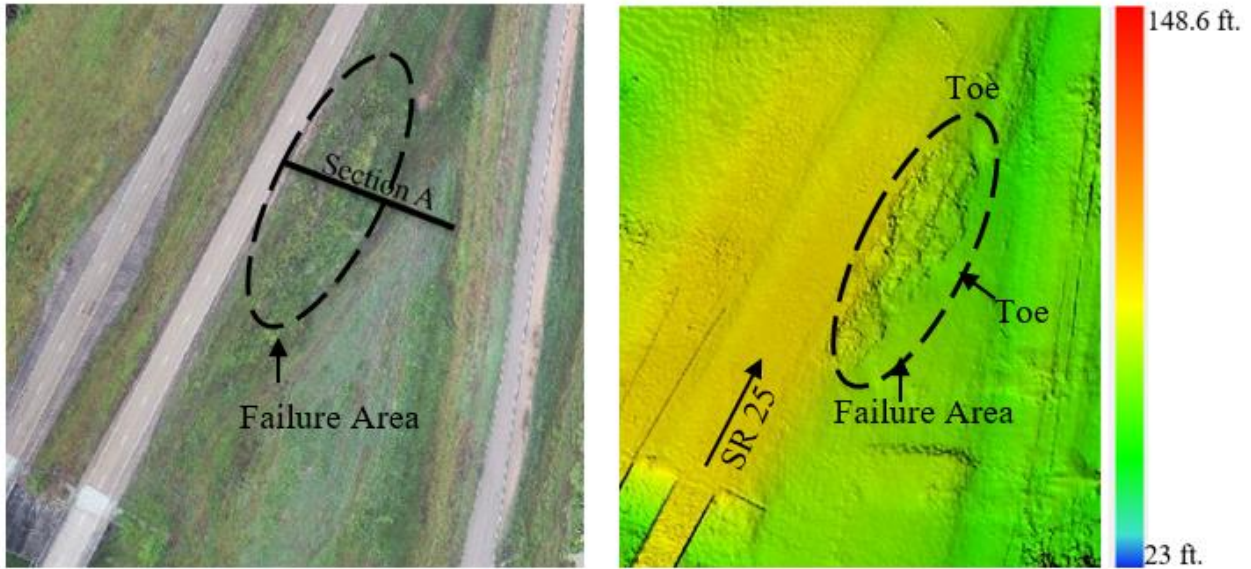


Figure 5.11 ERI Test Results of Line A, B, and C for Failed Slope along Hwy 25 at MS25/43 Interchange

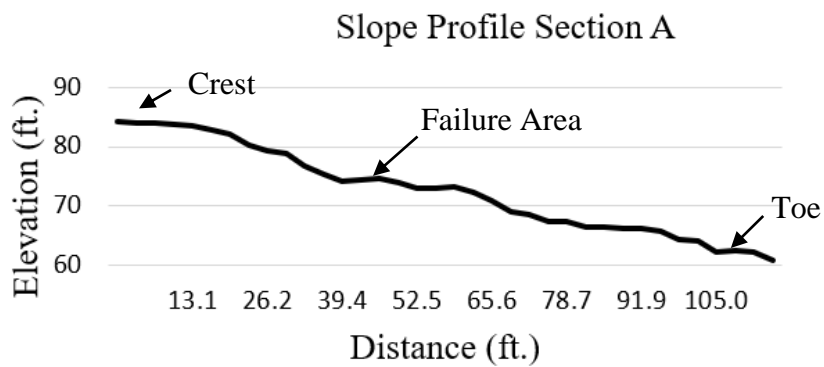
Drone Results

The characteristics of the failure along Highway 25 were identified using DEM. The failure profile was extracted using the DEM model, as shown in Figure 5.12. Based on the profile, the soil settlement is 3.15 ft. at 26 ft. horizontal distance from the crest, which is approximately the middle of the embankment. The failure depth, which was clearly defined by the DEM, was measured as 3.33 ft. at the toe of the embankment. The area of the soil moved was measured at 22,625.37 sq. ft.



(a)

(b)



(c)

Figure 5.12 Slope along SR 25: (a) UAV Orthomosaic Image, (b) UAV DSM, (c) UAV Surface Profile

LiDAR Results

Point cloud data collected from the terrestrial LiDAR survey was processed and analyzed, and the resulting surface topography and surface profiles are presented in Figure 5.13. The LiDAR surface profile is similar to that provided by the UAV, except that it is more detailed, once again proving that LiDAR point clouds provide greater detail in surface profiles than UAVs. The failure area can also be identified in the LiDAR surface profile by the drop in elevation on the surface profile view. The subsurface resistivity on the ERI profile at this point also indicated high resistivity soil, indicating the presence of loose deformed soil and thus providing corroboration. Continuous LiDAR monitoring of the slope can detect changes and variations in slope profiles over time.

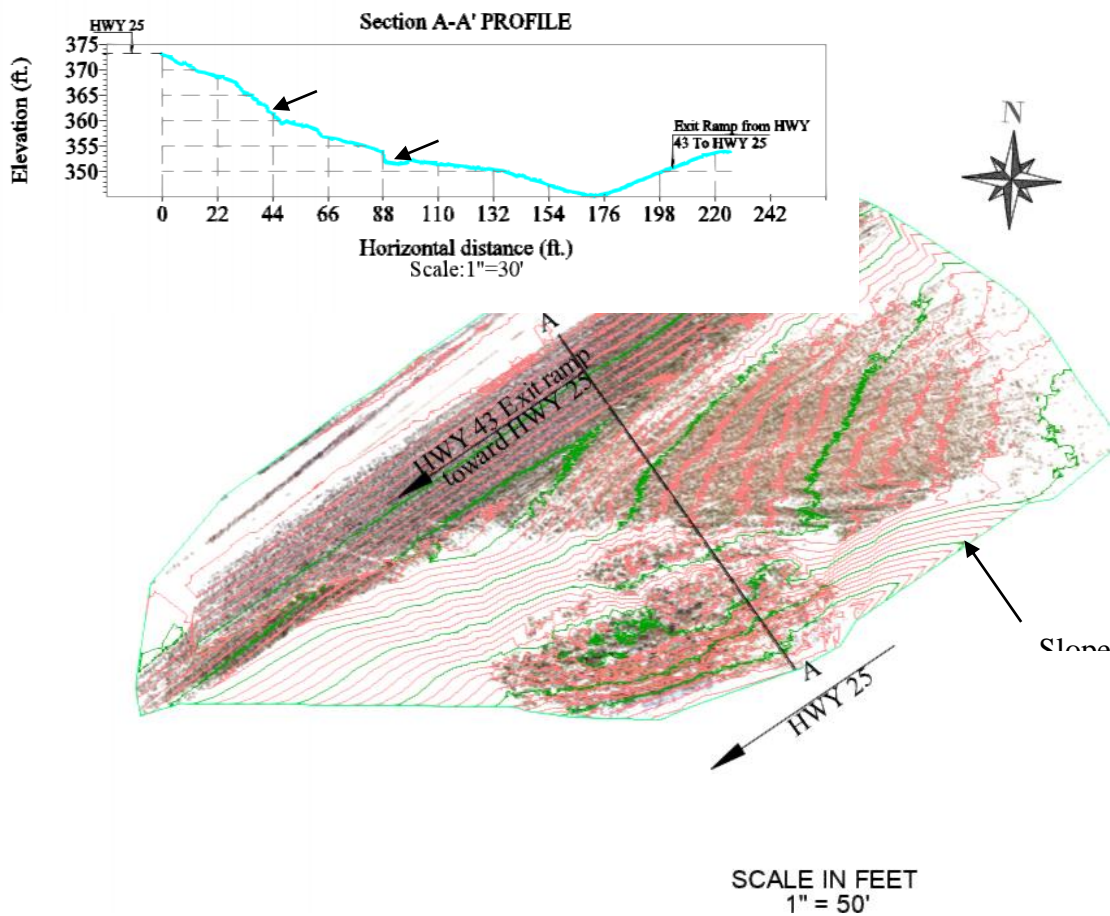


Figure 5.13 Slope along SR 25 LiDAR Results: Surface Topography and Profile

Evaluation

LiDAR research based on remote sensing offers a trustworthy substitute for destructive tools such as inclinometers in determining slope movement. LiDAR does not provide subsurface profiles, but it is clear from the findings of previous studies (Salunke et al., 2023) that movement is greater near the surface and gradually diminishes with depth. Hence, any considerable surface displacement should be immediately addressed when it is first noticed by routine LiDAR scanning. If a subsurface ERI survey reveals high saturation zones, then the wet soil under the shallow subsurface is more than likely causing the slope to move, as was observed in this case.

5.3 Predicting Soil Moisture from UAV Images and Machine Learning Methods

Imagery captured by unmanned aerial vehicles (UAVs) has proven to be effective in predicting important soil properties, such as moisture content. Salunke et al., (2023) conducted a study to develop a statistical and machine-learning model that could predict the amount of moisture in soil from UAV-captured optical and thermal images. The color and temperature information obtained from the images captured by a UAV was used to develop machine learning (ML) and statistical models that could predict soil moisture. The methodology used for this process is presented in Figure 5.14 below.

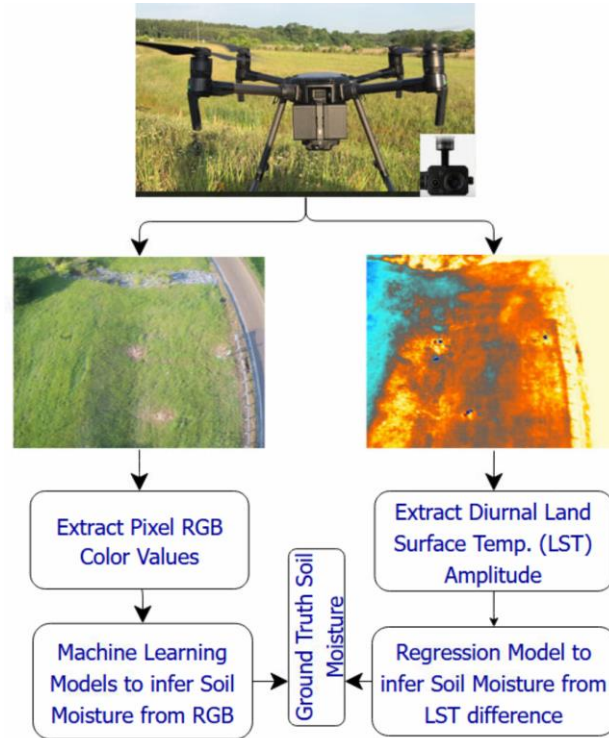


Figure 5.14 Methodology of Predicting Soil Moisture from UAV Images(Salunke et al., 2023)
SMC from Optical Images

The primary goal of the study was to develop soil moisture prediction models, using the color and temperature information obtained from optical and thermal images captured by a UAV. To achieve this, the red, green, and blue (RGB) color values of each pixel in the optical images were extracted and then correlated with the ground truth moisture content, using established machine-learning algorithms. The study was conducted on three repaired slope sites: Slope 2 located at the I55N & I220 N interchange, Slope 3 located on Terry Road, and Slope 5 on Sowell Road. Figure 5.15 shows the locations where the measurements for the ground truth soil moisture content were taken and the pixel color values extracted for developing the ML models.

Nonlinear regression models based on a support vector machine; an ensemble gradient tree-based algorithm, Extreme Gradient Boosting (XGB); and multiple linear regression (MLR) were implemented to predict soil moisture content using the pixel RGB values.

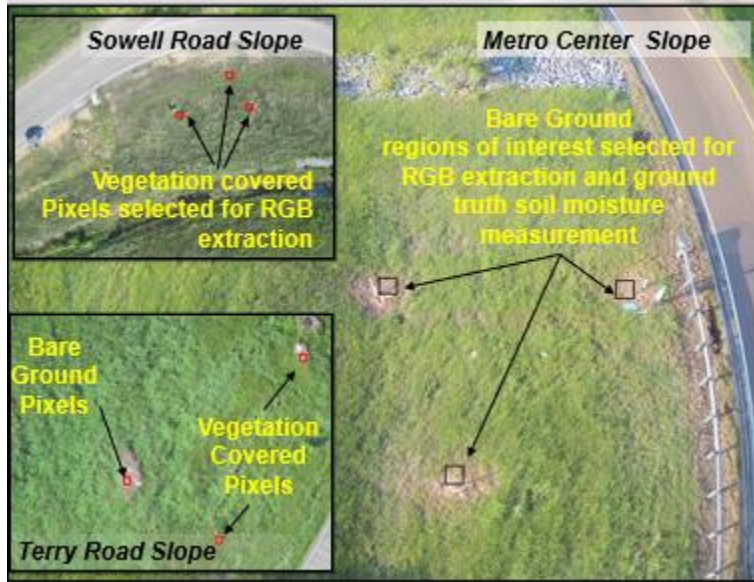


Figure 5.15 Regions of Interest in Optical Images for Pixel Value Extraction

The RGB model relies on the fact that bare ground pixels have higher red values and vegetation-covered areas have higher green values. A combination of vegetation-covered and bare-ground classes of RGB inputs was utilized to develop the RGB-SMC prediction model. This allowed for the averaging out of peaks and troughs, resulting in a model that can be applied across both bare-ground and vegetation-covered image classes. The XGB regression model performed better in predicting soil moisture from RGB colors than the support vector regression (SVR) model, and its predictions are presented in Figure 5.16.

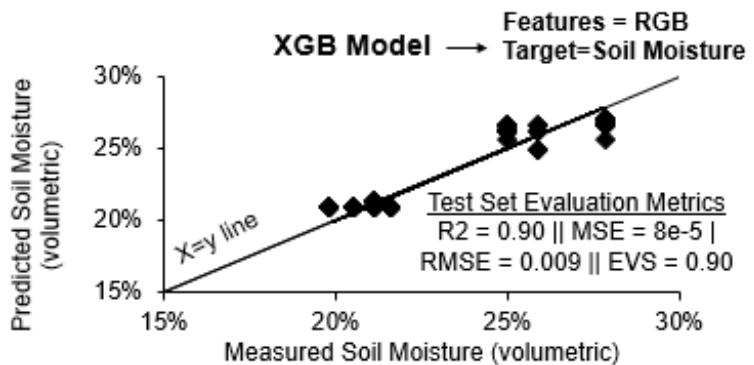


Figure 5.16 XGB Model's Prediction of Soil Moisture Content

Thermal infrared (TIR) images were taken of the highway slope's vegetative and bare ground areas of interest to identify where ground truth soil moisture is collected. The images were processed to obtain the temperature values (in Fahrenheit) of each pixel on the surface of the slope, and diurnal land surface temperature amplitudes (Δ LST) were extracted from TIR images captured at midday (peak temperature) and dawn (low temperature). The post-processed TIR images are presented in Figure 5.17.

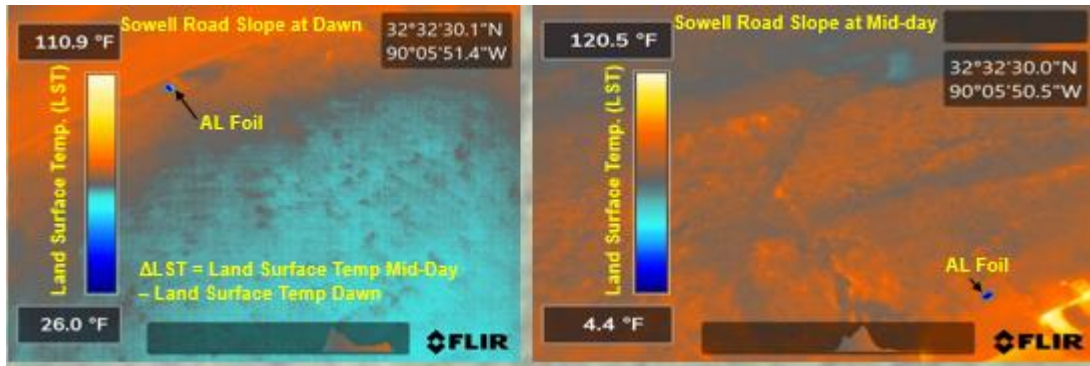


Figure 5.17 TIR Image of Sowell Road: (a) Dawn and (b) Mid-day

Δ LST values were compared with the actual soil moisture content (SMC) determined through soil sampling to establish a correlation between temperature and SMC. The study leveraged the relationship between soil surface thermal inertia and moisture content variations to develop a single-parameter regression model that was effective in predicting soil moisture in areas with vegetation cover. The linear regression model is presented in Figure 5.18 It's worth noting that the study was conducted on a field scale and not in a controlled environment, which enhanced the generalizability of the models.

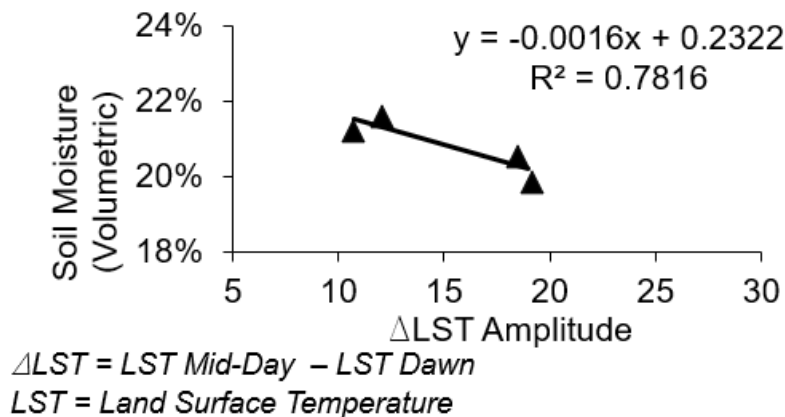


Figure 5.18 Soil Moisture Prediction Model based on Land Surface Temperature

The TIR-SMC model produced better prediction results for vegetation-covered areas than for bare-ground images. Using UAV-captured TIR imagery to predict soil moisture content is a time-efficient and non-contact method for site characterization, as it provides valuable information on soil moisture variations in highway slopes and helps predict shallow slide failures. In future studies, the models developed in this study could be compared with the established electrical resistivity imaging and SMC model.

5.4 Comparison of ERI and Instrumentation for Quantifying Soil Moisture Content and Soil Matric Suction

Several advantages of correlating electrical resistivity and data obtained from ground truth instrumentation (in-situ sensors) to measure soil moisture and suction are discussed in this section. ERI is a nondestructive technique that utilizes equipment that is durable, requires minimal

maintenance, and can be conducted over a large area as many times as needed. In contrast, installing borehole sensors is destructive; the equipment and sensors are expensive, subject to wear and tear, lose connectivity over time and eventually become worthless, and provide spatially restrictive readings of soil moisture and suction that can only cover a small area. The results from the ERI testing of six highway slopes in the Jackson metro area were correlated with instrumentation data to develop resistivity vs. soil moisture and resistivity vs. matric suction models. The methodology for developing these resistivity models is presented in Figure 5.19.

5.4.1 Field Instrumentation

Volumetric soil moisture content (θ), matric suction, and rainfall intensity were monitored by field instrumentation installed by the Mississippi Department of Transportation (MDOT) at the six slopes, as described in Chapter 3. Moisture and water potential sensors were installed at depths of 5 ft., 10 ft., and 15 ft. in 15 ft. boreholes drilled into the crest, middle, and bottom of the slopes, and the moisture content and water potential (matric suction or "suction") were measured and recorded hourly, as shown in Figure 5.20 (a). Data from the toe of the slopes was not considered for this study. The lab measurement of θ was compared with the volumetric water content obtained from sensor readings, and the validation is presented in Figure 5.20 (b)

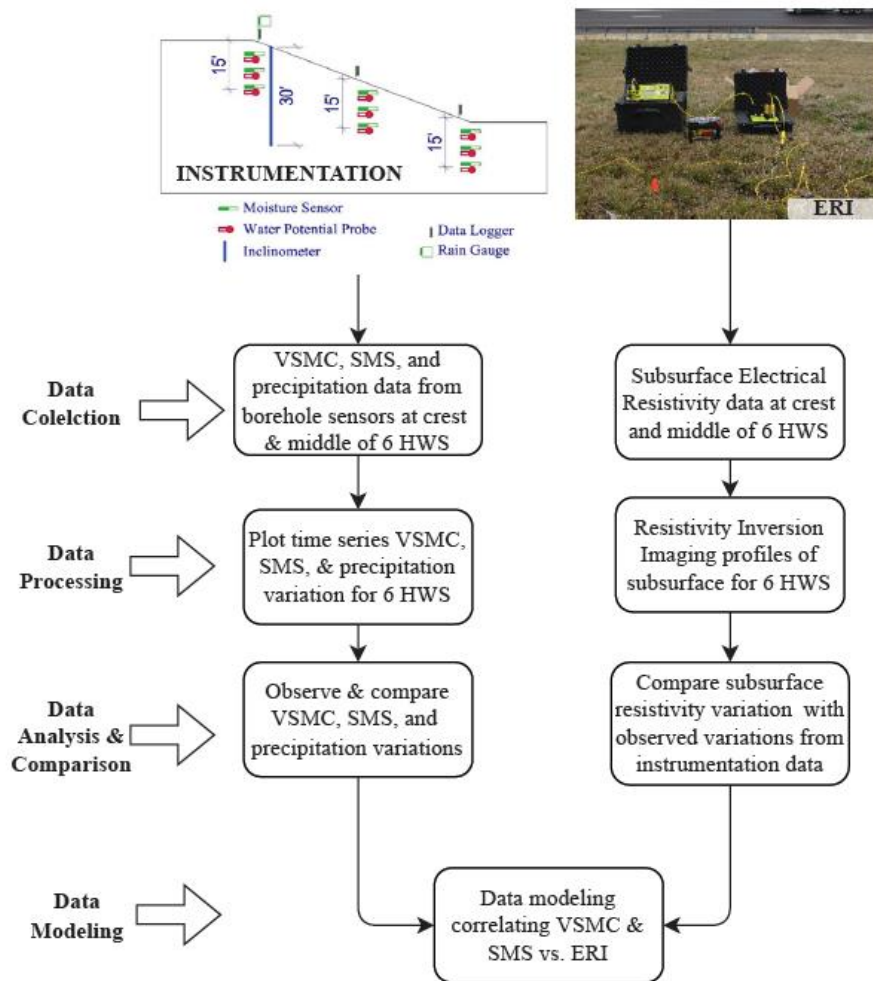


Figure 5.19 Methodology for Developing Resistivity vs Soil Moisture and Soil Suction Models (Nobahar et al. 2022 Geotechnics)

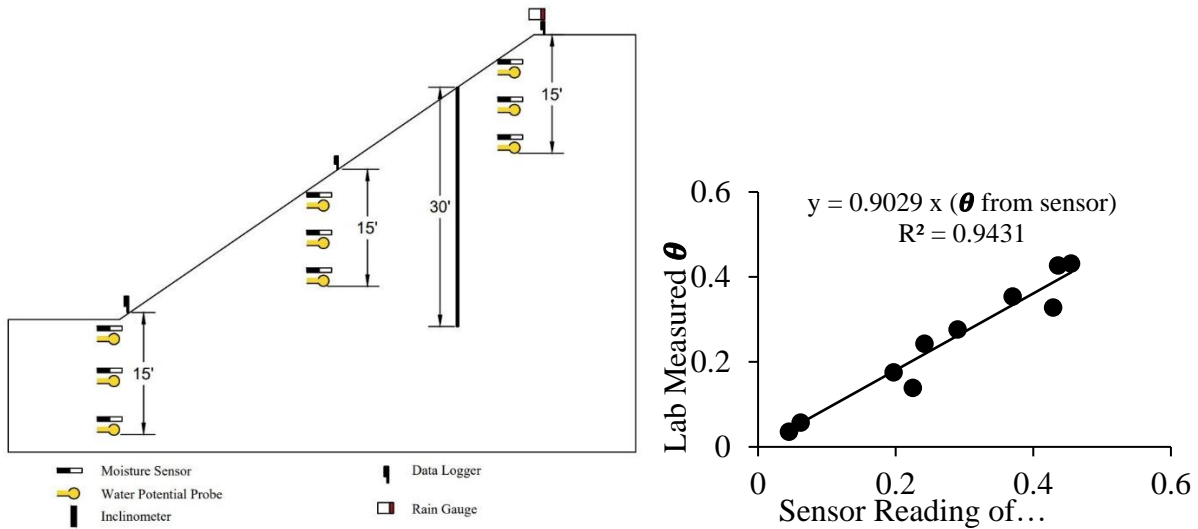


Figure 5.20 (a) Instrumentation in I-Slopes, (b) In-situ Sensor vs Lab Measurement of θ

5.4.1.1 Field Instrumentation Results

Variations in the matric suction and θ for the six I-slopes at different depths were studied based on field instrumentation data recorded for two years, between June 2019 and June 2021. The time-series variations of rainfall and suction and of rainfall and θ of I-Slope 3 are presented in Figure 5.21 and Figure 5.22, respectively. There was no notable variation in the potential of matric suction along the crest of I-slope 3, but the suction at 15 ft. depth was lower than that of soil closer to the surface. The moisture content at I-Slope 3 varied little at 5 ft. and 10 ft. depths, even with increased rainfall during some months, but considerable variations in moisture content were observed at the 15 ft. depth.

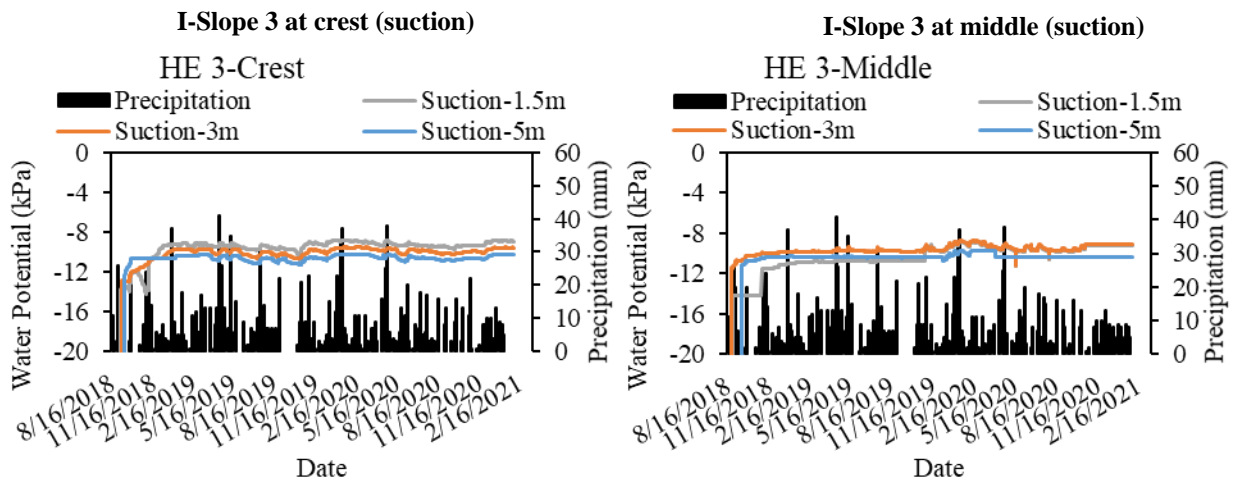


Figure 5.21 Results from Instrumentation for Suction vs. Rainfall at I-Slope 3: (a) Crest, (b) Middle.

I-Slope 3 at crest (θ)

I-Slope 3 at middle (θ)

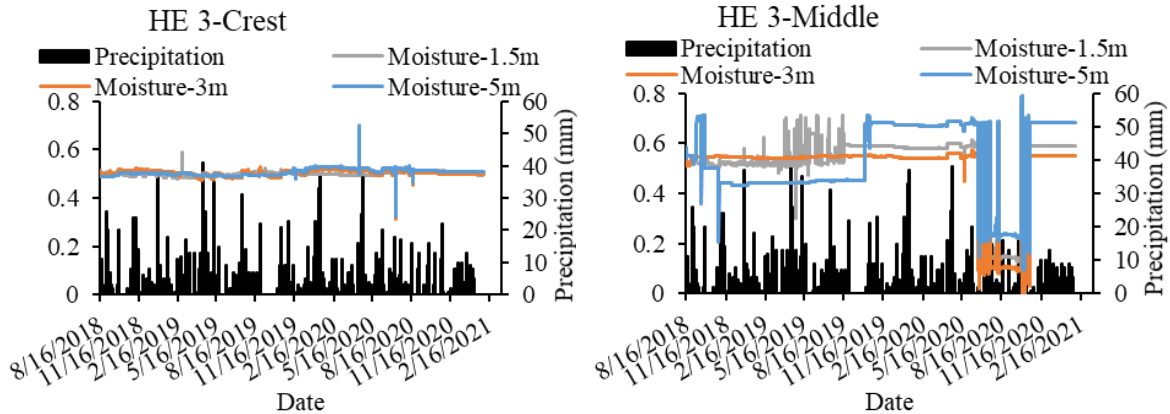


Figure 5.22 Instrumentation Results of θ vs Rainfall at I-Slope 3: (a) Crest, (b) Middle

The suction remained unchanged at all depths for most of the monitored I-slopes, including I-Slope 3. The moisture content remained at or above the saturation level at 5 ft. and 10 ft. depths but varied and remained below the saturation level at 15 ft. depth. This suggests that rainfall that runs off the crest of the slope only saturates the shallow depths of Yazoo Clay (Nobahar et al., 2020).

5.4.2 ERI Testing Results

The field instrumentation locations and results from the ERI inversion for I-Slope 3 at Line A (crest) and Line B (middle) are presented in Figure 5.23. The ERI inversion images show that high resistivity areas (represented by yellow and red) are typically found closer to the surface and suggest that the soil zone up to a depth of 5 feet is unsaturated. Areas with low resistivities (represented by blue) are at greater depths, indicating the presence of moisture and fully saturated soil. Pockets of high resistivities at the surface usually indicate that the soil has been disturbed, either by failure or other reasons. Pockets of low resistivities beneath the soil usually indicate the presence of perched water zones, which often initiate slide failures in Yazoo Clay embankments (Nobahar et al., 2020; Khan et al., 2020).

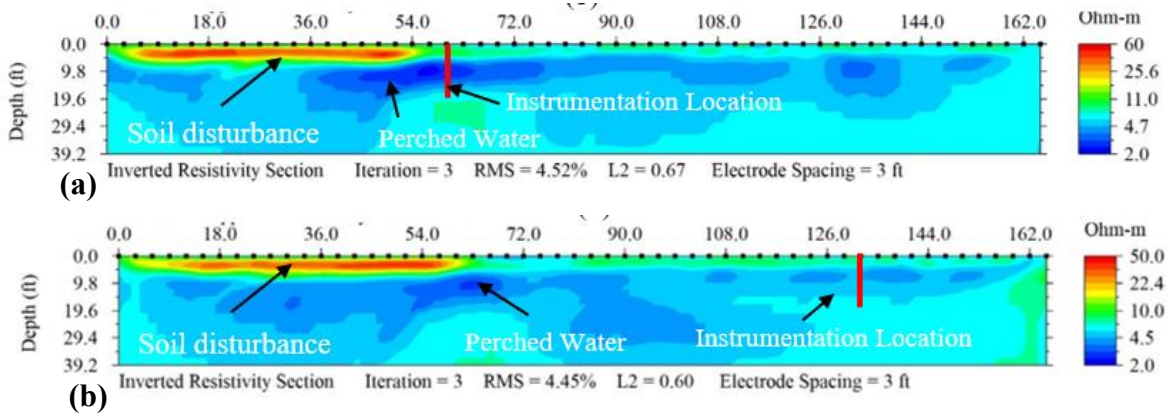


Figure 5.23 ERI Results of I-Slope 3: (a) Crest, (b) Middle

The relationship between soil resistivity and θ at the crest and middle of all six I-slopes is presented in Figure 5.24. A single parameter exponential model defined by Equation (1) was developed, based on previous studies, to correlate resistivity and soil moisture content.

$$\delta = 1.65e^{(-0.33)\varepsilon} \quad (1)$$

Where ε & δ are the soil resistivity and soil moisture content, respectively.

5.4.3 Soil Resistivity vs. Soil Matric Suction

Instrumentation data from the six highway slopes were compared with concurrent ERI test results, and a correlation was established between soil matric suction and resistivity. Normally, soil's matric suction potential is negative or less than zero at any given level. If it has a high matric suction potential or its granules can absorb water, it is rated as having a "less negative" potential. A "more negative" potential corresponds to a poor matric suction. For visualization purposes in this study, all negative matric suction values were converted into positive values. (See Figure 5.24 [b].)

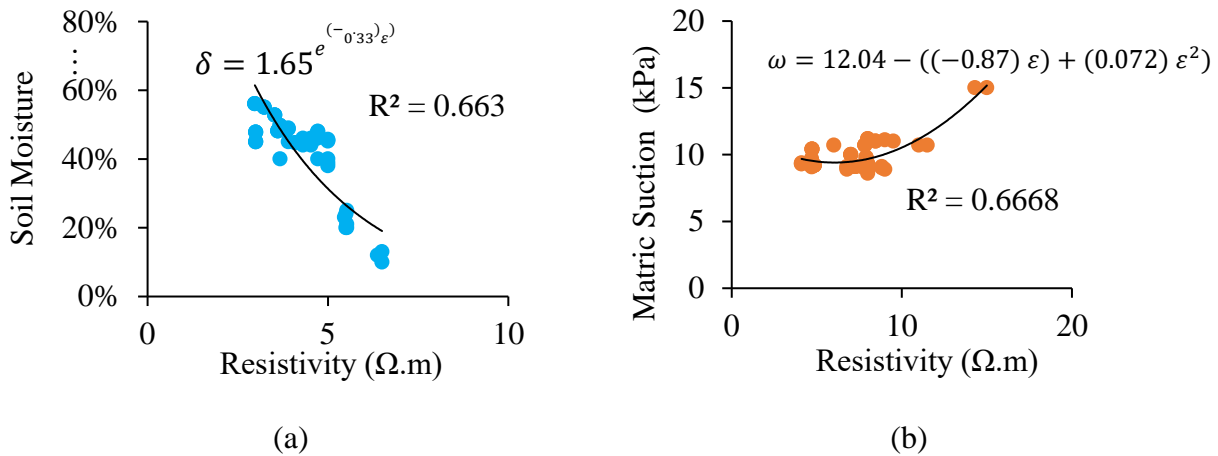


Figure 5.24 (a) Resistivity vs Soil Moisture Content, (b) Resistivity vs Matric Suction

Variations of resistivity with soil matric suction at the crest and middle of the Jackson metrocenter highway slopes are presented as a group in Figure 5.24. A polynomial function of the second degree was found to provide a better fit between resistivity and the matric suction. The single parameter model is expressed by Equation (2).

$$\omega = 12.04 - ((-0.87) \varepsilon) + (0.072) \varepsilon^2 \quad (2)$$

where soil resistivity and the soil SMS are denoted as ε and ω

5.5 Integrating ERI and UAV Results with Numerical Modeling for Back-Calculations of Soil Strength Properties

Back-analysis, using numerical modeling in PLAXIS, was performed for the failed Metrocenter slope to determine the soil's properties at failure. The ERI results are presented in Figure 5.25 and the drone results are presented in Figure 5.26. The analysis involved adjusting parameters and identifying the cohesive strength of the soil at failure by successive iterations.

Figure 5.27 illustrates the boundary condition of the embankment at a global scale. The initial depth of the water table for each referenced embankment was determined independently, based on field observations. It is important to note that the selection of the parameters and depths are key aspects of the back-analysis process. Soil parameters such as bulk unit weight, saturated unit weight, cohesion, internal friction angle, Young’s modulus, and Poisson’s ratio are defined in Table 5.1.

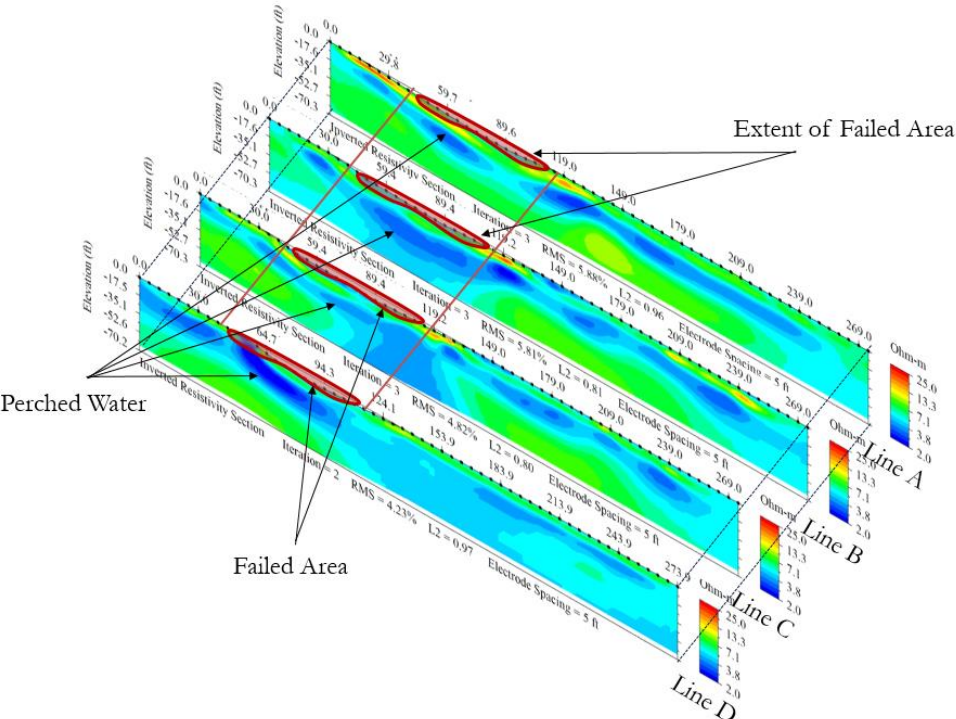


Figure 5.25 Metrocenter ERI Test Results (I220 S Exit 1B)

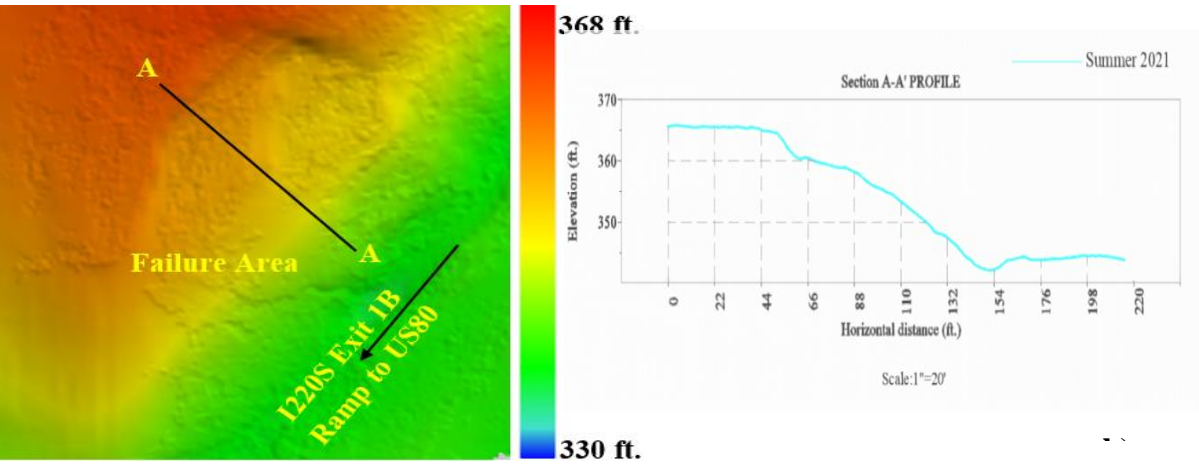


Figure 5.26 Metrocenter Drone DEM Deformation (I220S Exit 1B)

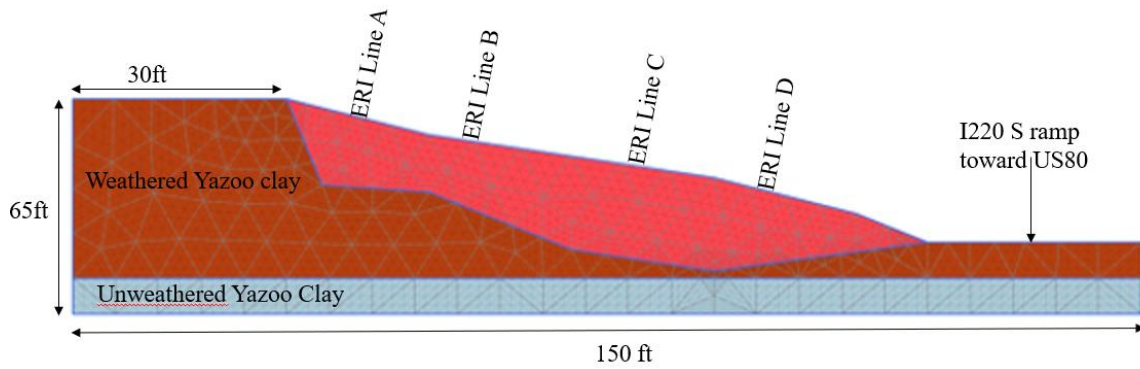


Figure 5.27 2D Finite Element Mesh of Slope 1

Table 5.1 Soil Parameters of Slope Back-calculated with Numerical Modeling

Soil Property	Unit	Slope 1
Bulk Unit Weight	Lbs./ft ³	126
Saturated Unit Weight	Lbs./ft ³	135
Cohesion (c)	Lbs./ft ²	51
Internal Friction Angle (Φ)	Degree	17
Young's Modulus (E)	Lbs./ft ²	7×10^4
Poisson's Ration (μ)	-	0.3

A deformation analysis of Slope 1 was conducted using 2-D FEM modeling. The integration of UAV surface profiles, ERI test results, and FEM back-analysis accurately identified the failure slip surface, matching the observed field slip surface. This methodology provides more accurate slip surface identification and extraction of soil properties compared to other post-failure analysis methods. The UAV and ERI data helped verify the post-failure surface geometry through numerical analysis.

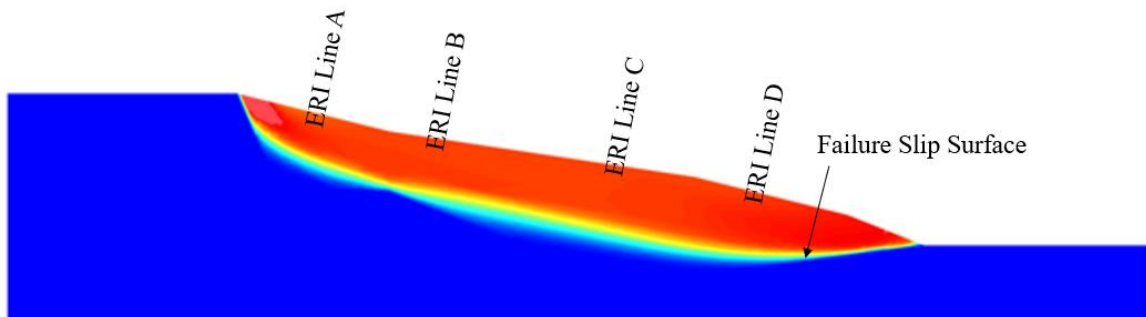


Figure 5.28 Deformation at Failure (when $FS < 1$) with Slip Surface Field Observations

CHAPTER 6 CONCLUSION

Geotechnical infrastructure (geo-infra) assets such as highway earth slopes and embankments are integral to transportation infrastructure. In Mississippi, these assets are becoming increasingly vulnerable due to the increasing intensity and amount of rainfall. The problem is compounded because many of the geo-infra-assets are built on expansive clay, whose shear strength properties are weakened by the scorching summers and extreme rainfall, causing shallow and deep-seated landslides and failures. Warning systems and timely evaluations are imperative preventative measures to reduce the risks to highway slopes and embankments. However, traditional in-situ evaluation methods are outdated, expensive, and produce spatially restricted information. In-situ confined monitoring systems do not provide a complete picture of the condition of the entire asset, such as a slope. Furthermore, many geo-infra-assets go unmonitored and fail without notice due to the lack of in-situ monitoring devices.

This study utilized instrumentation and advanced nondestructive testing methods to investigate the performance of 6 instrumented highway slopes and 20 failed slopes to evaluate the subsurface and surficial variations they underwent during different seasons. Geophysical and remote sensing techniques such as electrical resistivity imaging (ERI), LiDAR, and UAV imaging were used to monitor the slopes from Fall 2020 to Spring 2023. The collected data were analyzed and then compared with each other to understand the subsurface and surficial variations over time. Geo-referenced DEMs from LiDAR and drone surveys were used to develop stacked surficial profiles, monitor surficial movements over time, and compare them with the subsurface movement data obtained from an inclinometer. ERI subsurface imaging was compared with in-situ instrumentation. Advanced numerical modeling, using the Finite Element Method (FEM), was conducted to recreate the sliding failure based on UAV DEMs and ERI subsurface images, and the soil strength parameters were back-calculated. LiDAR imaging captured from a terrestrial scanning device and aerial surveys captured from drone images (photogrammetry) were used to monitor the soil deformation. ERI test results were compared with the data obtained from inclinometers, surface movement data obtained from LiDAR/aerial survey imaging, and a vast amount of diverse data provided by field instrumentation. Resistivity inversion, photogrammetry, 3D modeling, numerical modeling, statistical analysis, and machine learning methods were employed to extract meaningful information that provided the basis for comparative analysis. Based on the study, some of the key findings are highlighted in the following section.

Instrumentation Results: Field instrumentation revealed that the matric suction remained mostly consistent at 208.85 psf (10 kPa) at all three depths during the wet season, and the highway slopes were fully saturated once the matric suction reached an equilibrium condition with a low value. The suction generally remained constant at all depths at the peak of the crest of all the I-slopes; only a few slopes experienced a change in suction at shallow depths. The moisture content did not change between depths of 5 ft. and 10 ft. and remained at or above the saturation level; however, it varied at a depth of 15 ft. and was lower than that observed at shallow depths. This is attributed to rainfall running off from the slopes' crest, saturating the Yazoo clay's shallow depths without permeating the soil at deeper levels. These findings are consistent with previous studies on Yazoo Clay slopes (Khan et al., 2020) that suggest that rainfall becomes trapped in perched water zones at shallow levels of high-plastic Yazoo Clay slopes and takes significant time to infiltrate deeper levels.

Generally, an increase in suction should be met with a decrease in soil moisture and vice versa, but the anomalies observed in this study can be regarded as due to the characteristics of the Yazoo Clay, where water infiltration and permeation patterns are site-specific and depend on seasonal variations. The lack of variations in suction can be attributed to the soil being fully saturated from 5 ft. to 15 ft. depths. Considerable variations in the suction potential at the middle of the six I-slopes were observed in I-slopes 2 and 5; I-slopes 1, 3, 4, and 6 had little-to-no variations. On the other hand, the moisture content of all six highway I-slopes changed substantially in the middle.

ERI Results: The resistivity of expansive clay soil is typically low, ranging between 30-50 Ohm-m in a dry condition, mostly due to the ionic charge within the soil. In saturated clay soils, the ionic charge, combined with the moisture content, drastically reduces the soil's resistivity. Resistivity values less than 5 Ohm-m indicate a very saturated soil zone.

The results of the ERI testing performed in this study showed that shallower depths had higher resistivity values due to the existence of unsaturated soil, cracks, displaced disturbed soils, and air pockets that increased the air void ratio. In the middle of the highway slopes, the resistivity was high at unsaturated levels, and perched water existed under deformation. The moisture content was high at the crest in summer. In fall, it decreased in the crest but increased in the middle and toe of the slope, which explains the subsurface water flow from crest to toe during different seasons. The instrumentation data plot shows that the moisture content remained almost constant between summer 2021 and fall 2021 at all measured depths for most of the instrumented slopes. This observation matches ERI results along the middle of the slope, which coincides with the instrumentation location where wet areas indicated by low resistivities are present in both seasons.

Statistical models were developed by comparing ERI data on soil moisture and matric suction with data from in-situ sensors. An exponential model was developed to describe the correlation between resistivity and soil moisture content; a polynomial model was developed to explain the correlation between resistivity and matric suction.

UAV & LiDAR Results: Several valuable results were derived from the UAV photogrammetry and LiDAR scans. The DEMs generated from drone imagery helped estimate the amount of displaced soil, identify the depth of the slip surface, and recreate failure conditions in numerical modeling tools. The stacked surface profiles of the I-slopes developed from the LiDAR point cloud revealed details of surficial movement and reflected changes over time. The toes of I-slopes 4, 5, and 6 showed variations up to 3 inches in elevation over time, indicating that plastic movement pushes the soil down the slope. A significant change is visible in the surface profile of I-Slope 2 at the large voids (sink holes), which shows that the soil is gradually eroding, enlarging the voids. Investigating the failed slopes resulted in accurate DEMs and surface profiles that can be used as baseline data for future comparisons. Stacked surface profiles from DEMs developed at different times at the Mannsdale NB slope (failed Slope 19) showed settlement at the crest over time and changes in elevation at the toe of the slope. This has been an ongoing problem at this site, which has been continually repaved. A LiDAR-generated surface profile helps accurately quantify the settlement. In other applications of this study, machine learning models were developed to infer soil moisture from pixel color (Red, Blue, Green) values extracted from the drone optical imagery. A statistical model was also developed to infer soil moisture from land surface temperature variation data extracted from drone thermal imagery.

Results from ERI, drones, and instrumentation were used to perform numerical modeling in PLAXIS and recreate the slope failure conditions. Back analysis was performed to identify soil strength properties at failure.

The in-situ sensors, and traditional site investigation methods, offer valuable data for evaluating landslides and performance monitoring of slopes. However, they are spatially restrictive and can be enhanced by combining with advanced non-destructive investigation techniques such as geophysical and remote sensing methods. There are several benefits of adopting advanced geophysical and remote sensing techniques for landslide investigations and geotechnical asset evaluation in general. For instance, advanced monitoring techniques aid quick and accurate characterization of landslides and other failures from natural hazards, and evaluation results provide early warning of impending disasters. The high-resolution spatial and temporal information at the subsurface and surface level offer a wealth of information to understand the landslide's evolution and the general asset behavior.

Impacts from climate loading, such as precipitation and temperature variations, can be better characterized by studying the high-resolution spatial and temporal subsurface and surface characterization data. Furthermore, the advanced investigation techniques provide reliable risk information to plan for a future resilient design of the geotechnical assets.

Risk-informed smart design, enabled by the advanced investigation techniques described in this study, will help design the structure to address the actual risk and avoid redundant overdesigning. Such risk-informed design practice offers potential savings in the construction cost, reducing risks and increasing the resiliency of geo-infra-assets.

Early identification of vulnerable or failing assets is crucial for strategizing repairs and maintenance activities, and combining remote sensing methods with geophysical investigations will help develop a modern performance monitoring methodology to integrate into the GAM framework. The findings of this study show the merits of a cross-platform landslide evaluation protocol. Importantly, these advanced evaluation techniques can be easily implemented on other geotechnical assets such as retaining walls, foundations, levees, and bridge abutments.

Implementing these advanced tools in future research endeavors will yield substantial improvements in site investigations and enhance the reliability of transportation GEO infrastructure design in Mississippi. By incorporating techniques such as electrical resistivity imaging (ERI), LiDAR technology, and drone imaging, a more comprehensive understanding of the subsurface conditions can be achieved. This enhanced knowledge will contribute to more accurate assessments of soil properties, moisture content, and potential failure mechanisms. Ultimately, leveraging these advanced tools will promote more informed decision-making processes and lead to the development of robust and resilient transportation infrastructure in Mississippi.

REFERENCES

- Ahmad, M. N., Shao, Z., Aslam, R. W., Ahmad, I., Liao, M., Li, X., & Song, Y. (2022). Landslide hazard, susceptibility and risk assessment (HSRA) based on remote sensing and GIS data models: a case study of Muzaffarabad Pakistan. *Stochastic Environmental Research and Risk Assessment*, 36(12), 4041–4056. <https://doi.org/10.1007/s00477-022-02245-8>
- Alonso, E. E., Gens, A., & Josa, A. (1990). A constitutive model for partially saturated soils. *Géotechnique*, 40(3), 405–430. <https://doi.org/10.1680/geot.1990.40.3.405>
- Anderson, S. A., Schaefer, V. R., & Nichols, S. C. (2016). Taxonomy for Geotechnical Assets, Elements, and Features. Transportation Research Board 95th Annual Meeting.
- Bian, H., Bai, L., Wang, X., Liu, W., Chen, S. E., & Wang, S. (2011). “Effective LiDAR damage detection: comparing two detection algorithms.” *Struct. Eng.*, 27(137), 327–333.
- Blight, G. E. (1997). Interactions between the atmosphere and the Earth. *Geotechnique*, 47, 715–767.
- Bowels, J.E., 1988. Foundation analysis and design. McGraw-Hills Inc., U.S.A., pp: 312-316
- Bulut, R. and Wray, W.K. (2005). "Free energy of water suction in filter papers." *Geotechnical Testing J.*, Vol. 28 (4), pp. 355-364.
- Bordoni, M., Persichillo, M. G., Meisina, C., Crema, S., Cavalli, M., Bartelletti, C., Galanti, Y., Barsanti, M., Giannecchini, R., D', G., & Avanzi, A. (2018). Estimation of the susceptibility of a road network to shallow landslides with the integration of sediment connectivity. <https://doi.org/10.5194/nhess-2017-457>
- Burns, W. J., & Madin, I. P. (2009). Protocol for Inventory Mapping of Landslide Deposits from Light Detection and Ranging (LiDAR) Imagery Special Paper 42, 2009.
- Chen, F. H., (1988). “Foundations on expansive soils.” Elsevier Science Publishers, B. V.
- Chen, Jun, Ian Dowman, Songnian Li, Zhilin Li, Marguerite Madden, Jon Mills, Nicolas Paparoditis, et al., 2016. “Information from imagery: ISPRS scientific vision and research agenda.” *ISPRS Journal of Photogrammetry and Remote Sensing*, 115 (August 2018): 3–21. <https://doi.org/10.1016/j.isprsjprs.2015.09.008>.
- Chen, S. E. (2010). “Advances in remote sensing for bridge structural health evaluation.” *Proc.*, 7th Structural Engineering Convention (SEC2010), Annamalai Nagar, Tamilnadu, India, 18–28.
- Ciampalini, A., Raspini, F., Frodella, W., Bardi, F., Bianchini, S., & Moretti, S. (2016). The effectiveness of high-resolution LiDAR data combined with PSInSAR data in landslide study. *Landslides*, 13(2), 399–410. <https://doi.org/10.1007/s10346-015-0663-5>
- Conte, O. A., & Coffman, R. A. (2012). “Slope stability monitoring using remote sensing techniques.”
- Cruden DM, Varnes DJ (1996) Landslides: investigation and mitigation
- Gallipoli, M., Lapenna, V., Lorenzo, P., Mucciarelli, M., Perrone, A., Piscitelli, S., & Sdao, F. (2000). Comparison of geological and geophysical prospecting techniques in the study of a

- landslide in southern Italy. *Journal of Environmental & Engineering Geophysics*, 4, 117–128.
- Gargoum, S., & El-Basyouny, K. (2017). Automated extraction of road features using LiDAR data: A review of LiDAR applications in transportation. 2017 4th International Conference on Transportation Information and Safety, ICTIS 2017 - Proceedings, 563–574. <https://doi.org/10.1109/ICTIS.2017.8047822>
- Hatta Antah, F., Khoiry, M. A., Abdul Maulud, K. N., & Abdullah, A. (2021). “Perceived usefulness of airborne lidar technology in road design and management: A review. In Sustainability.” (Switzerland) (Vol. 13, Issue 21). MDPI. <https://doi.org/10.3390/su132111773>
- Hedayati, M., Hossain, Md. S., Mehdibeigi, A., & Thian, B. (2014). Real-Time Modeling of Moisture Distribution in Subgrade Soils. *Geo-Congress 2014 Technical Papers*, 3015–3024. <https://doi.org/10.1061/9780784413272.293>
- Hen-Jones, R. M., Hughes, P. N., Stirling, R. A., Glendinning, S., Chambers, J. E., Gunn, D. A., & Cui, Y. J. (2017). “Seasonal effects on geophysical–geotechnical relationships and their implications for electrical resistivity tomography monitoring of slopes.” *Acta Geotechnica*, 12(5), 1159–1173. <https://doi.org/10.1007/S11440-017-0523-7/FIGURES/9>
- Hossain, J., Hossain, M.S., & Hoyos, L.R. (2013). “Effect of rainfall on stability of unsaturated earth slopes constructed on expansive clay.” *Geo-Congress 2013, ASCE*, Vol. 1, pp. 417-425. Johnson, K.A., & Sitar, N. (1990). “Hydrologic Conditions Leading to Debris-Flow Initiation.” *Canadian Geotechnical Journal*, Vol. 27, pp. 789-801.
- Hossain, J., Khan, M.S., Hossain, M.S., Ahmed, A. (2016) “Determination of active zone in expansive clay in North Texas through field instrumentation.” *Proc. 95th Annual Meeting of Transportation Research Board*, January 10-14, 2016, Washington, DC, USA. <http://pubs.usgs.gov/bul/b2130/Chapter11.html> December 23rd.
- Hossain, M.S., Kibria, G. & Khan M.S. (2018). “Site investigation using resistivity imaging.” CRC Press, ISBN 9781138485938 - CAT# K349394.
- Hussain, S., Pan, B., Afzal, Z., Ali, M., Zhang, X., Shi, X., & Ali, M. (2023). Landslide detection and inventory updating using the time-series InSAR approach along the Karakoram Highway, Northern Pakistan. *Scientific Reports*, 13(1), 7485. <https://doi.org/10.1038/s41598-023-34030-0>
- Jaboyedoff, M., Oppikofer, T., Abellán, A., Derron, M. H., Loye, A., Metzger, R., & Pedrazzini, A. (2012). “Use of LIDAR in landslide investigations: A review.” In *Natural Hazards* (Vol. 61, Issue 1, pp. 5–28). <https://doi.org/10.1007/s11069-010-9634-2>
- Jones, D.E and Holtz, W.G, “Expansive soils, the hidden disaster”, *American Society of Civil Engineering Journal*, 31, 87-89, 1973.
- Jones, L.D., & Jefferson, I. (2012). “Problematic soils and site investigation.” In *ICE Manual of Geotechnical Engineering*, volume 1, *Geotechnical Engineering Principles*, pp. 413-441.
- Jongmans, D., & Garambois, S. (2007). “Geophysical investigation of landslides : a review.” *178(2)*, 101–112. <https://doi.org/10.2113/gssgfbull.178.2.101i>

- Juang CS, Stanley TA, Kirschbaum DB (2019) Using citizen science to expand the global map of landslides: introducing the cooperative open online landslide repository (COOLR). *PLoS One* 14:e0218657
- Kader, U. & Altunel, A. O. (2021). "Monitoring the stability of highway cut slopes utilizing drone photogrammetry." 2nd Intercontinental Geoinformation Days.
- Kalantari, B. (2012). Engineering significant of swelling soils. *Research Journal of Applied Sciences, Engineering and Technology*, 4(17), 2874-2878.
- Karl, T. R., Melillo, J. M., & Peterson, T. C. (2009). *Global climate change impacts in the United States: a state of knowledge report from the US Global Change Research Program*. Cambridge University Press.
- Kayen, R., Pack, R. T., Bay, J., Sugimoto, S., & Tanaka, H. (2006). "Terrestrial-LIDAR visualization of surface and structural deformations of the 2004 Niigata Ken Chuetsu, Japan, earthquake." *Earthq. Spectra*, 22(S1), 147–162.
- Khan, M. S., Amini, P. E. F., & Masoud Nobahar, P. E. (2020). MDOT State Study 286-Performance Evaluation of Highway Slopes on Yazoo clay final report.
- Khan M. S., Ivoke J & Nobahar M. (2019). "Coupled effect of wet-dry cycles and rainfall on highway slope made of Yazoo Clay." *Geosciences* 2019, 9 (341); DOI:10.3390/geosciences9080341
- Khan, M., Hossain, S., & Kibria, G., (2015). "Slope stabilization using recycled plastic pins." *J. Perform, Constr. Facil.*, 10.1061/(ASCE)CF.1943-5509.0000809, 04015054.
- Khan, M.S., Hossain, M.S., Ahmed, A. & Faysal, M. (2016). "Investigation of shallow slope failure on expansive clay in Texas." *Eng. Geol.*, <http://dx.doi.org/0.1016/j.enggeo.2016.10.004>
- Khan, M.S., Hossain, M.S., Hossain, J., & Kibria, G. (2012). "Determining unknown bridge foundation depth by resistivity imaging (RI) method." *GSP 225, Proc. Geo- Congress 2012: 275-284.*, March 25-29, ASCE, Reston, VA.
- Kibria, G. and Hossain, M.S. (2012). "Investigation of geotechnical parameters affecting electrical resistivity of compacted clays." *J. Geotechnical and Geoenvironmental Engineering*, Vol 138 (2), 1520-1529.
- Kim, J., Jeong, S., Park, S., & Sharma, J. (2004). Influence of rainfall-induced wetting on the stability of slopes in weathered soils. *Engineering Geology*, 75(3), 251–262. <https://doi.org/https://doi.org/10.1016/j.enggeo.2004.06.017>
- Kimmerling, R. E., & Thompson, P. D. (2015). Assessment of retaining wall inventories for geotechnical asset management. *Transportation Research Record*, 2510, 1–6. <https://doi.org/10.3141/2510-01>
- Koehn, W.J., Tucker-Kulesza, S.E., LeBow, V., Rahimi, S., Bernhardt, M.L. & Wood, C.M. (2019). "Enhanced analysis of landslide failure mechanisms in the Ozark plateau region with electrical resistivity tomography." In *Geo-Congress 2019: Engineering Geology, Site Characterization, and Geophysics* (pp. 197-203). Reston, VA: American Society of Civil Engineers.

- Lee Jr., L. T. (2012). "State study 151 and 236: Yazoo Clay investigation." MDOT State Study 236, US Army Corps of Engineers.
- Lefevre, R. J. (2000). "Radar bridge clearance sensor." IEEE 2000 International Radar Conf., Alexandria, VA, 660–665.
- Liu, W. Q. (2010). "Terrestrial LiDAR-based bridge evaluation." Ph.D. dissertation, Univ. of North Carolina, Charlotte, NC.
- Liu, W. Q., Chen, S. E., Boyajian, D., & Hauser, E. (2010). "Application of 3D LiDAR scan of the bridge under static load testing." *Mater. Eval.*, 68(12), 1359–1367.
- Liu, W., Chen, S., & Hauser, E. (2012). "Bridge clearance evaluation based on terrestrial LIDAR scan." *Journal of Performance of Constructed Facilities*, 26(4), 469–477. [https://doi.org/10.1061/\(ASCE\)CF.1943-5509.0000208](https://doi.org/10.1061/(ASCE)CF.1943-5509.0000208)
- Luino, F., De Graff, J., Biddoccu, M., Faccini, F., Freppaz, M., Roccati, A., Ungaro, F., D'Amico, M., & Turconi, L. (2022). The Role of Soil Type in Triggering Shallow Landslides in the Alps (Lombardy, Northern Italy). *Land*, 11(8). <https://doi.org/10.3390/land11081125>
- Luo, H., Wang, L., Wu, C., & Zhang, L. (2018). An Improved Method for Impervious Surface Mapping Incorporating LiDAR Data and High-Resolution Imagery at Different Acquisition Times. *Remote Sensing*, 10(9), 1349. <https://doi.org/10.3390/rs10091349>
- Lynch, K., Hughes, D., Bell, J., & Harley (2013). "Using geotechnical and LIDAR spatial monitoring to determine key environmental slope instability thresholds of a Jurassic coastal landslide: Straidkilly Point, Northern Ireland, UK." <http://www.geomontreal2013.ca/>
- Lytton, R. L., C. P. Aubeny, and R. Bulut. 2005. Design procedures for pavements on expansive soils. FHWA/TX-05/0-4518-1. College Station, TX: Texas Transportation Institute.
- Manzur, S. R., Hossain, M.S., Kemler, V. & Khan, M.S. (2016). "Monitoring extent of moisture variations due to leachate recirculation in an Elr/Bioreactor landfill using resistivity imaging." *Waste Management*, DOI: 10.1016/j.wasman.2016.02.035
- Marino, P., Peres, D. J., Cancelliere, A., Greco, R., & Bogaard, T. A. (2020). Soil moisture information can improve shallow landslide forecasting using the hydrometeorological threshold approach. *Landslides*, (9), 2041–2054. <https://doi.org/10.1007/s10346-020-01420>
- Marx, A., Chou, Y.-H., Mercy, K., & Windisch, R. (2019). A Lightweight, Robust Exploitation System for Temporal Stacks of UAS Data: Use Case for Forward-Deployed Military or Emergency Responders. *Drones*, 3(1), 29. <https://doi.org/10.3390/drones3010029>
- Maxwell, A.E. et al. (2020). "Slope failure prediction using random forest machine learning and LiDAR in an eroded folded mountain belt." *Remote Sensing*, 12(3), p.486.
- Meena, S. R., Ghorbanzadeh, O., van Westen, C. J., Nachappa, T. G., Blaschke, T., Singh, R. P., & Sarkar, R. (2021). Rapid mapping of landslides in the Western Ghats (India) triggered by 2018 extreme monsoon rainfall using a deep learning approach. *Landslides*, 18(5), 1937–1950. <https://doi.org/10.1007/s10346-020-01602-4>
- Mertzanides, Y., Tsakmakis, I., Kargiotis, E., & Sylaios, G. (2020). "Electrical resistivity tomography for spatiotemporal variations of soil moisture in a precision irrigation

- experiment.” *International Agrophysics*, 34(3), 309–319. <https://doi.org/10.31545/INTAGR/123943>
- Mitchell, P. W. The Concepts Defining the Rate of Swell of Expansive Soils. 4th International Conference on Expansive Soils, 1980 Denver. 106-116
- Mondini, A. C., Guzzetti, F., & Melillo, M. (2023). Deep learning forecast of rainfall-induced shallow landslides. *Nature Communications*, 14(1), 2466. <https://doi.org/10.1038/s41467-023-38135-y>
- Mulyono, A., Arisbaya, I., Sudrajat, Y., Djuwansah, M. R., Suriadikusumah, A., & Harryanto, R. (2019). “Determining soil resistivity by electrical resistivity tomography in agroforestry land system.” *IOP Conference Series: Earth and Environmental Science*, 393(1). <https://doi.org/10.1088/1755-1315/393/1/012063>
- Muñoz-Castelblanco, J. A., Pereira, J. M., Delage, P., & Cui, Y. J. (2012). The influence of changes in water content on the electrical resistivity of a natural unsaturated loess. In *ASTM Geotechnical Testing Journal* (Vol. 35, Issue 1).
- Murphy, V.N.S., 2010. *Soil Mechanics and Foundation engineering*. CBS Publishers and Distributors Pvt. Ltd., New Delhi, pp: 924-940
- Nappo, N., Mavrouli, O., Nex, F., van Westen, C., Gambillara, R., & Michetti, A. M. (2021). Use of UAV-based photogrammetry products for semi-automatic detection and classification of asphalt road damage in landslide-affected areas. *Engineering Geology*, 294, 106363. <https://doi.org/10.1016/j.enggeo.2021.106363>.
- Nelson, J. D., and Miller, D.J., “Expansive Soils: Problems and Practice in Foundation and Pavement Engineering,” John Wiley and Sons Inc., New York, 1992.
- Nobahar, M., Salunke, R., Alzeghoul, O. E., Khan, M. S., & Amini, F. (2023). Mapping of Slope Failures on Highway Embankments using Electrical Resistivity Imaging (ERI), Unmanned Aerial Vehicle (UAV), and Finite Element Method (FEM) Numerical Modeling for Forensic Analysis. *Transportation Geotechnics*, 40, 100949. <https://doi.org/10.1016/j.trgeo.2023.100949>
- Nobahar, M., Salunke, R., Khan, M. S., & Amini, F. (2022). Development of Soil Moisture Content and Soil Matric Suction Model Based on Field Instrumentation and Electrical Resistivity Imaging (ERI) for Highway Slopes Constructed on High Expansive Clay Soil. *Geotechnics*, 2(3), 671–705. <https://doi.org/10.3390/geotechnics2030033>
- Nobahar, M., Khan, M. S., and Ivoke, J. (2020). “Combined effect of rainfall and shear strength on the stability of highway embankments made of Yazoo Clay in Mississippi.” *Journal of Geotechnical and Geological Engineering*, Springer US, Online ISSN 0960-3182, Jan 9th.
- Nordiana, M. M., Azwin, I. N., Nawawi, M. N. M., & Khalil, A. E. (2018). Slope failures evaluation and landslides investigation using 2-D resistivity method. *NRIAG Journal of Astronomy and Geophysics*, 7(1), 84–89. <https://doi.org/10.1016/j.nrjag.2017.12.003>
- Olive, W. W., Chleborad, A.F., Frahme, C.W. , Julius Schlocker, Schneider, R.R., and Schuster R. L., *Swelling clays map of the conterminous United States*. (1989). <https://doi.org/10.3133/i1940>

- Perrone, A., Lapenna, V., & Piscitelli, S. (2014). "Electrical resistivity tomography technique for landslide investigation: A review." *Earth-Science Reviews*, 135, 65–82. <https://doi.org/10.1016/J.EARSCIREV.2014.04.002>
- Pieraccini, M., Parrini, F., Fratini, M., Atzeni, C., Spinelli, P., and Micheloni, M. (2007). "Static and dynamic testing of bridges through microwave interferometry." *NDT Int.*, 40(3), 208–214.
- Postance, B., Hillier, J., Dijkstra, T., & Dixon, N. (2018). Comparing threshold definition techniques for rainfall-induced landslides: A national assessment using radar rainfall. *Earth Surface Processes and Landforms*, 43(2), 553–560. <https://doi.org/10.1002/esp.4202>
- Pulat, H. F., Yukselen-Aksoy, Y., & Egeli, İ. (2014). The effect of soil mineralogy and pore fluid chemistry on the suction and swelling behavior of soils. *Bulletin of Engineering Geology and the Environment*, 73(1), 37–42. <https://doi.org/10.1007/s10064-013-0499-y>
- Ranjbar, H. (2011). Remote Sensing, Applications to Geophysics. In H. K. Gupta (Ed.), *Encyclopedia of Solid Earth Geophysics* (pp. 1035–1039). Springer Netherlands. https://doi.org/10.1007/978-90-481-8702-7_175
- Rashid, A. S. A., Sa, R., Mustaffar, M., Yusof, N. M., Rahman, N. A., & Dollah, R. (2022). "Investigation of rock slope stability using drone-based thermal sensor." *Journal of Advanced Geospatial and Science Technology* (Vol. 1, Issue 1). <https://jagst.utm.my>
- Sajinkumar, K. S., Rinu, S., Oommen, T., Vishnu, C. L., Praveen, K. R., Rani, V. R., & Muraleedharan, C. (2020). Improved rainfall threshold for landslides in data sparse and diverse geomorphic milieu: a cluster analysis based approach. *Natural Hazards*, 103(1), 639–657. <https://doi.org/10.1007/s11069-020-04004>
- Salunke, R., Nobahar, M., Alzeghoul, O. E., Khan, S., la Cour, I., & Amini, F. (2023). Near-Surface Soil Moisture Characterization in Mississippi's Highway Slopes Using Machine Learning Methods and UAV-Captured Infrared and Optical Images. *Remote Sensing*, 15(7), 1888. <https://doi.org/10.3390/rs15071888>
- Samouëlian, A., Cousin, I., Tabbagh, A., Bruand, A., & Richard, G. (2005). "Electrical resistivity survey in soil science: A review." In *Soil and Tillage Research* (Vol. 83, Issue 2, pp. 173–193). <https://doi.org/10.1016/j.still.2004.10.004>
- Samsonov, S., & Blais-Stevens, A. (2023). Satellite interferometry for regional assessment of landslide hazard to pipelines in northeastern British Columbia, Canada. *International Journal of Applied Earth Observation and Geoinformation*, 118, 103273. <https://doi.org/10.1016/j.jag.2023.103273>
- Shahmoradi, J., Talebi, E., Roghanchi, P., & Hassanalian, M. (2020). "A comprehensive review of applications of drone technology in the mining industry." In *Drones* (Vol. 4, Issue 3, pp. 1–25). MDPI AG. <https://doi.org/10.3390/drones4030034>
- Shirazi, M. R. (2014). Effect of temperature on hydro-mechanical behavior of compacted expansive soil (Doctoral dissertation, Eastern Mediterranean University (EMU)-Doğru Akdeniz Üniversitesi (DAÜ)).
- Siddiqui F. I., & Osman S. B. A. B. S. (2012). "Integrating geo-electrical and geotechnical data for soil characterization."

- Snethen, D. R., et al., "A Review of Engineering Experiences with Expansive Soils in Highway Subgrades," Report No. FHWA-RD-75-48, Jun 1975, Federal Highway Administration, Washington, D. C.
- Suk, J. W., Jeong, H. S., Jung, M. S., Kang, H. S., Kim, H. J., & Choi, S. G. (2022). Prediction of Shallow Failure on a Slope Using Volumetric Water Content Gradient Characteristics. *Applied Sciences (Switzerland)*, 12(11). <https://doi.org/10.3390/app12115308>
- Susaki, J. (2012). "Adaptive slope filtering of airborne lidar data in urban areas for digital terrain model (DTM) generation." *Remote Sensing*, 4(6), 1804–1819. <https://doi.org/10.3390/rs4061804>
- Tan, L., Zou, W., Liu, Z., & Pan, M. (2022). "Research on high-definition image acquisition method and fast image inspection equipment of highway slope based on UAV." <https://doi.org/10.1117/12.2658177>, 12460, 598–604. <https://doi.org/10.1117/12.2658177>
- Tardy, Y., Paquet, H., & Millot, G. (1970). Three types of montmorillonite genesis in soil weathering. *Bull. Grpe fr. Argiles*, 22, 69-77.
- Tilon, S., Nex, F., Vosselman, G., Sevilla de la Llave, I., & Kerle, N. (2022). Towards Improved Unmanned Aerial Vehicle Edge Intelligence: A Road Infrastructure Monitoring Case Study. In *Remote Sensing (Vol. 14, Issue 16)*. MDPI. <https://doi.org/10.3390/rs14164008>
- Van der Sluijs, J., Kokelj, S. v., Fraser, R. H., Tunnicliffe, J., & Lacelle, D. (2018). "Permafrost terrain dynamics and infrastructure impacts revealed by UAV photogrammetry and thermal imaging." *Remote Sensing*, 10(11). <https://doi.org/10.3390/rs10111734>
- Whitehurst, D., Joshi, K., Kochersberger, K., & Weeks, J. (2022). Post-Flood Analysis for Damage and Restoration Assessment Using Drone Imagery. *Remote Sensing*, 14(19), 4952. <https://doi.org/10.3390/rs14194952>
- Wolf, R. E., Bouali, H., Oommen, T., Cerminaro, D., Cunningham, K. W., Dobson, R., Brooks, C., Singh, C., & Director, P. E. (2014). Deliverable 2-A: Candidate Remote Sensing Techniques for the Different Transportation Environments, Requirements, Platforms, and Optimal Data Fusion Methods for Assessing the State of Geotechnical Assets.
- Wray, W.K. and Meyer, K.T. (2004) Expansive Clay Soil—A Widespread and Costly GeoHazard. *GeoStrata*, 5, 24-28.
- Wright, S.G., Zornberg, J.G., Aguetant, J.E. (2007). "The fully softened shear strength of high plasticity clays." *Transportation Research Board*, Washington DC, Number 0-52-2-3.
- Zapata, C. E., & Houston, W. N. (2008). Calibration and validation of the enhanced integrated climatic model for pavement design (Vol. 602). *Transportation Research Board*.